Ministry of Education and Science of the Russian Federation
Saint Petersburg National Research University of Information Technologies, Mechanics, and Optics

NANOSYSTEMS:

PHYSICS, CHEMISTRY, MATHEMATICS

2021, volume 12(2)

Наносистемы: физика, химия, математика
2021, том 12, № 2

NANO
Φ&X&M

NANOSYSTEMS:

PHYSICS, CHEMISTRY, MATHEMATICS

Address: University ITMO, Kronverkskiy pr., 49, St. Petersburg 197101, Russia.
Phone: +7(812) 607-02-54, **Journal site:** http://nanojournal.ifmo.ru/,
E-mail: popov1955@gmail.com

AIM AND SCOPE

The scope of the journal includes all areas of nano-sciences. Papers devoted to basic problems of physics, chemistry, material science and mathematics inspired by nanosystems investigations are welcomed. Both theoretical and experimental works concerning the properties and behavior of nanosystems, problems of its creation and application, mathematical methods of nanosystem studies are considered.

The journal publishes scientific reviews (up to 30 journal pages), research papers (up to 15 pages) and letters (up to 5 pages). All manuscripts are peer-reviewed. Authors are informed about the referee opinion and the Editorial decision.

CONTENT

MATHEMATICS

PHYSICS

CHEMISTRY AND MATERIAL SCIENCE

NANOSYSTEMS: PHYSICS, CHEMISTRY, MATHEMATICS, 2021, 12 (2), P. 135–141

Non-compact perturbations of the spectrum of multipliers given with functions

R. R. Kucharov[1], R. R. Khamraeva[1,2]

[1]National University of Uzbekistan, 100174, Tashkent, Uzbekistan
[2]Westminster International University in Tashkent, 100010, 12, Istiqbol str., Tashkent, Uzbekistan
ramz3364647@yahoo.com, r.khamraeva@wiut.uz

DOI 10.17586/2220-8054-2021-12-2-135-141

The change in the spectrum of the multipliers $H_0f(x,y) = x^\alpha + y^\beta f(x,y)$ and $H_0f(x,y) = x^\alpha y^\beta f(x,y)$ for perturbation with partial integral operators in the spaces $L_2[0,1]^2$ is studied. Precise description of the essential spectrum and the existence of simple eigenvalue is received. We prove that the number of eigenvalues located below the lower edge of the essential spectrum in the model is finite.

Keywords: essential spectrum, discrete spectrum, lower bound of the essential spectrum, partial integral operator.

Received: 25 January 2021

Revised: 10 March 2021

Final revision: 12 March 2021

1. Introduction

The first results on the finiteness of the discrete spectrum of N – particle Hamiltonians with $N > 2$ were obtained by Uchiyama in 1969 [1–3]. He found sufficient conditions for the finiteness of the number of discrete eigenvalues for energy operators in the space $L_2(\mathbb{R}^6)$ for the system of two identically charged particles in the field of a fixed center with or without an external electromagnetic field. In 1971, Zhislin proved the finiteness of the discrete spectrum for energy operators in symmetry spaces of negative atomic ions with nuclei of any mass and of molecules with infinitely heavy nuclei under the assumption that the total charge of the system is less than -1 [4].

Let Ω_1 and Ω_2 be closed bounded sets in $\mathbb{R}^{\nu_1}$ and $\mathbb{R}^{\nu_2}$, respectively. In the space $L_p(\Omega_1 \times \Omega_2),\ p \geq 1$ partially integral operator (PIO) T of the Fredholm type in general is given by the equality [5]:

$$T = T_0 + T_1 + T_2 + K, \tag{1}$$

where the operators T_0, T_1, T_2, K have the following view:

$$T_0f(x,y) = k_0(x,y)f(x,y), \quad T_1f(x,y) = \int\limits_{\Omega_1} k_1(x,s,y)f(s,y)d\mu_1(s),$$

$$T_2f(x,y) = \int\limits_{\Omega_2} k_2(x,t,y)f(x,t)d\mu_2(t), \quad Kf(x,y) = \int\limits_{\Omega_1}\int\limits_{\Omega_2} k(x,y;s,t)f(s,t)d\mu_1(s)d\mu_2(t).$$

Here, the functions k_0, k_1, k_2, and k are given measurable functions in the concept of Lebesque on $\Omega_1 \times \Omega_2$, $\Omega_1^2 \times \Omega_2$, $\Omega_1 \times \Omega_2^2$ and $(\Omega_1 \times \Omega_2)^2$, respectively, and integration of functions is understood in the concept of Lebesgue, where $\mu_k(\cdot)$ – Lebesque measure on $\Omega_k,\ k = 1, 2$.

In the Hilbert space $L_2(\Omega \times \Omega)$, where $\Omega = [a,b]^\nu$, consider the following model operator:

$$H = H_0 - (\gamma T_1 + \mu T_2),\ \gamma > 0,\ \mu > 0. \tag{2}$$

Here, the actions of the operators H_0, T_1 and T_2 are determined by formulas:

$$H_0f(x,y) = k_0(x,y)f(x,y),$$

$$T_1f(x,y) = \int\limits_{\Omega} \varphi_1(x)\varphi_1(s)f(s,y)ds, \quad T_2f(x,y) = \int\limits_{\Omega} \varphi_2(y)\varphi_2(t)f(x,t)dt,$$

where $k_0(x,y)$ is a nonnegative continuous function on $\Omega \times \Omega$, $\varphi_j(\cdot)$ is a continuous function on Ω and

$$\int\limits_{\Omega} \varphi_j^2(t)dt = 1,\ j = 1, 2.$$

Via $\rho(\cdot), \sigma(\cdot), \sigma_{ess}(\cdot)$ and $\sigma_{disc}(\cdot)$ denote, respectively, the resolvent set, spectrum, essential spectrum and discrete spectrum self-adjoint operators [6].

In [7], sufficient conditions for finiteness and infinity were obtained in the discrete spectrum for $\sigma_{ess}(H) = \sigma(H_0)$. In work [8] proved the existence of the Efimov effect in model (2) for given $k_0(x,y)$. In [9], the essential spectrum and the number eigenvalues below the lower bound of the essential spectrum in model (2), when the function $k_0(x,y)$ has the form: $k_0(x,y) = u(x)u(y)$, where $u(x)$ is a nonnegative continuous function on $\Omega = \Omega_1 = \Omega_2$ and $\int\limits_{\Omega} \frac{dx}{u(x)} < \infty$. In [10] studied the existence of an infinite number of eigenvalues (the existence of Efimov's effect) for a selfadjoint partial integral operators.

2. The lower boundary of the essential spectrum of V

Consider the multiplier:

$$V_0 f(x,y) = (x^\alpha + y^\beta) f(x,y), \ \alpha > 0, \ \beta > 0.$$

Let us define a partially integral operator (PIO) V:

$$V = V_0 - \gamma(T_1 + T_2), \ \gamma > 0, \tag{3}$$

where:

$$T_1 f(x,y) = \int\limits_0^1 f(s,y)ds, \quad T_2 f(x,y) = \int\limits_0^1 f(x,t)dt, \ f \in L_2[0,1]^2.$$

In the space $L_2[0,1]$ we define the operators H_1 and H_2 in Friedrichs models:

$$H_1\varphi(x) = x^\alpha \varphi(x) - \gamma \int\limits_0^1 \varphi(s)ds, \quad H_2\psi(y) = y^\beta \psi(y) - \gamma \int\limits_0^1 \psi(t)dt.$$

Lemma 1. [11] The number $\lambda \in \mathbb{R}\backslash[0,1]$ is the eigenvalue of the operator H_1 (of the operator H_2) if and only if $\Delta_1(\lambda) = 0$ ($\Delta_2(\lambda) = 0$), where:

$$\Delta_1(\lambda) = 1 - \gamma \int\limits_0^1 \frac{ds}{s^\alpha - \lambda}, \quad \Delta_2(\lambda) = 1 - \gamma \int\limits_0^1 \frac{ds}{s^\beta - \lambda}.$$

Lemma 2.

A)

$$\lim_{\lambda \to 0-} \Delta_1(\lambda) = \begin{cases} 1 - \dfrac{\gamma}{1-\alpha}, & \text{if } 0 < \alpha < 1; \\ -\infty, & \text{if } \alpha \geq 1, \end{cases}$$

B)

$$\lim_{\lambda \to 0-} \Delta_2(\lambda) = \begin{cases} 1 - \dfrac{\gamma}{1-\beta}, & \text{if } 0 < \beta < 1; \\ -\infty, & \text{if } \beta \geq 1. \end{cases}$$

Proof. First, we prove the statement A.

a) Let $0 < \alpha < 1$. Consider an arbitrary increasing sequence $\{\lambda_n\}_{n\in\mathbb{N}}$ of negative numbers approaching to zero, i.e $\lambda_n \leq \lambda_{n+1} < 0$ and $\lim\limits_{n\to\infty} \lambda_n = 0$. Then:

$$0 < \frac{1}{s^\alpha - \lambda_n} \leq \frac{1}{s^\alpha - \lambda_{n+1}}, \ n \in \mathbb{N}$$

and

$$\frac{1}{s^\alpha - \lambda_n} \leq \frac{1}{s^\alpha} \text{ for almost all } s \in [0,1].$$

The function $h_0(s) = \dfrac{1}{s^\alpha}$ is integrable by $[0,1]$ in the concept of Lebesgue and:

$$\int\limits_0^1 h_0(s)ds = \frac{1}{1-\alpha}.$$

Hence, due to Lebesgue theorem on limited transition under the sign of the Lebesgue integral it follows that:

$$\lim_{\lambda\to 0-}\int\limits_0^1 \frac{ds}{s^\alpha-\lambda}=\frac{1}{1-\alpha}.$$

Thus, we have:

$$\lim_{\lambda\to 0-}\Delta_1(\lambda)=1-\frac{\gamma}{1-\alpha}.$$

b) Let $\alpha\geq 1$. Suppose that $\alpha=1$. Then:

$$\lim_{\lambda\to 0-}\Delta_1(\lambda)=1-\gamma\lim_{\lambda\to 0-}\int\limits_0^1\frac{ds}{s-\lambda}=1-\gamma\lim_{\lambda\to 0-}\ln\left(1-\frac{1}{-\lambda}\right)=-\infty.$$

If $\alpha>1$, then we have:

$$\frac{1}{s^\alpha-\lambda}\geq\frac{1}{s-\lambda},\ \ s\in[0,1].$$

Hence:

$$\lim_{\lambda\to 0-}\int\limits_0^1\frac{ds}{s^\alpha-\lambda}\geq\lim_{\lambda\to 0-}\int\limits_0^1\frac{ds}{s-\lambda}=+\infty,$$

i.e.

$$\lim_{\lambda\to 0-}\Delta_1(\lambda)=-\infty.$$

Proposition 1. I) Let $0<\alpha<1$ $(0<\beta<1)$. Then:

a) if $\alpha+\gamma\leq 1$ $(\beta+\gamma\leq 1)$, then the operator H_1 (operator H_2) outside the essential spectrum has the only eigenvalue of the operator;

b) if $\alpha+\gamma>1$ $(\beta+\gamma>1)$, then the operator H_1 (operator H_2) outside the essential spectrum has the only eigenvalue of the operator ξ_1 (the eigenvalue value ξ_2), while ξ_k is a simple proper value H_k $\xi_k<0$, $k=1,2$.

II) Let $\alpha\geq 1$ $(\beta\geq 1)$. Then the operator H_1 (operator H_2) outside the essential spectrum has a unique eigenvalue ξ_1 (eigenvalue ξ_2), for this ξ_k is a simple eigenvalue of the operator H_k and $\xi_k<0$, $k=1,2$.

Proof. It is easy to note that the function $\Delta_1(\lambda)$ by $(-\infty,0)$ is strictly decreasing and $\Delta_1(\lambda)>0$ to $(1,\infty)$, thus, the operator H_1 on the set $(1,\infty)$ has no eigenvalue.

Let $0<\alpha<1$. By Lemma 2 and monotonicity, the function $\Delta_1(\lambda)$ to $(-\infty,0)$ states a and b, since:

$$\mathrm{Ran}(\Delta_1)=\left(1-\frac{\gamma}{1-\alpha},1\right).$$

Let $\alpha\geq 1$. Then from Lemma 2 we obtain: $\mathrm{Ran}(\Delta_1)=(-\infty,1)$. Due to monotonicity functions $\Delta_1(\lambda)$ $(-\infty,0)$ equation $\Delta_1(\lambda)=0$ $(-\infty,0)$ has a unique solution $\xi_1<0$ ξ_1 is a simple eigenvalue operator H_1.

Proposition 1 for the operator H_2 is proved similarly.

Theorem 1. Let $0<\alpha<1$ and $0<\beta<1$. Then:

a) if $\alpha+\gamma\leq 1$ and $\alpha+\beta\leq 1$, then:

$$\sigma(V)=\sigma_{ess}(V)=\sigma(V_0)=[0,2];$$

b) if $\alpha+\gamma>1$ and $\alpha+\beta\leq 1$, then

$$\sigma(V)=\sigma_{ess}(V)=\sigma(V_0)\cup[\xi_1,1+\xi_1],$$

where ξ_1 – negative eigenvalue of operator H_1;

c) if $\alpha+\gamma\leq 1$ and $\alpha+\beta>1$, then:

$$\sigma_{ess}(V)=\sigma(V_0)\cup[\xi_2,1+\xi_2],$$

where ξ_2 is a negative eigenvalue of operator H_2;

d) if $\alpha+\gamma>1$ and $\alpha+\beta>1$, then:

$$\sigma_{ess}(V)=\sigma(V_0)\cup[\xi_1,1+\xi_1]\cup[\xi_2,1+\xi_2]\ \text{ and }\ \sigma_{disc}(V)=\{\omega_0\},$$

where $\omega_0=\xi_1+\xi_2$ and ω_0 is a simple eigenvalue of operator V.

Proof. It is easy to note that the operator V will be unitarily equivalent to the operator $H_1\otimes E+E\otimes H_2$ (see [12]). Then $\sigma(V)=\sigma(H_1)+\sigma(H_2)$ and for of multiplicity $n_V(\omega)$ eigenvalue $\omega\in\sigma(V)\setminus\sigma_{ess}(V)$ of the operator V the following equality takes place:

$$n_V(\omega) = \sum_{\substack{p+q=\omega \\ (p,q)\in\sigma(H_1)\times\sigma(H_2)}} n_{H_1}(p)\cdot n_{H_2}(q),$$

where $n_{H_1}(p)$ and $n_{H_2}(q)$ – multiplicity of the eigenvalues p and q of the operators H_1 and H_2, respectively. This and Proposition 1 imply the proof the theorem.

Theorem 2. Let $\alpha \geq 1$ and $0 < \beta < 1$. Then:

a) if $\beta + \gamma \leq 1$, then:

$$\sigma(V) = \sigma_{ess}(V) = \sigma(V_0) \cup [\xi_1, 1 + \xi_1];$$

b) if $\beta + \gamma > 1$, then:

$$\sigma_{ess}(V) = \sigma(V_0) \cup [\xi_1, 1 + \xi_1] \cup [\xi_2, 1 + \xi_2] \text{ and } \sigma_{disc}(V) = \{\omega_0\},$$

where $\omega_0 = \xi_1 + \xi_2$ and ω_0 is a simple eigenvalue of the operator V.

Theorem 3. Let $\alpha \geq 1$ and $\beta \geq 1$. Then:

$$\sigma_{ess}(V) = \sigma(V_0) \cup [\xi_1, 1 + \xi_1] \cup [\xi_2, 1 + \xi_2] \text{ and } \sigma_{disc}(V) = \{\omega_0\},$$

where $\omega_0 = \xi_1 + \xi_2$ è ω_0 – is a simple eigenvalue of the operator V.

Corollary 1. Let $0 < \alpha < 1$ and $0 < \beta < 1$. Then:

$$E_{\min}(V) = \begin{cases} 0, & \text{if } \alpha + \gamma \leq 1 \text{ and } \beta + \gamma \leq 1, \\ \xi_1, & \text{if } \alpha + \gamma > 1 \text{ and } \beta + \gamma \leq 1, \\ \xi_2, & \text{if } \alpha + \gamma \leq 1 \text{ and } \beta + \gamma \geq 1, \\ \min\{\xi_1, \xi_2\}, & \text{if } \alpha + \gamma > 1 \text{ and } \beta + \gamma > 1. \end{cases}$$

3. Discrete spectrum of partial integral operators

Let's define the multiplier H_0:

$$H_0 f(x,y) = x^\alpha y^\beta f(x,y), \quad \alpha > 0, \ \beta > 0,$$

and the operators T_1, T_2:

$$T_1 f(x,y) = \int_0^1 f(s,y)ds, \quad T_2 f(x,y) = \int_0^1 f(x,t)dt.$$

Let us define a self-conjugate PIO H:

$$H = H_0 - \gamma(T_1 + T_2), \ \gamma > 0.$$

We have $\sigma(H_0) = [0,1]$. For each $\lambda \in \mathbb{R} \setminus [0,1]$ define the function $\Delta_1(y;\lambda)$ on [0,1] ($\Delta_2(x;\lambda)$ on $[0,1]$) by formula:

$$\Delta_1(y;\lambda) = 1 - \gamma \int_0^1 \frac{ds}{s^\alpha y^\beta - \lambda}, \quad \Delta_2(x;\lambda) = 1 - \gamma \int_0^1 \frac{ds}{x^\alpha s^\beta - \lambda}.$$

In the space $L_2[0,1]$ we define the family $\{H_1(t)\}_{t\in[0,1]}$ of the self-adjoint operators in the Friedrichs' model:

$$H_1(t)\varphi(x) = t^\beta x^\alpha \varphi(x) - \gamma \int_0^1 \varphi(s)ds.$$

Similarly, in the space $L_2[0,1]$ we define the family $\{H_2(t)\}_{t\in[0,1]}$:

$$H_2(t)\psi(y) = t^\alpha y^\beta \psi(y) - \gamma \int_0^1 \psi(s)ds.$$

Lemma 3. Function:

$$\pi_j(t) = \inf_{\|\varphi\|=1} (H_j(t)\varphi, \varphi), \ t \in [0,1] \ (j = 1,2) \tag{3}$$

is non-positive, continuous and increasing on $[0,1]$.

Proof. In work [9], there is a proof of the continuity and non-positivity of the function $\pi_j(t)$ on $[0,1]$. We will show the monotonicity of the function $\pi_j(t)$ on $[0,1]$. We define the family of the $\{H_0(t)\}_{t\in[0,1]}$ multipliers:

$$H_0(t)\varphi(x) = x^\alpha t^\beta \varphi(x),\ \ \varphi \in L_2[0,1].$$

Then it follows from $t_1 \le t_2,\ \ t_1, t_2 \in [0,1]$ that:

$$H_0(t_1) \le H_0(t_2).$$

Therefore, we have:

$$\pi_1(t_1) = \inf_{\|\varphi\|=1}(H_1(t_1)\varphi,\varphi) = \inf_{\|\varphi\|=1}\left[(H_0(t_1)\varphi,\varphi) - \gamma(K_1\varphi,\varphi)\right] \le$$

$$\inf_{\|\varphi\|=1}(H_1(t_2)\varphi,\varphi) = \inf_{\|\varphi\|=1}\left[(H_0(t_2)\varphi,\varphi) - \gamma(K_1\varphi,\varphi)\right] = \pi_1(t_2),$$

Where:

$$K_1\varphi(x) = \int\limits_0^1 \varphi(s)ds.$$

This means that the function $\pi_1(t)$ is increasing on the set $[0,1]$.

Obviously, for each $y \in [0,1]$ the function $\Delta_1(\lambda) = \Delta_1(y;\lambda)$ is strictly decreasing on $(-\infty, 0)$. Therefore, for each $y \in [0,1]$ there exists finite or infinite limit $\lim\limits_{\lambda\to 0-}\Delta_1(y;\lambda)$. Moreover, there is:

Lemma 4. a) if $0 < \alpha < 1$, then for each $y \in (0,1]$:

$$\lim_{\lambda\to 0-}\Delta_1(y;\lambda) = 1 - \frac{\gamma}{1-\alpha}\cdot\frac{1}{y^\beta};$$

b) if $\alpha \ge 1$, then for each $y \in (0,1]$:

$$\lim_{\lambda\to 0-}\Delta_1(y;\lambda) = -\infty.$$

Proof. a) Let $0 < \alpha < 1$. Then, for $y \in (0,1]$ we get

$$\frac{1}{s^\alpha y^\beta - \lambda} \le h_0(s,y) = \frac{1}{s^\alpha y^\beta}$$

and for any ascending sequence $\{\lambda_n\}$ negative numbers decreasing to zero we have:

$$\frac{1}{s^\alpha y^\beta - \lambda_n} \le \frac{1}{s^\alpha y^\beta - \lambda_{n+1}},\ \ n \in \mathbb{N}.$$

On the other hand, for each $y \in (0,1]$ there exists a Lebesgue integral from function $h_1(s,y)$ on $s \in [0,1]$:

$$\int\limits_0^1 h_0(s,y)ds = \frac{1}{1-\alpha}\cdot\frac{1}{y^\beta}.$$

Then, by Lebesgue's theorem on the limited transition under the sign of the Lebesgue integral, we obtain:

$$\lim_{\lambda\to 0-}\Delta_1(y;\lambda) = 1 - \frac{\gamma}{1-\alpha}\cdot\frac{1}{y^\beta},\ \ y \in (0,1];$$

b) Let $\alpha \ge 1$ and assume that $\alpha = 1$. It is obvious that for $y = 0$ we have: $\lim\limits_{\lambda\to 0-}\Delta_1(y;\lambda) = -\infty$. For each $y \in (0,1]$ we have:

$$\int\limits_0^1 \frac{ds}{s^\alpha y^\beta - \lambda} = \int\limits_0^1 \frac{ds}{sy^\beta - \lambda} = \frac{1}{y^\beta}\ln\left(1 - \frac{y^\beta}{\lambda}\right).$$

Therefore for $y \in (0,1]$ we get:

$$\lim_{\lambda\to 0-}\Delta_1(y;\lambda) = 1 - \frac{\gamma}{y^\beta}\lim_{\lambda\to 0-}\ln\left(1 - \frac{y^\beta}{\lambda}\right) = -\infty;$$

Suppose that $\alpha > 1$. Then from inequality:

$$\int\limits_0^1 \frac{ds}{s^\alpha y^\beta - \lambda} \geq \int\limits_0^1 \frac{ds}{sy^\beta - \lambda},\ \ y \in [0,1]$$

we get that

$$\lim_{\lambda\to 0-} \int\limits_0^1 \frac{ds}{s^\alpha y^\beta - \lambda} = +\infty,\ \ y \in [0,1]$$

and accordingly, $\lim\limits_{\lambda\to 0-} \Delta_1(y;\lambda) = -\infty$.

Obviously, the function:

$$h_1(y) = \lim_{\lambda\to 0-} \Delta_1(y;\lambda) = 1 - \frac{\gamma}{1-\alpha}\cdot\frac{1}{y^\beta}$$

increases by $(0,1]$ from $-\infty$ to $h_1^{\max} = h_1(1) = 1 - \dfrac{\gamma}{1-\alpha}$.

We put:

$$\pi_j^{\max} = \max_{t\in[0,1]} \pi_j(t),\ \ j = 1,2.$$

Then $\pi_j^{\max} = \pi_j(1)$.

Lemma 5. Let $0 < \alpha < 1$ $(0 < \beta < 1)$. Then:

a) if $\gamma + \alpha \leq 1$ $(\gamma + \beta \leq 1)$, then $\pi_1^{\max} = 0$ $(\pi_2^{\max} = 0)$;

b) if $\gamma + \alpha > 1$ $(\gamma + \beta > 1)$, then $\pi_1^{\max} < 0$ $(\pi_1^{\max} < 0)$.

Proof. Let $0 < \alpha < 1$. a) Assume that: $\gamma + \alpha = 1$. We have:

$$h_1^{\max} = h_1(1) = \lim_{\lambda\to 0-} \Delta_1(1;\lambda) = 1 - \frac{\gamma}{1-\alpha} = 0.$$

Hence, taking into account the monotonicity of the function $\Delta_1(1;\lambda)$ by $\lambda < 0$ we get that $\Delta_1(1;\lambda) > 0$ for any $\lambda < 0$. Then, according to Proposition 1, the operator $H_1(1)$ has no eigenvalue below the bottom edge the essential spectrum of the operator $H_1(1)$. By the minmax principle and from equality (3) we obtain that $\pi_1^{\max} = \pi_1(1) = E_{\min}(H_1(1)) = 0$.

If $\gamma+\alpha < 1$. Then $h_1^{\max} = h_1(1) > 0$. On the other hand $\Delta_1(1;\lambda) > h_1^{\max}$. Then according to the proposition 1, the operator $H_1(1)$ has no negative eigenvalue value. It follows that $\pi_1^{\max} = 0$.

b) Let $\gamma + \alpha > 1$. Then:

$$h_1(y) \leq h_1^{\max} = 1 - \frac{\gamma}{1-\alpha} < 0.$$

Therefore, for for each $y \in (0,1]$ we have $h_1(y) = \lim\limits_{\lambda\to 0-} \Delta_1(y;\lambda) < 0$. Hence, since the function $\Delta_1(y;\lambda)$ is monotonic with respect to $\lambda < 0$ implies the existence of a unique number $\lambda_0 = \lambda_0(y) < 0$ (for each $y \in (0,1]$) such that $\Delta_1(y;\lambda_0(y)) = 0$. For $y = 0$ we have $\Delta_1(0;-\gamma) = 0$, i.e $\lambda_0 = \lambda_0(0) = -\gamma$ is a solution to the equation $\Delta_1(0;\lambda) = 0$. Due to minmax principle [13] solution of $\lambda_0(y)$ equation $\Delta_1(y;\lambda) = 0$ is defined using continuous function $\pi_1(t)$, i.e. $\lambda_0(t) = \pi_1(t)$, $t \in [0,1]$. However $\lambda_0(y) < 0$, $y \in [0,1]$. Therefore $\pi_1(1) = \pi_1^{\max} < 0$.

Lemma 6. Let $\alpha \geq 1$ $(\beta \geq 1)$. Then $\pi_1^{\max} < 0$ $(\pi_2^{\max} < 0)$.

Proof. For $y = 1$ we get:

$$\Delta_1(\lambda) = \Delta_1(1;\lambda) = 1 - \int\limits_0^1 \frac{ds}{s^\alpha - \lambda}.$$

We have:

$$\lim_{\lambda\to-\infty} \Delta_1(\lambda) = 1 \text{ and } \lim_{\lambda\to 0-} \Delta_1(\lambda) = -\infty.$$

Then, due to the monotonicity of the function $\Delta_1(\lambda)$ for $\lambda < 0$ we obtain the existence of unique number $\lambda_0 < 0$, such as $\Delta_1(\lambda_0) = 0$. Therefore, $\lambda_0 = \pi_1^{\max} < 0$.

By the theorem 3.3 [14] and Lemma 3,4 or the essential spectrum operator H we obtain the following statement.

Theorem 4. For the essential spectrum of the operator H there is a place for equality:

$$\sigma_{ess}(H) = [-\gamma, \gamma_0] \cup [0,1],$$

where $\gamma_0 = \max\{\pi_1^{\max}, \pi_2^{\max}\}$.

From the positivity of the operators H_0, T_1 and T_2 for the operator H we have:

$$\sigma(H) \subset (-\infty, 1],$$

i.e. above the upper edge of the essential spectrum $\sigma_{ess}(H)$ of the operator H eigenvalues are missing. Then, by the theorem 4 the discrete spectrum of the operator H lies in the set of negative numbers.

We put:

$$\xi_0 = \frac{1}{(1+\alpha)(1+\beta)}.$$

Theorem 5. If $\gamma > \xi_0$, then the operator H has the negative eigenvalue, lying to the left of the bottom edge of the essential spectrum.

Proof. Assume the conditions $\gamma > \xi_0$. Put $f_0(x,y) = 1$. Then $\|f_0\| = 1$ and

$$(Hf_0, f_0) = (H_0 f_0, f_0) - \gamma((T_1 f_0, f_0) + (T_2 f_0, f_0)) = \xi_0 - 2\gamma.$$

Then, by the theorem 4 we have $E_{\min}(H) = -\gamma$ and from $\gamma > \xi_0$ we get that

$$\lambda_0 = (Hf_0, f_0) < -\gamma = E_{\min}(H).$$

Hereof and according to the minmax principle we get that $\lambda_0 \in \sigma_{disc}(H)$, i.e. $\lambda_0 = \xi_0 - 2\gamma$ – is the eigenvalue of the operator H.

Corollary 2. Number of eigenvalues of the operator H is at most one and for $\gamma > \xi_0$ the discrete spectrum of the operator H is not empty.

References

[1] Uchiyama J. Finiteness of the Number of Discrete Eigenvalues of the Schrodinger Operator for a Three Particle System. 1969, *Publ. Res. Inst. Math. Sci.*, **5** (1), P. 51–63.

[2] Uchiyama J. Corrections to "Finiteness of the Number of Discrete Eigenvalues of the Schrodinger Operator for a Three Particle System". *Publ. Res. Inst. Math. Sci.*, 1970, **6** (1), P. 189–192.

[3] Uchiyama J. Finiteness of the Number of Discrete Eigenvalues of the Schrodinger Operator for a Three Particle System. *Publ. Res. Inst. Math. Sci.*, 1970, **6** (1), P. 193–200.

[4] Zhislin G.M. On the finiteness of the discrete spectrum of the energy operator of negative atomic and molecular ions. *Theor. Math. Phys.*, 1971, **7**, P. 571–578.

[5] Appell J., Frolova E.V., Kalitvin A.S., Zabrejko P.P. Partial integral operators on $C([a,b] \times [c,d])$. *Integral Equ. Oper. theory*, 1997, **27**, P. 125–140.

[6] Faddeev L.D. On a model of Friedrichs in the theory of perturbations of the continuous spectrum. *Trudy Mat. Inst. Steklov*, 1964, **73**, 292 [in Russian].

[7] Albeverio S., Lakaev S.N., Muminov Z.I. On the number of eigenvalues of a model operator associated to a system of three-particles on lattices. *Russ. J. Math. Phys.*, 2007, **14** (4), P. 377—387.

[8] Rasulov T.Kh. Asymptotics of the discrete spectrum of a model operator assotiated with a system of three particles on a lattice. *Theor. and Math. Phys.*, 2010, **163** (1), P. 429–437.

[9] Eshkabilov Yu.Kh., Kucharov R.R. Essential and discrete spectra of the three-particle Schrodinger operator on a lattice. *Theor. Math. Phys.*, 2012, **170** (3), P. 341-–353.

[10] Eshkabilov Yu.Kh., Kucharov R.R. Efimov's effect for partial integral operators of Fredholm type. *Nanosystems: Physics, Chemistry, Mathematics*, 2013, **4** (4), P. 529–537.

[11] Eshkabilov Yu.Kh. On infinity of the discrete spectrum of operators in the Friedrichs model. *Siberian Adv. Math.*, 2012, **22** (1).

[12] Reed M., Simon B. *Methods of Modern Mathematical Physics, Vol. 4, Analysis of Operators*, Acad. Press, New York, 1982.

[13] Eshkabilov Yu.Kh. Efimov's effect for a 3-particle model discrete Schrodinger operator. *Theor. Math. Phys.*, 2010, **164** (1), P. 896-–904.

[14] Eshkabilov Yu.Kh. On a discrete "three-particle" Schrodinger operator in the Hubbard model. *Theor. Math. Phys.*, 2006, **149** (2), P. 1497–1511.

NANOSYSTEMS: PHYSICS, CHEMISTRY, MATHEMATICS, 2021, 12 (2), P. 142–150

Chemical applicability of Gourava and hyper-Gourava indices

B. Basavanagoud, Shruti Policepatil

Department of Mathematics, Karnatak University, Dharwad – 580 003, Karnataka, India

b.basavanagoud@gmail.com, shrutipatil300@gmail.com

DOI 10.17586/2220-8054-2021-12-2-142-150

Topological indices are extensively used as molecular descriptors in building Quantitative Structure-Activity Relationship (QSAR), Quantitative Structure-Property Relationship (QSPR) and Quantitative Structure-Toxicity Relationship (QSTR). In this paper, Gourava and hyper-Gourava indices are tested with physico-chemical properties of octane isomers such as entropy, acentric factor and DHVAP using linear regression models. The first Gourava index highly correlates with entropy (coefficient of correlation 0.9644924) and the second Gourava index highly correlates with acentric factor (coefficient of correlation 0.962243). Further, Gourava and hyper-Gourava indices are obtained for the line graph of subdivision graph of 2D-lattice, nanotube and nanotorus of $TUC_4C_8[p,q]$.

Keywords: topological indices, Gourava indices, hyper-Gourava indices, 2D-lattice of $TUC_4C_8[p,q]$, $TUC_4C_8[p,q]$ nanotube, $TUC_4C_8[p,q]$ nanotorus.

Received: 12 March 2021

Revised: 17 March 2021

1. Introduction

Let $G=(V,E)$ be a graph with a vertex set $V(G)$ and an edge set $E(G)$ such that $|V(G)|=n$ and $|E(G)|=m$. The degree of a vertex $d_G(v)$ is the number of edges incident to it in G. For undefined graph theoretic terminologies and notations refer to [1] or [2]. The *line graph* [1] $L(G)$ of a graph G with vertex set as the edge set of G and two vertices of $L(G)$ are adjacent whenever the corresponding edges in G have a vertex incident in common. The *subdivision graph* [1] $S(G)$ of a graph G whose vertex set is $V(G)\cup E(G)$ where two vertices are adjacent if and only if one is a vertex of G and other is an edge of G incident with it.

Topological indices promise to have far-reaching applications in drug design, cancer research and bonding theory etc. Among them, first degree based topological index is first Zagreb index developed in 1972 [3]. Further, the second Zagreb index [4] and F-index [5] were studied. Motivated by the definitions of the Zagreb indices and their wide applications, Kulli introduced the first Gourava index and second Gourava index of a molecular graph [6] as follows:

$$GO_1(G)=\sum_{uv\in E(G)}\big[d_G(u)+d_G(v)+d_G(u)d_G(v)\big],$$

$$GO_2(G)=\sum_{uv\in E(G)}\big[\big(d_G(u)+d_G(v)\big)\big(d_G(u)d_G(v)\big)\big].$$

In [7], Kulli introduced the first and second hyper-Gourava indices of a molecular graph G which are defined as:

$$HGO_1(G)=\sum_{uv\in E(G)}\big[d_G(u)+d_G(v)+d_G(u)d_G(v)\big]^2,$$

$$HGO_2(G)=\sum_{uv\in E(G)}\big[\big(d_G(u)+d_G(v)\big)\big(d_G(u)d_G(v)\big)\big]^2.$$

Alkanes are the important organic compounds classified under hydrocarbons and they are saturated, that is the carbon backbone consists of carbon to carbon single bonds only. There are a wide variety of alkanes that play vital roles in our daily life. Alkanes are used in LPG (Liquefied Petroleum Gas), propellants, disposable lighters etc. Alkanes containing 5 – 8 carbon atoms are used as fuel and as good solvents for nonpolar substances. For this purpose, they are widely used in industries and research work. Two or more compounds having same molecular formula but different chemical structures are called isomers. Eighteen isomers of octane are depicted in Fig. 1.

A nanostructure is an object that has at least one dimension equal to or smaller than 100 nanometers. There are various types of nanostructures such as nanoparticles, nanotubes and nanopores etc., In the last few years, much research has been concentrated on the use of nanostructures towards problems of biology and medicine. Topological index of $TURC_4C_8(S)$ nanotube, armchair polyhex nanotube, V-phenylenic nanotube and V-phenylenic nanotori are discussed in [8]. For more discussion on nanostructures, readers are referred to [9–11].

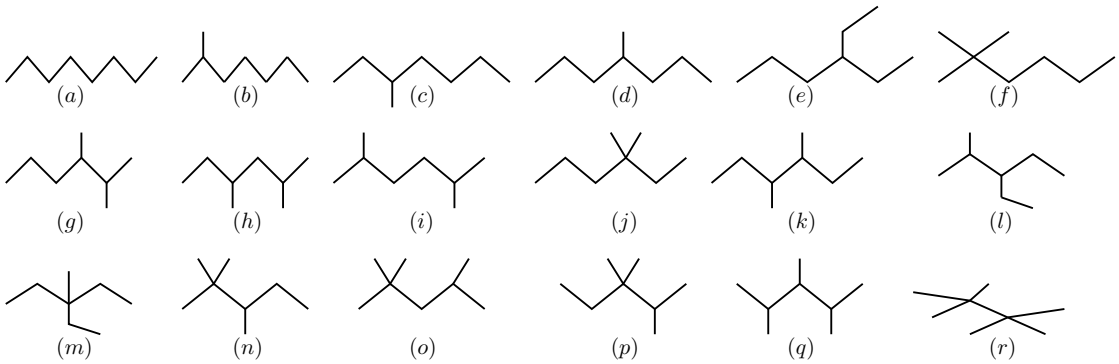

FIG. 1. (a) n-octane; (b) 2-methyl heptane; (c) 3-methyl heptane; (d) 4-methyl heptane; (e) 3-ethyl hexane; (f) 2,2-dimethyl hexane; (g) 2,3-dimethyl hexane; (h) 2,4-dimethyl hexane; (i) 2,5-dimethyl hexane; (j) 3,3-dimethyl hexane; (k) 3,4-dimethyl hexane; (l) 3-ethyl-2-methyl pentane; (m) 3-ethyl-3-methyl pentane; (n) 2,2,3-trimethyl pentane; (o) 2,2,4-trimethyl pentane; (p) 2,3,3-trimethyl pentane; (q) 2,3,4-trimethyl pentane; (r) 2,2,3,3-tetramethyl butane.

2. Chemical applicability of Gourava and hyper-Gourava indices

In this section, we present a linear regression model of these physical properties with the Gourava and hyper-Gourava indices. Gourava and hyper-Gourava indices are degree based indices. These indices have good correlation with physical properties of chemical compounds like entropy (S), acentric factor (AcentFac) and standard enthalpy of vaporization (DHVAP) of octane isomers. Gourava and hyper-Gourava indices are tested using a data set of octane isomers found at `http://www.moleculardescriptors.eu/dataset.htm`. The columns 5, 6, 7 and 8 of Table 2 are computed by using the definition of first Gourava index, second Gourava index, first hyper-Gourava index and second hyper-Gourava index, respectively.

The linear regression models for entropy, acentic factor and DHVAP using the data of Tables 2 are obtained using the least squares fitting procedure as implemented in R software [12].

Gourava indices values against entropy, acentric factor and DHVAP values are plotted in Figs. 2, 4 and 6. Hyper-Gourava indices values against entropy, acentric factor and DHVAP values are plotted in Figs. 3, 5 and 7.

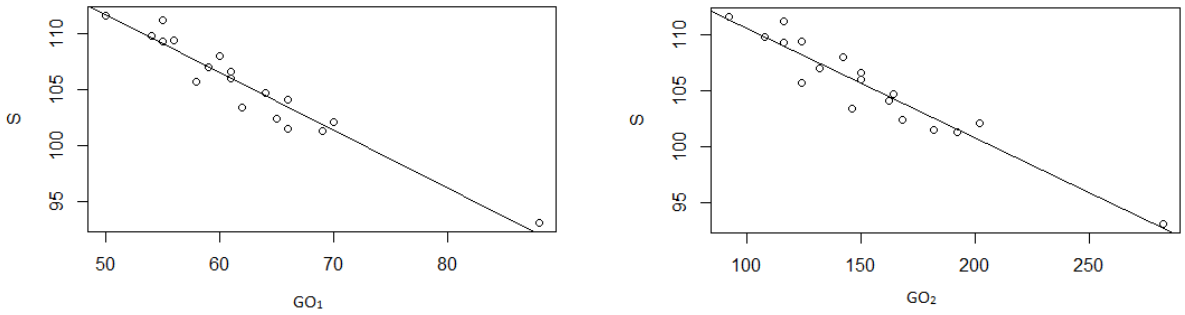

FIG. 2. Scatter diagram of S on GO_1(left) and GO_2(right), superimposed by the fitted regression line

The fitted models for GO_1 are:

$$S = 137.6(\pm 2.2) - 0.52(\pm 0.04)GO_1, \tag{2.1}$$

$$AcentFac = 0.6(\pm 0.02) - 0.004(\pm 0.0003)GO_1, \tag{2.2}$$

$$DHVAP = 11.5(\pm 0.4) - 0.04(\pm 0.006)GO_1. \tag{2.3}$$

The fitted models for GO_2 are:

$$S = 120.5(\pm 1.2) - 0.1(\pm 0.008)GO_2, \tag{2.4}$$

$$AcentFac = 0.5(\pm 0.009) - 0.0008(\pm 0.00006)GO_2, \tag{2.5}$$

$$DHVAP = 10.2(\pm 0.2) - 0.007(\pm 0.001)GO_2. \tag{2.6}$$

TABLE 1. Experimental values of entropy, acentric factor, DHVAP and the corresponding values of first Gourava index, second Gourava index, first hyper-Gourava index and second hyper-Gourava index of octane isomers

Alkane	S	AcentFac	DHVAP	GO_1	GO_2	HGO_1	HGO_2
n-octane	111.67	0.397898	9.915	50	92	370	1352
2-methyl-heptane	109.84	0.377916	9.484	54	108	436	1992
3-methyl-heptane	111.26	0.371002	9.521	55	116	469	2528
4-methyl-heptane	109.32	0.371504	9.483	55	116	469	2528
3-ethyl-hexane	109.43	0.362472	9.476	56	124	502	3064
2, 2-dimethyl-hexane	103.42	0.339426	8.915	62	146	592	4052
2, 3-dimethyl-hexane	108.02	0.348247	9.272	60	142	582	4540
2, 4-dimethyl-hexane	106.98	0.344223	9.029	59	132	535	3168
2, 5-dimethyl-hexane	105.72	0.35683	9.051	58	124	502	2632
3, 3-dimethyl-hexane	104.74	0.322596	8.973	64	164	668	5736
3, 4-dimethyl-hexane	106.59	0.340345	9.316	61	150	615	5076
2-methyl-3-ethyl-pentane	106.06	0.332433	9.209	61	150	615	5076
3-methyl-3-ethyl-pentane	101.48	0.306899	9.081	66	182	744	7420
2, 2, 3-trimethyl-pentane	101.31	0.300816	8.826	69	192	799	9336
2, 2, 4-trimethyl-pentane	104.09	0.30537	8.402	66	162	658	4692
2, 3, 3-trimethyl-pentane	102.06	0.293177	8.897	70	202	842	3428
2, 3, 4-trimethyl-pentane	102.39	0.317422	9.014	65	168	695	6552
2, 2, 3, 3-tetramethyl-butane	93.06	0.255294	8.41	88	282	1202	20724

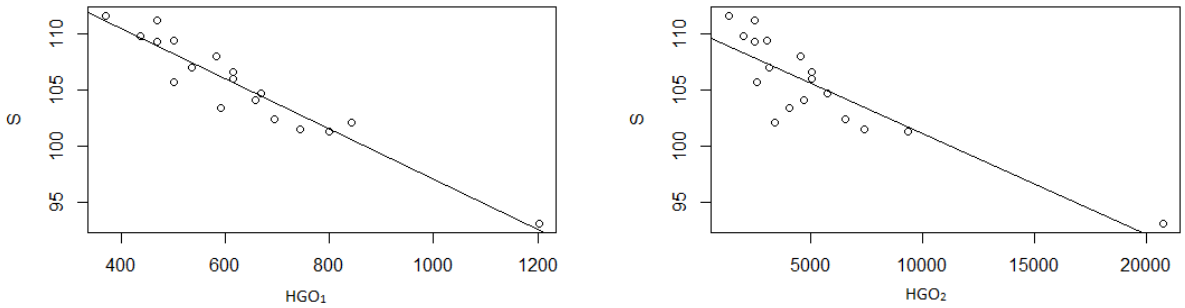

FIG. 3. Scatter diagram of S on HGO_1(left) and HGO_2(right), superimposed by the fitted regression line

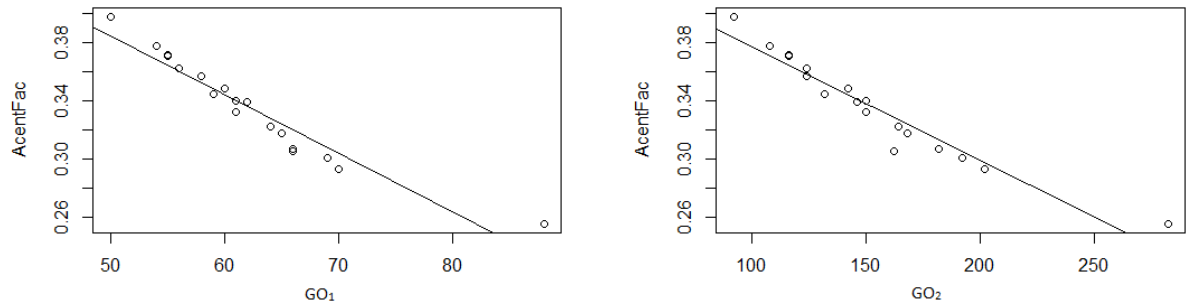

FIG. 4. Scatter diagram of Acent Fac on GO_1(left) and GO_2(right), superimposed by the fitted regression line

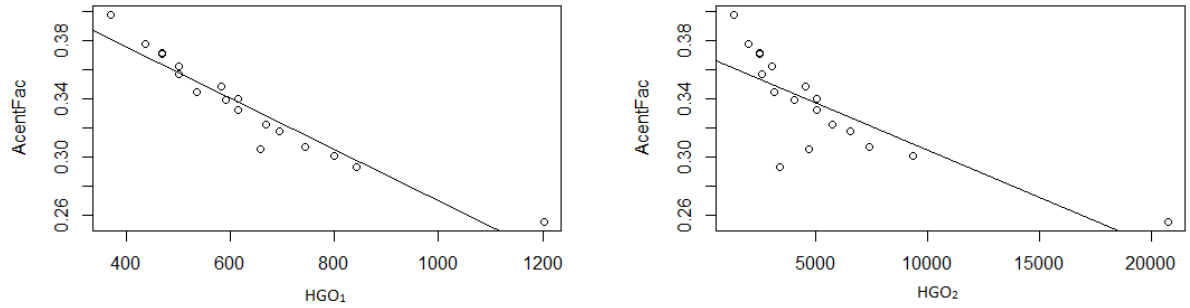

FIG. 5. Scatter diagram of Acent Fac on HGO_1(left) and HGO_2(right), superimposed by the fitted regression line

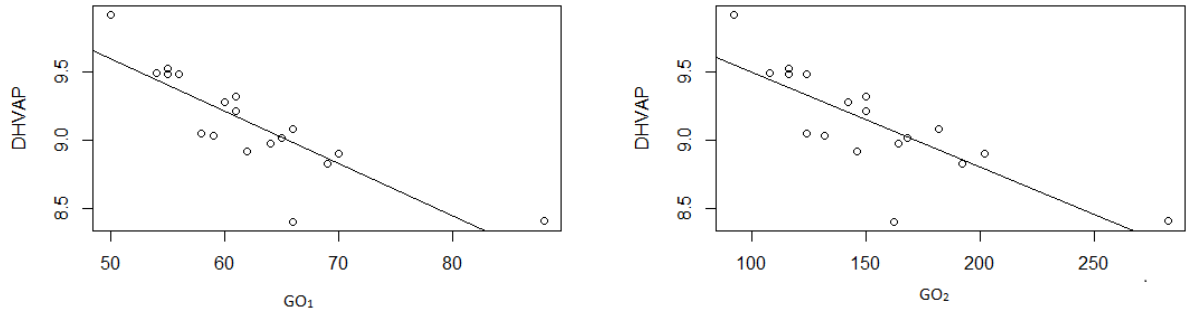

FIG. 6. Scatter diagram of DHVAP on GO_1(left) and GO_2(right), superimposed by the fitted regression line

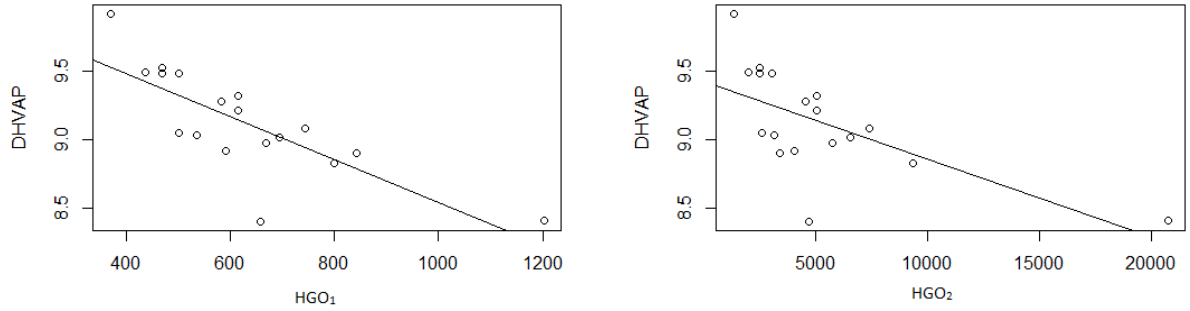

FIG. 7. Scatter diagram of DHVAP on HGO_1(left) and HGO_2(right), superimposed by the fitted regression line

The fitted models for HGO_1 are:

$$S = 119.5(\pm 1.2) - 0.02(\pm 0.002)HGO_1, \tag{2.7}$$

$$AcentFac = 0.4(\pm 0.009) - (0.0002)(\pm 0.00001)HGO_1, \tag{2.8}$$

$$DHVAP = 10.1(\pm 0.2) - 0.002(\pm 0.0003)HGO_1. \tag{2.9}$$

The fitted models for HGO_2 are:

$$S = 110.1(\pm 0.9) - 0.0009(\pm 0.0001)HGO_2, \tag{2.10}$$

$$AcentFac = 0.4(\pm 0.01) - 0.00001(\pm 0.000001)HGO_2, \tag{2.11}$$

$$DHVAP = 9.4(\pm 0.1) - 0.00006(\pm 0.00002)HGO_2. \tag{2.12}$$

Note: The values in brackets of Eqns. (2.1) to (2.12) are the corresponding standard errors of the regression coefficients. The index is better as $|r|$ approaches 1.

From Table 2, Figs. 2, 4 and 6 we can observe that GO_1 correlates highly with entropy and the correlation coefficient $|r| = 0.9644924$. Also, GO_1 has good correlation $(|r| > 0.9)$ with Acentric Factor and $(|r| > 0.8)$ with DHVAP.

From Table 3, Figs. 2, 4 and 6 we can observe that GO_2 correlates highly with Acentric Factor and the correlation coefficient $|r| = 0.9644924$. Also, GO_2 has good correlation $(|r| > 0.9)$ with entropy and $(|r| > 0.75)$ with DHVAP.

From Table 4, Figs. 3, 5 and 7 we can observe that HGO_1 correlates highly with Acentric Factor and the correlation coefficient $|r| = 0.9554303$. Also, HGO_1 has good correlation $(|r| > 0.9)$ with entropy and $(|r| > 0.75)$ with DHVAP.

From Table 5, Figs. 3, 5 and 7 HGO_2 has good correlation $(|r| > 0.85)$ with entropy, $(|r| > 0.75)$ with Acentric Factor and $(|r| > 0.6)$ with DHVAP.

TABLE 2. Correlation coefficient and residual standard error of regression models for GO_1

Physical properties	Absolute value of the correlation coefficient ($\|r\|$)	Residual standard error
Entropy	0.9644924	1.23
Acentric Factor	0.9595891	0.01028
DHVAP	0.8368024	0.2163

TABLE 3. Correlation coefficient and residual standard error of regression models for GO_2

Physical properties	Absolute value of the correlation coefficient ($\|r\|$)	Residual standard error
Entropy	0.9561406	1.364
Acentric Factor	0.962243	0.009946
DHVAP	0.7896431	0.2424

TABLE 4. Correlation coefficient and residual standard error of regression models for HGO_1

Physical properties	Absolute value of the correlation coefficient ($\|r\|$)	Residual standard error
Entropy	0.953055	1.41
Acentric Factor	0.9554303	0.01079
DHVAP	0.779148	0.2477

TABLE 5. Correlation coefficient and residual standard error of regression models for HGO_2

Physical properties	Absolute value of the correlation coefficient ($\|r\|$)	Residual standard error
Entropy	0.8691773	2.303
Acentric Factor	0.798397	0.022
DHVAP	0.6442586	0.3022

3. Gourava and hyper-Gourava indices of line graph of subdivision graphs of 2D-lattice, nanotube and nanotorus of $TUC_4C_8[p, q]$

In this section, we obtain the Gourava and hyper-Gourava indices of line graph of subdivision graphs of 2D-lattice, nanotube and nanotorus of $TUC_4C_8[p, q]$. Let p and q denote the number of squares in a row and the number of rows of squares, respectively in 2D-lattice, nanotube and nanotorus of $TUC_4C_8[4, 3]$ as shown in Fig 8 (a), (b) and (c) respectively.

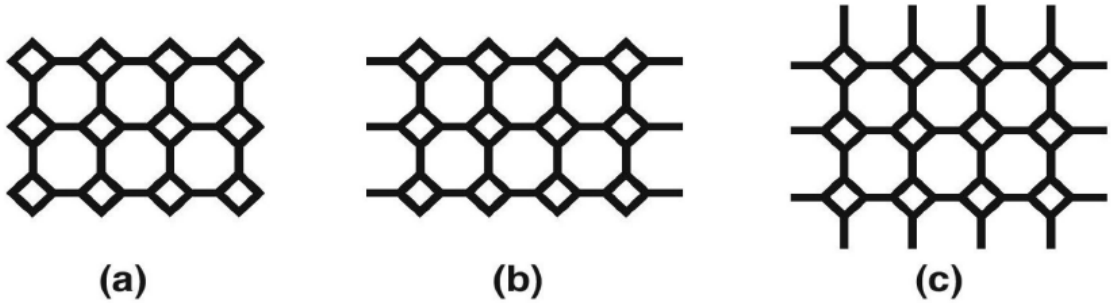

FIG. 8. (a) 2D-lattice of $TUC_4C_8[4, 3]$; (b) $TUC_4C_8[4, 3]$ nanotube; (c) $TUC_4C_8[4, 3]$ nanotorus

The number of vertices and edges of 2D-lattice, nanotube and nanotorus of $TUC_4C_8[p, q]$ are given in Table 6.

TABLE 6. Order and size of graphs

Graph	Order	Size
2D-lattice of $TUC_4C_8[p, q]$	$4pq$	$6pq - p - q$
$TUC_4C_8[p, q]$ Nanotube	4pq	6pq-p
$TUC_4C_8[p, q]$ Nanotorus	4pq	6pq

For more details about topological indices of the line graph of subdivision graphs of 2D-lattice, nanotube and nanotorus of $TUC_4C_8[p, q]$, refer [9–11].

The following theorem gives the Gourava and hyper-Gourava indices of line graph of subdivision graphs of 2D-lattice of $TUC_4C_8[p, q]$.

Theorem 3.1. *Let A be the line graph of the subdivision graph of 2D-lattice of $TUC_4C_8[p, q]$ (See Fig. 9). Then*

1. $GO_1(A) = 270pq - 105(p + q) + 4$,
2. $GO_2(A) = 972pq - 442(p + q) + 40$,
3. $HGO_1(A) = 4050pq - 1863(p + q) + 188$,
4. $HGO_2(A) = 52488pq - 27964(p + q) + 5488$.

Proof. Let A be the line graph of the subdivision graph of 2D-lattice of $TUC_4C_8[p, q]$. The graph A has $2(6pq-6-q)$ vertices and $18pq - 5p - 5q$ edges.

1. By using definition of first Gourava index and information in Table 7, we have:

$$\begin{aligned} GO_1(A) &= \sum_{(u,v)\in E(A)} \big[\big(d_A(u)+d_A(v)\big)+\big(d_A(u)d_A(v)\big)\big] \\ &= |E_{2,2}|[(2+2)+(2\times 2)]+|E_{2,3}|[(2+3)+(2\times 3)]+|E_{3,3}|[(3+3)+(3\times 3)] \\ &= 2(p+q+2)(4+4)+4(p+q-2)(5+6)+(18pq-11p-11q+4)(6+9) \\ &= 270pq-105(p+q)+4. \end{aligned}$$

2. By using definition of second Gourava index and information in Table 7, we have:

$$\begin{aligned} GO_2(A) &= \sum_{(u,v)\in E(A)} \big[\big(d_A(u)+d_A(v)\big)\big(d_A(u)d_A(v)\big)\big] \\ &= |E_{2,2}|[(2+2)(2\times 2)]+|E_{2,3}|[(2+3)(2\times 3)]+|E_{3,3}|[(3+3)(3\times 3)] \\ &= 2(p+q+2)(4\times 4)+4(p+q-2)(5\times 6)+(18pq-11p-11q+4)(6\times 9) \\ &= 972pq-442(p+q)+40. \end{aligned}$$

3. By using definition of first hyper-Gourava index and information in Table 7, we have:

$$\begin{aligned} HGO_1(A) &= \sum_{(u,v)\in E(A)} \big[\big(d_A(u)+d_A(v)\big)+\big(d_A(u)d_A(v)\big)\big]^2 \\ &= |E_{2,2}|[(2+2)+(2\times 2)]^2+|E_{2,3}|[(2+3)+(2\times 3)]^2+|E_{3,3}|[(3+3)+(3\times 3)]^2 \\ &= 2(p+q+2)(4+4)^2+4(p+q-2)(5+6)^2+(18pq-11p-11q+4)(6+9)^2 \\ &= 4050pq-1863(p+q)+188. \end{aligned}$$

4. By using definition of second hyper-Gourava index and information in Table 7, we have:

$$\begin{aligned} HGO_2(A) &= \sum_{(u,v)\in E(A)} \big[\big(d_A(u)+d_A(v)\big)\big(d_A(u)d_A(v)\big)\big]^2 \\ &= |E_{2,2}|[(2+2)(2\times 2)]^2+|E_{2,3}|[(2+3)(2\times 3)]^2+|E_{3,3}|[(3+3)(3\times 3)]^2 \\ &= 2(p+q+2)(4\times 4)^2+4(p+q-2)(5\times 6)^2+(18pq-11p-11q+4)(6\times 9)^2 \\ &= 52488pq-27964(p+q)+5488. \end{aligned}$$

□

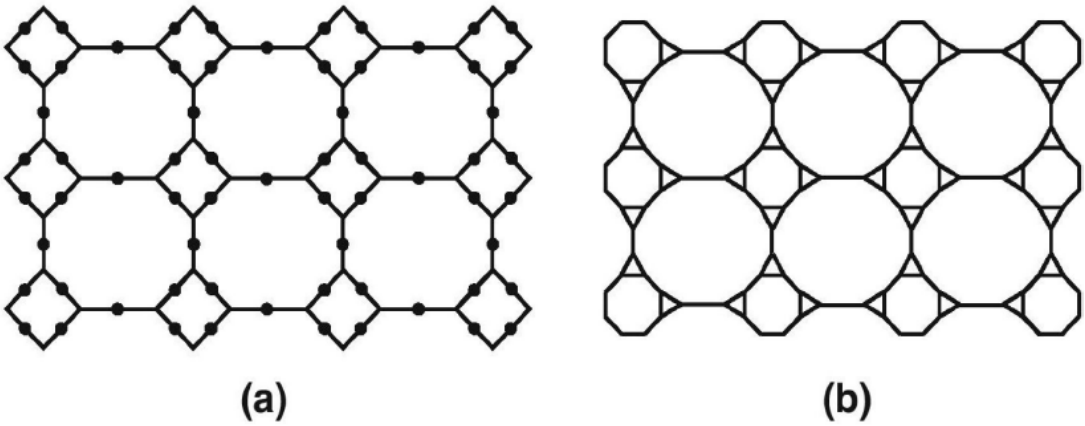

FIG. 9. (a) Subdivision graph of 2D-lattice of $TUC_4C_8[4,3]$; (b) Line graph of the subdivision graph of 2D-lattice of $TUC_4C_8[4,3]$

The following theorem gives the Gourava and hyper-Gourava indices of line graph of subdivision graphs of $TUC_4C_8[p,q]$ of nanotube.

TABLE 7. The edge partition of A based on degree of each edge

$d_A(u), d_A(v) : uv \in E(A)$	$(2,2)$	$(2,3)$	$(3,3)$
Number of edges	$2(p+q+2)$	$4(p+q-2)$	$18pq-11p-11q+4$

Theorem 3.2. *Let B be the line graph of the subdivision graph of $TUC_4C_8[p,q]$ nanotube (See Fig. 10). Then*

1. $GO_1(B) = 270pq - 105p$,
2. $GO_2(B) = 972pq - 442p$,
3. $HGO_1(B) = 4050pq - 1863p$,
4. $HGO_2(B) = 52488pq - 27964p$.

Proof. By using the definition of Gourava and hyper-Gourava indices and information given in Table 8, we obtain the desired result. □

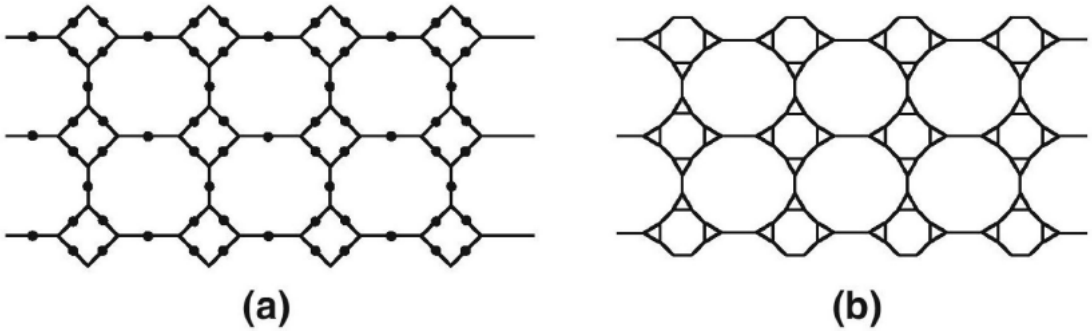

FIG. 10. (a) Subdivision graph of $TUC_4C_8[4,3]$ of nanotube; (b) Line graph of the subdivision graph of $TUC_4C_8[4,3]$ of nanotube

TABLE 8. The edge partition of B based on degree of each edge

$d_B(u), d_B(v) : uv \in E(B)$	$(2,2)$	$(2,3)$	$(3,3)$
Number of edges	$2p$	$4p$	$18pq-11p$

The following theorem gives the Gourava and hyper-Gourava indices of line graph of subdivision graphs of $TUC_4C_8[p,q]$ of nanotorus.

Theorem 3.3. *Let C be the line graph of the subdivision graph of $TUC_4C_8[p,q]$ nanotorus (See Fig. 11). Then*

1. $GO_1(C) = 270pq$,
2. $GO_2(C) = 972pq$,
3. $HGO_1(C) = 4050pq$,
4. $HGO_2(C) = 52488pq$.

Proof. By using the definition of Gourava and hyper-Gourava indices and information given in Table 9, we obtain the desired result. □

TABLE 9. The edge partition of C based on degree of each edge

$d_C(u), d_C(v) : uv \in E(C)$	$(3,3)$
Number of edges	$18pq$

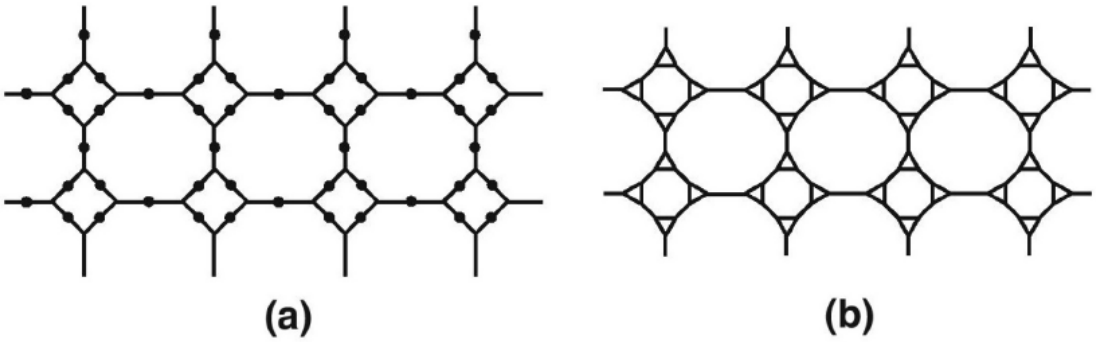

FIG. 11. (a) Subdivision graph of $TUC_4C_8[4,3]$ of nanotorus; (b) Line graph of the subdivision graph of $TUC_4C_8[4,3]$ of nanotorus

4. Conclusion

In this paper, we have studied the chemical applicability of Gourava and hyper-Gourava indices. These indices show good correlation with physico-chemical properties. The first Gourava index highly correlates with entropy (coefficient of correlation is 0.9644924 and residual standard error is 1.23) which is better than the modified first Kulli-Basava index ($|r| = 0.9476403$ and residual standard error is 1.363) [13], the first Kulli-Basava index ($|r| = 0.956207$ and residual standard error is 1.415) [13] and the first neighbourhood Zagreb index ($|r| = 0.9526144$ and residual standard error is 1.416) [14]. The second Gourava index highly correlates with acentric factor (coefficient of correlation is 0.962243 and residual standard error is 0.009946) which is better than (β, α) connectivity index ($|r| = 0.95802$ and residual standard error is 0.01047) [15]. In addition, we computed Gourava and hyper-Gourava indices of the line graph of subdivision graph of 2D-lattice, nanotube and nanotorus of $TUC_4C_8[p,q]$. These results would help to understand the chemical reactivity and biological activity of the nanostructures.

Acknowledgements

B. Basavanagoud is supported by the University Grants Commission (UGC), New Delhi, through UGC-SAP DRS-III for 2016–2021: F.510/3/DRS-III/2016(SAP-I).

References

[1] Harary F. *Graph Theory*, Addison-Wesely, Reading Mass, 1969.
[2] Kulli V.R. *College Graph Theory*, Vishwa Int. Publ., Gulbarga, India, 2012.
[3] Gutman I., Trinajstić N. Graph theory and molecular orbitals, Total π-electron energy of alternant hydrocarbons. *Chem. Phys. Lett.*, 1972, **17** (4), P. 535–538.
[4] Gutman I., Ruščić B., Trinajstić N., Wilcox C.F. Graph theory and molecular orbitals. XII. Acyclic polyenes. *J. Chem. Phys.*, 1975, **62**, P. 3399–3405.
[5] Furtula B., Gutman I. A forgotten topological index. *J. Math. Chem.*, 2015, **53** (4), P. 1184–1190.
[6] Kulli V.R. The Gourava indices and coindices of graphs. *Annals of Pure and Applied Mathematics*, 2017, **14** (1), P. 33–38.
[7] Kulli V.R. On hyper-Gourava indices and coindices. *Int. Journal of Mathematical Archieve*, 2017, **8** (12), P. 116–120.
[8] Mondal S., Bhosale A., De N., Pal A. Topological properties of some nanostructures. *Nanosystems: Physics, Chemistry, Mathematics*, 2020, **11** (1), P. 14–24.
[9] Hosamani S.M. Computing Sanskruti index of certain nanostructures. *J. Appl. Math. Comput.*, 2017, **54**, P. 425–433.
[10] Nadeem M.F., Zafar S., Zahid Z., On certain topological indices of the line graph of subdivision graphs. *Appl. Math. Comput.*, 2015, **271**, P. 790–794.
[11] Nadeem M.F., Zafar S., Zahid Z. On topological properties of the line graph of subdivision graphs of certain nanostructures. *Appl. Math. Comput.*, 2016, **273**, P. 125–130.
[12] R Core Team. R: A language and environment for statistical computing. *R Foundation for Statistical Computing, Vienna, Austria* , 2016, `URL: https://www.R-project.org/`.
[13] Basavanagoud B., Jakkannavar P. Kulli-Basava indices of graphs. *Int. J. Appl. Eng. Res.*, 2019, **14** (1), P. 325–342.
[14] Basavanagoud B., Barangi A.P., Hosamani S.M. First neighbourhood Zagreb index of some nanostructures. *Proc. Inst. Appl. Math.*, 2018, **7** (2), P. 178–193.
[15] Basavanagoud B., Desai V., Patil S. (β, α) connectivity index of graphs. *Appl. Math. Nonlinear Sci.*, 2017, **2** (1), P. 21–30.

NANOSYSTEMS: PHYSICS, CHEMISTRY, MATHEMATICS, 2021, 12 (2), P. 151–155

On the choice of parameters for a model of small window

A. S. Melikhova, M. P. Faleeva, I. Y. Popov

ITMO University, Kroverkskiy pr. 49, St. Petersburg, 197101, Russia

alina.s.melikhova@gmail.com, faleeva.masha@gmail.com, popov1955@gmail.com

PACS 73.23.-b, 73.23.Hk, 73.23.Ra, 03.65.Yz **DOI 10.17586/2220-8054-2021-12-2-151-155**

Scattering of plane waves and Gaussian beams by a screen with small opening is considered. The asymptotics far from the obstacle is obtained. The results can be useful for description of perforated nanolayers and for fitting the model based on the operator extensions theory.

Keywords: scattering, Green's function, asymptotics.

Received: 25 March 2021

1. Introduction

Wave scattering by perforated screens was studied over a long period [1]. Nevertheless, last decade, one observe an intensive discussion of the problem related to nanoscience, e.g., to studying of perforated nanolayers and nanofilms (see, e.g., [2, 3]). Several mathematical models were suggested for the process description, particularly, a model of point-like windows based the theory of self-adjoint extensions of symmetric operators [4–6]. The model is explicitly solvable. It is an evident advantage. Unfortunately, fitting of the model is not simple. One should consider the asymptotics of the solution for the realistic problem if the window is small (see, e.g., [7–9]) and choose the proper values of the model parameters ensuring good approximation of the realistic solution by the model one. For this purpose, it is possible to consider a benchmark problem with simpler geometry [10]. In our case, we can deal with a plane with an orifice. In the present paper we consider the scattering problem for the plane $z = 0$ in $\mathbb{R}^3$ with the Cartesian coordinates (x, y, z).

2. Scattering

Let the incoming plane wave is in the upper half-space $z > 0$. Correspondingly, the reflected wave is also in this half-space. Consider the scattered wave U in the lower half-space. Function $U(\mathbf{r})$ (where $\mathbf{r} = \{r, \theta, \varphi\}$ in spherical coordinates or $\mathbf{r} = \{x, y, z\}$ in Cartesian coordinates) can be written in the following form:

$$U(\mathbf{r}) = \iint\limits_D \frac{\partial}{\partial \mathbf{n}'} G\left(\mathbf{r}, \mathbf{r}', k\right) \psi_{in}\left(\mathbf{r}'\right) d\mathbf{r}', \tag{1}$$

where D is a window (aperture), ψ_{in} is the incoming wave, G is the Green function, k is the wave number. Here vector $\mathbf{r}'$ can be also presented in spherical or Cartesian coordinates with following notations: $\mathbf{r}' = \{r', \theta', \varphi'\}$ (in spherical coordinates), $\mathbf{r}' = \{x', y', z'\}$ (in Cartesian coordinates).

Let one examine integrand functions from (1) separately. Firstly, consider the normal derivative of Green's function. It can be presented as follows:

$$\frac{\partial}{\partial \mathbf{n}'} G\left(\mathbf{r}, \mathbf{r}', k\right) = \frac{1}{4\pi} \frac{\partial}{\partial \mathbf{n}'} \left(\frac{\mathrm{e}^{\mathrm{i}k|\mathbf{r}-\mathbf{r}'|}}{|\mathbf{r}-\mathbf{r}'|} - \frac{\mathrm{e}^{\mathrm{i}k|\mathbf{r}-\mathbf{r}'^{\star}|}}{|\mathbf{r}-\mathbf{r}'^{\star}|} \right). \tag{2}$$

It is clear that in our case the normal derivative $\partial/\partial\,\mathbf{n}'$ is equal to the derivative with respect to the Z'-axis (in Cartesian coordinates).

One can obtain:

$$\frac{\partial}{\partial \mathbf{n}'} G\left(\mathbf{r}, \mathbf{r}', k\right) = -\frac{z}{2\pi} \frac{\mathrm{e}^{\mathrm{i}k|\mathbf{r}-\mathbf{r}'|}}{|\mathbf{r}-\mathbf{r}'|} \left(\frac{\mathrm{i}k}{|\mathbf{r}-\mathbf{r}'|} - \frac{1}{|\mathbf{r}-\mathbf{r}'|^2} \right). \tag{3}$$

Now we can examine the second integrand function $\psi_{in}\left(\mathbf{r}'\right)$. In upper half-plane it can presented as a following sum:

$$\psi_{in}\left(\mathbf{r}'\right) = \mathrm{e}^{\mathrm{i}\mathbf{k}^{in}\cdot\mathbf{r}'} + \mathrm{e}^{\mathrm{i}\mathbf{k}^{ref}\cdot\mathbf{r}'},$$

where vectors $\mathbf{k}^{in}$, $\mathbf{k}^{ref}$ and $\mathbf{r}'$ can be described as follows:

$$\mathbf{k}^{in} = k\mathbf{v}^{in}, \quad \mathbf{k}^{ref} = k\mathbf{v}^{ref}, \quad \mathbf{r}' = r'\mathbf{v}'; \qquad |\mathbf{v}^{in}| = |\mathbf{v}^{ref}| = |\mathbf{v}'| = 1;$$
$$\mathbf{v}^{in} = \{1; \varphi_{in}; \theta_{in}\}, \quad \mathbf{v}^{ref} = \{1; \varphi_{ref}; \theta_{ref}\} = \{1; \varphi_{in}; \pi - \theta_{in}\}, \quad \mathbf{v}' = \{1; \varphi'; \theta'\}.$$

Let us consider the solution in the lower half-plane where the reflected plane wave is absent:

$$\psi_{in}\left(\mathbf{r}'\right) = \mathrm{e}^{\mathrm{i}\mathbf{k}^{in}\cdot\mathbf{r}'} = \mathrm{e}^{\mathrm{i}kr'\mathbf{v}^{in}\cdot\mathbf{v}'},$$

Since we are mostly interested in asymptotic behavior of function $U\left(\mathbf{r}\right)$ when r tends to infinity, we can express function $U\left(\mathbf{r}\right)$ from (1) in the following asymptotic form:

$$U\left(r,\theta,\varphi\right) \approx A\left(\theta,\varphi\right)\frac{\mathrm{i}k\mathrm{e}^{\mathrm{i}kr}}{r} \text{ for } r\to\infty, \tag{4}$$

and then examine only the coefficient $A\left(\theta,\varphi\right)$. To meet this goal we have to single out the factor $\mathrm{i}k\mathrm{e}^{\mathrm{i}kr}/r$ from the formula (1).

First of all, we can properly approximate expression for the normal derivative of Green's function (3). We will do it in several steps. In the first step, we can approximate the expression for the modulus of the difference of radius vectors $\mathbf{r}$ and $\mathbf{r}'$:

$$|\mathbf{r}-\mathbf{r}'| = \sqrt{r^2+\left(r'\right)^2-2rr'\cos\left(\mathbf{r},\hat{\mathbf{r}'}\right)} = r\sqrt{1+\frac{\left(r'\right)^2}{r^2}-2\frac{r'}{r}\cos\left(\mathbf{r},\hat{\mathbf{r}'}\right)} \approx$$

$$\approx r - r'\cos\left(\mathbf{r},\hat{\mathbf{r}'}\right) \text{ for } r\to\infty. \tag{5}$$

In the second step, one can find an approximation for the second factor in the expression (3) as follows:

$$\frac{\mathrm{e}^{\mathrm{i}k|\mathbf{r}-\mathbf{r}'|}}{|\mathbf{r}-\mathbf{r}'|} \approx \frac{\mathrm{e}^{\mathrm{i}kr}\mathrm{e}^{-\mathrm{i}kr'\cos\left(\mathbf{r},\hat{\mathbf{r}'}\right)}}{r\left(1+\frac{1}{2}\left(\frac{\left(r'\right)^2}{r^2}-2\frac{r'}{r}\cos\left(\mathbf{r},\hat{\mathbf{r}'}\right)\right)\right)} \approx$$

$$\approx \frac{\mathrm{e}^{\mathrm{i}kr}}{r}\mathrm{e}^{-\mathrm{i}kr'\cos\left(\mathbf{r},\hat{\mathbf{r}'}\right)}\left(1-\frac{1}{2}\left(\frac{\left(r'\right)^2}{r^2}-2\frac{r'}{r}\cos\left(\mathbf{r},\hat{\mathbf{r}'}\right)\right)\right) \approx$$

$$\approx \frac{\mathrm{e}^{\mathrm{i}kr}}{r}\mathrm{e}^{-\mathrm{i}kr'\cos\left(\mathbf{r},\hat{\mathbf{r}'}\right)}\left(1+\frac{r'}{r}\cos\left(\mathbf{r},\hat{\mathbf{r}'}\right)\right) \text{ for } r\to\infty. \tag{6}$$

In the next step, one can easily find approximations for the terms in the third factor in the expression (3):

$$\frac{\mathrm{i}k}{|\mathbf{r}-\mathbf{r}'|} \approx \frac{\mathrm{i}k}{r}\left(1+\frac{r'}{r}\cos\left(\mathbf{r},\hat{\mathbf{r}'}\right)\right) \text{ for } r\to\infty; \tag{7}$$

$$\frac{1}{|\mathbf{r}-\mathbf{r}'|^2} = \frac{1}{r^2\left(1+\frac{\left(r'\right)^2}{r^2}-2\frac{r'}{r}\cos\left(\mathbf{r},\hat{\mathbf{r}'}\right)\right)} \approx \frac{1}{r^2} \text{ for } r\to\infty. \tag{8}$$

And finally, by substituting expressions (5)–(8) into formula (3) we derive an approximate expression for the normal derivative of Green's function in the following form:

$$\frac{\partial}{\partial\mathbf{n}'}G\left(\mathbf{r},\mathbf{r}',k\right) = -\frac{z}{2\pi}\frac{\mathrm{e}^{\mathrm{i}k|\mathbf{r}-\mathbf{r}'|}}{|\mathbf{r}-\mathbf{r}'|}\left(\frac{\mathrm{i}k}{|\mathbf{r}-\mathbf{r}'|}-\frac{1}{|\mathbf{r}-\mathbf{r}'|^2}\right) \approx -\frac{\cos\theta}{2\pi}\frac{\mathrm{i}k\mathrm{e}^{\mathrm{i}kr}}{r}\mathrm{e}^{-\mathrm{i}kr'\cos\left(\mathbf{r},\hat{\mathbf{r}'}\right)} \text{ for } r\to\infty. \tag{9}$$

Secondly, by matching expressions (1), (9) with asymptotic formula (4), one can obtain the following form of the coefficient $A\left(\theta,\varphi\right)$:

$$A\left(\theta,\varphi\right) = -\frac{\cos\theta}{2\pi}\iint\limits_{D}\mathrm{e}^{-\mathrm{i}kr'\cos\left(\mathbf{r},\hat{\mathbf{r}'}\right)}\mathrm{e}^{\mathrm{i}kr'\mathbf{v}^{in}\cdot\mathbf{v}'}\,d\mathbf{r}'. \tag{10}$$

And due to the last formula one can examine the asymptotic behaviour of the function $U\left(\mathbf{r}\right)$ for every specific domain D.

3. A round domain D

In this section we will discuss the case when the domain D is a circle in the plane $z=0$ of radius R:

$$D = \left\{(x',y'):\ \left(x'\right)^2+\left(y'\right)^2\le R^2\right\} \text{ or } D = \left\{(r',\varphi'):\ 0\le r'\le R^2,\ \varphi'\in[0;2\pi)\right\}$$

For such domain D we can find the coefficient $A\left(\theta,\varphi\right)$ in non-integral form. To do this we should investigate the integrand function from (10) at first and after few simplifications integrate it.

Let examine function $\mathrm{e}^{-\mathrm{i}kr'\cos\left(\mathbf{r},\hat{\mathbf{r}'}\right)}\mathrm{e}^{\mathrm{i}kr'\mathbf{v}^{in}\cdot\mathbf{v}'}$. Firstly, we can present $\cos\left(\mathbf{r},\hat{\mathbf{r}'}\right)$ as a function of angles θ, φ and φ':

$$\cos\left(\mathbf{r},\hat{\mathbf{r}'}\right)=\frac{\mathbf{r}\cdot\mathbf{r}'}{rr'}=\left(\cos\varphi\cos\varphi'+\sin\varphi\sin\varphi'\right)\sin\theta=\cos\left(\varphi-\varphi'\right)\sin\theta.$$

Secondly, we can examine scalar products from $\mathrm{e}^{\mathrm{i}kr'\mathbf{v}^{in}\cdot\mathbf{v}'}$:

$$\mathbf{v}^{in}\cdot\mathbf{v}'=\cos\varphi_{in}\sin\theta_{in}\cos\varphi'\sin\theta'+\sin\varphi_{in}\sin\theta_{in}\sin\varphi'\sin\theta'+\cos\theta_{in}\cos\theta'=$$
$$=\left(\cos\varphi_{in}\cos\varphi'+\sin\varphi_{in}\sin\varphi'\right)\sin\theta_{in}=\cos\left(\varphi_{in}-\varphi'\right)\sin\theta_{in}. \quad (11)$$

From (11), it follows:

$$\mathrm{e}^{\mathrm{i}kr'\mathbf{v}^{in}\cdot\mathbf{v}'}=\mathrm{e}^{\mathrm{i}kr'\cos\left(\varphi_{in}-\varphi'\right)\sin\theta_{in}}. \quad (12)$$

And finally, (3) and (12) yield us the following result about the integrand function being under discussion:

$$\mathrm{e}^{-\mathrm{i}kr'\cos\left(\mathbf{r},\hat{\mathbf{r}'}\right)}\mathrm{e}^{\mathrm{i}kr'\mathbf{v}^{in}\cdot\mathbf{v}'}=\mathrm{e}^{\mathrm{i}kr'\left(\cos\left(\varphi_{in}-\varphi'\right)\sin\theta_{in}-\cos\left(\varphi-\varphi'\right)\sin\theta\right)}. \quad (13)$$

It remains only to integrate expression (10) using the form (13) of integrand function:

$$A\left(\theta,\varphi\right)=-\frac{\cos\theta}{2\pi}\iint\limits_{D}\mathrm{e}^{-\mathrm{i}kr'\cos\left(\mathbf{r},\hat{\mathbf{r}'}\right)}\mathrm{e}^{\mathrm{i}kr'\mathbf{v}^{in}\cdot\mathbf{v}'}\,d\mathbf{r}'=$$
$$=-\frac{\cos\theta}{2\pi}\int\limits_{0}^{R}r'\left(\int\limits_{0}^{2\pi}\exp\left(\mathrm{i}kr'\left(\cos\left(\varphi_{in}-\varphi'\right)\sin\theta_{in}-\cos\left(\varphi-\varphi'\right)\sin\theta\right)\right)\,d\varphi'\right)dr'. \quad (14)$$

Firstly, one can calculate the inner integral from (14):

$$\int\limits_{0}^{2\pi}\exp\left(\mathrm{i}kr'\left(\cos\left(\varphi_{in}-\varphi'\right)\sin\theta_{in}-\cos\left(\varphi-\varphi'\right)\sin\theta\right)\right)\,d\varphi'=$$
$$\int\limits_{0}^{2\pi}\exp\left(\mathrm{i}kr'\left(c_1\cos\varphi'+c_2\sin\varphi'\right)\right)\,d\varphi'=2\pi I_0\left(\sqrt{-\left(kr'c_1\right)^2-\left(kr'c_2\right)^2}\right)=$$
$$=2\pi I_0\left(\mathrm{i}k\sqrt{c_1^2+c_2^2}\,r'\right)=2\pi I_0\left(\mathrm{i}k\Theta\left(\theta_{in},\varphi_{in};\theta,\varphi\right)r'\right),$$
$$\Theta\left(\theta_{in},\varphi_{in};\theta,\varphi\right)\overset{def}{=}\sqrt{\sin^2\theta_{in}-2\cos\left(\varphi_{in}-\varphi\right)\sin\theta_{in}\sin\theta+\sin^2\theta}.$$

where $I_0\left(z\right)$ is the modified Bessel function of the first kind of the 0-th order. Secondly, one can calculate the outer integral from (17) excluding constant terms:

$$\int\limits_{0}^{R}r'I_0\left(\mathrm{i}k\Theta\left(\theta_{in},\varphi_{in};\theta,\varphi\right)r'\right)dr'=\frac{R\,J_1\left(k\,\Theta\left(\theta_{in},\varphi_{in};\theta,\varphi\right)R\right)}{k\,\Theta\left(\theta_{in},\varphi_{in};\theta,\varphi\right)},$$

where $J_1\left(z\right)$ is the Bessel function of the first kind of the 1-st order. Thus, one can obtain coefficient $A\left(\theta,\varphi\right)$ as follows:

$$A\left(\theta,\varphi\right)=-\frac{\cos\theta}{\pi}\pi\frac{R\,J_1\left(k\,\Theta\left(\theta_{in},\varphi_{in};\theta,\varphi\right)R\right)}{k\,\Theta\left(\theta_{in},\varphi_{in};\theta,\varphi\right)}=-\frac{R\cos\theta}{\Theta\left(\theta_{in},\varphi_{in};\theta,\varphi\right)}\frac{J_1\left(k\,\Theta\left(\theta_{in},\varphi_{in};\theta,\varphi\right)R\right)}{k}.$$

For further discussions we can rewrite the obtained expression in more convenient for us form:

$$A\left(\theta,\varphi\right)=-R^2\cos\theta\,\frac{J_1\left(\Theta\left(\theta_{in},\varphi_{in};\theta,\varphi\right)kR\right)}{\Theta\left(\theta_{in},\varphi_{in};\theta,\varphi\right)kR}. \quad (15)$$

4. A round domain D: discussions.

First of all, one can note that in the case of normal wave incident function $\Theta(\theta_{in}, \varphi_{in}; \theta, \varphi)$ is very simple and does not depend on φ_{in} and φ:

$$\Theta(\theta_{in}, \varphi_{in}; \theta, \varphi) = |\theta_{in} = \pi| = \Theta_{norm}(\theta) = |\sin\theta|.$$

Secondly, in the case with $kR \ll 1$ one can easily obtain the following approximation:

$$A(\theta, \varphi) \approx -R^2 \cos\theta \, \frac{\Theta(\theta_{in}, \varphi_{in}; \theta, \varphi) \, kR/2}{\Theta(\theta_{in}, \varphi_{in}; \theta, \varphi) \, kR} = -\frac{R^2}{2} \cos\theta \ \text{ for } kR \ll 1.$$

Id est, in this case coefficient $A(\theta, \varphi)$ does not depend on φ and is proportional to $\cos\theta$. In other cases we have a non-trivial dependence of this coefficient on φ.

As for the model of point-like window in the screen, it looks like the following one. Let us consider the Laplace operators in $L_2(\Omega^+)$ and $L_2(\Omega^-)$ with Neumann boundary conditions on $\partial\Omega^\pm$ (here $\Omega^\pm$ is upper (lower) half-plane), namely

$$\left.\frac{\partial f}{\partial n}\right|_{\partial\Omega^\pm} = 0,$$

where n denotes the external unit normal vector to $\partial\Omega^\pm$, i.e. $n = (0, 0, \pm 1)$.

Let us construct a point-like window at point $x^0 \in \partial\Omega^\pm$. If we restrict the considered operators onto the set of smooth functions that vanish in the neighbourhood of x^0, it is well known that the closures Δ_0^+ and Δ_0^- of the considered operators are symmetric operators with deficiency indices $(1, 1)$. Thus, the operator

$$\Delta_0 = \Delta_0^+ \oplus \Delta_0^-$$

is symmetric and has deficiency indices $(2, 2)$. As long as the deficiency indices are equal, we may conclude that the considered operator does have self-adjoint extensions. This operator gives one the model in question.

However, if we impose the Dirichlet boundary conditions

$$u|_{\partial\Omega^\pm} = 0,$$

we immediately face the following problem: the operator obtained via restriction onto the set of smooth functions that vanish in the vicinity of $x^0 \in \partial\Omega$ is essentially self-adjoint. There is no element in the L_2 space which can be taken as a deficiency element. All candidates have too strong singularities. Respectively, constructing of the model is based on the extension of the initial space up to a so-called Pontryagin space (with indefinite inner product). The version of the model for the Dirichlet case based on the theory of self-adjoint operator extensions in Pontryagin space was suggested in [6, 11, 12]. It is important to choose the extension parameters in such a way that the model solution coincides with the main term of the asymptotics (in the window width) of the realistic solution, corresponding to small windows [5, 6]. It can be made by comparison of the asymptotics of the scattering problem described above and the model solution ([6]).

One more application of the result is atmospheric quantum communication description. For quantum channel through turbulent atmosphere, the main reason for error is a shift in the Gaussian beam with respect to the input aperture of the receiver [13, 14]. For calculation of this error, one can use the obtained formulas with the replacement of plane waves by the Gaussian beam [15], e.g., such as:

$$\psi = \frac{w_0}{w} \exp\left(-ik(L - z) + i\phi - \left(\frac{ik}{2b} + \frac{1}{w^2}\right)(x^2 + y^2)\right),$$

where w, w_0, ϕ, b are parameters of the Gaussian beam, L is the distance from the sender, x, y, z are the Cartesian coordinates. One can also take higher modes of the Gaussian beam.

Aknowledgements

This work was partially financially supported by grant 19-31-90154 of RFBR.

References

[1] Morse F.M., Feshbach G. *Methods of theoretical physics*, V. 2. Foreign Literature Publishing House, Moscow, 1960, 986 p.

[2] H. Wang, Sh. Zou. Extremely low scattering cross section of a perforated silver film. *Appl. Phys. Lett.*, 2009, **94**, P. 073119.

[3] Mirin N.A., Ali T.A., Nordlander P., Halas N.J. Perforated semishells: far-field directional control and optical frequency magnetic response. *ACS Nano*, 2010, **4**(5), P. 2701–2712.

[4] Kiselev A.A., Pavlov B.S. The eigenfrequencies and eigenfunctions of the Laplace operator of the Neumann problem in a system of two coupled resonators. *Theor. Math. Phys.*, 1994, **100**, P. 354–366.

[5] Popov I.Yu. The extension theory and localization of resonances for the domain of trap type. *Mathematics of the USSR-Sbornik*, 1992, **71**(1), P. 209–234.

[6] Popov I.Yu. The resonator with narrow slit and the model based on the operator extensions theory. *J. Math. Phys.*, 1992, **33**(11), P. 3794–3801.
[7] Gadyl'shin R.R. Influence of the position of the opening and its shape on the properties of a Helmholtz resonator. *Theor. Math. Phys.*, 1992, **93**, P. 1151–1159.
[8] Borisov D., Exner P. Distant perturbation asymptotics in window-coupled waveguides. I. The non-threshold case. *J. Math. Phys.*, 2006, **47**(11), P. 113502(1-24).
[9] Vorobiev A.M., Popov I.Y., Trifanova E.S. Resonance asymptotics for a pair quantum waveguides with common semitransparent perforated wall. *Nanosystems: Physics, Chemistry, Mathematics*, 2020, **11**(6), P. 619–627.
[10] Kiselev A.A., Popov I.Yu. Indefinite metrics and scattering by a domain with small aperture. *Mathematical Notes*, 1995, **58**(6), P. 1276–1285.
[11] Popov I.Yu. Helmholtz resonator and the operator extension theory in a space with an indefinite metrics. *Matematicheskii sbornik*, 1992, **183**(3), P. 2-38; English translation in *Russian Acad. Sci. Sb. Math.*, 1993, **75**(2), P. 285–315.
[12] Shondin Yu.G. Quantum mechanical models in $\mathbb{R}_n$ connected with extensions of the energy operator in a Pontryagin space. *Teoret. Mat. Fiz.*, 1988, **74**, P. 331–344. English transl. in *Theoret. and Math. Phys.*, 1988, **74**.
[13] Faleeva M.P., Popov I.Y. On quantum bit coding by Gaussian beam modes for the quantum key distribution. *Nanosystems: Physics, Chemistry, Mathematics*, 2020, **11**(6), P. 651–658.
[14] Vasylyev D.Yu., Semenov A.A., Vogel W. Atmospheric quantum channels with weak and strong turbulence. *Phys. Rev. Lett.*, 2016, **117**, P. 090501.
[15] Goncharenko A.M. Gaussian Beams of Light. Minsk, Science and Techn, 1977, 144 p.

NANOSYSTEMS: PHYSICS, CHEMISTRY, MATHEMATICS, 2021, 12 (2), P. 156–160

Quantum random number generator using vacuum fluctuations

B. E. Pervushin[1], M. A. Fadeev[1,2], A. V. Zinovev[1], R. K. Goncharov[1], A. A. Santev[1], A. E. Ivanova[1,2], E. O. Samsonov[1,2]

[1]ITMO University, Kronverkskiy, 49, St. Petersburg, 197101, Russia
[2]Quanttelecom LLC, 6 liniya, Vasilievsky island d.59, korp. 1, lit. B, St. Petersburg, 199178, Russia

borispervushin@itmo.ru, wertsam@itmo.ru, avzinovev15@yandex.ru, rkgoncharov@itmo.ru, aasantev@itmo.ru, aeivanova@itmo.ru, eosamsonov@itmo.ru

PACS 03.67.-a **DOI 10.17586/2220-8054-2021-12-2-156-160**

Experimental implementation of a quantum random number generator based on vacuum fluctuation is presented in this paper. A Y-splitter is used in optical setup of the quantum random number generator. The generation of random numbers in real time with a speed of 300 Mb/s is demonstrated. The conditional minimum entropy is used to estimate the randomness. A cryptographic hashing function is used for post-processing. The resulting sequence has passed DieHard and NIST statistical tests successfully.

Keywords: quantum random number generation, homodyne detection, vacuum fluctuation.

Received: 1 March 2021

Revised: 4 March 2021

1. Introduction

There is a demand for random numbers in many fields of science and technology [1–4]. Existing random number generators (RNG) can be divided into two groups: pseudo-random [5] and physical [6]. Pseudo-random RNGs are based on the use of mathematical algorithms, the output bit sequences of such generators can be predictable. Physical generators using classical physical processes as a source of entropy can also be potentially predictable due to the determinism inherent in classical processes. Such generators can be used in fields that do not require true randomness. However, for certain tasks, more reliable random number generation devices should be used. In particular, the generation of encryption keys in cryptographic systems requires truly random numbers, which can be obtained only by using a quantum random number generator (QRNG). QRNGs are based on quantum processes, which are nondeterministic. Randomness in such generators can be extracted based on the principle of detecting single photons in different optical modes [7], using entangled photons [8], laser phase noise [9], or measuring fluctuations of vacuum [10, 13]. The last type of QRNGs is of the interest due to the simplicity of implementation, relatively compact size, and high speed of random sequence generation. On-chip implementations of the QRNG have been actively developed, due to small dimensions and stability of work [11, 12]. This paper demonstrates the implementation of a quantum random number generator based on vacuum fluctuations using a Y beam splitter. The presented device provides generation of random numbers in real time at a speed of 300 Mb/s. To determine the unpredictability of the output sequence, an estimate of the conditional minimum entropy was employed using the approach described in [15, 16]. The resulting random sequence was tested using the well-known battery of statistical tests DieHard [17] and NIST [18].

2. Quantum randomness generation system

The result of the interference of the reference field, described by Poisson statistics, and the vacuum field on an optical beam splitter with two input and two output ports is described in operator form in [19], these beam splitters were used in the QRNG based on vacuum fluctuations in a number of works [10, 13, 14]. In this work, for the experimental implementation of QRNG based on vacuum fluctuations, the Y-beam splitter is used, the mathematical substantiation of the possibility of using it is presented in [20, 21]. The QRNG scheme based on vacuum fluctuations is shown in Fig. 1.

In the presented QRNG, laser beam (reference field) is mixed with the vacuum field at a polarizing Y beam splitter [22]. A polarization controller is used to fine-tune the division ratio. Thus, two inputs of the balanced detector receive signals containing an amplified vacuum signal as one of its components, which appears as shot noise as a result of detection.

After detection, the differential photocurrent is amplified using a transimpedance amplifier. The resulting voltage, randomly varying in time, is converted into a numerical sequence by an ADC. An extractor is used to extract a truly

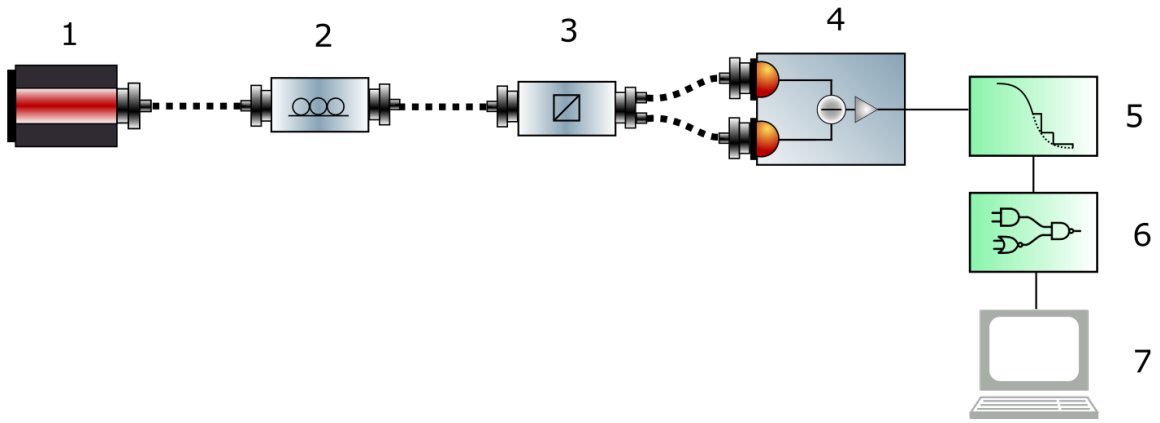

FIG. 1. Scheme of the quantum random number generator based on vacuum fluctuation. 1 – laser; 2 – polarization controller; 3 – Y beam splitter; 4 – balanced detector; 5 – ADC; 6 – FPGA; 7 – computer.

random normally distributed sequence. In particular, to extract a random sequence, an AES-based cryptographic hashing algorithm is used.

3. Experiment

In the proposed experimental implementation, the laser power is set to 40 mW. The reference field is divided on the beam splitter after polarization controller, the total loss of which is 1.06 dB. Two outputs of the Y-splitter are connected to two inputs of a balanced detector, the bandwidth of which is 100 MHz. The electrical signals from the two photodiodes are subtracted and the resulting current is converted to voltage using a transimpedance amplifier. The resulting voltage signal is digitized using a high-speed 8-bit ADC with 100 MHz bandwidth and 150 MHz sampling rate.

The rate of generating a raw sequence of random numbers is:

$$v = \min\left(\tau^{-1}, 2BW\right) \cdot n, \tag{1}$$

where τ^{-1} is the ADC measurement frequency, BW is the smallest bandwidth of the analog signal, n is a number of bits per measurement.

From the formula (1) it can be seen that the generation rate is limited by the measurement frequency and the smallest bandwidth in the circuit. Thus, the raw sequence speed is 1200 Mb/s.

Since, in addition to quantum noise, the system contains untrusted electronic noises, it is necessary to estimate the conditional entropy of the source, taking into account that the intruder can control classical noise. For this purpose, the minimum entropy is used, which, in comparison with the Shannon entropy, is a more rigorous estimate and is generally determined by:

$$H_{\min}\left(M_{dis}\right) = -\log_2\left(\max_i p_i\right), \tag{2}$$

where M_{dis} is a measured discrete signal, p_i are probabilities of different measurement outcomes.

When taking into account the eavesdropper, the conditional minimum entropy in our case is [15]:

$$H_{\min}\left(M_{\text{dis}} \mid E\right) = -\log_2\left(\max\left\{\frac{1}{2}\left[\operatorname{erf}\left(\frac{e_{\max} - R + 3\delta/2}{\sqrt{2}\sigma_q}\right) + 1\right], \operatorname{erf}\left(\frac{\delta}{2\sqrt{2}\sigma_q}\right)\right\}\right), \tag{3}$$

where R is a half the dynamic range of the ADC, $\delta = R/2^{n-1}$, $e_{\max}$ is a maximum value of the electronic signal, and σ_q is a standard deviation of a quantum signal.

Due to the independence of the quantum and electronic signals, the standard deviation of the quantum signal is defined as:

$$\sigma_m^2 = \sigma_e^2 + \sigma_q^2, \tag{4}$$

where σ_m is a standard deviation of the measured signal (sums of quantum and electronic signals), σ_e is a standard deviation of the electronic signal. In the experimental QRNG system, the minimum entropy of the source was 4.78.

The unpredictability of the resulting bit sequence can be guaranteed by the Leftover Hash Lemma [23]. If the hash function converts k bits to

$$l < k \cdot H_{\min}/n - 2\log_2(1/\varepsilon), \tag{5}$$

then the output sequence will be ε-close to the uniform distribution. In this case $k = 1024$, $l = 256$, then the security parameter is less than 2^{-177}. A rather strict security parameter was chosen here, since the hashing algorithm used in this work is not universal [15]. The final sequence generation rate is:

$$V = v \text{ Mb/s} \cdot \frac{256}{1024} = 300 \text{ Mb/s}. \tag{6}$$

DieHard and NIST statistical tests were used to check the resulting output sequence. The results are shown in Tables 1 and 2.

TABLE 1. DieHard statistical test results. The obtained p-value for successful passing of the test must lie in the interval $0.025 <$ p-value < 0.975

No.	Test	p-value
1	BIRTHDAY SPACINGS TEST	0.165456
2	THE OVERLAPPING 5-PERMUTATION TEST	0.654752
3	the BINARY RANK TEST for 31x31 matrices BINARY RANK TEST for 32x32 matrices	0.792586
4	BINARY RANK TEST for 6x8 matrices	0.431478
5	THE BITSTREAM TEST	0.437767
6	OPSO	0.427352
	OQSO	0.481557
	DNA	0.482048
7	the COUNT-THE-1's TEST on a stream of bytes	0.095081
8	the COUNT-THE-1's TEST for specific bytes	0.563297
9	THIS IS A PARKING LOT TEST	0.896585
10	THE MINIMUM DISTANCE TEST	0.815571
11	THE 3DSPHERES TEST	0.039996
12	the SQEEZE test	0.134697
13	The OVERLAPPING SUMS test	0.470491
14	the RUNS test	0.290913
15	CRAPS TEST	0.466673

4. Conclusion

The paper describes an experimental implementation of a system for the generation of random numbers in real time, based on vacuum fluctuations. The quantification of unpredictability is determined by the conditional minimum entropy, taking into account the presence of the eavesdropper. The minimum entropy was 4.78. The resulting sequence has successfully passed the NIST and DieHard statistical test batteries. The parameters of the experimental model of the system made it possible to achieve a generation rate of 300 Mb/s.

Conflict of interest

The authors declare no conflicts of interest.

TABLE 2. Results of passing NIST statistical tests. The p-values must be p-value > 0.025 to pass successfully

No.	Test	p-value
1	BIRTHDAY SPACINGS TEST	0.165456
2	THE OVERLAPPING 5-PERMUTATION TEST	0.654752
3	the BINARY RANK TEST for 31x31 matrices BINARY RANK TEST for 32x32 matrices	0.792586
4	BINARY RANK TEST for 6x8 matrices	0.431478
5	THE BITSTREAM TEST	0.437767
6	OPSO	0.427352
	OQSO	0.481557
	DNA	0.482048
7	the COUNT-THE-1's TEST on a stream of bytes	0.095081
8	the COUNT-THE-1's TEST for specific bytes	0.563297
9	THIS IS A PARKING LOT TEST	0.896585
10	THE MINIMUM DISTANCE TEST	0.815571
11	THE 3DSPHERES TEST	0.039996
12	the SQEEZE test	0.134697
13	The OVERLAPPING SUMS test	0.470491
14	the RUNS test.	0.290913
15	CRAPS TEST	0.466673

Acknowledgements

This work was funded by Government of Russian Federation (grant MK-777.2020.8).

References

[1] Ferrenberg A.M., Landau D.P., et. al. Monte Carlo simulations: Hidden errors from "good" random number generators. *Physical Review Letters*, 1992, **69** (23), 3382.
[2] Gennaro R. Randomness in cryptography. *IEEE security & privacy*, 2006, **4** (2), P. 64–67.
[3] Gisin N., Ribordy G., et. al. Quantum cryptography. *Reviews of modern physics*, 2002, **74** (1), 145.
[4] Metropolis N., Ulam S. The monte carlo method. *Journal of the American statistical association*, 1949, **44** (247), P. 335–341.
[5] Nisan N., Wigderson A. Hardness vs randomness. *Journal of computer and System Sciences*, 1994, **49** (2), P. 149–167.
[6] Johnston D. *Random Number Generators – Principles and Practices: A Guide for Engineers and Programmers*. Walter de Gruyter GmbH & Co KG: 2018, 439 p.
[7] Jennewein T., Achleitner U., et. al. A fast and compact quantum random number generator. *Review of Scientific Instruments*. 2000, **71** (4), P. 1675–1680.
[8] Pironio S., Acin A., Massar S., et. al. Random numbers certified by Bell's theorem. *Nature*, 2010, **464** (7291), P. 1021–1024.
[9] Guo H., Tang W., et. al. Truly random number generation based on measurement of phase noise of a laser. *Physical Review E*, 2010, **81** (5), 051137.
[10] Shi Y., Chng B., et. al. Random numbers from vacuum fluctuations. *Applied Physics Letters*, 2016, **109** (4), 041101.
[11] Kiselev F.D., Samsonov E.O., Gleim A.V. Modeling of linear optical controlled-Z quantum gate with dimensional errors of passive components. *Nanosyst.: Phys. Chem. Math.*, 2019, **10** (6), P. 627–631.
[12] Raffaelli F., et al. A homodyne detector integrated onto a photonic chip for measuring quantum states and generating random numbers. *Quantum Science and Technology*, 2018, **3** (2), 025003.
[13] Gabriel C., Wittmann C., et al. A generator for unique quantum random numbers based on vacuum states. *Nature Photonics*, 2010, **4** (10), P. 711–715.
[14] Ivanova A.E., Chivilikhin S.A., et al. How scatter of the experimental parameters affects the statistical characteristics of a quantum random-number generator. *J. Opt. Technol.*, 2014, **81** (8), P. 427–430.

[15] Haw J.Y., Assad S.M., et. al. Maximization of extractable randomness in a quantum random-number generator. *Physical Review Applied*, 2015, **3** (5), 054004.

[16] Guo X., Liu R., et. al. Enhancing extractable quantum entropy in vacuum-based quantum random number generator. *Entropy*, 2018, **20** (11), 819.

[17] Marsaglia G. DIEHARD Test suite, 1998. `URL: http://www. stat. fsu. edu/pub/diehard`.

[18] Rukhin A., et. al. *A statistical test suite for random and pseudorandom number generators for cryptographic applications*. National Institute of Standards & Technology, 2010.

[19] Grynberg G., et. al. *Introduction to quantum optics: from the semi-classical approach to quantized light*. Cambridge university press, 2010.

[20] Ivanova A.E., Chivilikhin S.A., Miroshnichenko G.P., Gleim A.V. Fiber quantum random number generator, based on vacuum fluctuations. *Nanosyst.: Phys. Chem. Math.*, 2017, **8** (4), P. 441–446.

[21] Ivanova A.E., Chivilikhin S.A., Gleim A.V. The use of beam and fiber splitters in quantum random number generators based on vacuum fluctuations. *Nanosyst.: Phys. Chem. Math.*, 2016, **7** (2), P. 378–383.

[22] Ivanova A.E. Quantum generation of random bit sequences based on vacuum fluctuations in a fiber-optic circuit. PhD Thesis, St. Petersburg, 2017, 121 p.

[23] Tomamichel M., et. al. Leftover hashing against quantum side information. *IEEE Transactions on Information Theory*, 2011, **57** (8), P. 5524–5535.

NANOSYSTEMS: PHYSICS, CHEMISTRY, MATHEMATICS, 2021, 12 (2), P. 161–166

Heterodyne-based subcarrier wave quantum cryptography under the chromatic dispersion impact

R. K. Goncharov[1], A. V. Zinovev[1], F. D. Kiselev[1,2], E. O. Samsonov[1,2]

[1]St. Petersburg National Research ITMO University, Kronverkskiy, 49, St. Petersburg, 197101, Russia
[2]Quanttelecom LLC, Vasilievsky island, 6 Line, 59, St. Petersburg, 199178, Russia

eosamsonov@itmo.ru, rkgoncharov@itmo.ru

PACS 03.67.-a, 42.50.-p **DOI 10.17586/2220-8054-2021-12-2-161-166**

In this paper, we investigate the effect of chromatic dispersion on a continuous variable quantum key distribution system with heterodyne detection, in which information is encoded in the sidebands of modulated laser radiation. We consider the system in which a balanced detector output is downconverted to an intermediate frequency and propose a non-standard methods of dispersion compensation using RF phase shifters.

Keywords: heterodyne detection, subcarrier wave, quantum key distribution, chromatic dispersion.

Received: 5 March 2021

Revised: 13 March 2021

1. Introduction

Rapidly evolving quantum technologies bring a threat to most of the contemporary cryptography protocols, since quantum computers are able to solve several tasks such as factorization remarkably faster than classical ones [1]. This fact explains the emerging interest in the field of quantum key distribution (QKD), which is the only known method of transfer of cryptographic keys in real time with an unconditional security. It was established in 1984 by seminal work of Brassard and Bennett [2].

There exists two major approaches to quantum key distribution: discrete-variable (DV) QKD and continuous-variable (CV) QKD. The essence of CV-QKD is the detection of signal quadratures of a coherent state [3–11]. Such protocols are appealing since its practical implementations can be manufactured from off-the-shelf components [12–14].

This paper describes a CV-QKD protocol based on subcarrier wave (SCW) modulation method. In SCW QKD protocols [15–20] multimode weak coherent states are generated by electro-optic phase modulation. As a result, sideband spectrum is formed with its phase, relative to the initial carrier field, containing the quantum information [21–23] (detailed descriptions of SCW DV-QKD and CV-QKD protocols can be found in [15] and [20], respectively). The main advantages of SCW QKD are the simplification of the phase shift matching between Alice and Bob and lack of complex interference schemes and efficient usage of the channel's bandwidth. It was shown that such method is suitable both for DV-QKD and CV-QKD. Detection scheme extracts information from coherent multimode states in a way similar to classical heterodyning. Feasibility and advantages of such scheme is fully described in [24].

However, this method is extremely prone to the chromatic dispersion, since in this case each sideband in the channel undergoes a different phase shift depending on the frequency. Its influence on SCW DV-QKD and possible ways to reduce the negative impact were examined in [25].

In this paper, we investigate the dispersion influence on the proposed scheme. We suggest a numerical model that takes dispersion of the optical fiber channel into account. We demonstrate the main feature of introduced scheme, which is the ability to compensate the difference between phase shifts of different subcarrier modes.

This paper is organized as follows. In Section 2, we describe suggested scheme, using plain classical model. In Section 3 dispersion influence on the protocol is discussed. In this paper, we consider only a simple analytical dispersion model of the SCW QKD protocol.

2. Proposed scheme

Here, we describe a scheme for SCW QKD, based on the method of coherent detection [24]. The main advantage of the method lies in the simultaneous detection of two quadrature components without the need for two balanced detectors and double homodyning. It is worth noting that proposed scheme has not only the advantage of detecting both of the quadratures, but also has only passive optical components on the receiver's side. Hence, such scheme is both affordable and easy to adjust.

Let us describe the BB84-like SCW CV-QKD protocol first (Fig. 1). Alice emits coherent pulses with a laser (1), then they get modulated with a phase modulator (2) and attenuated (3) in order to achieve a single-photon level of energy at the sidebands. Bob receives the signal and uses a low frequencies filter (5) to pass a half of central frequency and positive sidebands to the first arm of the balanced detector (6) and uses circulator (4) to send the second part of the central frequency and negative sidebands to the second arm of detector.

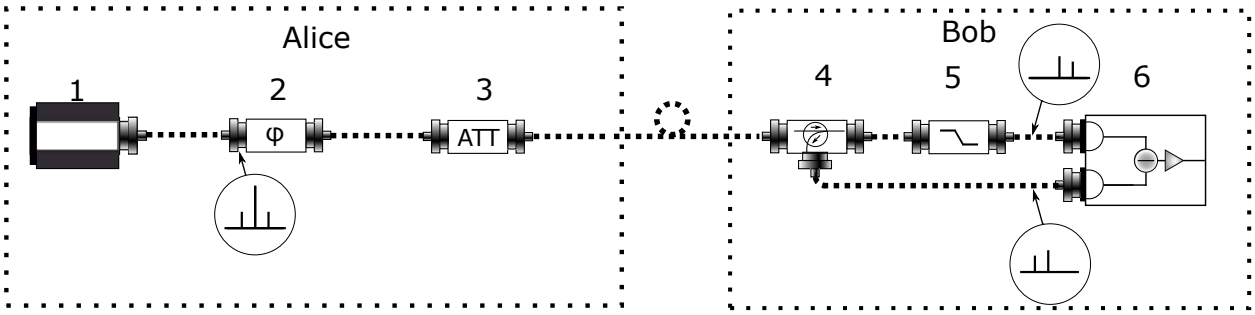

FIG. 1. Proposed SCW detection scheme. 1 – laser, 2 – phase modulator, 3 – attenuator, 4 – circulator, 5 – low frequency filter, 6 – balanced detector. Diagrams in circles show the simplified power spectrum.

We can obtain the expressions for the incident fields for both arms of the balanced detector before detection as:

$$E_1(t) = E_0 e^{i\omega t}\left(\sum_{k=1}^{\infty} i^k J_k(m_a) e^{ik(\Omega t+\phi_a)} + \sqrt{0.5} J_0(m_a)\right), \tag{1}$$

$$E_2(t) = E_0 e^{i\omega t}\left(\sum_{k=1}^{\infty} i^k J_k(m_a) e^{-ik(\Omega t+\phi_a)} + \sqrt{0.5} J_0(m_a)\right), \tag{2}$$

where J_k is the k-order Bessel function of the first kind, m_a is the modulation index, which is typically smaller than unity.

The output of the balanced detector can be written as [24]:

$$\begin{aligned} I(t) &= R(\lambda) G C \left(|E_1(t)|^2 - |E_2(t)|^2\right) \\ &= R(\lambda) G C \left(2\sqrt{2} E_0^2 J_0(m_a) J_1(m_a) \sin(\Omega t + \phi_a)\right). \end{aligned} \tag{3}$$

where $R(\lambda)$ is the responsivity of photodiodes, G is the electronic gain of the photodetector and $C = S/2\xi$ is the ratio of the effective beam area S and the doubled impedance ξ of the medium.

Turns out that the resulting signal detected by Bob has exactly the same frequency as the modulating signal, while the phase is shifted by 90°.

The resulting output, as one may see on Fig. 2, has the sinusoidal form. The most exiting feature of this oscillation is that it contains full information about the phase chosen by Alice. The possibility of extraction of this phase was experimentally proven in [24]. Hence, such detecting technique allows one to measure both quadratures simultaneously. However, a conflict between spectral filtering and the detector's bandwidth emerges here. To obtain the phase information correctly, the bandwidth of a balanced detector should be equal or more than Ω. Therefore, one may find themselves at the crossroads choosing the optimal Ω for practical implementation of the system. On the one hand, rise of modulation frequency causes the increase of required detector's bandwidth, which leads to additional electronic noises. Typical balanced detectors' bandwidth used for quantum measurements is less than 1 GHz. On the other hand, decrease of modulation frequency complicates the spectral filtering.

It is important to note that within last years there were several works dedicated to balanced detectors for quantum measurements with a bandwidth of several GHz. Kleis et al. [26] applied deep learning methods to adjust a CV-QKD system for the noises emerging from the expanding of the bandwidth. As the result, they have achieved a 9.2 Mbit/s key rate for a fiber line of 26 km. Huang and al. [27] reported about 1 Mbps secure key rate over 25 km of optical fiber. One major implementation that allowed us to achieve such results was the balanced detector with the bandwidth of 1 GHz. Hence, the development of wideband balanced detectors suitable for quantum measurements will remove the main obstacle for practical implementation of the scheme proposed in this paper.

Usage of these highly-sensitive and wideband balanced detectors in the scheme would allow us to successfully bring to life a system with several major advantages. First, the receiver's side has no active optical elements, which

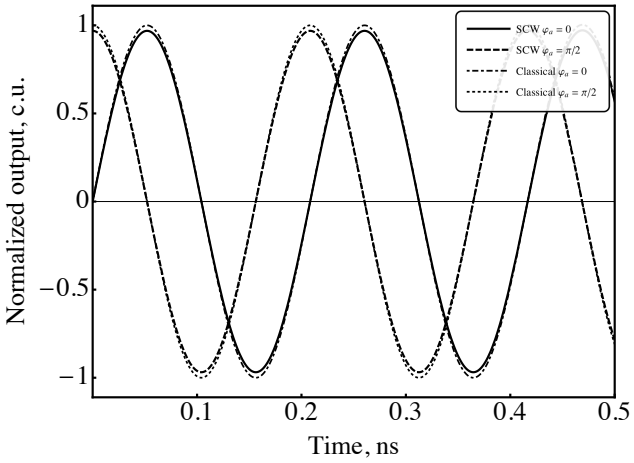

FIG. 2. Time dependence of the normalized heterodyne-derived signals for the SCW and the classical detection schemes. For the sake of thoroughness, two different phase shifts are depicted.

significantly enlarges the robustness and usability of the method. The lack of second phase modulator (which presence is fairly common for most of the SCW QKD schemes) also positively boosts the affordability of the system. Moreover, since the detector measure both quadratures, there is no need to shift the key. In addition, such system will be also resistant to the influence of chromatic dispersion, which is discussed in the next section.

3. Dispersion effects in the SCW CV-QKD

The influence of chromatic dispersion on the DV-SCW system was investigated in [25]. There was shown that SCW QKD systems are prone to the influence of the chromatic dispersion. The worst part of it is that for certain fiber lengths quantum key distribution is fundamentally impossible without any dispersion compensation.

One of the methods of mitigating the dispersion influence, proposed in [25], is to send only one half of the spectrum to the channel. In the case of QKD with coherent detection, one have to carry out classical heterodyning via spectral filter and beam splitter. Another method to reduce the dispersion effect is using a dispersion compensation module. Both methods increase the attenuation in optical channel, which is extremely undesirable for QKD system. Another downside is that such elements are expensive, what nullify affordability as one of the CV QKD system's major advantage.

Here we propose the system which is resistant to the chromatic dispersion influence. Let us begin from the description of the dispersion mathematical model for the system. Dependence of the propagation constant of the fundamental mode in single-mode optical fibers on wavelength can be represented as Taylor series within the vicinity of some wavelength [28]:

$$\beta(\omega) \approx \beta_0 + \beta_1 \Delta\omega + \frac{\beta_2}{2}\Delta\omega^2 + \frac{\beta_3}{6}\Delta\omega^3, \tag{4}$$

where $\delta\omega = \omega - \omega_0$.

Proposed protocol fits in the frame of such description since the both sidebands are situated spectrally close to the carrier band. Then, within the framework of the description, the central frequency ω is the frequency of the carrier mode. Taking into account the first two orders in the Eq. (4), the phase shift of the sidebands, depending on the fiber length L, can be calculated as follows:

$$\Phi_+ = \left(\beta_1 + \frac{\beta_2}{2}\Omega\right)\Omega L \tag{5}$$

for the "right" subcarrier and:

$$\Phi_- = -\left(\beta_1 - \frac{\beta_2}{2}\Omega\right)\Omega L \tag{6}$$

for the "left" subcarrier.

According to [28] the β-parameters can be calculated as:

$$\beta_1 = 1/v_g, \tag{7}$$

$$\beta_2 = -\frac{D\lambda^2}{2\pi c}, \tag{8}$$

where v_g is a group velocity, D is a dispersion parameter, λ is a wavelength, and c is a velocity of light. For the SMF-28e fiber that was also used in [25], $\beta_1 = 4.8964 \cdot 10^{-6}$ s/km and $\beta_2 = -2.0407 \cdot 10^{-23}$ s^2/km.

While such model is an analytical simplification, taking into account only two sidebands, in [25] it was extensively investigated in the context of its application to SCW QKD; the results were also compared with the results obtained by numeric solution of the nonlinear Schrodinger equation.

Now let us write the simplified expressions for the electric fields considering the dispersion phase shifts:

$$E_1(t) \approx E_0 \left(iJ_1(m_a)e^{i((\omega+\Omega)t+\phi_a+\Phi_+)} + \sqrt{0.5}J_0(m_a)e^{i\omega t} \right), \tag{9}$$

$$E_2(t) \approx E_0 \left(iJ_1(m_a)e^{i((\omega-\Omega)t-\phi_a+\Phi_-)} + \sqrt{0.5}J_0(m_a)e^{i\omega t} \right). \tag{10}$$

Mimicking the way of obtaining the expression for the balanced detector output (3), we obtain:

$$\begin{gathered} I(t) \sim \\ \sqrt{2}J_1(m_a)J_0(m_a)\Big(\sin(\Omega t + \varphi_a + \Phi_+) + \sin(\Omega t + \varphi_a - \Phi_-) \Big) \\ = 2\sqrt{2}J_0(m_a)J_1(m_a) \sin\left(\Omega t + \varphi + \frac{\Phi_+ - \Phi_-}{2} \right) \cos\left(\frac{\Phi_+ + \Phi_-}{2} \right). \end{gathered} \tag{11}$$

Obviously, for the observed sine function, the term $\dfrac{\Phi_+ - \Phi_-}{2} = \beta_1 \Omega L$ introduces only an additional phase shift, which can be easily compensated. However, the external cosine factor affects the output's visibility which, disregarding chromatic dispersion, is equal to one in the considered lossless scenario. Therefore we express it as follows:

$$V = \left| \cos\left(\frac{\Phi_+ + \Phi_-}{2} \right) \right| = |\cos(\beta_2 \Omega^2 L/2)|. \tag{12}$$

In case of the $L\beta_2\Omega^2/2 = \pi k/2$ with $k \in \mathbb{Z}$, visibility will always be zero, thus, it would be impossible to generate a secure key without any compensation of the dispersion effects. As is seen from Fig. 3 and Fig. 4, the visibility, as well as the detector output, drops to zero at the distance of 169.25 km, in case of SMF-28e fiber usage.

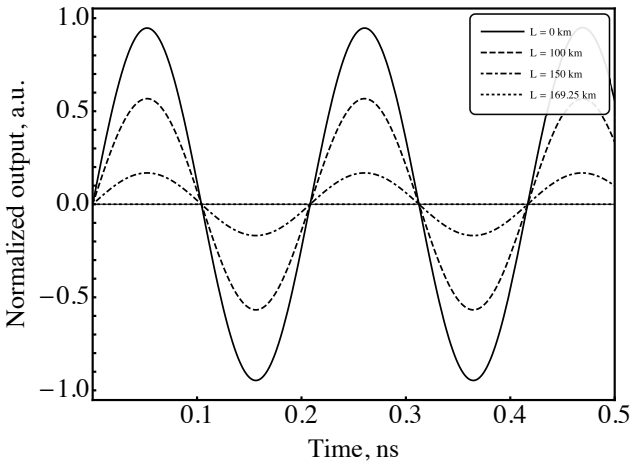

FIG. 3. Balanced detector output under the chromatic dispersion influence. The distance is fixed at certain values.

Such signal degradation greatly reduces the potential of practical implementation. Since the key rate would decrease along with the visibility of the signal, a successful dispersion compensation is exceptionally important milestone on the way of implementation of this scheme.

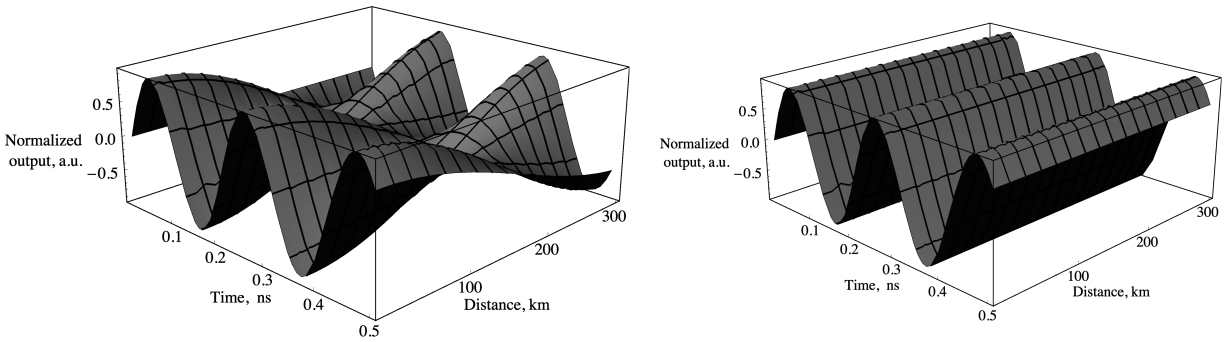

(A) (B)

FIG. 4. Balanced detector output with a full dispersion compensation.

The best way to compensate dispersion effect for the proposed scheme is to install a RF phase shifter to one arm of the balanced detector, after photodiodes [29]. To completely mitigate the distorting influence of the chromatic dispersion, we propose to shift the phase in the upper arm by a known value $-(\Phi_- + \Phi_+)$ (or by $(\Phi_- + \Phi_+)$ in the lower arm) in order to achieve the same common phase in both arms that can be compensated afterwards [30]. This result can be represented graphically, as in Fig. 4b.

4. Conclusion

We have considered an analytical model of chromatic dispersion for the case of subcarrier wave quantum cryptography system with heterodyne detection. Due to the phase matching requirement in the proposed scheme, dispersion has a significant negative impact on the detector output. However, with a usage of RF electrical phase shifters and oscilloscope adjustment, one can fully compensate phase deviation between balanced detector arms. In future works, this can be implemented experimentally, as well as with a cohesive QKD security proof in terms of quantum model.

Acknowledgements

This work was funded by Government of Russian Federation (grant MK-777.2020.8).

Conflict of interest

The authors declare no conflicts of interest.

References

[1] Pirandola S., Andersen U.L., et al. Advances in quantum cryptography. *Advances in Optics and Photonics*, 2020, **12** (4), P. 1012–1236.
[2] Bennett C., Brassard G. Quantum cryptography: public key distribution and coin tossing. *Proceedings of "IEEE International Conference on Computers, Systems and Signal"*, Bangalore, India, IEEE, 1984, P. 175–179.
[3] Lo H.-K., Curty M., Tamaki K. Secure quantum key distribution. *Nature Photonics*, 2014, **8** (8), P. 595–604.
[4] Ralph T.C. Continuous variable quantum cryptography. *Physical Review A*, 1999, **61** (1), 010303.
[5] Grosshans F., Van Assche G., et al. Quantum key distribution using gaussian-modulated coherent states. *Nature*, 2003, **421** (6920), P. 238–241.
[6] Hirano T., Yamanaka H., et al. Quantum cryptography using pulsed homodyne detection. *Physical Review A*, 2003, **68** (4), 042331.
[7] Leverrier A., Grangier P. Continuous-variable quantum-key-distribution protocols with a non-gaussian modulation. *Physical Review A*, 2011, **83** (4), 042312.
[8] Heid M., Lütkenhaus N. Efficiency of coherent-state quantum cryptography in the presence of loss: Influence of realistic error correction. *Physical Review A*, 2006, **73** (5), 052316.
[9] Brádler K., Weedbrook C. Security proof of continuous-variable quantum key distribution using three coherent states. *Physical Review A*, 2018, **97** (2), 022310.
[10] Papanastasiou P., Lupo C. , Weedbrook C. , Pirandola S. Quantum key distribution with phase-encoded coherent states: Asymptotic security analysis in thermal-loss channels. *Physical Review A*, 2018, **98** (1), 012340.
[11] Lin J., Upadhyaya T., Lütkenhaus N. Asymptotic security analysis of discrete-modulated continuous-variable quantum key distribution. *Physical Review X*, 2019, **9** (4), 041064.
[12] Comandar L.C., Brunner H.H., et al. A flexible continuous-variable QKD system using off-the-shelf components. *Quantum Information Science and Technology III*, 2018, **10442**, P. 37–43.
[13] Wang H., Pi Y., et al. High-speed gaussian-modulated continuous-variable quantum key distribution with a local oscillator based on pilot-tone-assisted phase compensation. *Optics Express*, 2020, **28** (22), P. 32882–32893.

[14] Fossier S., Diamanti E., et al. Field test of a continuous-variable quantum key distribution prototype. *New Journal of Physics*, 2009, **11** (4), 045023.
[15] Gleim A.V., Egorov V.I., et al. Secure polarization-independent subcarrier quantum key distribution in optical fiber channel using BB84 protocol with a strong reference. *Optics Express*, 2016, **24** (3), P. 2619–2619.
[16] Miroshnichenko G.P., Kozubov A.V., et al. Security of subcarrier wave quantum key distribution against the collective beam-splitting attack. *Optics Express*, 2018, **26** (9), P. 11292–11308.
[17] Kynev S.M., Chistyakov V.V., et al. Free-space subcarrier wave quantum communication. *Journal of Physics: Conference Series*, 2017, **917**, 052003.
[18] Merolla J.-M., Mazurenko Y., et al. Phase-modulation transmission system for quantum cryptography. *Optics Letters*, 1999, **24** (2), P. 104–106.
[19] Chistiakov V., Kozubov A., et al. Feasibility of twin-field quantum key distribution based on multi-mode coherent phase-coded states. *Optics Express*, 2019, **27** (25), P. 36551–36561.
[20] Samsonov E., Goncharov R., et al. Subcarrier wave continuous variable quantum key distribution with discrete modulation: mathematical model and finite-key analysis. *Scientific Reports*, 2020, **10** (1), P. 1–9.
[21] Miroshnichenko G.P., Kiselev A.D., Trifanov A.I., Gleim A.V. Algebraic approach to electro-optic modulation of light: exactly solvable multimode quantum model. *Journal of the Optical Society of America B*, 2017, **34** (6), P. 1177–1190.
[22] Capmany J., Fernández-Pousa C.R. Quantum model for electro-optical phase modulation. *Journal of the Optical Society of America B*, 2010, **27** (6), A119–A129.
[23] Kumar P., Prabhakar A. Evolution of quantum states in an electro-optic phase modulator. *IEEE journal of quantum electronics*, 2008, **45** (2), P. 149–156.
[24] Samsonov E., Goncharov R., et al. Coherent detection schemes for subcarrier wave continuous variable quantum key distribution. ArXiv:2006.16543, 2020.
[25] Kiselev F., Samsonov E., et al. Analysis of the chromatic dispersion effect on the subcarrier wave QKD system. *Optics Express*, 2020, **28** (19), P. 28696–28712.
[26] Kleis S., Rueckmann M., Schaeffer C.G. Continuous-variable quantum key distribution with a real local oscillator and without auxiliary signals. ArXiv:1908.03625, 2019.
[27] Huang D., Lin D.,et al. Continuous-variable quantum key distribution with 1 Mbps secure key rate. *Optics Express*, 2015, **23** (13), P. 17511–17519.
[28] Agrawal G.P. *Fiber-optic communication systems*. John Wiley & Sons, Hoboken, 2012, 626 p.
[29] Horowitz P., Hill W. *The art of electronics*. Cambridge University Press, Cambridge, 1989, 1220 p.
[30] Xinyi T. Broadband phase shifter design for phased array radar systems. PhD Thesis, National University of Singapore, 2011.

NANOSYSTEMS: PHYSICS, CHEMISTRY, MATHEMATICS, 2021, 12 (2), P. 167–174

A quantum chemical study on the magnetic nanocarrier-tirapazamine drug delivery system

S. Avarand, A. Morsali, M. M. Heravi, S. A. Beyramabadi

Department of Chemistry, Mashhad Branch, Islamic Azad University, Mashhad, Iran

sadaf.avarand@gmail.com, almorsali@yahoo.com, drmh45@yahoo.com, abeyramabadi@gmail.com

PACS 78.67.-n, 78.67.Ch **DOI 10.17586/2220-8054-2021-12-2-167-174**

Magnetic nanoparticles are among the most important carriers for the delivery of anticancer drugs. Four important noncovalent interactions between tirapazamine anticancer drug (TPZ) and magnetic nanoparticle $Fe_6(OH)_{18}(H_2O)_6$ (MNP) have been examined by using density functional theory (DFT). Important interactions are those where the drug approaches the magnetic nanocarrier via NH_2 (MNP/TPZ1), NO (MNP/TPZ2-3) and intraring N-atom (MNP/TP4) functional groups. The negative values of binding energies and quantum molecular descriptor showed that these interactions contribute to the stability of the system. By increasing the temperature, TPZ can bond to MNP through NH_2 (NH_2 mechanism), NO (NO mechanisms) and intraring N-atom (N mechanism) functional groups. The activation parameters of four mechanisms were evaluated using quadratic synchronous transit method. Relative energies indicate that the product of the NH_2 mechanism is more stable but is produced more slowly (thermodynamic product). In contrast, the products of the NO mechanisms are kinetic products.

Keywords: magnetic nanoparticles, tirapazamine, DFT, noncovalent interactions, reaction mechanism.

Received: 15 August 2020

Revised: 19 January 2021

1. Introduction

Magnetic nanoparticles have shown significant applications in chemical, biological and drug delivery systems [1–7]. These nanoparticles include iron, cobalt and nickel elements and their oxides, among which iron oxide nanoparticles are the most widely used. In addition to advantages such as high surface area to volume ratio and unique electronic and chemical properties, iron oxide nanoparticles, due to their magnetic properties, can be targeted to the cancerous tissue by an external magnetic field [8–12]. Once the drug reaches the target tissue, it is released by factors such as temperature, pH and enzymatic activity [13, 14]. In spite of modern methods based on the use of nanocarriers [15–19], traditional chemotherapy methods have many side effects [20, 21].

Maghemite (γ-Fe_2O_3) and Magnetite (Fe_3O_4) nanoparticles are most commonly used in drug delivery systems. Iron oxide nanoparticles have been used to deliver anti-cancer drugs like 5-flurouracil [22], cisplatin [23], camptothecin [24], doxorubicin [25], methotrexate [26], tamoxifen [27], paclitaxel [28], sorafenib [29], gemcitabine [30], 6-mercaptopurine [31] and mitoxantrone [32] to the target tissue. These nanoparticles have also been used along with other carriers such as gold [33], chitosan [34], silica [35], carbon nanotubes [36], surfactant [37], C_{60} [38], peptide nanotubes [39],lipid [40], liposome [41], dextran [42], polymers [43, 44] and DNA [45].

Quantum chemical calculations have been widely used to investigate drug delivery systems from a molecular point of view [46–53]. In this work, quantum mechanics was used to investigate a drug delivery system, including iron oxide nanoparticles and 1,3-amino-1,2,4-benzotriazine-1,4-N,N-dioxide (tirapazamine). Tirapazamine is an anticancer drug used to treat neck cancer, head cancer, cervical cancer and prostate cancer [54, 55]. Such computations can inspire scientists to manufacture new systems for drug delivery.

2. Computational details

We used GAUSSIAN 09 package [56] to perform all the calculations at B3LYP /6-31G(d,p). For Fe atoms the LANL2DZ basis set has been used. The zero-point and thermal corrections were also considered to calculate binding, solvation and activation energies. The transition states have been checked to possess only one imaginary frequency. Polarized continuum model (PCM) was employed for the evaluation of implicit solvent effects [57, 58].

The Chemical reactivity and stability were examined using quantum descriptors. If $I = -E_{HOMO}$ and $A = -E_{LUMO}$ are the ionization potential and the electron affinity, then the global hardness (η) is defined by Eq. (1):

$$\eta = (I - A)/2. \tag{1}$$

The electrophilicity index (ω) has been evaluated by Eq. (2) [59]:

$$\omega = (I + A)^2/4\eta. \tag{2}$$

3. Results and discussion

3.1. Nonbonded interactions

Tirapazamine (TPZ) is an anticancer drug that has four important functional groups (NH_2 and NO1, NO2 and N groups as shown in Fig. 1. Fig. 1 shows the optimized structures of TPZ and magnetic nanoparticle (MNP: $Fe_6(OH)_{18}(H_2O)_6$ ring cluster model [60]). This model has been developed for magnetite (Fe_3O_4) and maghemite (γ-Fe_2O_3) nanoparticles, which are widely used in drug delivery. The reason is related to the superparamagnetic properties of these particles, which can be directed to the cancerous tissue by applying an external magnetic field [61,62]. The interactions between magnetic nanoparticle (MNP) and TPZ through NH_2 (MNP/TPZ1) and N-oxide 1 (MNP/TPZ2), N-oxide 2 (MNP/TPZ3) and intraring N-atom (MNP/TP4) groups in aqueous solution have been illustrated in Fig. 1.

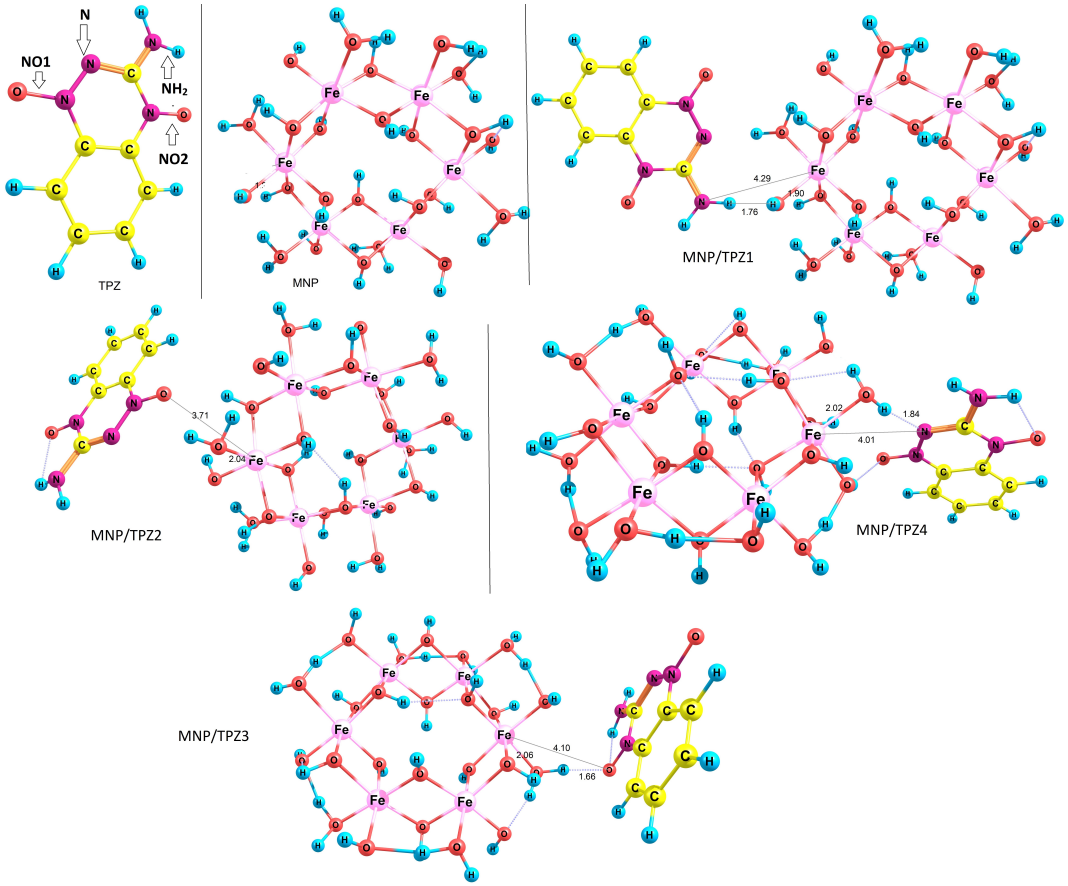

FIG. 1. Optimized structures of TPZ, MNP and MNP/TPZ1-4

For the binding energies (ΔE), we have (Table 1):

$$\Delta E = E_{MNP/TPZ1-4} - (E_{MNP} + E_{TPZ}), \tag{3}$$

where E is the sum of electronic and zero-point energies. The negative binding energies in both phases indicate that the drug absorption on the MNP carrier is thermodynamically desirable. Also, MNP/TPZ1 and MNP/TPZ4 are more stable than MNP/TPZ2 and MNP/TPZ3 in both phases.

Table 1 also represents E_g (energy difference between LUMO and HOMO), ω and η for all configurations. E_g and η are indicators to identify more stable structures. These two quantities of MNP/TPZ1 and MNP/TPZ4 have greater amounts than MNP/TPZ2 and MNP/TPZ3. Also, η and E_g of TPZ are higher than those of MNP/TPZ1-4, indicating the reactivity of TPZ increases in drug-carrier systems. This is important because it raises the possibility of a reaction between the drug and the carrier in appropriate conditions, which will be discussed in the next section. An increase in ω of TPZ in the drug-carrier systems indicates that TPZ acts as an electron acceptor.

TABLE 1. Binding energies (kJ mol^{-1}) and quantum molecular descriptors (eV) of calculated structures

Species	E_{HOMO}	E_{LUMO}	E_g	η	ω	ΔE
		Solution phase (water)				
TPZ	−5.54	−2.62	2.92	1.46	5.70	
MNP	−5.58	−4.48	1.10	0.55	22.95	
MNP/TPZ1	−5.55	−4.42	1.13	0.56	22.07	−11.73
MNP/TPZ2	−5.56	−4.52	1.04	0.52	24.42	−5.09
MNP/TPZ3	−5.53	−4.43	1.10	0.55	22.49	−6.26
MNP/TPZ4	−5.67	−4.56	1.11	0.56	23.49	−12.54
		Gas phase				
TPZ	−5.39	−2.52	2.87	1.44	5.45	
MNP	−5.41	−4.36	1.05	0.53	22.68	
MNP/TPZ1	−5.49	−4.42	1.07	0.53	23.00	−31.41
MNP/TPZ2	−5.37	−4.40	0.97	0.48	24.68	−14.14
MNP/TPZ3	−5.35	−4.30	1.05	0.53	22.19	−15.77
MNP/TPZ4	−5.39	−4.25	1.14	0.57	20.46	−32.76

3.2. Covalent functionalization

One possibility of forming a covalent bond between the drug and the carrier is to replace the surface hydroxyl groups of the magnetic nanoparticle with the drug. In this mechanism (NH_2 mechanism) the amino group of TPZ transfers a hydrogen to the hydroxyl group of MNP so that by leaving a H_2O molecule, the drug bonds to the Fe atom and therefore, product MNPTPZ1/H_2O is produced (Fig. 2). Fig. 3 shows the optimized structure of product MNPTPZ1/H_2O.

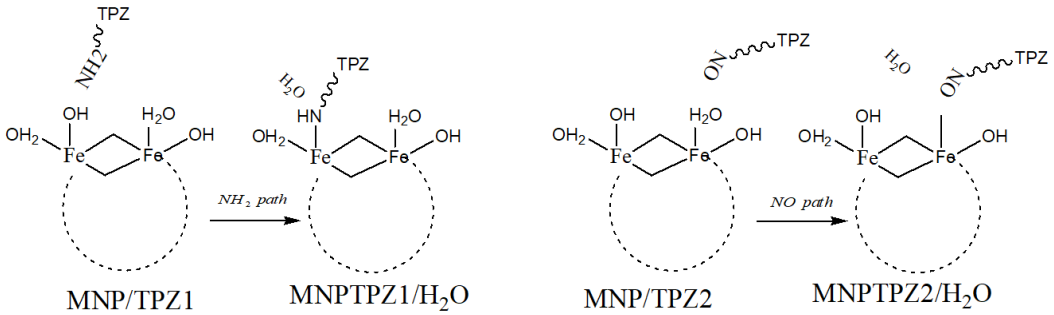

FIG. 2. NH_2 and NO mechanisms

The transition state of this mechanism (TS1) was obtained by Quadratic Synchronous Transit (QST3) method and presented in Fig. 4. Changes in the important bond lengths have been shown in Fig. 1 (reactant MNP/TPZ1), Fig. 3 (product MNPTPZ1/H_2O) and Fig. 4 (TS1).

Relative energies (Gibbs free energy ($\Delta G^{\ddagger}$), activation enthalpy ($\Delta H^{\ddagger}$) and activation energy (E_a)) for reactants, products and transition states have been presented in Table 2. The energy values of the product MNPTPZ1/H_2O indicate that the process is exothermic ($\Delta H < 0$) and spontaneous ($\Delta G < 0$). E_a, $\Delta H^{\ddagger}$ and $\Delta G^{\ddagger}$ for NH_2 mechanism are 103.66, 102.71 and 116.82 kJ mol^{-1}, respectively (Table 2).

The other reactions (NO1 and NO2 mechanisms) have been illustrated in Fig. 2. In these reactions surface H_2O molecules of MNT are substituted by NO functional groups of TPZ to produce MNPTPZ2/H_2O and MNPTPZ3/H_2O. The optimized structures of products MNPTPZ2/H_2O and MNPTPZ3/H_2O are shown in Fig. 3.

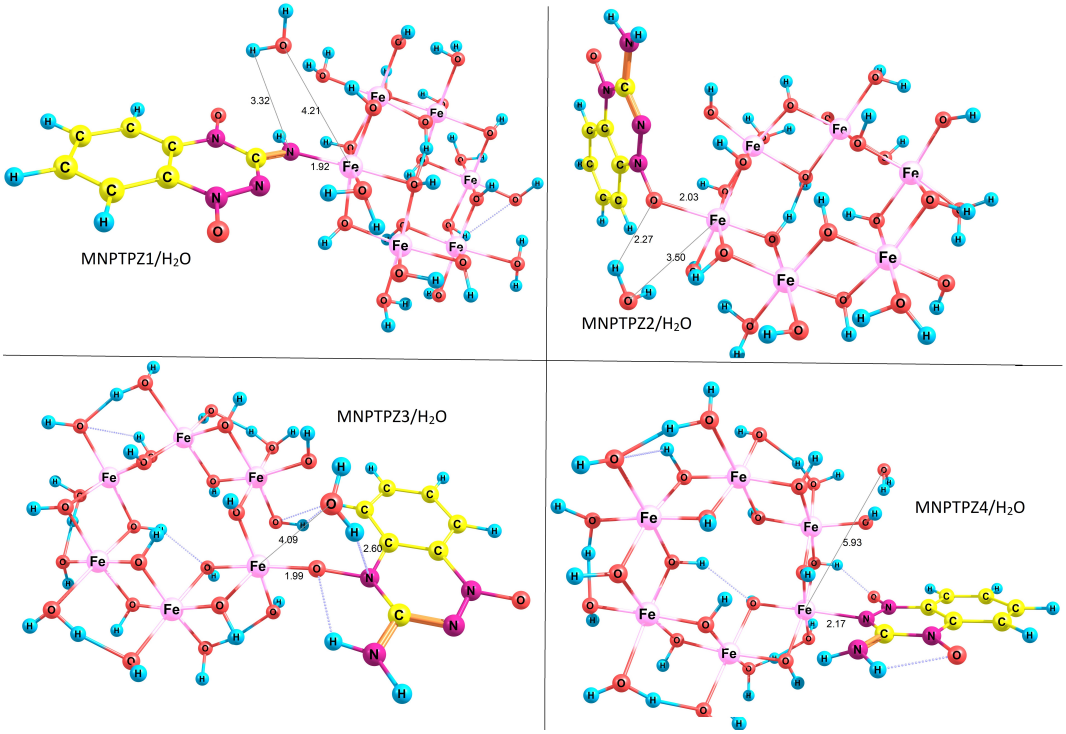

FIG. 3. Optimized structures of MNPTPZ1-4/H_2

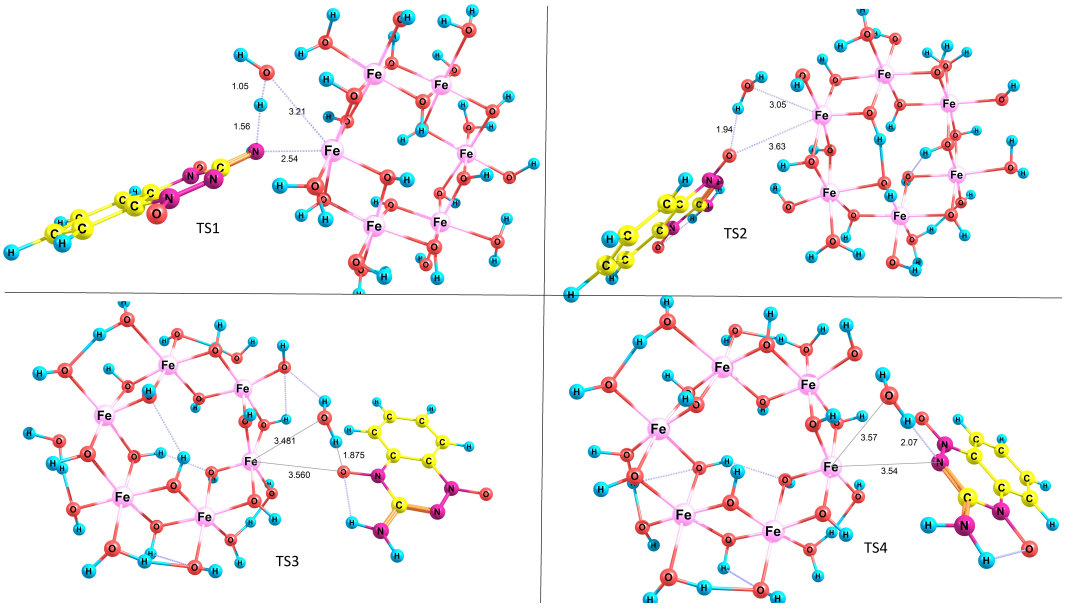

FIG. 4. Optimized structures of TS1-4

TABLE 2. Relative energies (kJ mol^{-1}) in NH2 and NO mechanisms

Species	**E**	**H**	**G**
	NH_2(OH) mechanism		
MNP/TPZ1	0.00	0.00	0.00
TS1	103.66	102.71	116.82
MNPTPZ1/H_2O	−16.67	−21.70	−5.34
	NO1 mechanism		
MNP/TPZ2	0.00	0.00	0.00
TS2	38.89	44.10	51.74
MNPTPZ2/H_2O	−5.88	−11.51	−2.28
	NO2 mechanism		
MNP/TPZ3	0.00	0.00	0.00
TS3	37.22	43.08	50.91
MNPTPZ3/H_2O	−7.60	−14.03	−3.26
	N mechanism		
MNP/TPZ3	0.00	0.00	0.00
TS4	65.47	69.84	77.27
MNPTPZ3/H_2O	9.43	3.39	12.46
	NH_2(H_2O) mechanism		
MNP/TPZ1+	0.00	0.00	0.00
TS1+	81.31	87.99	94.69
MNPTPZ1+/H_2O	11.02	6.06	13.80

Using reactants MNP/TPZ2 and MNPTPZ3/H_2O and products MNPTPZ2/H_2O and MNPTPZ3/H_2O, the transition states of NO pathways (Fig. 4) were found (TS2 and TS3). E_a, $\Delta H^{\ddagger}$ and $\Delta G^{\ddagger}$ of NO1 mechanism (NO2 mechanism) are 38.89 (37.22), 44.10 (43.08) and 51.74 kJ mol^{-1} (50.91 kJ mol^{-1}), respectively (Table 2). Similar to the previous reaction, these reactions are also spontaneous and exothermic.

The N mechanism is similar to NO mechanism. In this mechanism, the surface H_2O molecule of MNP is substituted by the intraring N-atom functional group of TPZ to produce product MNPTPZ4/H_2O (Fig. 3). Using MNP/TPZ4 and MNPTPZ4/H_2O, the transition state of N mechanism (Fig. 4) was optimized (TS4). E_a, $\Delta H^{\ddagger}$ and $\Delta G^{\ddagger}$ of N mechanism are 65.47, 69.74 and 77.27 kJ mol^{-1}, respectively (Table 2). Another possibility is to consider a mechanism similar to NO and N mechanisms for NH_2 functional group (NH_2+ mechanism). Fig. 5 shows the reactant (MNP/TPZ1+), product (MNPTPZ1+/H_2O) and transition state (TS1+) for this reaction. E_a, $\Delta H^{\ddagger}$ and $\Delta G^{\ddagger}$ of NH_2+ mechanism are 81.31, 87.99 and 94.69 kJ mol^{-1}, respectively (Table 2). The latter two mechanisms are endothermic and nonspontaneous (endergonic reactions), unlike the previous ones.

The first reaction product (MNPTPZ1/H_2O) has more negative energy (is more stable) than the other reaction products, therefore, MNPTPZ1/H_2O is the thermodynamic product. On the other hand, the values of activation parameters related to the NO1 and NO2 mechanisms are lower than those of the NH_2, N and NH_2+ mechanisms. For example, the activation energy of the second mechanism (NO1) is lower than the former (NH_2) by 64.79 kJ mol^{-1}. So, MNPTPZ2/H_2O and MNPTPZ3/H_2O are kinetic products. Increasing the temperature (for example, using ultrasonic irradiation) will increase the contribution of the product MNPTPZ1/H_2O (NH_2 mechanism) which has higher activation energy due to the proton transfer from the amino group of TPZ to the hydroxyl group of MNP.

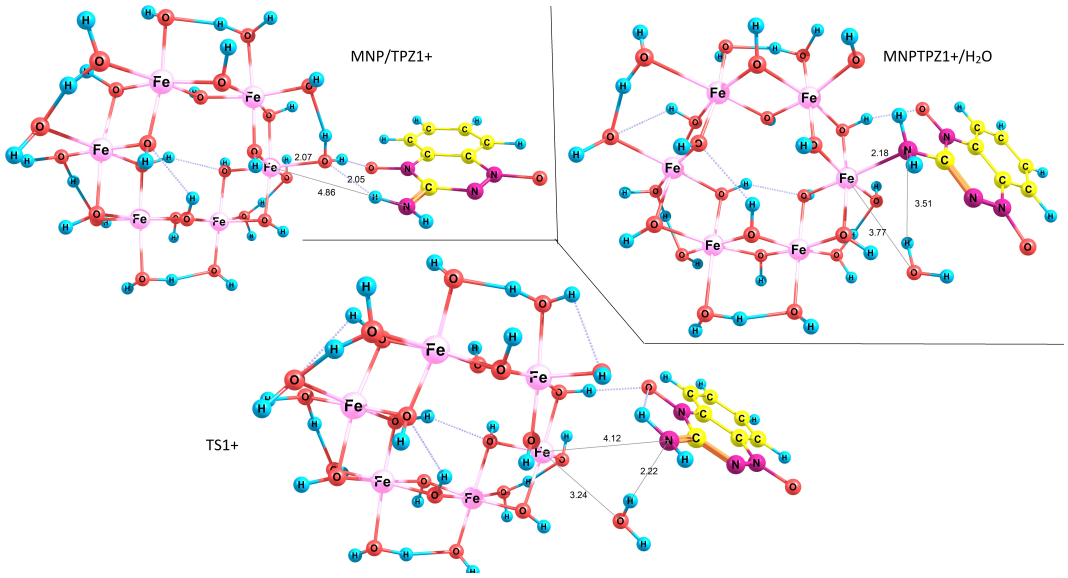

FIG. 5. Optimized structures of MNP/TPZ1+, MNPTPZ1+/H_2O and TS1+

4. Conclusion

Four noncovalent interactions related to the orientations of the NH_2 (MNP/TPZ1), NO (MNP/TPZ2-3) and intraring N-atom (MNP/TP4) functional groups of tirapazamine anticancer drug (TPZ) towards the magnetic nanocarrier $Fe_6(OH)_{18}(H_2O)_6$ (MNP) were investigated using a quantum mechanical approach (DFT). The negative values of binding energies and quantum molecular descriptor such global hardness and HOMO-LUMO energy gap indicate all interactions in gas phase and aqueous solution are energetically suitable and MNP/TPZ1 and MNP/TPZ4 are more stable than MNP/TPZ2-3.

As the temperature increases, a covalent bond can be formed between the drug and the carrier. Four mechanisms thorough NH_2 (NH_2 mechanism), NO (NO mechanisms) and intraring N-atom (N mechanism) functional groups have been examined. It was specified that the products of the NO mechanisms have lower activation energies than the others but are more unstable than that of NH_2 mechanism (kinetic product). Therefore, the product of NH_2 mechanism is a thermodynamic product.

References

[1] Lu A.H., Salabas E.e.L., Schüth F. Magnetic nanoparticles: synthesis, protection, functionalization, and application. *Angew. Chem. Int. Ed.*, 2007, **46**, P. 1222–1244.

[2] Jun Y.-w., Seo J.-w., Cheon J. Nanoscaling laws of magnetic nanoparticles and their applicabilities in biomedical sciences. *Acc. Chem. Res.*, 2008, **41**, P. 179–189.

[3] Goll D. Magnetism of nanostructured materials for advanced magnetic recording. *Int. J. Mater. Res.*, 2009, **100**, P. 652–662.

[4] Albadi Y., Martinson K.D., et al. Synthesis of $GdFeO_3$ nanoparticles via low-temperature reverse co-precipitation: the effect of strong agglomeration on the magnetic behavior. *Nanosystems: Phys. Chem. Math.*, 2020, **11**, P. 252–259.

[5] Galli M., Guerrini A., et al. Superparamagnetic iron oxide nanoparticles functionalized by peptide nucleic acids. *RSC Adv.*, 2017, **7**, P. 15500–15512.

[6] Neamtu J., Verga N. Magnetic nanoparticles for magneto-resonance imaging and targeted drug delivery. *Dig. J. Nanomater. Biostruct.*, 2011, **6**, P. 969–978.

[7] Liu Y.-L., Chen D., Shang P., Yin D.-C. A review of magnet systems for targeted drug delivery. *J. Controlled Release*, 2019, **302**, P. 90–104.

[8] Pankhurst Q.A., Connolly J., Jones S.K., Dobson J. Applications of magnetic nanoparticles in biomedicine. *J. Phys. D: Appl. Phys.*, 2003, **36**, R167.

[9] Arruebo M., Fernández-Pacheco R., Ibarra M.R., Santamaría J. Magnetic nanoparticles for drug delivery. *Nano today*, 2007, **b**, P. 22–32.

[10] Akbarzadeh A., Samiei M., Davaran S. Magnetic nanoparticles: preparation, physical properties, and applications in biomedicine. *Nanoscale Res. Lett.*, 2012, **7**, 144.

[11] Bi H., Han X. Magnetic field triggered drug release from lipid microcapsule containing lipid-coated magnetic nanoparticles. *Chem. Phys. Lett.*, 2018, **706**, P. 455–460.

[12] Roohi R., Emdad H., Jafarpur K. A comprehensive study and optimization of magnetic nanoparticle drug delivery to cancerous tissues via external magnetic field. *J. Test. Eval.*, 2019, **47**, P. 681–703.

[13] Dobson J. Magnetic nanoparticles for drug delivery. *Drug Dev. Res.*, 2006, **67**, P. 55–60.

[14] Namdeo M., Saxena S., et al. Magnetic nanoparticles for drug delivery applications. *J. Nanosci. Nanotechnol.*, 2008, **8**, P. 3247–3271.

[15] Hossen S., Hossain M.K., et al. Smart nanocarrier-based drug delivery systems for cancer therapy and toxicity studies: A review. *J. Adv. Res.*, 2019, **15**, P. 1–18.
[16] Ostroushko A.A., Gagarin I.y.D., Danilova I.G., Gette I.F. The use of nanocluster polyoxometalates in the bioactive substance delivery systems. *Nanosystems: Phys. Chem. Math.*, 2019, **10**, P. 318–349.
[17] Shanmuganathan R., Edison T.N.J.I., et al. Chitosan nanopolymers: an overview of drug delivery against cancer. *Int. J. Biol. Macromol.*, 2019, **130**, P. 727–736.
[18] Popova N., Popov A., Shcherbakov A., Ivanov V. Layer-by-layer capsules as smart delivery systems of CeO_2 nanoparticle-based theranostic agents. *Nanosystems: Phys. Chem. Math.*, 2017, **8**, P. 282–289.
[19] Ramasamy T., Ruttala H.B., et al. Smart chemistry-based nanosized drug delivery systems for systemic applications: a comprehensive review. *J. Controlled Release*, 2017, **258**, P. 226–253.
[20] Pennock G.D., Dalton W.S., et al. Systemic toxic effects associated with high-dose verapamil infusion and chemotherapy administration. *J. Natl. Cancer Inst.*, 1991, **83**, P. 105–110.
[21] Lindley C., McCune J.S., et al. Perception of chemotherapy side effects cancer versus noncancer patients. *Cancer pract.*, 1999, **7**, P. 59–65.
[22] Arias J.L., Gallardo V., Ruiz M.A., Delgado Á.V. Magnetite/poly (alkylcyanoacrylate)(core/shell) nanoparticles as 5-Fluorouracil delivery systems for active targeting. *Eur. J. Pharm. Biopharm.*, 2008, **69**, P. 54–63.
[23] Wagstaff A.J., Brown S.D., et al. Cisplatin drug delivery using gold-coated iron oxide nanoparticles for enhanced tumour targeting with external magnetic fields. *Inorg. Chim. Acta*, 2012, **393**, P. 328–333.
[24] Cengelli F., Grzyb J.A., et al. Surface-Functionalized Ultrasmall Superparamagnetic Nanoparticles as Magnetic Delivery Vectors for Camptothecin. *ChemMedChem*, 2009, **4**, P. 988–997.
[25] Zhu K., Deng Z., et al. Photoregulated cross-linking of superparamagnetic iron oxide nanoparticle (spion) loaded hybrid nanovectors with synergistic drug release and magnetic resonance (MR) imaging enhancement. *Macromolecules*, 2017, **50**, P. 1113–1125.
[26] Kohler N., Sun C., et al. Methotrexate-Immobilized Poly (ethylene glycol) Magnetic Nanoparticles for MR Imaging and Drug Delivery. *Small*, 2006, **2**, P. 785–792.
[27] Majd M.H., Asgari D., et al. Tamoxifen loaded folic acid armed PEGylated magnetic nanoparticles for targeted imaging and therapy of cancer. *Colloids and Surfaces B: Biointerfaces*, 2013, **106**, P. 117–125.
[28] Chen Y.C., Lee W.F., Tsai H.H., Hsieh W.Y. Paclitaxel and iron oxide loaded multifunctional nanoparticles for chemotherapy, fluorescence properties, and magnetic resonance imaging. *J. Biomed. Mater. Res. A*, 2012, **100**, P. 1279–1292.
[29] Depalo N., Iacobazzi R.M., et al. Sorafenib delivery nanoplatform based on superparamagnetic iron oxide nanoparticles magnetically targets hepatocellular carcinoma. *Nano Research*, 2017, **10**, P. 2431–2448.
[30] Kim D.H., Guo Y., et al. Temperature-Sensitive Magnetic Drug Carriers for Concurrent Gemcitabine Chemohyperthermia. *Adv. Healthc. Mater.*, 2014, **3**, P. 714–724.
[31] Dorniani D., bin Hussein M.Z., et al. Preparation and characterization of 6-mercaptopurine-coated magnetite nanoparticles as a drug delivery system. *Drug Des. Devel. Ther.*, 2013, **7**, 1015.
[32] Krukemeyer M.G., Krenn V., Jakobs M., Wagner W. Mitoxantrone-iron oxide biodistribution in blood, tumor, spleen, and liver—magnetic nanoparticles in cancer treatment. *J. Surg. Res.*, 2012, **175**, P. 35–43.
[33] Sood A., Arora V., et al. Multifunctional gold coated iron oxide core-shell nanoparticles stabilized using thiolated sodium alginate for biomedical applications. *Mater. Sci. Eng.: C*, 2017, **80**, P. 274–281.
[34] Hemalatha T., Prabu P., Gunadharini D.N., Gowthaman M.K. Fabrication and characterization of dual acting oleyl chitosan functionalised iron oxide/gold hybrid nanoparticles for MRI and CT imaging. *Int. J. Biol. Macromol.*, 2018, **112**, P. 250–257.
[35] Santra S., Tapec R., et al. Synthesis and characterization of silica-coated iron oxide nanoparticles in microemulsion: the effect of nonionic surfactants. *Langmuir*, 2001, **17**, P. 2900–2906.
[36] Khashan K.S., Sulaiman G.M., Mahdi R. Preparation of iron oxide nanoparticles-decorated carbon nanotube using laser ablation in liquid and their antimicrobial activity. *Artif. Cells Nanomed. Biotechnol.*, 2017, **45**, P. 1699–1709.
[37] Kim D., Zhang Y., et al. Synthesis and characterization of surfactant-coated superparamagnetic monodispersed iron oxide nanoparticles. *J. Magn. Magn. Mater.*, 2001, **225**, P. 30–36.
[38] Hou X., Zhang X., et al. Surface-enhanced Raman scattering of C60 on co-modified substrate of Fe3O4 and Au nanoparticles. *Chem. Phys.*, 2010, **372**, P. 1–5.
[39] Emtiazi G., Zohrabi T., et al. Covalent diphenylalanine peptide nanotube conjugated to folic acid/magnetic nanoparticles for anti-cancer drug delivery. *Journal of Drug Delivery Science and Technology*, 2017, **41**, P. 90–98.
[40] Jiang S., Eltoukhy A.A., et al. Lipidoid-coated iron oxide nanoparticles for efficient DNA and siRNA delivery. *Nano Lett.*, 2013, **13**, P. 1059–1064.
[41] Sharifabad M.E., Mercer T., Sen T. Drug-loaded liposome-capped mesoporous core–shell magnetic nanoparticles for cellular toxicity study. *Nanomedicine*, 2016, **11**, P. 2757–2767.
[42] Tassa C., Shaw S.Y., Weissleder R. Dextran-coated iron oxide nanoparticles: a versatile platform for targeted molecular imaging, molecular diagnostics, and therapy. *Acc. Chem. Res.*, 2011, **44**, P. 842–852.
[43] Kievit F.M., Veiseh O., et al. PEI–PEG–chitosan-copolymer-coated iron oxide nanoparticles for safe gene delivery: synthesis, complexation, and transfection. *Adv. Funct. Mater.*, 2009, **19**, P. 2244–2251.
[44] Lee H., Lee E., et al. Antibiofouling polymer-coated superparamagnetic iron oxide nanoparticles as potential magnetic resonance contrast agents for in vivo cancer imaging. *J. Am. Chem. Soc.*, 2006, **128**, P. 7383–7389.
[45] McBain S., Yiu H., El Haj A., Dobson J. Polyethyleneimine functionalized iron oxide nanoparticles as agents for DNA delivery and transfection. *J. Mater. Chem.*, 2007, **17**, P. 2561–2565.
[46] Shabani Z., Morsali A., Bozorgmehr M.R., Beyramabadi S.A. Quantum chemical modeling of iron oxide magnetic nanoparticles functionalized with cytarabine. *Chem. Phys. Lett.*, 2019, **719**, P. 12–21.
[47] Lotfi M., Morsali A., Bozorgmehr M.R. Comprehensive quantum chemical insight into the mechanistic understanding of the surface functionalization of carbon nanotube as a nanocarrier with cladribine anticancer drug. *Appl. Surf. Sci.*, 2018, **462**, P. 720–729.
[48] Naghavi F., Morsali A., Bozorgmehr M.R. Molecular mechanism study of surface functionalization of silica nanoparticle as an anticancer drug nanocarrier in aqueous solution. *J. Mol. Liq.*, 2019, **282**, P. 392–400.

[49] Hadi L., Ali M., Momen H.M. The prediction of COOH functionalized carbon nanotube application in melphalan drug delivery. *Nanosystems: Phys. Chem. Math.*, 2019, **10**, P. 438–446.
[50] Najafi M., Morsali A., Bozorgmehr M.R. DFT study of SiO 2 nanoparticles as a drug delivery system: structural and mechanistic aspects. *Struct. Chem.*, 2018, P. 1–12.
[51] Nasrabadi M., Beyramabadi S.A., Morsali A. Surface functionalization of chitosan with 5-nitroisatin. *Int. J. Biol. Macromol.*, 2020, **147**, P. 534–546.
[52] Bokarev A., Plastun I. Possibility of drug delivery due to hydrogen bonds formation in nanodiamonds and doxorubicin: molecular modeling. *Nanosystems: Phys. Chem. Math.*, 2018, **9**, P. 370–377.
[53] Khoshbayan B., Morsali A., Bozorgmehr M.R. Structural and Electronic Properties of Cyclic Peptide-gold Nanoparticle as a Drug Delivery System. *Chinese J. Struc. Chem.*, 2019, **38**, P. 566–580.
[54] Denny W.A. Prospects for hypoxia-activated anticancer drugs. *Curr. Med. Chem. Anticancer Agents*, 2004, **4**, P. 395–399.
[55] Zeman E.M., Brown J.M., et al. SR-4233: a new bioreductive agent with high selective toxicity for hypoxic mammalian cells. *Int. J. Radiat. Oncol. Biol. Phys.*, 1986, **12**, P. 1239–1242.
[56] Frisch M., Trucks G.,et al. G09 Gaussian Inc. Gaussian 09, revision B.01. Gaussian, Inc., Wallingford, CT, 2009.
[57] Cammi R., Tomasi J. Remarks on the use of the apparent surface charges (ASC) methods in solvation problems: Iterative versus matrix-inversion procedures and the renormalization of the apparent charges. *J. Comput. Chem.*, 1995, **16**, P. 1449–1458.
[58] Tomasi J., Persico M. Molecular interactions in solution: an overview of methods based on continuous distributions of the solvent. *Chem. Rev.*, 1994, **94**, P. 2027–2094.
[59] Parr R.G., Szentpaly L.v., Liu S. Electrophilicity index. *J. Am. Chem. Soc.*, 1999, **121**, P. 1922–1924.
[60] Jayarathne L., Ng W.J., et al. Fabrication of succinic acid-γ-Fe_2O_3 nano core–shells. *Colloids Surf. A*, 2012, **403**, P. 96–102.
[61] Douziech-Eyrolles L., Marchais H., et al. Nanovectors for anticancer agents based on superparamagnetic iron oxide nanoparticles. *Int. J. Nanomedicine*, 2007, **2**, P. 541–550.
[62] Mahmoudi M., Sant S., et al. Superparamagnetic iron oxide nanoparticles (SPIONs): development, surface modification and applications in chemotherapy. *Adv. Drug Deliv. Rev.*, 2011, **63**, P. 24–46.

NANOSYSTEMS: PHYSICS, CHEMISTRY, MATHEMATICS, 2021, 12 (2), P. 175–181

Additive effects of green LED light and cerium oxide nanoparticles on the planarian's regeneration

A. M. Ermakov[1], K. A. Kamenskikh[1], A. L. Popov[1],
O. N. Ermakova[1], V. A. Afanasyeva[1], V. K. Ivanov[2]

[1]Institute of Theoretical and Experimental Biophysics of the Russian Academy of Sciences, Institutskaya str., 3, Pushchino, 142290, Russia

[2]Kurnakov Institute of General and Inorganic Chemistry of the Russian Academy of Sciences, Leninskiy prosp., 31, Moscow, 119991, Russia

ao_ermakovy@rambler.ru, kristina.kamensk@mail.ru, antonpopovleonid@gmail.com, beoluchi@yandex.ru, va_vera_afanaseva@mail.ru, van@igic.ras.ru

PACS 61.46.+w, 87.50.-a, 87.19.-j **DOI 10.17586/2220-8054-2021-12-2-175-181**

Nanotechnology makes it possible to design advanced materials being able to effectively modulate radiation effects on a cell, depending on the radiation intensity, wavelength, and type. Today, one of the most promising UV and X-ray protective biomaterials is nanocrystalline cerium oxide (CeO_2), which has a unique redox activity due to its surface reducibility. Meanwhile, the modulating properties of CeO_2 nanoparticles when the cells are exposed to visible light remain completely unexplored. Here, we analyzed the impact of CeO_2 nanoparticles on the process of planarian regeneration after exposure to low-intensity green LED light. It was found that a one-time exposure (10 or 25 min) of regenerating planarians with low-intensity green light reduced head blastema growth rate by up to 20%. At the same time, the preliminary treatment of planaria with CeO_2 nanoparticles in nanomolar concentrations (10^{-11} M) ensures the restoration of the neoblasts activity and a significant acceleration of blastema regeneration. Thus, we have firstly demonstrated that the planarian regeneration process can be promoted by cerium oxide nanoparticles even under adverse action of low-intensity green light radiation.

Keywords: cerium oxide nanoparticles, green LED, planarian regeneration.

Received: 29 January 2021

Revised: 22 March 2020

1. Introduction

The unique antioxidant activity of cerium oxide nanoparticles is based on their ability to participate easily in various redox processes involving reactive oxygen species (ROS) under physiological conditions [1, 2]. According to numerous quantum mechanical calculations, the energy of oxygen vacancies formation on the cerium oxide nanoparticle surface decreases with decreasing particle size [3]. Consequently, ultra-small nanoparticles with a high degree of monodispersity are considered to be the most biologically active.

The development of new experimental test models for screening the toxicity and biological activity of new substances and compounds, including nanomaterials, is still an urgent task. Freshwater flatworms – planaria, which have a unique ability to regenerate due to neoblast stem cells, can serve as a good model for such testing [4]. Planarian neoblasts are the only totipotent stem cells in animals that differentiate into all types of cells, including reproductive cells, in an adult organism. The number of neoblasts in the body of planarians is 20–30% of the total number of cells [5]. These cells allow for unlimited regeneration of planarians both in the event of damage and during the ongoing process of self-renewal of tissues and organs [6]. Moreover, regeneration is even possible from very small fragments where at least one stem cell has been preserved [7]. The specific features of planarians made them a classical experimental model for research of stem cell proliferation and differentiation in vivo, regeneration of differentiated tissue, cell cycle, and aging [8].

We have previously shown that cerium oxide and cerium fluoride nanoparticles are able to accelerate blastema growth due to redox activated expression of genes associated with wound healing [9]. A significant increase in the number of neoblasts in animals treated with CeO_2 or CeF_3 nanoparticles was observed 3 days after decapitation of the tested planaria. It is worth noting that cerium fluoride nanoparticles showed a higher regenerating ability and efficiency, which is probably associated with the presence of only trivalent cerium (Ce^{3+}). It was also shown earlier that cerium oxide nanoparticles provide anti-inflammatory, antioxidant and wound-healing effects in living tissue [10], which makes it possible to develop new cerium-based regenerative preparations [11]. Additionally, cerium oxide nanoparticles exhibit very special antioxidant properties, acting as a scavenger for reactive oxygen species (ROS). It was previously shown that CeO_2 nanoparticles act as inorganic nanozyme which has a mimetic activity

of various endogenous enzymes, such as catalase, glutathione peroxidase, SOD, phosphatase, and a number of other enzymes [12, 13]. Due to its antioxidant properties, nano-CeO_2 is an efficient UV protector capable of protecting mammalian cells from UVA [14, 15] and UVB [16, 17] radiation. The UV-protective role of CeO_2 nanoparticles is not only associated with a decrease in the production of intracellular ROS, pro-inflammatory cytokines, β-galactosidase activity and suppression of the phosphorylation of N-terminal c-Jun kinases (JNK), but also with the activation of the DNA repair system induced by UV rays. In this case, electromagnetic radiation is capable of damaging biological objects through various mechanisms, including direct damage to DNA or indirect, through the formation of ROS.

Even low doses of UV radiation can cause DNA damage with subsequent activation of the repair system. DNA damage causes activation of signaling protein kinases ATM and ATR [18]. Previously, it was shown that CeO_2 nanoparticles are capable of accelerating the repair of damaged DNA fragments, increasing the survival of cells after high-dose irradiation [19]. The antioxidant system of a cell is also activated through increased levels of antioxidant enzymes, e.g. SOD, catalase, glutathione peroxidase, etc. The possibility for activating different cell defense mechanisms depends on the moment of the onset of an unfavorable factor and its duration. The protection against primary (direct) damage is possible only immediately at the moment of irradiation. Protection against secondary damage is determined by the lifetime of the ROS formed during irradiation. Thus, CeO_2 nanoparticles are able to reduce radiation-induced cell damage after exposure to high doses of X-ray irradiation [20–22], reducing the level of intracellular ROS and the number of apoptotic cells, as well as the number of cytogenetic lesions. It has also been shown that the radioprotective efficiency of CeO_2 nanoparticles varies greatly depending on the radiation energy. For example, Briggs et al. [21] found a significant decrease in the efficiency of radioprotection of cells exposed to CeO_2 nanoparticles and irradiated with 10 MV or 150 kVp X-rays. When exposed to low energy irradiation, CeO_2 nanoparticles function as a radiosensitizer, which is associated with an increase in the production of Auger electrons with high linear energy transfer. This study highlights an interesting phenomenon which should be considered when CeO_2 nanoparticles are used as radiation shielding drugs in radiation therapy. Thus, it can be concluded that the protective efficiency of CeO_2 under irradiation conditions is determined not only by the conditions of its synthesis or stabilizer used, but can also vary greatly depending on the type of radiation and its energy.

Here, we investigated the effect of citrate-stabilized ultra-small CeO_2 nanoparticles on the rate of regeneration of planarians upon the irradiation with green light ($\lambda_{\max} = 520$ nm), and analyzed the factors that determine the possibility of increasing the efficiency of such protection.

2. Materials and methods

2.1. Preparation of cerium oxide nanoparticles and their characterization

To prepare cerium oxide nanoparticles sol, 0.24 g of citric acid was dissolved in 25 ml of 0.05 M aqueous solution of cerium nitrate (III), rapidly poured into 100 ml of 3 M ammonia solution with stirring and allowed to stand for 2 h. According to the transmission electron microscopy data the obtained sol consisted of slightly aggregated isotropic CeO_2 nanoparticles of 2.0–2.5 nm size. The pH of cerium oxide sol was in the range of 7.2–7.4. The size and shape of CeO_2 nanoparticles were determined by transmission electron microscopy (TEM), on a Leo912 AB Omega electron microscope (accelerating voltage 100 kV). The hydrodynamic size and zeta-potential of CeO_2 nanoparticles were measured using a Malvern Zetasizer Nano ZS Analyzer.

2.2. Green irradiation of planarians

The LED matrix (LED) with a wavelength of $\lambda_{\max} = 520$ nm was used as a light source. The spectral characteristics of the LEDs were analyzed using a set of spectral equipment based on the MDR-41 monochromator (OKB-SPEKTR, Russia) (see Fig. 1A). The luminous flux density was measured using a CMR 3 pyranometer (Kipp@Zonen, the Netherlands). The LED power was set at 1.46 W/m^2 varying the distance from the detector to the source.

Before the experiments, citrate-stabilized ceria sol was mixed with a pond water to obtain a colloid solution containing 10^{-11} M CeO_2. Planarians (30 animals in each group) were decapitated with a scalpel and placed in a Petri dish (diameter of 6 cm) filled with ceria-containing colloid solution (2 mm deep). The petri dish was placed on a flat glass plate, the light source was fixed under the glass plate. The emission spectrum of the light source is shown in Fig. 1A (insert). The whole scheme of experiment showed in Fig. 1B. After 10 min, the green LED light source was switched on, and the irradiation was conducted for 10 or 25 min (the radiation doses of 70.1 and 175.2 mJ/cm^2, respectively). After irradiation, the planarians were left in CeO_2 colloid solution for 72, 96 or 120 h. After such incubation, morphometric analysis was performed.

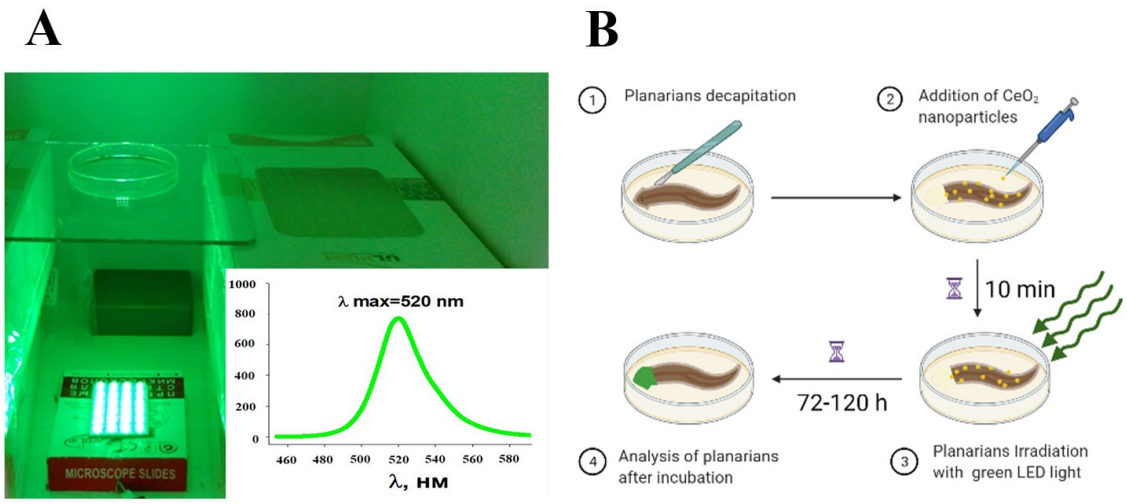

FIG. 1. The spectral characteristics of the LED matrix used for light irradiation of regenerating planarians (A) and the scheme of experiment (B)

2.3. The morphometry of regenerating planarians

The growth dynamics of the planarian blastema (a new regenerating head tissue) was evaluated by intravital morphometry [23]. For this purpose, planarians were photographed on the 3rd, 4th and 5th regeneration days using a MRc camera (Carl Zeiss, Germany) mounted on the binocular microscope MBS-10 eyepiece. In the obtained photos, we determined the total area of the animal's body (S) and the area of the blastema (s) using the Plana 4.4 software. The regeneration index R=s/S served as a quantitative growth criterion. Each of the measured R values is the result of averaging the measurements of 30+ animals. The regeneration index changes in the experiment (R_E) compared to the control (R_C) was determined by the formula:

$$\Delta R = \frac{(R_E - R_C) \pm (\delta_E + \delta_C)}{R_C} 100\%$$

where ΔR is the difference (%) between the R_E and R_C values, $\delta_{(E,C)}$ are the standard errors of measurements for the control and experimental groups. The standard error (ΔR) did not exceed 6,5%. The control animals were not treated with light and/or nanoceria.

2.4. Statistical processing

The data obtained were treated statistically by the Sigma-Plot 9.11 software (Systat Software Inc., Germany) using the one-way ANOVA method.

2.5. Ethical standards

All the procedures involving animals were performed in accordance with the ethical standards of the institution at which the studies were conducted (ITEB RAS).

3. Results and discussion

The synthesis of CeO_2 nanoparticles was carried out according to the previously reported protocol [24]. Transmission electron microscopy data confirm the ultra-small size of cerium oxide nanoparticles and their high degree of crystallinity (Fig. 2A). The hydrodynamic radius of the nanoparticles upon dilution in bidistilled water was 4–7 nm (Fig. 2B). The obtained cerium(IV) oxide nanoparticles possessed catalase-like properties, as we showed earlier by the polarographic method [25], which confirms their antioxidant activity.

As Fig. 3 shows, cerium oxide nanoparticles at a concentration of 10^{-11} M stimulated the growth rate of the planarian head blastema. Thus, after 72 h of regeneration, the size of head blastema was on average 38.7% larger than in the control group. In the subsequent observation periods of head growth after decapitation (96 and 120 h), the stimulation effect of ceria on regeneration remained, while the average values of the blastema area increment somewhat decreased, 27.2% and 20.8%, respectively, which agrees well with our recently reported data [9].

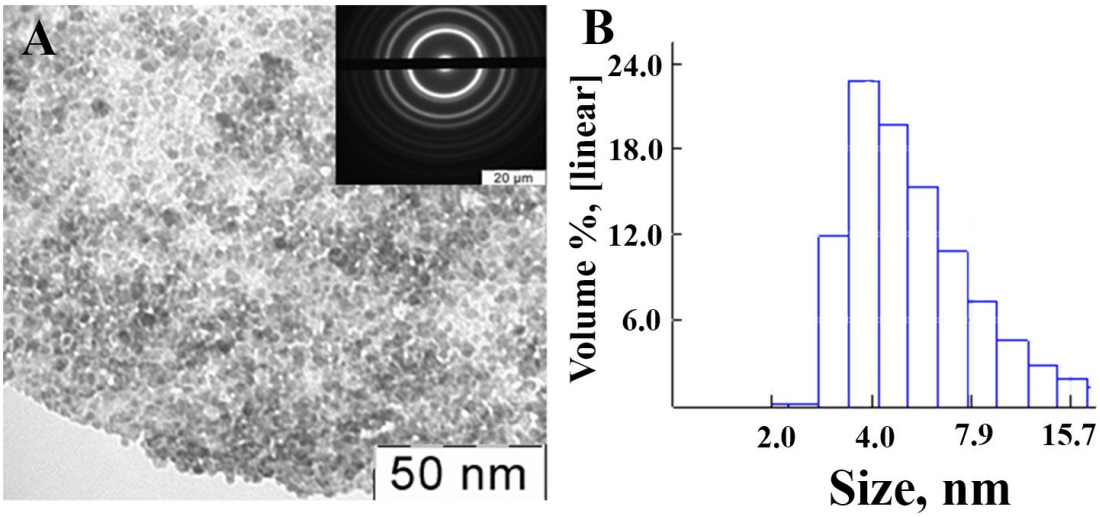

FIG. 2. The transmission electron microscopy image (A), hydrodynamic radii distribution (B) of citrate-stabilized cerium(IV) oxide nanoparticles

Oppositely, irradiation of regenerating planarians with green LED light slowed down the head blastema growth in comparison with the control group which is in accordance with our previous results [26]. The effect of the retard in regeneration depended on the radiation dose. Thus, after 96 h of regeneration, the size of the blastema for planarians irradiated for 10 min was less than in the control group by 16.6%, while for planarians irradiated for 25 min, the size of blastema was less by 25.3% against the controls. In the subsequent observation periods, the inhibitory effect of exposure to the green LED light remained, while the difference from the control group became lower. In irradiated planarians, after 96 h of regeneration, the growth slowed down by 13.3% and 17.2% (for 10 and 25 min exposure, respectively). After 120 h of regeneration, the growth rate decreased by 10.8% and 12.8%, respectively.

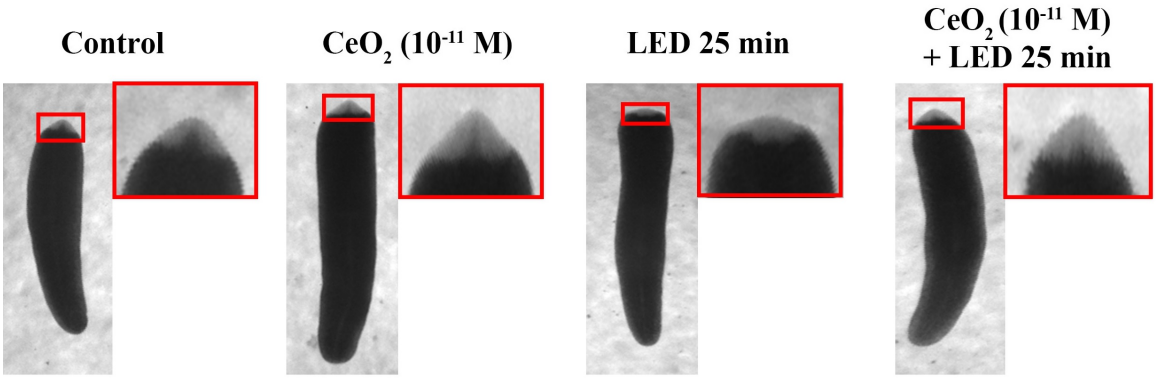

FIG. 3. Micrographs of regenerating planarians after irradiation with green LED source for 25 min and incubation with CeO_2 nanoparticles for 72 h

Illumination with green light inhibited the regeneration of planaria, meanwhile the presence of CeO_2 nanoparticles stimulated planaria regeneration. When the animals were exposed to green light for 10 min, the subsequent 72 h incubation with CeO_2 nanoparticles resulted in the higher regeneration rate (17%) than in the control. The similar difference in ΔR values (19.4%) was observed between planarians irradiated with green light for 25 min with subsequent incubation for 72 h in the presence of CeO_2 nanoparticles and the controls.

Further, after 96 and 120 h of regeneration, a decrease in the difference between the regeneration indices for irradiated and untreated planarians was observed, but the stimulating effect of ceria nanoparticles was still significant. Particularly, the animals irradiated with green light for 10 min with subsequent regeneration for 96 and 120 h in the presence of CeO_2 nanoparticles showed the ΔR values of 9.7% and 8.4%, respectively. Similarly, after 25 min of green light irradiation and subsequent regeneration of planarians for 96 and 120 h in the presence of CeO_2 nanoparticles, ΔR values amounted to 14.5% and 12.8%, respectively.

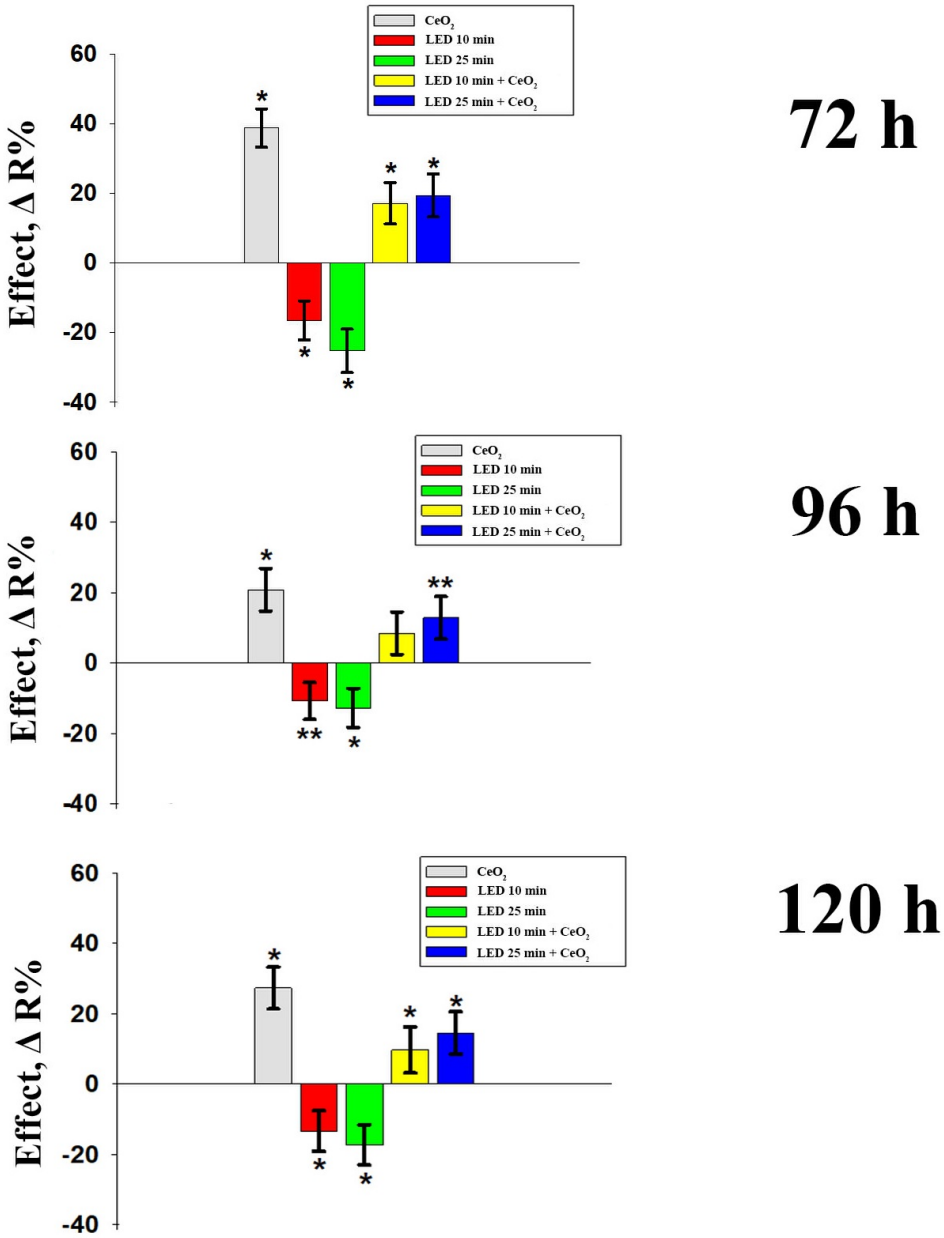

FIG. 4. The effect of cerium(IV) oxide nanoparticles (10^{-11} M) and irradiation with green LED light (525 nm, duration of irradiation – 10 and 25 min) on planarian blastema regeneration. The effect is shown as a percentage of untreated control after 72, 96 and 120 h of regeneration. $^{*}p < 0.001$; $^{**}p < 0.01$

Our experiments have unambiguously shown that ceria nanoparticles, even in very low concentrations (10^{-11} M), effectively neutralize the negative effect of green light irradiation on the regeneration processes in planarians. In our opinion, this effect cannot be associated with the photoprotective property of ceria nanoparticles [27] due to low concentration of CeO_2 in the aqueous medium. Moreover, being a wide band-gap semiconductor (band gap of 3.2 eV [28]), CeO_2 is unable to absorb green light. Thus, the effect is connected with the molecular mechanisms of ceria interaction with biological systems.

Upon damage to the planarian body, stem cells (neoblasts) begin to migrate actively into the area of injury where a burst of ROS levels occurred. According to our recent results, CeO_2 nanoparticles greatly promote the mitotic activity of the neoblasts in decapitated planarians [9] probably due to the modulation of ROS level in the apical layer of the blastema.

The main mechanism of the reaction of biological systems to visible light irradiation is considered to be due to the absorption of photons by certain photoacceptor molecules (photoreceptors or chromophores) [29–31]. Planarians have photo- and chemoreceptors not only in the area of their eye-spots (ocelli), but also throughout the body being able to respond the external light stimuli even upon decapitation. Opsins are G-protein-coupled photoreceptors responsible for ocular light detection in all animals. Opsins are typically located within either rhabdomeric or ciliary photoreceptor cells, activating r-opsin or c-opsin signal transduction cascades, respectively [32]. C-opsins initiate a pathway that closes cyclic-nucleotide-gated (CNG) ion channels [33], whereas r-opsins are associated with the opening of transient receptor potential cation (TRPC) channels [34]. In planarians, the homologs of CNG and TRPC channels are transient receptor potential cation (TRPA1) channels, which are evolutionarily conserved detectors of reactive oxygen species [35]. Therefore, we can assume that through ROS level regulation by cerium oxide nanoparticles, it is possible to indirectly influence biochemical processes governed by photosensitive opsins.

Cerium oxide nanoparticles, as shown earlier, are able to influence the signaling pathways of the cell through the regulation of the redox status of the cell [36]. CeO_2 nanoparticles can interact with many biomolecules triggering a cascade of cellular activities [37]. CeO_2 nanoparticles-targeted signaling pathways can induce a variety of cellular responses dependent or independent from free radical scavenging. Thus, it can be concluded that the mechanisms of the biological activity of CeO_2 nanoparticles are mostly associated with their effect on intracellular signaling pathways. However, specific pathways of signal transduction upon exposure to green light in the presence of CeO_2 nanoparticles require additional research.

4. Conclusions

Ultra-small citrate-stabilized cerium oxide nanoparticles do not cause toxic effects on planarians and are able to stimulate the mitotic activity of their stem cells during blastema growth. Exposure to green light for 15 and 25 min significantly inhibits the process of planarian regeneration, which is most likely associated with down-regulated expression of genes associated with wound healing. At the same time, cerium oxide nanoparticles, even in nanomolar concentrations, are able to neutralize the negative effects of green light on the regeneration processes in planarians, increasing the rate of regeneration and increasing the mitotic index.

Acknowledgements

This work was supported by the Russian Science Foundation, project no. 19-13-00416. This research was partly performed using the equipment of the JRC PMR IGIC RAS.

References

[1] Seminko V., Maksimchuk P., Grygorova G., Okrushko E., Avrunin O., Semenets V., Malyukin Y. Mechanism and Dynamics of Fast Redox Cycling in Cerium Oxide Nanoparticles at High Oxidant Concentration. *J. Phys. Chem. C*, 2021, **125**(8), P. 4743–4749.

[2] Malyukin Y., Maksimchuk P., Seminko V., Okrushko E., Spivak N. Limitations of Self-Regenerative Antioxidant Ability of Nanoceria Imposed by Oxygen Diffusion. *J. Phys. Chem. C*, 2018, **122**(28), P. 16406–1641.

[3] Wang Z.-Q., Zhang M.-J., Hu X.-B., et al. CeO_{2-x} quantum dots with massive oxygen vacancies as efficient catalysts for the synthesis of dimethyl carbonate. *Chem. Commun.*, 2020, **56**, P. 403–406.

[4] Rink, J.C. Stem cell systems and regeneration in planaria. *Dev. Genes Evol.*, 2013, **223**, P. 67–84.

[5] Reddien P.W., Alvarado A.S. Fundamentals of Planarian Regeneration. *Annual Review of Cell and Developmental Biology*, 2004, **20**, P. 725–75.

[6] Cutie S., Hoang A.T., Payumo A.Y., Huang G.N. Unconventional Functions of Muscles in Planarian Regeneration. *Dev. Cell*, 2017, **43**(6), P. 657–658.

[7] Reddien P.W. Specialized progenitors and regeneration. *Development*, 2013, **140**(5), P. 951–957.

[8] Pagán O.R. Planaria: an animal model that integrates development, regeneration and pharmacology. *Int. J. Dev. Biol.*, 2017, **61**(8-9), P. 519–529.

[9] Ermakov A., Popov A., Ermakova O., et al. The first inorganic mitogens: Cerium oxide and cerium fluoride nanoparticles stimulate planarian regeneration via neoblastic activation. *Materials Science and Engineering: C*, 2019, **104**, P. 109924.

[10] Popov A.L., Shcherbakov A.B., Zholobak N.M. et al. Cerium dioxide nanoparticles as third-generation enzymes (Nanozymes). *Nanosystems: Physics, Chemistry, Mathematics*, 2017, **8**(6), P. 760–781.

[11] Popova N.R., Andreeva V.V., Khohlov N.V., Popov A.L., Ivanov V.K. Fabrication of CeO_2 nanoparticles embedded in polysaccharide hydrogel and their application in skin wound healing. *Nanosystems: Physics, Chemistry, Mathematics*, 2020, **11**(1), P. 99–109.

[12] Baldim V., Bedioui F., Mignet N., Margaill I., Berret J.-F. The enzyme-like catalytic activity of cerium oxide nanoparticles and its dependency on Ce^{3+} surface area concentration. *Nanoscale*, 2018, **10**, P. 6971–6980.

[13] Singh R., Singh S. Redox-dependent catalase mimetic cerium oxide-based nanozyme protect human hepatic cells from 3-AT induced acatalasemia. *Colloids and Surfaces B: Biointerfaces*, 2019, **175**, P. 625–635.

[14] Li Y., Hou X., Yang C. et al. Photoprotection of cerium oxide nanoparticles against UVA radiation-induced senescence of human skin fibroblasts due to their antioxidant properties. *Scientific Reports*, 2019, **9**, P. 2595.

[15] Caputo F., De Nicola M., Sienkiewicz A. et al. Cerium oxide nanoparticles, combining antioxidant and UV shielding properties, prevent UV-induced cell damage and mutagenesis. *Nanoscale*, 2015, **7**, P. 15643–15656.

[16] Arya A., Gangwar A., Singh S. K., Bhargava K. Polyethylene glycol functionalized cerium oxide nanoparticle confer protection against UV-induced oxidative damage in skin: evidences for a new class of UV filter. *Nano Ex.*, 2020, **1**, P. 010038.
[17] Miri A., Birjandi S.A., Sarani M. Survey of cytotoxic and UV protection effects of biosynthesized cerium oxide nanoparticles. *J. Biochem. Mol. Toxicol.* 2020, **34**(6), P. e22475.
[18] Yang J., Xu Z.-P., Huang Y. et al. ATM and ATR: Sensing DNA damage. *World J Gastroenterol.*, 2004, **10**(2), P. 155–160.
[19] Caputo F., Giovanetti A., Corsi F. et al. Cerium oxide nanoparticles re-establish cell integrity checkpoints and apoptosis competence in irradiated HaCat cells via novel redox-independent activity front. *Pharmacol*, 2018, **9**, P. 1183.
[20] Popov A. L., Zaichkina S. I., Popova N. R. et al. Radioprotective effects of ultra-small citrate-stabilized cerium oxide nanoparticles. *RSC Advances*, 2016, **6**, P. 106141–106149.
[21] Briggs A., Corde S., Oktaria S. et al. Cerium oxide nanoparticles: influence of the high-Z component revealed on radioresistant 9L cell survival under X-ray irradiation. *Nanomedicine: Nanotechnology, Biology and Medicine*, 2013, **9**(7), P. 1098–1105.
[22] Shinpaugh J.L. et al Protection and sensitization of normal and tumor cells to proton radiation by cerium oxide nanoparticles. *J. Phys.: Conf. Ser.*, 2015, **635**, P. 032032.
[23] Ermakov A.M., Ermakova O.N., Maevsky E.I. A role of some intracellular signaling cascades in planarian regeneration activated under irradiation with low-temperature argon plasma. *Biophysics*, 2014, **59**, P. 453–457.
[24] Ivanova O.S., Shekunova T.O., Ivanov V.K. et al. One-step synthesis of colloidal solutions of cerium dioxide for biomedical applications. *Doklady Chemistry*, 2011, **437**(2), P. 103–106.
[25] Popov A., Popova, N., Gould D., Shcherbakov A.; Sukhorukov G.; Ivanov V. Ceria nanoparticles-decorated microcapsules as a smart drug delivery/protective system: Protection of encapsulated P. pyralis luciferase. *ACS Appl. Mater. Interfaces*, 2018, **10**(17), P. 14367–14377.
[26] Ermakov A.M., Ermakova O.N., Popov A.L., Manokhin A.A., Ivanov V.K. Opposite effects of low intensity light of different wavelengths on the planarian regeneration rate. *Journal of Photochemistry and Photobiology, B: Biology*, 2020, **202**, P. 111714.
[27] Ribeiro F.M., de Oliveira M.M., Singh S., Sakthivel T.S., Neal C.J., Seal S., Ueda-Nakamura T., Lautenschlager S., Nakamura C. Ceria Nanoparticles Decrease UVA-Induced Fibroblast Death Through Cell Redox Regulation Leading to Cell Survival, Migration and Proliferation. *Front. Bioeng. Biotechnol.*, 2020, **8**, P. 577557.
[28] Shcherbakov A.B., Zholobak N.M., Ivanov V.K. Biological, biomedical and pharmaceutical applications of cerium oxide. In *Cerium Oxide (CeO_2): Synthesis, Properties and Applications*. Elsevier. Amsterdam. 2020, 402 p.
[29] de Freitas L.F., Hamblin M.R. Proposed Mechanisms of Photobiomodulation or Low-Level Light Therapy. *IEEE J. Sel. Top. Quantum. Electron.*, 2016, **22**(3), P. 7000417.
[30] Passarell S., Karub T. Absorption of monochromatic and narrow band radiation in the visible and near IR by both mitochondrial and non-mitochondrial photoacceptors results in photobiomodulation. *Journal of Photochemistry and Photobiology B*, 2014, **140**, P. 344–358.
[31] Arendt D. Evolution of eyes and photoreceptor cell types. *Int J Dev Biol.*, 2003, **47**(7-8), P. 563–571.
[32] Shettigar N., Joshi A., Dalmeida R., Gopalkrishna R., Chakravarthy A., Patnaik S., Mathew M., Palakodeti D., Gulyani A. Hierarchies in light sensing and dynamic interactions between ocular and extraocular sensory networks in a flatworm. *Science Advances*, 2017, **3**(7), P. e1603025.
[33] Kaupp B. and Seifert R., Cyclic nucleotide-gated ion channels. *Physiol Rev.*, 2002, **82**(3), P. 769–824.
[34] Katz B., Payne R., Minke B. TRP Channels in Vision. In: *Neurobiology of TRP Channels*. CRC Press/Taylor & Francis. Boca Raton, 2017, 347 p.
[35] Birkholz T.R., Beane W.S. The planarian TRPA1 homolog mediates extraocular behavioral responses to near ultraviolet light. *Journal of Experimental Biology*, 2017, 152298.
[36] Weng Q. et al., Catalytic activity tunable ceria nanoparticles prevent chemotherapy-induced acute kidney injury without interference with chemotherapeutics. *Nat. Commun.*, 2021, **12**, P. 1436.
[37] Pesaraklou A., Matin M. M. Cerium oxide nanoparticles and their importance in cell signaling pathways for predicting cellular behavior. *Nanomedicine*, 2020, **15**, P. 17.

NANOSYSTEMS: PHYSICS, CHEMISTRY, MATHEMATICS, 2021, 12 (2), P. 182–187

Layer-by-layer synthesis of Zn-doped MnO_2 nanocrystals as cathode materials for aqueous zinc-ion battery

A. A. Lobinsky, M. V. Kaneva

Saint Petersburg State University, Peterhof, 198504 Saint Petersburg, Russia

lobinsky.a@gmail.com

PACS 81.07.Bc **DOI 10.17586/2220-8054-2021-12-2-182-187**

This work first described the new oxidation-reduction route for the synthesis of Zn-doped MnO_2 nanocrystals via layer-by-layer method as cathode material for an aqueous zinc-ion battery. The obtained nanolayers were characterized by SEM, XRD, XPS and FTIR spectroscopy. The results show the synthesized nanolayers were formed from two-dimensional nanocrystals $Zn_{0.3}MnO_2$ the thickness of about 3–8 nm and the morphology of "nanosheets" with the birnessite-like crystal structure. Benefiting from the aqueous 2M $ZnSO_4$ electrolyte and $Zn_{0.3}MnO_2$ nanocrystals-based cathode, the zinc-ion battery delivers a high specific capacity (216 mAh/g at 1 A/g) and excellent cycling stability (95% capacity retention after 1000 charge-discharge cycles). The obtained results demonstrate the manganese oxide-based aqueous zinc-ion battery is a promising technology for powering next-generation electronics.

Keywords: Manganese oxide, zinc, nanocrystals, layer-by-layer, electrode materials, zinc-ion battery.

Received: 17 February 2021

Revised: 9 April 2021

1. Introduction

In recent years, zinc-ion batteries are receiving much attention as low-cost and safe energy storage technology for emerging applications in flexible and safe devices [1]. However, deficiency of high energy-density electrode materials is now the main limit for obtaining high-performance zinc-ion batteries. Thus, the development of high-performance electrode materials is the key to improving the capacity and increase the commercial application of zinc-ion batteries [2–4].

The main function of a zinc-ion battery cathode is to provide a stable structure in which Zn^{2+} ions can be chemically bonded with low binding energy and fast kinetics [5]. Thus, the cathode must have a crystal structure with suitable crystallographic sites for Zn^{2+} accommodation, low-energy paths for ion diffusion, and high electronic conductivity for charge transfer [6]. To meet these requirements, layered and tunnel structured compounds with redox components are often chosen. In this case, the cathode must also have sufficient porosity to allow the penetration of the electrolyte solution, thereby increasing the number of active sites for the maximum charge transfer rate [7]. The materials that meet the presented requirements include analogs of Prussian blue, manganese and cobalt oxides, vanadium oxides, as well as organic compounds [8–10]. Among these materials, manganese oxides are of the greatest interest from the point of view of their further commercialization, since they have a high specific capacity and a wide working potential window, while they can be synthesized from relatively inexpensive precursors [11, 12]. However, these cathode materials have low electronic conductivity, which does not allow them to approach the theoretical values of the specific capacitance.

The solution to this problem may consist of obtaining 2D nanocrystals with a graphene-like morphology of the so-called "nanosheets", which is due to a set of their unique physical and chemical properties. The flat 2D structure of such materials provides a sufficient number of active adsorption centers. Another key characteristic of 2D materials is their ultra-small thickness, on the order of a few nanometers, so charge carriers can travel extremely short distances from the volume to the surface, while significantly improving electronic conductivity [13–15].

New possibilities of manganese oxides nanocrystals synthesis rose after the development of Layer-by-Layer (LbL) synthesis techniques that make it possible to deposit MnO_2 layers on the surface of samples with an irregular shape, providing an exact thickness of the layer [16]. The purpose of the present study was to explore the feasibility of synthesis of the MnO_2 nanolayers by the Successive Ionic Layer Deposition (SILD) method [17], also called the Successive Ionic Layer Adsorption and Reaction (SILAR) [18]. The method is based on multiple and successive treatments of a substrate by solutions of reagents which enter into reaction at its surface and form a layer of poorly soluble substance. The distinctive features of this method are its capability of deposition of the layers of controlled thickness on the surface of parts of any shape, which are exactly the requirements to the methods of synthesis of the layers on the surface of electrodes for the zinc-ion battery.

In the present paper, we report a new simple oxidation-reduction route for the synthesis of Zn-doped MnO_2 nanolayers via the SILD method. The obtained nanolayers consist of MnO_2 nanocrystals, including zinc atoms, with nanosheets-like morphology. We also describe their properties as electroactive cathode materials for an aqueous zinc-ion battery.

2. Experimental

As a substrate for the synthesis of Zn-doped MnO_2 nanolayers $0.3 \times 5 \times 25$ mm polycrystalline Ni foam (NF) (110 ppi) plates were used, on which electrochemical experiments were performed, and also $0.35 \times 10 \times 25$ mm single-crystal Si plates with $\langle 100 \rangle$ orientation, were used for physical characterization. Extra pure water (Milli-Q) was used in all experiments. Si substrates were cleaned in an ultrasonic bath filled with acetone for 10 min. Then plates of Si were sequentially treated for 10 min in concentrated HF, water, 70% HNO_3, water, 0.1 M KOH and then flushed out by water. Ni plates were treated according to the technique described in [19] for 15 min in 6 M HCl solution, then several times rinsed by water and dried on air at 120°C for 30 min.

A solution of mixed salts manganese and zinc was prepared by dissolving dry analytical grade salts $MnSO_4$ and $ZnSO_4$ ($C = 0.01$ M) in deionized water. An aqueous solution of NaClO ($C = 0.01$ M) was used as an oxidizer. The pH of this solution was 10.5 and adjusted by the addition of 1M NaOH solution. For the synthesis of Zn-doped MnO_2 nanolayers, substrate plates were sequentially immersed for 30 seconds into a solution of mixed manganese and zinc salt, washed in water, and then it was immersed for 30 seconds into the NaClO solutionand again washed in water. The sequence corresponds to one SILD cycle, which is repeated 30 times to obtain desired film thickness. Then samples were calcined on air at 150°C for 10 min at a heating rate of 5°C/min.

The morphology and composition of synthesized films were investigated by scanning electron microscope (SEM) at accelerating voltage 1–10 kV on Zeiss Merlin microscope and X-ray photoelectron spectroscopy (XPS) was obtained used ESCALAB 250Xi electron spectrometer, with Al Kα radiation (14866 eV). XRD patterns were obtained using a Rigaku Miniflex II X-ray diffractometer with CuKα radiation ($\lambda = 0.154056$ nm). FT-IR transmission spectra of synthesized films on silicon surface were registered by FCM-2201 spectrophotometer using a different technique with respect to spectra of bare silicon plate.

The electrochemical measurements of NF electrodes with the synthesized nanolayers were carried out in a two-electrode electrochemical cell using Elins P-45X potentiostat. The cathode was prepared by deposition Zn-doped MnO_2 nanolayers on NF surface as a result of 30 treatment cycles by the SILD method. Zinc foil serves as an anode. Electrochemical characterization of the films was made by cyclic voltammetry (CV) and galvanostatic charge-discharge (CD) techniques.

The specific capacitance C (mAh/g) as an electrode for alkaline battery at different current densities can be calculated via eq (1):

$$C = \int \frac{I \mathrm{d}t}{m} \tag{1}$$

where I (mA) is a galvanostatic current, $\mathrm{d}t(h)$ is the discharge time of a cycle and $m(g)$ is the mass of the active material in the film electrode [20]. The electroactive mass of Zn-doped MnO_2 for the cathode was measured using an OHAUS Pioneer ^{TM} PA54C microbalance.

3. Results and discussion

Morphological characteristics of the sample are shown in the SEM images in Fig. 1. The layer was synthesized on the nickel foam via the SILD method by 30 cycles of treatment. It is clear from the image that the layers formed of nanocrystals with nanosheets-like morphology with a thickness of 3–8 nm. Synthesized nanolayer has a uniform dark brown color.

On the X-ray diffraction pattern of the synthesized sample (Fig. 2) the crystallographic planes (001), (002), and (-111) is corresponding to the birnessite-like crystal phase of MnO_2 (JCPDS 42-1317) [21].

In the FTIR spectrum (Fig. 3), one can observe absorption bands with maximums at 3400 and 1620 cm^{-1} referring to valence oscillations of O–H groups in the molecules of adsorbed water [22]. The band with a maximum of about 440 cm^{-1} results from valence oscillations of manganese-oxygen bonds in MnO_2 [23].

The X-ray photoelectron spectra of the synthesized sample are shown in Fig. 4. Following the results of Ref. [24] the peaks at 642.1 eV (Mn $2p_{3/2}$) and 653.8 eV (Mn $2p_{1/2}$) in these spectra for the Mn $2p$ electrons with an energy separation ΔE of 11.7 eV (Fig. 4a) and energy separation of Mn $3s$ (ΔE = 5.1 eV Fig. 4b) may be assigned to manganese atoms in the 4+ oxidation state [25]. The peak at 529.5 eV (Fig. 4c) corresponding to atoms of oxygen in the manganese oxide crystalline lattice, respectively [26]. The XPS spectrum also indicates the presence of Zn and Mn elements with an atomic ratio of 0.3/1.0.

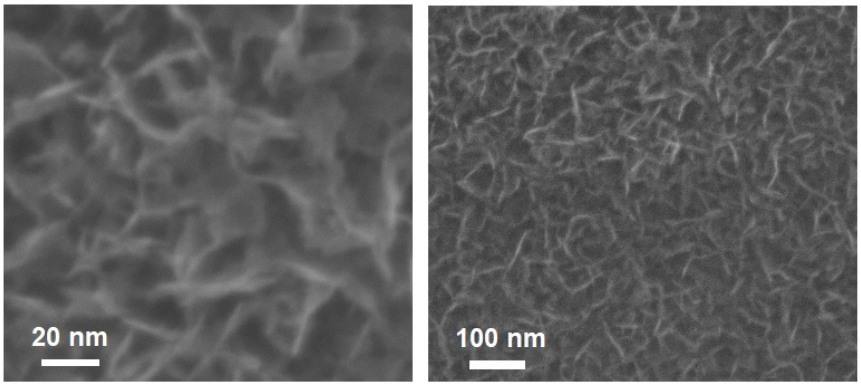

FIG. 1. SEM images of manganese contained nanolayers

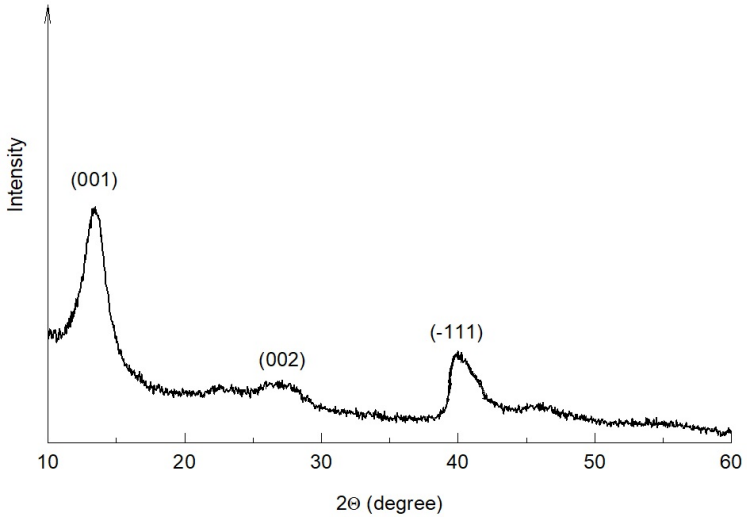

FIG. 2. XRD patterns of manganese contained nanolayers

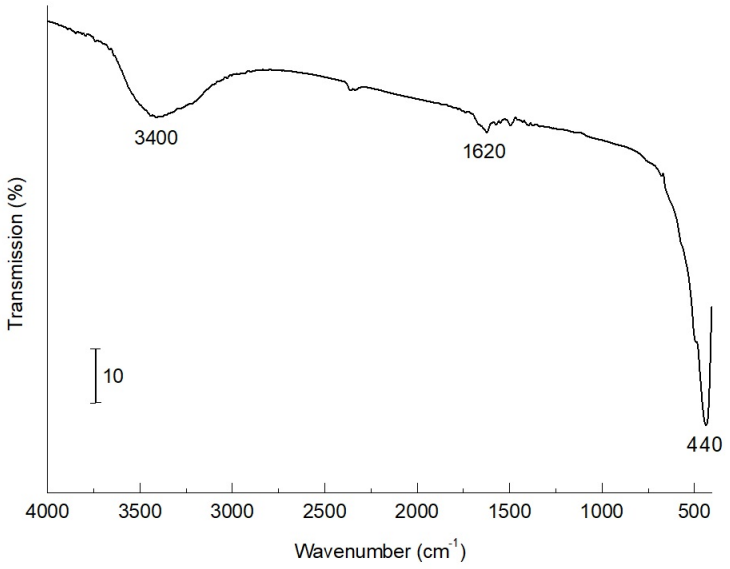

FIG. 3. FTIR transmission spectra of manganese contained nanolayers on a silicon surface

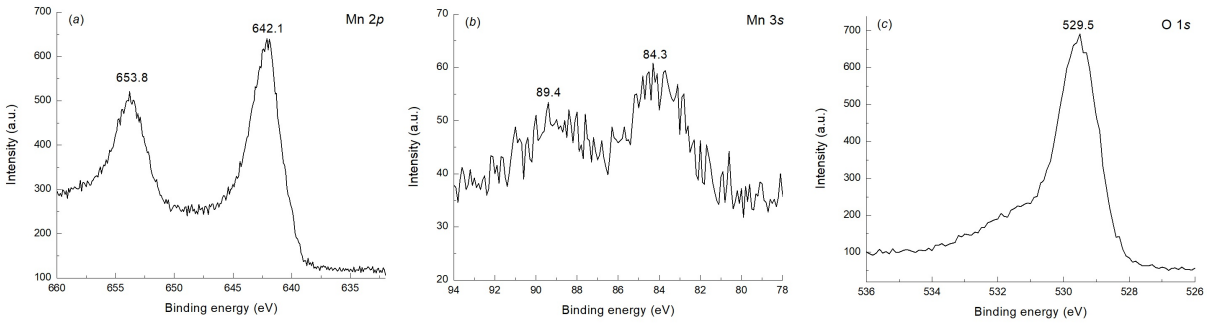

FIG. 4. XPS spectra Mn 2p (a), Mn 3s (b) and O 1s (c) of manganese contained nanolayers on a silicon surface

Comparison of research results, conducted via XRD, XPS and FTIR methods, allows us to conclude: obtained nanolayers consist of manganese oxide, doped zinc atoms, which are likely to be included in the crystal structure of birnessite MnO_2. Based on these results, we propose a formula synthesized layer as $Zn_{0.3}MnO_2$.

For explaining the obtained results, a description of chemical reactions, occurring on the surface can be suggested. At the first step, after dipping in the solution of mixed salts, $MnSO_4$ and $ZnSO_4$ on the surface occur adsorption of cations Mn^{2+}_{aq} and Zn^{2+}_{aq}. Then, after treatment in the solution of NaClO, these cations form on the surface of the nucleus of the MnO_2 nanocrystals, which are then, after treatment in the solution of $MnSO_4$, on the second SILD cycle form layered birnessite-like MnO_2 nanocrystal with Zn^{2+} ions in the interlayer space. After several repetitions of SILD cycles, the number of such nanocrystals and their length increases from the so-called nanosheets morphology.

We assume that such structure can possess interesting and practical electrochemical performance as cathode materials of aqueous zinc-ion battery. The cyclic voltammograms of the NF electrode with Zn-doped MnO_2 nanolayer were recorded in a potential window from 500 to 2000 mV vs. Zn/Zn^{2+} electrode in 2M $ZnSO_4$ electrolyte at scanning rates of 5, 10 and 15 mV/s (Fig. 5). At a scan rate of 5 mV/s, two electrochemical processes take place in the layer, including the intercalation of zinc ions at 1780 mV and their de-intercalation at 1230 mV. The proportionality of currents to scan rate provides information that the film is thick enough, and the charge transfer rate is limited by diffusion of charge carriers in the film.

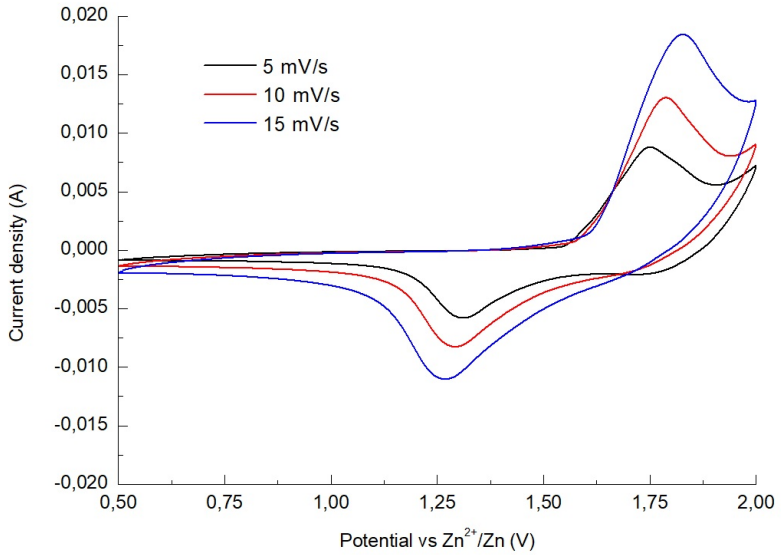

FIG. 5. CVA curves for NF electrode with Zn-doped MnO_2 nanolayers at a scan rate of 5, 10 and 15 mV/s

The specific capacitance of the Zn-doped MnO_2 NF electrode is calculated from charge-discharge curves (Fig. 6) by eq (1) to be 216 mAh/g at the current densities of 1 A/g. The high value of specific capacity can be explaining by

the good conductivity of MnO_2 nanosheets and also the significant influence of zinc atoms on the crystal structure of the sample.

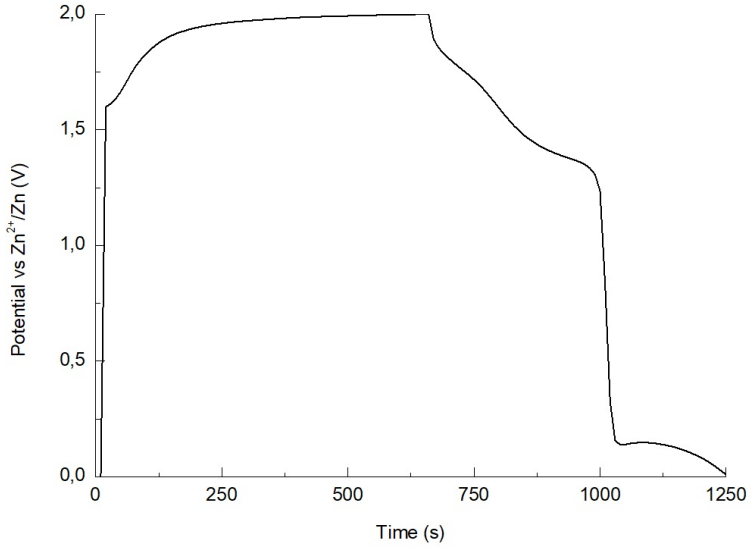

FIG. 6. Galvanostatic charge-discharge curve (at the current densities of 1 A/g) of the electrode with Zn-doped MnO_2 nanolayers

Cyclic stability is also an important property for electroactive materials. The capacity retention of NF electrode with Zn-doped MnO_2 nanolayer after 1000 charge-discharge cycles at a current density of 1 A/g maintained 95% of its initial capacity, which shows good cycling stability of this material. High cycling stability can be explained feature morphology of ultrathin nanocrystals of MnO_2 which provide fast diffusion of zinc ions and while not being destroyed.

The high value of specific capacitance for the electrodes synthesized by the SILD method can be explained, in our opinion, by the relatively smaller size of oxide nanocrystals formed during the layer deposition, which enlarges the effective surface area of the electrode,and consequently, results in the higher specific capacitance. Additionally, the smaller size of nanocrystals brings about good intercalation/de-intercalation of zinc ions on the electrode surface and hence affects positively the electrochemical stability. We believe that these electrochemical capacity characteristics of Zn-doped MnO_2 nanocrystals, synthesized via the SILD method, can be improved through a new scheme of their synthesis, including nanocomposite with carbon materials (CNT, graphene) formation that has been obtained after a new sequence of reagent treatment. However, these experiments fall beyond the scope of the present paper.

4. Conclusion

In summary, the possibility was shown forobtaining Zn-doped MnO_2 nanolayers via the SILD method used mixed manganese and zinc salts aqueous solution and NaClO as an oxidant. The results show the synthesized nanolayers were formed nanocrystals of the thickness of about 3–8 nm with the nanosheets morphology and the monoclinic birnessite-like crystal structure of MnO_2. The electrochemical study of Zn-doped MnO_2 nanolayers-modified nickel foam electrodes, prepared by 30 SILD cycles, demonstrates that the specific capacitance is 216 mAh/g at a current density of 1 A/g. Repeated cycling for 1000 charge-discharge cycles demonstrates a relatively small 5% capacitance fade. Thus this material can be potentially applied as an effective electroactive material for an aqueous zinc-ion battery.

Acknowledgements

This research was financial supported by an RSF grant, project number 19-73-00304. The authors are grateful to the Centers for X-ray diffraction studies and Nanotechnology of Saint Petersburg State University.

References

[1] Kaiyue Zhu, Tao Wu, Shichen Sun, Yeting Wen, Kevin Huang. Electrode Materials for Practical Rechargeable Aqueous Zn Ion Batteries. *Challenges and Opportunities, ChemElectroChem*, 2020, 7, P. 2714–2734.

[2] Jianping Yan, Edison Huixiang Ang, Yang Yang, Yufei Zhang, Minghui Ye, Wencheng Du, Cheng Chao Li. High Voltage Zinc Ion Batteries. *Design Strategies and Challenges, Advanced Functional Materials*, 2021, **335**, P. 2010213.

[3] Yanxia Yu, Jinhao Xie, Haozhe Zhang, Ruofei Qin, Xiaoqing Liu, Xihong Lu. High Voltage Rechargeable Aqueous Zinc Based Batteries. *Latest Progress and Future Perspectives, Small Science*, 2021, **355**, P. 2000066.

[4] Niklas Borchers, Simon Clark, Birger Horstmann, Kaushik Jayasayee, Mari Juel, Philippe Stevens.Innovative zinc-based batteries. *Journal of Power Sources*, 2021, **484**, P. 229309.

[5] Nengyan Ma, Peijun Wu, Yixue Wu, Donghao Jiang, Gangtie Lei. Progress and perspective of aqueous zinc-ion battery. *Functional Materials Letters*, 2019, **12**(5), P. 1930003.

[6] Dinesh Selvakumarana, Anqiang Pana, Shuquan Lianga, Guozhong Cao. A review on recent developments and challenges of cathode materials for rechargeable aqueous Zn-ion batteries. *J. Mater. Chem. A*, 2019, **7**, P. 18209–18236.

[7] Zixuan Fan, Wei He, Meng Ni, Peigeng Zhang, Wubian Tian, Wei Zhang, Long Pan, ZhengMing Sun. Recent Developments of Preintercalated Cathodes for Rechargeable Aqueous Zn-Ion Batteries. *Energy Technol*, 2021, **9**, P. 2000829.

[8] Wen Shi, Wee Siang Vincent Lee, Junmin Xue. Recent Development of Mn-based Oxides as Zinc-Ion Battery Cathode. *ChemSusChem*, 2021, **14**, P. 1–26.

[9] Muhammad Rashad, Muhammad Asif, Yuxin Wang, Zhen He, Iftikhar Ahmed. Recent advances in electrolytes and cathode materials for magnesium and hybrid-ion batteries. *Energy Storage Materials*, 2020, **25**, P. 342–375.

[10] Na Liu, Bin Li, Zhangxing He, Lei Dai, Haiyan Wang, Ling Wang. Recent advances and perspectives on vanadium- and manganese-based cathode materials for aqueous zinc ion batteries. *Journal of Energy Chemistry*, 2021, **59**, P. 134–159.

[11] Tong Xue, Hong Jin Fan, From aqueous Zn-ion battery to Zn-MnO_2 flow battery: A brief story. *Journal of Energy Chemistry*, 2021, **54**, P. 194–201.

[12] Boya Tang, Lutong Shan, Shuquan Liang, Jiang Zhou. Issues and opportunities facing aqueous zinc-ion batteries. *Energy Environ. Sci.*, 2019, **12**, P. 3288.

[13] Yingchang Yang, Xuejing Qiu, Wei Shi at all. Controllable fabrication of two-dimensional layered transition metal oxides through electrochemical exfoliation of non-van der Waals metals for rechargeable zinc-ion batteries. *Chemical Engineering Journal*, 2021, **15**, P. 127247.

[14] Huicong Xia, Qun Xu, Jianan Zhang. Recent Progress on Two-Dimensional Nanoflake Ensembles for Energy Storage Applications. *Nanomicro Lett.*, 2018, **10**.

[15] Wang Xiao, Li Yaguang, Wang Sen, Zhou Feng, Das Pratteek, Sun Chenglin, Zheng Shuanghao, Wu Zhong Shuai. 2D Amorphous V_2O_5/Graphene Heterostructures for High Safety Aqueous Zn Ion Batteries with Unprecedented Capacity and Ultrahigh Rate Capability. *Advanced energy materials*, 2020, **10**.

[16] Shamsayei M., Yamini Y., Asiabi H. Layer-by-layer assembly of layered double hydroxide/histidine/δ-MnO_2 nanosheets: Synthesis, characterization, and applications. *Applied Clay Science*, 2020, **188**, P. 105540.

[17] Kodintsev I.A., Martinson K.D., Lobinsky A.A., Popkov V.I. SILD synthesis of the efficient and stable electrocatalyst based on CoO-NiO solid solution toward hydrogen production. *Nanosystems: Physics, Chemistry, Mathematics*, 2019, **10**(6), P. 681–685.

[18] Mangesh A. Desai, Aditi Kulkarni, Girish Gund, Shrikrishna. D. Sartale, SILAR-grown K+ and Na+ions pre-inserted MnO_2 nanostructures for supercapacitor applications: A comparative study. *Energy Fuels*, 2021, **35**, P. 4577–4586.

[19] Tolstoy V.P., Lobinsky A.A., Levin O.V., Kuklo L.I. Direct synthesis of $Ni_2Al(OH)_{7-x}(NO_3)_x \cdot nH_2O$ layered double hydroxide nanolayers by SILD and their capacitive performance. *Materials Letters*, 2015, **139**, P. 4–6.

[20] Tolstoy V.P., Lobinsky A.A. Synthesis of 2D Zn-Co LDH nanosheets by a successive ionic layer deposition method as a material for electrodes of high-performance alkaline battery-supercapacitor hybrid devices. *RSC Advances*, 2018, **8**, P. 29607–29612.

[21] Hongjun Yue, Xingkang Huang, Yong Yang. Preparation and electrochemical performance of manganese oxide/carbon nanotubes composite as a cathode for rechargeable lithium battery with high power density. *Mater. Lett.*, 2008, **62**, P. 3388–3390.

[22] Kodintsev I.A., Martinson K.D., Lobinsky A.A., Popkov V.I. Successive ionic layer deposition of Co-doped $Cu(OH)_2$ nanorods as electrode material for electrocatalytic reforming of ethanol. *Nanosystems: Physics, Chemistry, Mathematics*, 2019, **10**(5), P. 573–578.

[23] Yu Xin Zhang, Xiao Long Guo, Ming Huang, Xiao-Dong Hao, Yuan Yuan, Chao Hua. Engineering birnessite-type MnO_2 nanosheets on fiberglass for pH-dependent degradation of methylene blue. *J. Phys. and Chem. of Sol.*, 2015, **83**, P. 40–46.

[24] Shumin Sun, Shen Wang, Tongchi Xia, Xiaofeng Li, Qingxian Jin, Qiong Wu. Hydrothermal synthesis of a MnOOH/three-dimensional reduced graphene oxide composite and its electrochemical properties for supercapacitors. *J. Mater. Chem. A.*, 2015, **3**, P. 20944–20951.

[25] Biesinger M.C., Payne B.P., Grosvenor A.P., Lau L.W.M., Gerson A.R., Smart R.St.C. Resolving surface chemical states in XPS analysis of first-row transition metals, oxides and hydroxides: Cr, Mn, Fe, Co and Ni. *Appl. Surf. Sci.*, 2011, **257**, P. 2717–2730.

[26] Lobinsky A.A., Tolstoy V.P. Synthesis of γ-MnOOH nanorods by successive ionic layer deposition method and their capacitive performance. *Journal of Energy Chemistry*, 2017, **26**, P. 336–339.

NANOSYSTEMS: PHYSICS, CHEMISTRY, MATHEMATICS, 2021, 12 (2), P. 188–198

Comparative study of synthesis and structural by using different precursors of copper oxide nanoparticles and their application in the adsorption capacity

Bahga-Saleh[1], Samreen Fatema[1], Mazhar Farooqui[1], Shaikh Yusuf[2]

[1]Maulana Azad College of Arts, Science and Commerce, Aurangabad (MS), India
[2]Shivaji College, Kannad (MS), India
yshaikh@gmail.com

DOI 10.17586/2220-8054-2021-12-2-188-198

Copper oxide nanoparticles were prepared by five sol-gel methods. The comparative study was made by the characterization such as FTIR, SEM-EDX, XRD. Out of these protocols, method five is more suitable and gives more accurate and appropriate results. From the data of EDX it is also found that method five gives higher yields of copper oxide nanoparticles. The efficiency of these nanoparticles as low cost adsorbent for the removal of methylene blue (MB) capacity from aqueous solutions was investigated. The effect of different parameters such as amount of adsorbent, concentration of dye, contact time, pH, temperature were studied the adsorption capacity and adsorption behavior of nanoparticles under various conditions. The experimental isotherm data has been studied. The kinetic study of the adsorption obeys Pseudo-first order model. The thermodynamic parameters namely Gibbs free energy, enthalpy, and entropy have revealed that the adsorption of methylene blue on the nanoparticles are feasible, spontaneous and exothermic.

Keywords: nanoparticals, sol-gel method, copper oxide, adsorption, FTIR, SEM-EDX, XRD.

Received: 25 November 2020

Revised: 19 January 2021

1. Introduction

Nanotechnology is a rare science that deals with materials in a very small size between (1 – 100 nm) with various crystal shapes such as spherical nanoparticles, flower like, nano rods, nano ribbons, nano platelets [1,2]. The synthesis of metal nanoparticles, has been an area of interest recently because of their unusual structural, electrical, optical and magnetic properties. These specific properties of nanoparticles can be adjusted during nanoparticles growth, as these properties are usually dependent upon particle size and surface area [3]. Generally there are numerous metal oxides available in nature but some of the metal oxides are most useful in conjunction with their applications in day to day life in science and technology. In the periodic table transition metals are high in number and have variety of applications in different fields [4]. Copper (Cu) nanoparticles have attracted considerable attention due to their properties among various metal nanoparticles. In recent years, copper oxide has increasingly attracted fundamental as well as practical interests [5]. Cupric oxide (CuO) has a monoclinic crystal structure and a p-type semiconductor with band gap of 1.2 – 1.9 eV [6, 7]. It has gained the most interest because of its wide applications, such as in solar transformation and electronics, field emissions, magnetic storage devices, lithium ion batteries, gas sensing, drug delivery, magnetic resonance imaging, and many more. The CuO-NPs also have an application in heat transfer, photoconductive, photothermal and photovoltaic applications. These nanoparticles display superior catalytic activity, with very good selectivity. Moreover they have excellent antimicrobial activity against various bacterial strains. It is used in the fields like catalysis, organic catalysis, photo catalysis, superconductors and ceramics as a kind of important inorganic materials [8–12]. They are used in nano-fluids, where dispersed nanoparticles are used for increase fluid thermal conductivity [13]; athey are also effectively used in anti-fouling paint, wood preservatives, sterile surface coatings, water filters or in textiles and bandages. On the other hand, the biocidal activity of CuO-NPs could be unintentionally harmful to the environment and human health [14]. A low cost production and excellent stability at room temperature, non-toxic nature of the copper oxide material makes it an attractive option for these applications; in addition, strong hole mobility, large minority carrier diffusion length, and a direct energy gap are suitable qualities for efficient absorption. For these applications, CuO is technologically interesting due to its chemical and physical properties, which depend on its composition, structure, phase, shape, size, and size distribution [15]. There is wide variety of preparation methods for the synthesis of CuO nanoparticles. Among of these methods our method for the synthesis of CuO nanoparticles belongs to the chemical method, which is sol-gel method [16]. The sol-gel process involves the formation of a colloidal suspension (sol) and gelatin of the sol to form a network in a continuous liquid phase (gel) [17]. It is one of the most important wet chemical methods used for the preparation of metal oxide nanoparticles [18] and it is widely used due to its diverse advantages. Among the advantages of sol-gel method is the fact that almost every metal oxide structure could be examined and no special apparatus or equipment is required.

This method works well for the synthesis of high purity complex metal oxides [19]. Several synthetic dyes, including cationic (basic dyes), anionic dyes (direct, acid and reactive dyes), and nonionic dyes (disperse dyes and vat dyes) are widely used in textile, leather and paper dyeing [20]. Some dyes or their metabolites are either toxic or mutagenic and carcinogenic, and thus exert unfavorable effects on the environment and human organs such as the skin and the lungs [21]. There are several methods for removing dyes, which can be categorized into physical, chemical, and biological methods. In general, physical methods, which include adsorption, ion exchange, and membrane filtration are effective for removing reactive dyes without producing undesirable by-products [22, 23]. Great attention has recently been focused on the benefits from processes involving nanoparticles. Nano-sized metal oxides have proven to be effective materials as adsorbents due to their high surface reactivity, adsorption capacity and destructive sorbent compared to their commercial analogues, and their simple synthesis from abundant natural minerals [24]. Adsorption is one of the most studied techniques for the effective removal of dyes primarily due to its simplicity, cost effectiveness and high performance. The effect of various variables such as contact time, pH, adsorbent dosage, effect of volume of dye solution [25, 26]. Methylene blue (MB) is an essential dye that is used in many industries for coloring and dying purposes and disinfect in pesticides, pharmaceuticals, dye stuffs and varnishes and is commonly adopted as a representative organic pollutant to test the adsorption performance for the removing organic pollutants from waste water [27, 28].

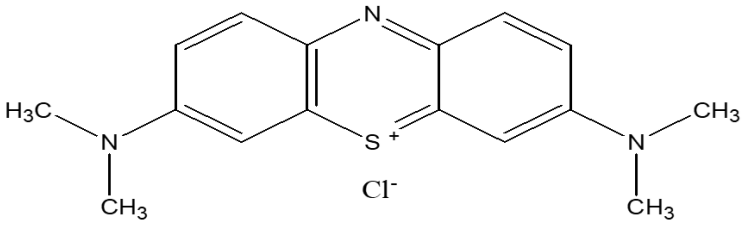

FIG. 1. Chemical structure of methylene blue dye

2. Materials and methods

In this study, CuO is prepared by sol-gel method by five different ways. All five nanoparticles were characterized by FT-IR, SEM-EDX, XRD and subjected for the adsorption on Methylene blue by different parameters i.e. change in time, change in concentration of dye, change in weight of adsorbent, change in pH. The variation is presented by graph. For the present work double distilled water is used, copper chloride, sodium hydroxide, methanol, absolute ethanol, oxalic acid, glacial acetic acid, and methylene blue were of AR grade from SD fine chemical Ltd India. Contract analytical services of various labs were taken for SEM, EDX, XRD etc. Five methods were used for the preparation of nanoparticles. These are as follows.

Method 1 (M1): copper oxide NPs prepared by dissolving 2 g of copper chloride in distilled water. In a separate flask HCl (36.5 % HCl in distilled water) and absolute ethanol were refluxed at 70 °C. The pH was maintained at 3. The copper solution was added dropwise until the solution gave a black precipitate. The precipitate was centrifuged and kept in muffle furnace at 5000 °C for two hrs [30].

Method 2 (M2): A solution of 6 gm of oxalic acid in 200 ml of methanol is prepared 0.2 gm of copper chloride is dissolved in about 200 ml of methanol at 35 °C under constant stirring for 30 min to obtain a clear solution. The oxalic acid solution was then added to warm solution to yield a thick gel. That solution was subsequently dried in a hot air oven at 80 °C for 20 hrs to produce copper oxide powder. The powder was subjected to pyrolysis in a muffle furnace at 500 °C for 2 hrs to give black powder [31].

Method 3 (M3): In the third method of synthesis of copper nanoparticles, 9 gm of copper chloride and 5.4 gm of sodium hydroxide pellet were dissolved in 100 ml methanol separately. A methanolic solution of copper chloride was magnetically stirred. Dropwise addition of sodium hydroxide solution was carried out with continuous stirring at room temperature. The color of the solution was turned to black. The black precipitate was then centrifuged and washed with deionized water and calcined at 450 °C for 2 hrs [32].

Method 4 (M4): copper nanoparticles were prepared by using 0.2 gm copper chloride was dissolved in 100 ml of double distilled water. This solution was continuously stirred. To this stirred solution 1 ml of glacial acetic acid was added. The solution was heated at 100 °C for 30 min. Dropwise addition of sodium hydroxide (8 M) was carried out with continuous stirring until the color of solution turned to black from green. The precipitate was centrifuged and washed several time with deionized water and kept in muffle furnace at 450 °C for 2 hrs [33].

Method 5 (M5): 0.2 M of copper chloride was prepared for CuO nanoparticles. KOH solution was prepared in benzene and hexane mixture (in 1:1 ratio). This mixture was added to copper chloride solution with continuous stirring. The solution was stirred and refluxed for 2 hrs. The precipitate was centrifuged and dried in muffle furnace at 450 °C for 2 hrs [34].

The nanoparticles so formed were subjected to SEM, EDX and XRD analysis.

2.1. Adsorption

The adsorption study was carried out using batch adsorption method. The effect of initial concentration of dye, pH, dosage form, contacts time,etc., was carried out as described in earlier work.The nanoparticles were washed several times with distilled water until it was free from NaCl.

A model anionic dye was selected in this study as because of its complex chemical structure. Solubility in aqueous solution and it is persistence, once it is discharged in to natural environment. The concentration of MB was determined by using UV-visible spectrophotometer (S2-159) at $\lambda_{\max} = 660$ nm. The adsorption experiments were carried out in stirred batch mode. For experiment, 10 ml of MR, dye solution of specified concentration was continuously stirred unit 0.1 gm of powder at room temperature [35].

3. Result and discussion

3.1. Fourier transform infrared spectroscopy (FTIR) analysis

The FTIR spectrum of CuO within the 400 – 4000 cm^{-1} range is shown in Fig. 2. FTIR spectra provide information about the nature of the copper oxide nanoparticles are essential for verifying the purity of the oxide. The band at 447.404 cm^{-1} was ascribed to CuO vibration, whereas that at 624.823 cm^{-1} can be assigned to the Cu–O stretching [36]. The bandat 578.54 cm^{-1} indicated the formation of the CuO-NPs [32]. The vibration frequencies at 516.829 cm^{-1} in the FTIR spectra of CuO nanoparticles have been assigned to Cu–O stretching [37]. A wide absorption band at around 3467.38 cm^{-1} is observed which occurs due to the absorption of moisture by the nanoparticles. The metal-oxygen bond is observed at 1133.94, 1542.77 and 1654.62 cm^{-1}, indicating the formation of CuO from Copper Chloride [38].

3.2. Scanning electron microscopy (SEM-EDX)

The surface morphologies of the synthesized copper oxide nanoparticles have been examined through scanning electron microscopy. The morphologies of CuO nanoparticle prepared with different precursors via the sol-gel method. Fig. 3 show the SEM images copper oxide show irregular morphology with different shapes and sizes 58.7, 83.3, 72.4, 46.1 and 83.9 nm. The effect of reaction time plays a significant role in the morphology of nanoparticles.

Figure 4 shows the EDX analysis of CuO-NPs annealed at 450 °C. The EDX analysis was carried out CuO NPs at 20 keV. Results revealed the presence of copper (Cu) and oxygen (O) elements in CuO in nanoparticles and other peaks are also obtained in EDAX which may be due to the chemicals which were added during processing of nanoparticles. Copper nanoparticles synthesized by five procedures in which M5 gives more amounts of copper nanoparticles is 42.22 ± 0.82, while M3 gives least amount of nanoparticles that is 20.48 ± 0.10. Table 1 shows the percentage of all elements present in the nano powder.

TABLE 1. Percentage of elements present in the sample from EDX

Element	M1	M2	M3	M4	M5
C	19.18±0.49	13.25±0.20	9.84±0.24	19.21±0.92	43.22±1.10
O	33.67±0.30	33.56±0.20	22.83±0.24	29.01±0.92	37.87±0.50
Na	1.22±0.07	...	15.43±0.17	1.10±0.48	...
Cl	3.33±0.05	0.52±0.01	10.48±0.10	...	1.21±0.09
Cu	31.54±0.15	28.87±0.07	20.48±0.10	20.68±0.39	42.22±0.82

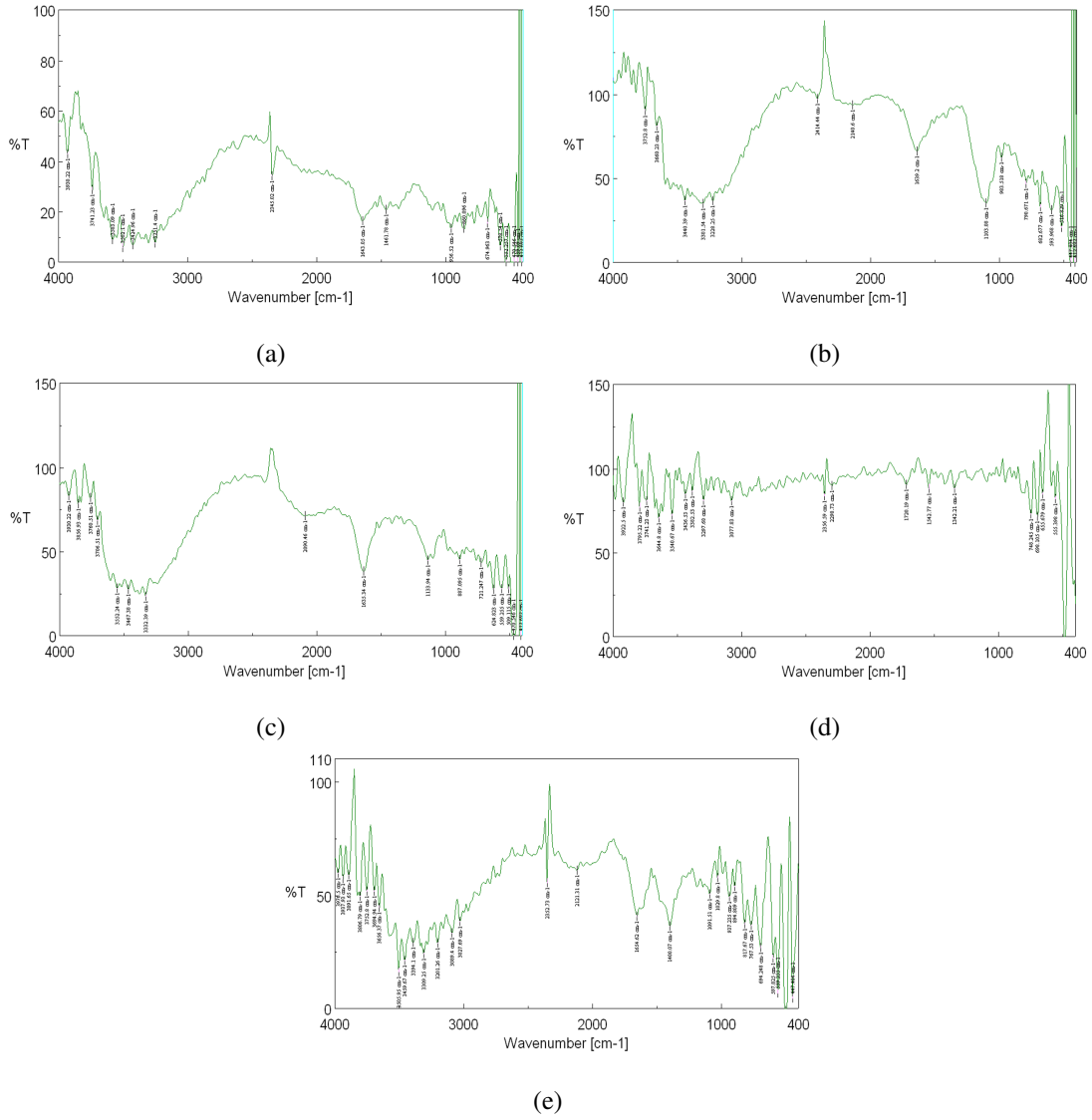

FIG. 2. FTIR of CnO Nanoparticle: Method 1 (a); Method 2 (b); Method 3 (c); Method 4 (d); Method 5 (e)

3.3. X-ray diffraction analysis (XRD)

The XRD patterns of as-synthesized and calcined CuO nanoparticles using different precursors are shown in Fig. 5. XRD peaks confirm that the formation of CuO from each precursor was in the monoclinic phase. The figure shows sharp peaks of CuO, which indicate the crystallinity in nature. The XRD pattern of the powder sample.

M1 was recorded in the fraction angle range from 5 to 40°. The characteristic peaks located at 2θ = 16.53, 32.03, and 35.85° are assigned to (101), (202) and (210). The highest peak is at angle 32.03° at (202) plane with 3723.25 intensity account.

M2 was recorded in the fraction angle range 5° to 20°. The characteristic peaks located at 2θ = 7.61°, 9. 82° and 15.10o are assigned to (100), (110) and (200). The highest peak is at angle 7.61° at (100) plane with 3089.19 intensity.

M3 was recorded in the fraction angle range from 5 to 75°. The characteristic peaks located at 2θ = 27.36, 31.69, 35. 53, 38.72, 45.42, 56.45 and 66.23° are assigned to (221), (222), (400), (330), (430), (610) and (632). The highest peak is at angle 31.691° at (222) plane with 50880.95 intensity.

M4 was recorded in the fraction angle range from 5 to 50°. The characteristic peaks located at 2θ = 11.53, 17.03, 19.14, 22.62, 26.98, 29.81, 31.78, 32.61, 33.74, 34.53, 35.62, 36.66, 37.99, 38.81, 39.94, 41.56, 43.41 and 45.52° are assigned to (111), (220), (221), (320), (330), (332), (430), (431), (333), (432), (521), (441), (531), (442), (532), (541), (542) and (632). The highest peak is at angle 29.81° at (332) plane with 24594.34 intensity.

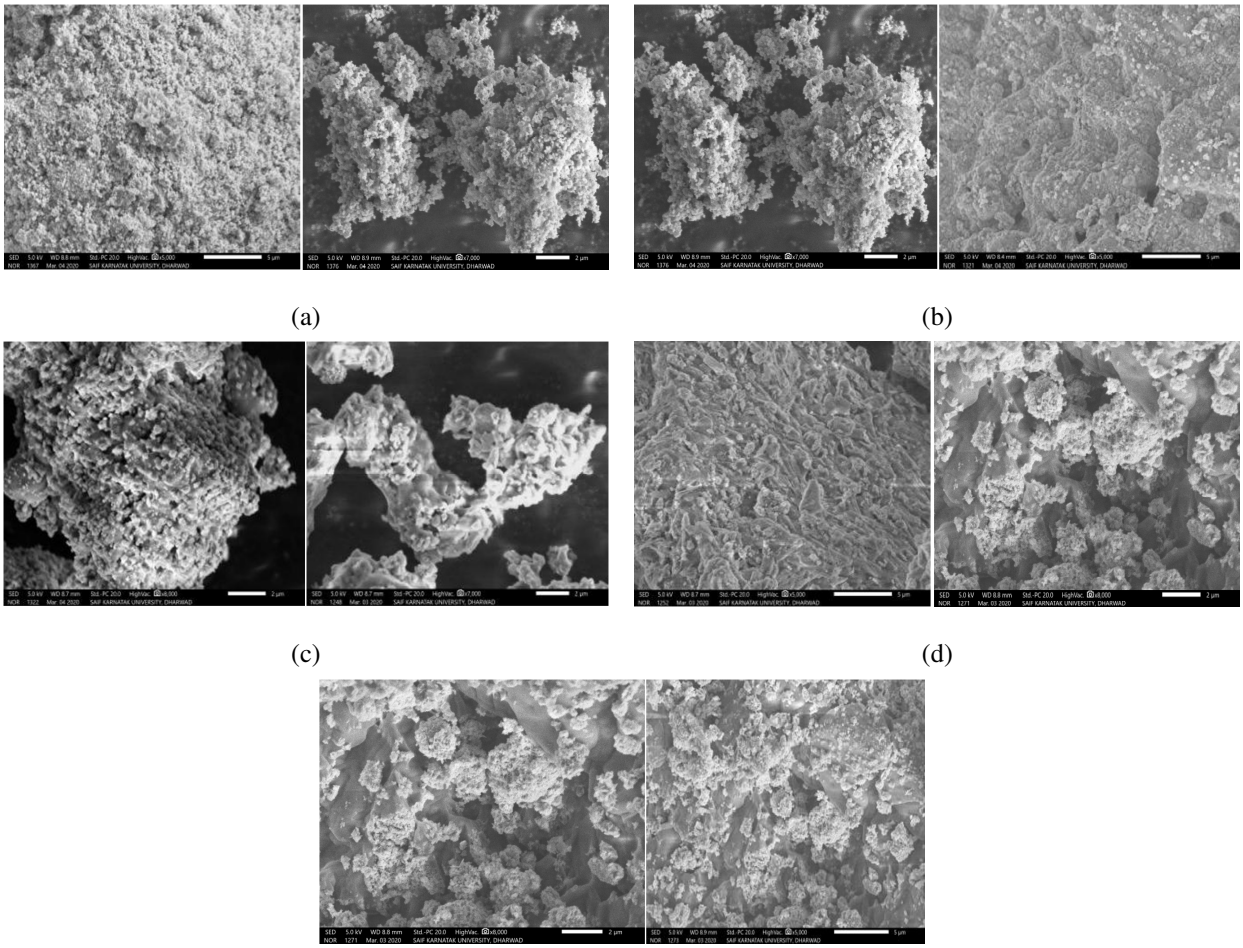

FIG. 3. SEM images of CuO: Method 1 (a); Method 2 (b); Method 3 (c); Method 4 (d); Method 5 (e)

M5 was recorded in the fraction angle range from 5 to 75°. The characteristic peaks located at 2θ = 27.41, 31.73, 35.61, 38.84, 45.47, 56.49 and 66.23° are assigned to (321), (330), (332), (333), (442), (552) and (660). The highest peak is at angle 31.73° at (330) plane with 105773.40 intensity.

The average Crystalline sizes respectively 19.9, 27.9, 28.8, 26.9 and 33.6 nm which calculated from the Debye–Scherrer equation [39].

$$D = \frac{K\lambda}{\beta \cos\theta},$$

where D is crystallite size (nm), K – constant ($K = 0.9$), λ is X-ray wavelength ($\lambda = 0.15406$ nm), β is Full-Width Half Maximum (FWHM) of the peak in XRD pattern, θ is peak obtained angle.

The IR and XRD confirms the confirmation of CuO nanoparticles. These nanoparticles are used for the evaluation of their adsorption capacities. The SEM images proves that the surface of particles is rough and can adsorb the dye. For present study, Methylene blue (MB) is used as adsorbate.

3.4. Adsorption study

In adsorption studies, effect of contact time plays vital role irrespective of other experimental parameters effecting adsorption kinetics. The sample of dye was taken in separate flasks and adsorption studies were carried out at different contact time from 5 to 25 min. The results are given in Fig. 6.

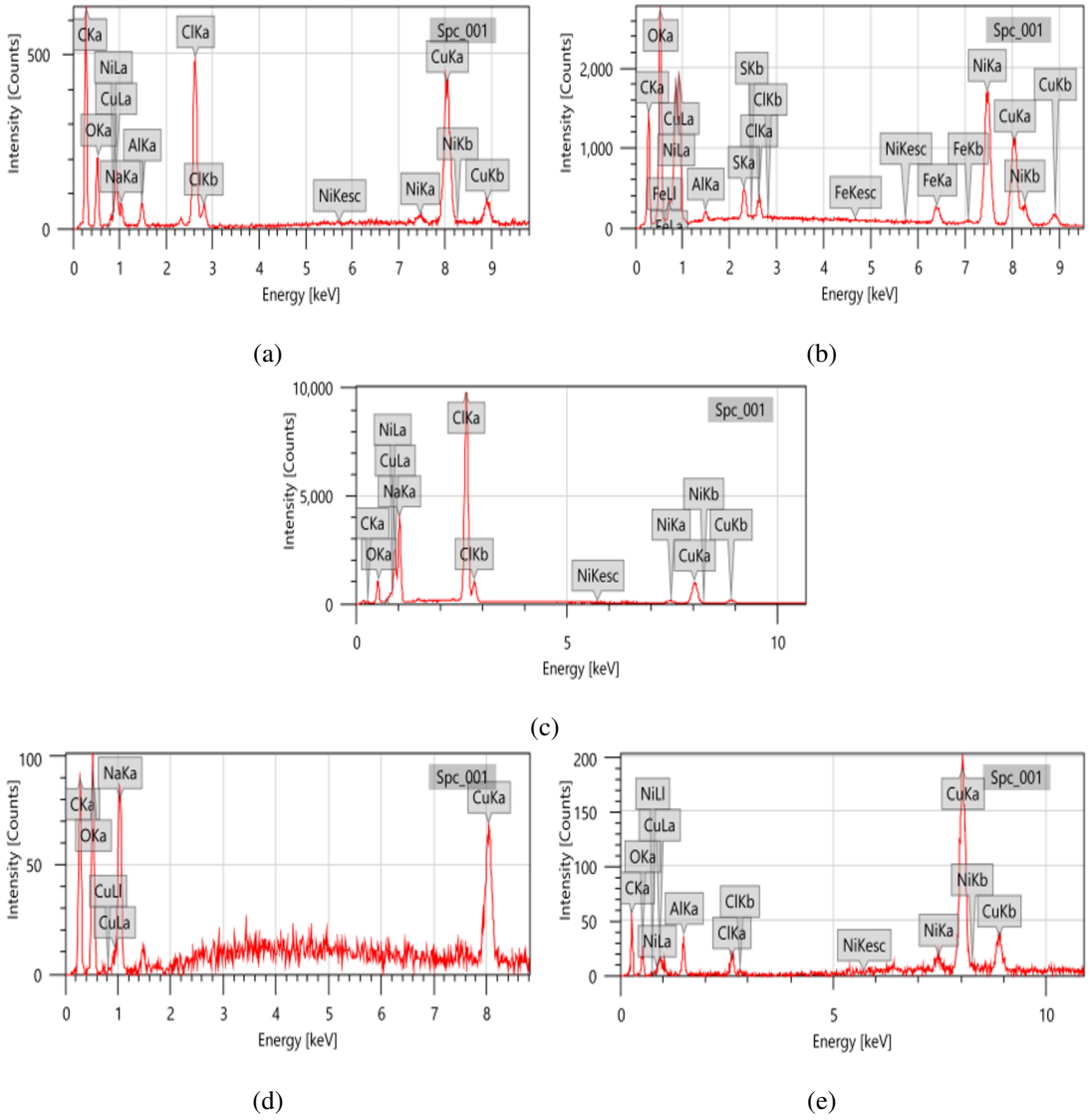

FIG. 4. FTIR of CnO Nanoparticle: Method 1 (a); Method 2 (b); Method 3 (c); Method 4 (d); Method 5 (e)

3.5. Adsorption isotherm

Kinetic isotherm: In the present work, Pseudo first order and Pseudo second order kinetic models can be expressed in a linear form as the following equations. Calculated results for pseudo-first order and second order kinetic are shown in Table 2:

$$\log(q_e - q_t) = \log q_e \frac{K_1 t}{2.303}, \tag{1}$$

$$\frac{t}{q_t} = \frac{1}{K_2 q_e^2} + \frac{t}{q_e}, \tag{2}$$

where q_e and q_t are the amount of MB adsorbed at equilibrium and different times (min) respectively K1 represents the first order constant (min^{-1}) [40–42].

The equilibrium adsorption data have been analyzed using well known Langmuir and Freundlich model. A mathematical expression of the Langmuir isotherm is given by the following equation:

$$\frac{C_e}{Q_e} = \frac{1}{Q^0} + \frac{C_e}{Q^0}, \tag{3}$$

where C_e is the equilibrium concentration of the MB, Q_e is MB amount adsorbed at equilibrium q_m and K_L are Langmuir constants related to the adsorption capacity and adsorption energy, which can be calculated from linear regression of C_e/Q_e V/s C_e.

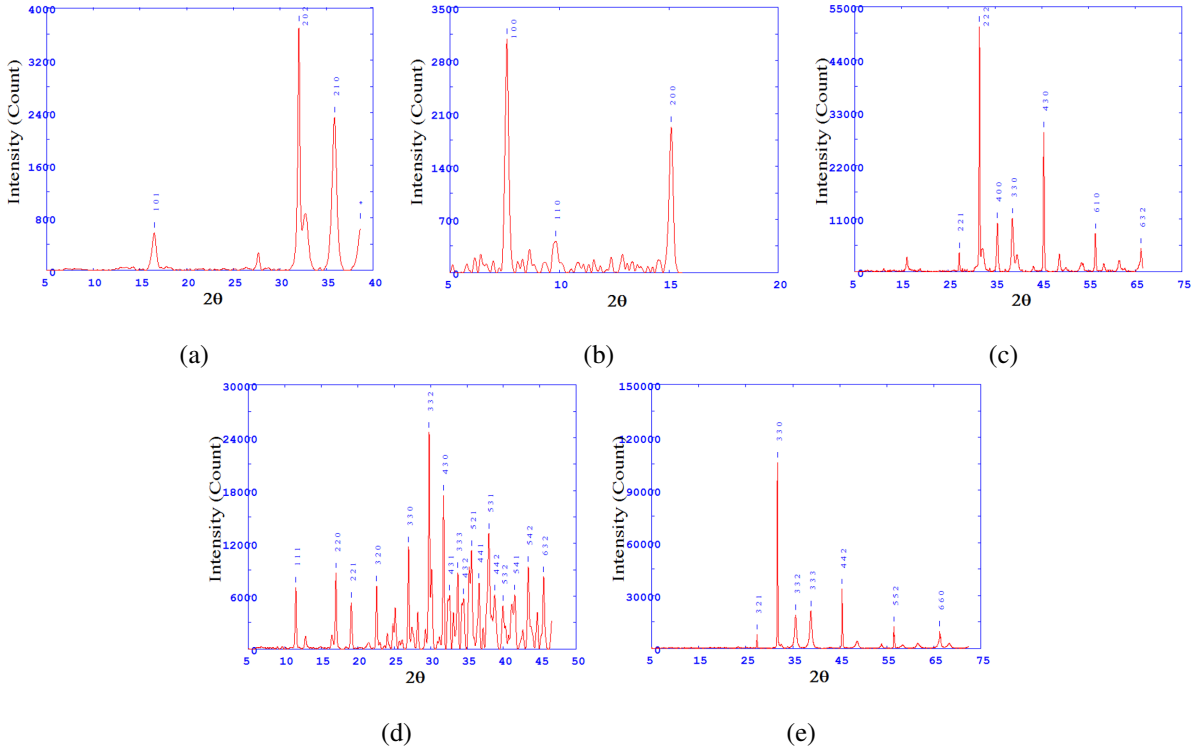

FIG. 5. XRD spectra of CuO: Method 1 (a); Method 2 (b); Method 3 (c); Method 4 (d); Method 5 (e)

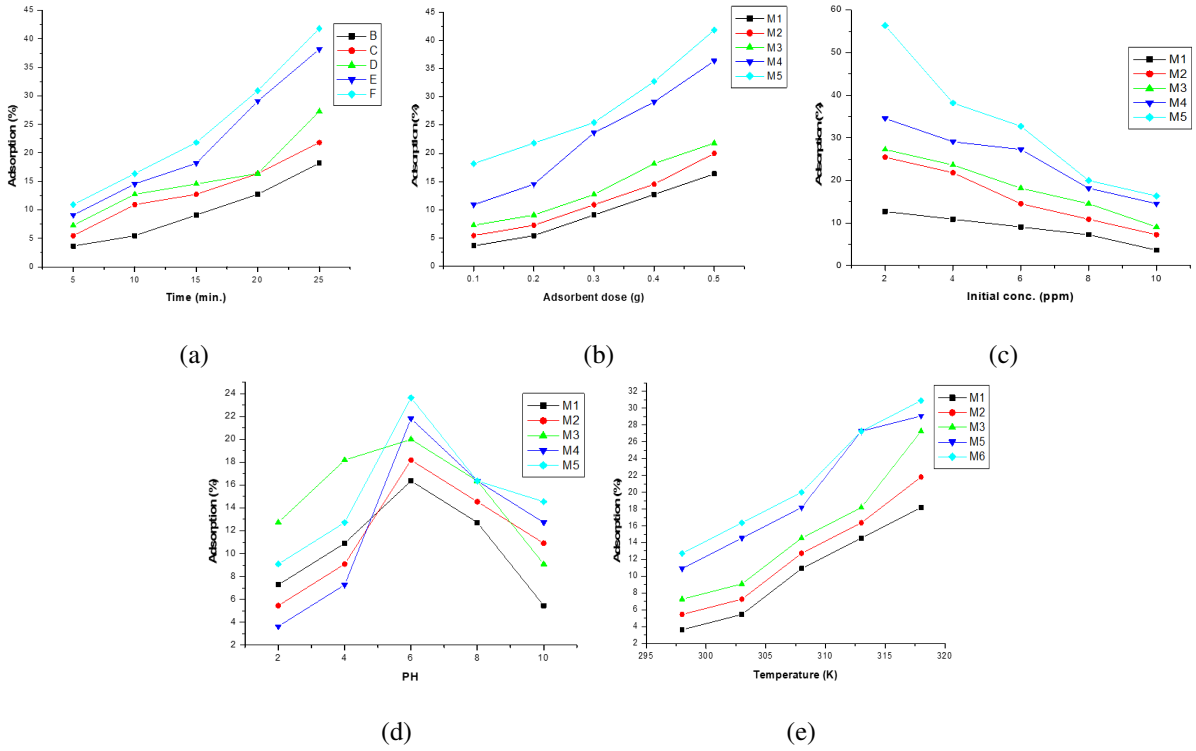

FIG. 6. Variation in time (a); Variation in adsorbent dose (b); Variation in concentration (c); Variation of pH (d); Variation in temperature (e)

TABLE 2. Comparison of the experiments and the kinetic model of MB dye on MnO_2 adsorbent

	Conc. of MR (mg/L)	Pseudo-first order			Second order		
		K_1 (min^{-1})	q_e (mg/gm)	R_2	K_2 (gm/mg·min)	q_e (mg/gm)	R_2
M1	10	0.08731	8192.756	0.96054	1.71×10^{-7}	19091.26	0.045309
M2	10	0.11852	8732.930	0.88619	3.98×10^{-7}	16366.61	0.095704
M3	10	0.10684	8425.972	0.86020	2.08×10^{-6}	−10687.00	0.164877
M4	10	0.22498	8300.419	0.93805	2.84×10^{-7}	23866.35	0.113529
M5	10	2.24596	8724.690	0.94341	7.84×10^{-7}	15878.06	0.329866

A dimensionless constant separation factor R_L is used to express the essential characteristic of the Langmuir isotherm, which is given by:

$$R_L = \frac{1}{1 - bC_0}, \tag{4}$$

where C_0 (mg/L) is the initial in liquid phase. The values of R_L indicates the adsorption isotherm model of characteristic as follows: $R_L > 1$ (unfavorable), $R_L = 1$ (Linear), $0 < R_L < 1$ (favorable) and $R_L = 0$ (irreversible). Results are shown in Table 3.

TABLE 3. Adsorption constant

	Conc. of MR (mg/L)	Langmuir constant				Freundlich constant		
		Q_0 (mg/g)	$b \cdot 10^{-5}$ (L/g)	R_L	R_2	n	K_f (mg/g·(L/g))$1/n$	R_2
M1	10	−4376.37	−0.03510	−0.39841	0.985652	0.21211	0.000156	0.919432
M2	10	−3385.24	−0.02902	−0.52583	0.988451	0.18504	4.98×10^{-6}	0.921468
M3	10	−3784.44	−0.03051	−0.4875	0.987042	0.19826	2.38×10^{-5}	0.920180
M4	10	−1631.85	−0.02061	−0.94293	0.992693	0.12191	1.14×10^{-11}	0.981394
M5	10	−4194.63	−0.02135	−0.66017	0.984004	0.21501	7.75×10^{-5}	0.925983

Compared with the Langmuir and Freundlich isotherm accredit the heterogeneity of the surface and consider, the adsorption occurs at sites with different energy of adsorption. This equation can also apply for multilayer adsorption and expressed by the following equation:

$$\log q_e = \log K_f + \frac{1}{n \log C_e}, \tag{5}$$

where K_f and n are the adsorption capacity of the adsorbent and adsorption intensities, respectively. The values of K_f and n are calculated from the interception and slope of the plot of $\log q_e$ v/s $\log C_e$ [43–45].

Thermodynamic parameter: To determine the possibility of spontaneously occurring of the MB adsorption, thermodynamic parameters were calculated. These parameters such as change in standard Gibb's free energy (ΔG^0, J/mol/K), enthalpy (ΔH^0, KJ/mol), and entropy (ΔS^0, J/mol/K) were determine from experimental data observed over the temperature range of 303 – 323 K. These parameters can be calculated as:

$$K_e = \frac{q_e}{C_e}, \tag{6}$$

$$\Delta G^0 = -RT \log K_e, \tag{7}$$

$$\ln K_e = \frac{\Delta S^0}{R} - \frac{\Delta H^0}{RT}, \tag{8}$$

where K_e is the equilibrium constant defined by q_e/C_e (q_e is the equilibrium amount of adsorbate that adsorbed on adsorbent surface (mg/L) and C_e is the equilibrium amount of unadsorbed remains in the solution). R and T are the universal gas constant. The values for ΔH^0 and ΔS^0 can be calculated using the plot of K_d v/s $1/T$ (Table 4 and Table 5) [46].

TABLE 4. Thermodynamic parameter values

Sr. No.	Temp. (K)	ΔG^0 (M1)	ΔG^0 (M2)	ΔG^0 (M3)	ΔG^0 (M4)	ΔG^0 (M5)
1	298	37943.4089	52328.80669	33185.6802	27394.87892	30092.49601
2	303	38495.7025	53108.85743	33665.4808	27793.94939	30544.53897
3	308	39047.9961	53888.90816	34145.2813	28193.01987	30996.58193
4	313	39600.2896	54668.9589	34625.0819	28592.09035	31448.62489
5	318	40152.5832	55449.00963	35104.8825	28991.16083	31900.66785

TABLE 5. Values of entropy and enthaply

Sr. No.	Method	ΔS^0	ΔH^0
1	M1	-55.22935668	21208.91391
2	M2	-78.00507357	28693.2694
3	M3	-47.98005725	18647.72288
4	M4	-39.90704777	15303.04344
5	M5	-45.20429608	16395.5943

4. Conclusion

The present study concludes that all the considered methods are good for the preparation of nanoparticles but fifth method is more appropriate and gives higher yields of copper oxide nanoparticle. The results of FTIR, SEM-EDX and XRD of all five samples reveals the presence of nanoparticles. The synthesized nanoparticles were studied for the removal of dyes from aqueous solutions. It was found that removal of MB dye from aqueous solutions using these synthesized nanoparticles is both highly efficient and environmentally-friendly. In this respect, the adsorption is followed by first a pseudo-first order model. The thermodynamic parameters such as Gibb's free energy, enthalpy, and entropy have revealed that the adsorption of methylene blue on the nanoparticles is feasible, spontaneous and exothermic.

References

[1] Saja M.J. Synthesis of CuO Nano structure via sol-gel and Precipitation Chemical Methods. *Al-Khwarizmi Engineering Journal*, 2016, **12** (4), P. 126–131.

[2] Hadeel K.T., Kadhim A.H., Ahmed A.A. Synthesis of copper oxide nanoparticles via sol-gel method. *Int. Journal of Research in Engineering and Innovation*, 2017, **1** (4), P. 43–45.

[3] Jeevan J.M., Umesh K.G. Sol-gel Synthesis of Copper, Silver and Nickel Nanoparticles and Comparison of their Antibacterial activity. *Int. Journal of Theor. & Appl. Sciences*, 2017, **9** (2), P. 151–156.

[4] Kankanit P., Sineenart S., Wanichaya M., Wisanu P. Synthesis of CuO Nanoparticles by Precipitation Method Using Different Precursors. *Energy Procedia*, 2013, **3** (4), P. 740–745.

[5] Rejitha S.G., Krishnanb C. Synthesis of cadmium-doped copper oxide nanoparticles: Optical and structural characterizations. *Advances in Applied Science Research*, 2013, **4** (2), P. 103–109.

[6] Daniel-Umeri R., Osuji F.I., Ezema R.U. Synthesis and Characterization of Copper Oxide Thin Films Using Successive Ionic Layer Adsorption Reaction (SILAR) Method. *Chemistry and Materials Research*, 2016, **8** (6), P. 68–76.

[7] Sanjay S., Mahendra K., Arvind A., Sudhanshu K.D. Synthesis and Characterisation of Copper Oxide nanoparticles. *IOSR Journal of Applied Physics (IOSR-JAP)*, 2013, **5** (4), P. 61–65.
[8] Etefagh R., Azhir E., Shahtahmasebi N. Synthesis of CuO nanoparticles and fabrication of nanostructural layer biosensors for detecting Aspergillus niger fungi. *Scientia Iranica Transactions F: Nanotechnology*, 2013, **20** (3), P. 1055–1058.
[9] Nithya K., Yuvasree P., et al. Preparation and Characterization of Copper Oxide Nanoparticles. *Int. Journal of ChemTech Research*, 2014, **6** (3), P. 2220–2222.
[10] TranT. H., Nguyen V.T. Copper Oxide Nanomaterials Prepared by Solution Methods, Some Properties, and Potential Applications. *Int. Scholarly Research Notices*, 2014, 856592.
[11] Soltanianfard M.J., Firoozadeh A. Synthesis and Characterization of Copper (II)-Oxide Nanoparticles from Two Cu (II) Coordination Polymers. *Journal of Sciences, Islamic Republic of Iran*, 2016, **27** (2), P. 113–117.
[12] Khashan K.S., Jabir M.S., Abdulameer F.A. Preparation and characterization of copper oxide nanoparticles decorated carbon nanoparticles using laser ablation in liquid. *Journal of Physics: Conf. Series*, 2018, **1003**, 012100.
[13] Manimaran R., Palaniradja K., et al. Preparation and characterization of copper oxide nanofluid for heat transfer applications. *Appl. Nanosci.*, 2014, **4**, P. 163–167.
[14] Rejitha S.G., Krishnan C. Synthesis of cadmium-doped copper oxide nanoparticles: Optical and structural characterizations. *Advances in Applied Science Research*, 2013, **4** (2), P. 103–109.
[15] Diachenko O.V., Opanasuyk A.S., et al. Structural Features of Nanostructured Copper Oxide Thin Films, Synthesized by Spray Pyrolysis Technique. *Proc. Nap*, 2015, **4** (4), P. 1–4.
[16] Aparna Y., Enkateswara Rao K.V., Srinivasa Subbarao P. Synthesis and Characterization of CuO Nano Particles by Novel Sol-Gel Method. *IPCBEE*, 2012, **48**.
[17] Jagdeep M., Kshirsagar S., Ramakant S., Prakash S.A. Preparation and characterization of copper oxide nanoparticles critical heat flux. *Thermal science*, 2017, **21** (1A), P. 233–242.
[18] Arindam G., Navnita K., Ayon B. Investigations on structural and optical properties of Cu doped ZnO. *Journal of NanoScience and NanoTechnology*, 2014, **2** (4), P. 485–489.
[19] Catherine W.C.L. Synthesis and Characterization of Manganese Dioxide Nanoparticles and Thin Films. A dissertation submitted in partial fulfilment of the requirement for the degree of Bachelor of Science, University Malaysia Sarawak, 2007.
[20] Radwan N.R.E., Hagar M., Chaieb K. Adsorption of Crystal Violet Dye on Modified Bentonites. *Asian Journal of Chemistry*, 2016, **28** (8), P. 1643–1647.
[21] Ameeth B.I., Nagalakshmi R., Shanthi T. Removal of congo red and magenta dyes from industrial waste water by thorn apple leaf powder. *Int. J. Chem. Sci*, 2016, **14** (1), P. 57–64.
[22] Subir C., Tapan K.S. Adsorption of Reactive Blue 4 (RB4) onto Rice Husk in Aqueous Solution. *Int. Journal of Scientific & Engineering Research*, 2016, **7** (3), P. 7–12.
[23] Masoud S-R. Mohsen I., et al. Removal, preconcentration and determination of methyl red in water samples using silica coated magnetic nanoparticles. *Journal of Applied Research in Water and Wastewater*, 2014, **1**, P. 6–12.
[24] Muhammad N.Z., Qamar D., et al. Effective adsorptive removal of azo dyes over spherical ZnO. *JMR&T journal research and technology*, 2019, **8** (1), P. 713–725.
[25] Maryam N.A., Niyaz M.M., et al. Adsorption of organic dyes using copper oxide nanoparticles: isotherm and kinetic studies. *Journal Desalination and Water Treatment*, 2016, **57** (52), P. 25278–25287.
[26] Oannis A., Ahmad H-B, et al. Use of nanoparticles for dye adsorption: Review. *Journal of Dispersion Science and Technology*, 2018, **39** (6), P. 836–847.
[27] Li L.H., Xiao J., Liu P., Yang G.W. Super adsorption capability from amorphousization of metal oxide nanoparticles for dye removal. *Science Reports*, 2015, **5**, 9028.
[28] Chandrakala M., Anima U. Adsorption Efficiency of Phosphoric Acid Activated Gulmohar (Delonix regia) Fruit Shell Charcoal using Methylene Blue. *Int. Journal for Research in Applied Science & Engineering Technology*, 2018, **6** (4), P. 480–484.
[29] Lotfi M., Lazhar B., et al. Removal of methylene blue from aqueous solutions by adsorption on kaolin: Kinetic and equilibrium studies. *Applied clay science*, 2018, **153**, P. 38–45.
[30] Sanchez E., Lapez T. Effect of the preparation method on the band gap of titania and platinum-titania sol-gel materials. *Mat. latt.*, 1995, **25**, P. 271–275.
[31] Parmvir S., Rishab J., et al. Synthesis of Manganese Oxide NPs Using Similar Process and Different Precursors — A Comparative Study. *Nanotech R. J.*, 2015, **8** (3), P. 419–427.
[32] Ismat Z.L., Lutfun N.H., et al. Preparation and Characterization of Copper Oxide NPs Synthesized via Chemical Precipitation Method. *Open Access Library Journal*, 2015, **2**, e1409.
[33] Hadeel K.T., Kadhim A.H., Al-Amiery A.A. Synthesis of copper oxide NPs via sol-gel method. *IJREI*, 2017, **1** (4), P. 43–45.
[34] Sanjay S., Mahendra K., Arvind A., Sudhanshu K.D. Synthesis and Characterisation of Copper Oxide NPs. *IOSR-JAP*, 2013, **5** (4), P. 61–65.
[35] Rajesh D., Milind U., Farooqui M., Shantilal R. Adsorption study for the Removal of Hazrdous Dye Congo Red by Biowaste Materials as Adsorbents. *IJAIEM*, 2016, **5** (11).
[36] Anita S.E., Dae J.K. Synthesis and characterization of CuO nanowires by a simple wet chemical method. *Ethiraj and Kang Nanoscale Research Letters*, 2012, **7**, 70.
[37] Ensieh S., Nourollah F., Aliakbar D.K. Copper Oxide Nanoparticles Prepared by Solid State Thermal Decomposition: Synthesis and Characterization. *Journal of Ultrafine Grained and Nanostructured Materials*, 2016, **49** (1), P. 48–50.
[38] Kalita C., Karmakar S. Analysis of Structural and Optical Features of CuO Nanoparticles Synthesized at Different Molarities. *Int. Journal of Scientific Research in Physics and Applied Sciences*, 2018, **6** (2), P. 30–34.
[39] Deepak P., Shikha S., Pardeep S. Removal of methylene blue by adsorption ontoactivated carbon developed from Ficus carica bast. *Arabian Journal of Chemistry*, 2017, **10**, P. 1445–1451.
[40] Soheila H., Marzieh T., Seyed J.S. Removal of crystal violet from water by magnetically modified activated carbon andnanomagnetic iron oxide. *Journal of Environmental Health Science & Engineering*, 2015, P. 2–7.

[41] Dattatraya J., Bashir A.D., Farooqui M. Husk of gram seeds as a low-cost adsorbent for the removal of methylene blue dye from aqueous solutions. *Journal of enviromental science and water resources*, 2013, **2** (7), P. 226–232.

[42] Abdo T., Mohd M., Farooqui M., Maqdoom F. Studies on the isotherms, kinetics and thermodynamics of adsorption of crystal violet on low cost materials. *Journal of advanced scientific research*, 2012, **3** (1), P. 36–44.

[43] Jiancheng S., Renlog L.,et al. Adsorption of methylene blue on modified electrolytic manganse residue: Kinetics, isotherm, thermodynamics and mechanism analysis. *Journal of Taiwan Inst. of Chem. Eng.*, 2018, **82**, P. 351–359.

[44] Jirekar D.B., Ghumare P., Farooqui M. Kinetics and isotherm studies on crystal violet dye adsorption onto black gram seed husk. *Int. Journal of Chemtech research*, 2015, **7** (1), P. 427–434.

[45] Jirekar D.B., Farooqui M. Adsorption of congo red dye from aqueous solution using ecofriendly low cost material prepared from Cicerarientinum. *Arab journal of physical chemistry*, 2015, **2** (1).

[46] Youssef M., Anisa L., et al. Adsorption of methylene blue dye from aqueous solutions onto walnut shell powder: equilibrium and kinetics studies. *Surface and interfaces*, 2018, **11**, P. 74–81.

[47] Sanaz M., Dariush B., Hadi S. Methylene blue removal using modified celery (Apium graveolens) as a low cost biosorbent in batch mode: Kinetic, equilibrium and thermodynamic studies. *Journal of molecular structure*, 2018, **1173**, P. 541–551.

NANOSYSTEMS: PHYSICS, CHEMISTRY, MATHEMATICS, 2021, 12 (2), P. 199–209

Nanostructured tetragonal crystal $NdVO_4$ for the detection of liquefied petroleum gas

D. R. Kamble[1], S. V. Bangale[2*], S. R. Bamane[3]

[1]Department of Chemistry, Shankarrao Mohite Mahavidyalay, Akluj 413 101,
PAH University of Solapur, Maharashtra, India
[2]Department of Chemistry, G. M. Vedak College of Science, Tala 402 111, University of Mumbai, Maharashtra, India
[3]Sushila Shankarrao Mahavidyalay, Khandala, Dist. Satara, shivaji University Kolhapur Maharashtra, India
[*]sachinbangale98@gmail.com

DOI 10.17586/2220-8054-2021-12-2-199-209

Semiconductive nanometer-sized $NdVO_4$ was synthesized by a solution combustion reaction of $Nd(NO_3)_3{\cdot}6H_2O$, $V(NO_3)_3$ and urea as a fuel. The process was a convenient, environment friendly, inexpensive and efficient preparation method for the $NdVO_4$ nanomaterial. Effects of the 800 °C calcining temperature on the phase constituents was characterized by TG-DTA, X-ray diffraction (XRD), which was used to confirm the material's structure. The as-prepared samples were further characterized by scanning electron microscopy (SEM) equipped with energy-dispersive X-ray spectroscopy (EDX), and transmission electron microscopy (TEM), to depict the crystallite microstructure. Conductance responses of the nanocrystalline $NdVO_4$ thick film were measured by exposing the film to reducing gases like acetone, ethanol, ammonia (NH_3), and liquefied petroleum gas (LPG). It was found that the sensors exhibited various sensing responses to these gases at different operating temperatures. Furthermore, the sensor exhibited a fast response and a good recovery. The results demonstrated that $NdVO_4$ can be used as a new type of gas-sensing material which has a high sensitivity and good selectivity to Liquefied petroleum gas (LPG).

Keywords: solution combustion reaction, Synthesis, $NdVO_4$ nanoparticles, gas sensor.

Received: 1 February 2021

Revised: 8 March 2021

Final revision: 15 March 2021

1. Introduction

With the growing attention to environmental problems and the increase of standard of living, there are imperative needs for solid state gas sensors with high sensitivity and excellent selectivity, in air quality monitoring. LPG is widely used as a fuel for industrial and domestic purposes. It is one of the potentially proved hazardous gases due to explosive accidents when accidently leaked. It is therefore important to develop a good sensor for the detection of LPG. Gas sensors based on metal oxide semiconductors generally involve a catalytic reaction of the gas or vapor on the surface of sensor. Gas sensors prepared with metal oxides have been used as detectors for some combustible and toxic gases. Rare earth and transition metal oxides are very important materials for use in the advanced technologies such as solid oxide fuel cells, as catalysts, as materials for electrodes and for chemical sensors because of their functional properties. Rare earth metal oxides are very promising for monitoring the environment due to their high sensitivities and appropriate selectivity. Simple metal oxides such as SnO_2, WO_3, $ZeFe_2O_4$, $ZeCo_2O_4$, $MgFe_2O_4$, and TiO_2 are well known for their high sensitivity to changes in the surrounding gas atmosphere, as can be shown by the growing number of papers [1–7]. Gas sensors based on rare earth mixed oxides materials reported mainly focused on detecting ethanol or NO_x. For example: Aono et al. have carried out more systemic research about $SmFeO_3$ and $REFeO_3$ (Re = La, Nd, Sm, Gd, and Dy) detecting NO_2 [8, 9]. Vanadium doped tin dioxides exhibit a higher response towards SO_2 gas, because of their redox activity for SO_2 oxidation to SO_3 [10]. Catalytic additives, such as CuO [11], MoO_3 [12,13] and Fe_2O_3 [14] are known to lower sensor temperature and increase gas response. In spite of so many excellent results, experimental studies combining electrical with spectroscopic measurements to elucidate sensing mechanisms are still rather limited [15].

The mixed metal oxide materials are well known for their good stability, low cost and catalytic activity. Mixed metal oxides such as Co, Zn, and Ni, along with rare earths like La and Ce, are reported to be synthesized by sol-gel auto combustion method [16]. For these nanomaterials, the size of the particles becomes smaller as the ratio of total surface area to volume increases, which can affect many physical, chemical, mechanical, optical, and magnetic properties of these materials. Vanadates are particularly suitable hosts for luminescent applications. Among the rare earth vanadates, $NdVO_4$ belongs to zircon structure with space group $I4_1/$ amd. It crystallizes in the tetragonal structure, composed of slightly distorted ${VO_4}^{3-}$ tetrahedral and rare earth ion Nd^{3+} between the neighboring tetrahedral. Each Nd^{3+} ion is surrounded by eight oxygen ions. $NdVO_4$ nanoparticles were prepared by wet chemical methods. Au et al. synthesized $NdVO_4$ particles using the citrate method, and their catalytic properties were studied by oxidative

dehydrogenation of propane. The effects of $Eu3^{+}$ doping on morphology and fluorescent properties of neodymium vanadate nanorod-arrays were studied [17,18]. Fan et al. synthesized single crystalline tetragonal nanorods of $NdVO_4$ through hydrothermal method and explained the growth mechanism [19]. The synthesis of $NdVO_4$ nanoparticles by a microwave method and the photocatalytic activity of $NdVO_4$ for degradation of methylene blue were studied [20]. The magnetic susceptibility of single crystal $NdVO_4$ was assessed at temperatures ranging from 10 mK to 300 K [21]. Magnetic properties of $NdVO_4$ particles through temperature dependence magnetic field [22]. $NdVO_4$ nanoparticles have many unique photoelectric properties which could be suggested to use extensively into the fields of X-ray imaging, biological labeling, solid state laser and displays. High ordered $NdVO_4$ nanotubes were fabricated using porous anodized aluminum oxide template (AAO) combined with sol-gel method [23].

Herein, we prepared $NdVO_4$ nanopowder by this simple solution combustion reaction. One of our aims is to develop a general synthesis method and explore the gas sensing properties of the $NdVO_4$ nanopowder obtained. We found that the process is a convenient, environment friendly, inexpensive and efficient for preparation of $NdVO_4$ nanomaterial with the grain size of about 15 – 35 nm. Furthermore, the $NdVO_4$ obtained possessed excellent gas-sensing responses to reducing gas. In the present paper we report the development of thick film $NdVO_4$ LPG sensors.

2. Experimental

2.1. Sample preparation and characterization

In this study polycrystalline $NdVO_4$ powder was prepared via the combustion route using urea as the fuel. The materials used as precursors were $Nd(NO_3)_3{\cdot}6H_2O$, $V(NO_3)_3{\cdot}6H_2O$ and urea (Nuclear band). Urea possesses a high heat of combustion. It is an organic fuel and provides a platform for redox reactions during the course of combustion. Initially the Neodymium Nitrate, Vanadium Nitrate and urea are combined in a 1:1:4 stoichiometric ratio and dissolved in a 250 ml beaker then slowly stirred using a glass rod, providing a clear solution. Solution formed was evaporated on hot plate in temperature range 70 to 80 °C gives thick gel. The gel was kept on a hot plate for auto combustion and heated in the temperature range 180 to 190 °C. The nanocrystalline $NdVO_4$ powder was formed within 40 – 50 minute. And then sintered at about 800 °C for about 4 hours then we obtain a yellow shining powder of nanocrystalline $NdVO_4$.

Neodymium Vanadate oxide powder was ground in an agate mortar and pestle to ensure sufficiently fine particle size. The fine powder was calcined at 800 °C for 24 h in air and re-ground. The thixotropic paste [24, 25] was formulated by mixing the resulting $NdVO_4$ fine powder with a solution of ethyl cellulose (a temporary binder) in a mixture of organic solvents such as butyl carbitol acetate, and turpineol. The ratio of inorganic and organic path was kept as 75:25 in formulating the paste. The paste was then used to prepare thick films. The thixotropic paste was screen printed on a glass substrate in desired patterns. The films prepared were fired at 500 °C for 24 h.

2.2. Characterization techniques

The synthesized $NdVO_4$ nanoparticles are characterized using Thermogravimetric Differential Thermal Analyzer (TG-DTA, PERKIN ELMER, USA, and Diamond TG/DTA). The crystallinity and crystal phase were characterized by X-ray diffraction (XRD, Bruker, D8 – advanced diffractometer) pattern measured with Cu-Kα Radiation ($\lambda = 1.5406$ Å) in the range of 20 – 60 °. The morphology and composition of the synthesized $NdVO_4$ nanoparticles were examined by scanning electron microscopy (SEM, JEOL, JSM-6360), SEM coupled energy dispersive X-ray spectroscopy (EDX, Bruker, XFlash 6130). The exact morphological structure and size of $NdVO_4$ nanoparticles were examined by Transmission Electron Microscopy (TEM) with Selected Area Electron Diffraction (SEAD) by using a Philips, CM 200 with an accelerating voltage of 200 kV. The Fourier Transform Infrared (FT-IR) spectrum was recorded by JASCO 4100 in the range of 4000 – 400 cm^{-1}. The optical properties were measured by UV-Visible Spectrophotometer (JASCO-Spectrophotometer, V-770) and DRS is obtained at the scanning range of 200 – 800 nm.

2.3. Fabrication and analysis of gas sensors

The sensing performance of the sensors was examined using a static gas-sensing system. There were electrical feeds through the base plate. The heating was constant on the base plate to heat the sample under test up to required operating temperatures. The current passing through the heating element was monitored using a relay with adjustable ON/OFF time intervals. A Cr–Al thermocouple was used to sense the operating temperature of the sensors. The output of the thermocouple was connected to digital temperature indicators. A gas inlet valve was fitted at one port of the base plate. The required gas concentration inside the static system was achieved by injecting a known volume of test gas using a gas-injecting syringe. A constant voltage was applied to the sensors, and current was measured by a digital Pico-ammeter. Air was allowed to pass into the glass dome after every gases exposure cycle in shown Fig. 1.

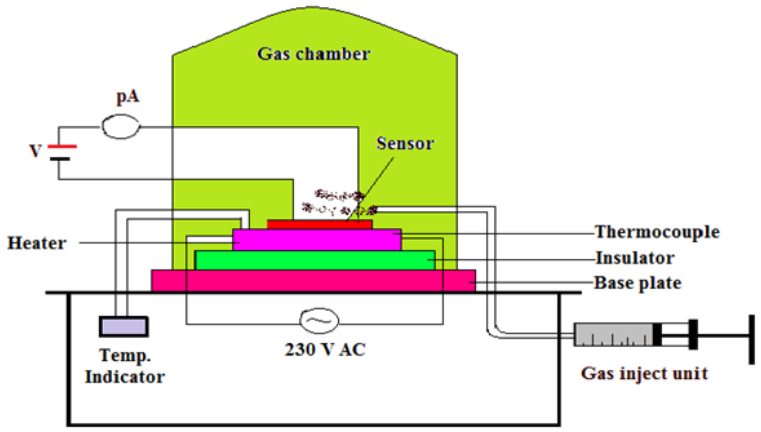

FIG. 1. Block diagram of static gas sensing setup

3. Result and discussion

3.1. TG-DTA analysis

When reactants were heated at 180 °C the reaction proceeded by the mechanism indicated in Eq. (1.1) to give the final product $NdVO_4$.

$$Nd(NO_3)_3 + V(NO_3)_3 + 4CON_2H_4 \rightarrow NdVO_4 + 4CO_2 \uparrow + 8H_2O \uparrow + 5N_2 \uparrow. \quad (1)$$

The TG curve recorded for thermal decomposition of $NdVO_4$ is shown in Fig. 2. The curve indicates that the slight weight loss in $NdVO_4$ powder was due to little loss of moisture, carbon dioxide and nitrogen gas. The DTA curve of $NdVO_4$ recorded in static air and shown in Fig. 2. The curve shows that $NdVO_4$ did not decompose, but weight loss was due to dehydrogenation, decarboxylation and denitration and yield final product at 800 °C. This weight change in the synthesized powder was stable from the beginning.

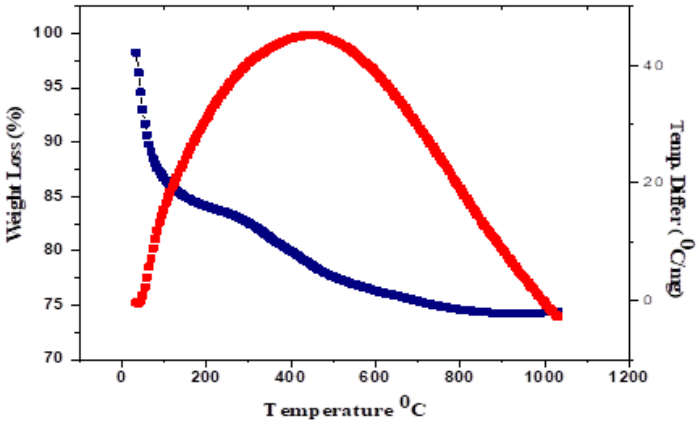

FIG. 2. TG-DTA curve of mixed precursor $NdVO_4$

3.2. XRD analysis

The synthesis of $NdVO_4$ was confirmed by characteristic peaks observed in the XRD pattern as shown in Fig. 2. Such a powder XRD was carried out using monochromatic CuKα-1 radiation (wavelength = 1.5406 Å) operating at a voltage of 40 KV and a current of 40 mA in the angular range 2θ of 20 – 60 degree. XRD analysis showed a series of diffraction peaks at 24.18, 32.84, 34.60, 39.39, 48.40 and 49.78° corresponding to (200), (112), (220), (301), (312) and (400) crystal planes of tetragonal $NdVO_4$ nanostructures (JCPDS No. 82-1971). The sharp XRD peaks exposed for synthesized $NdVO_4$ nanoparticles are good crystalline in nature and show tetragonal structure with lattice constants

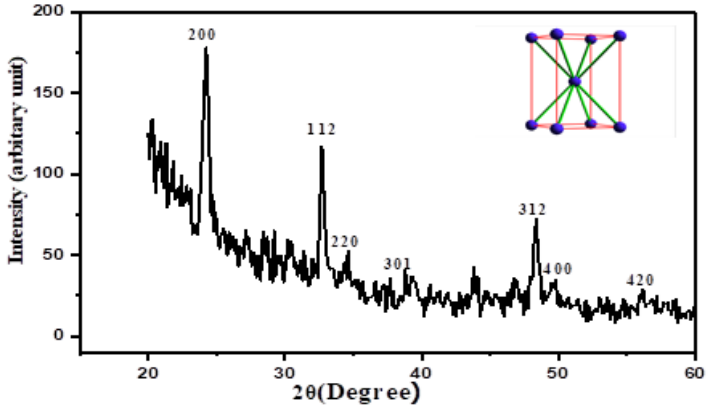

FIG. 3. XRD pattern of calcinied mixed precursor $NdVO_4$ at 800 °C

$a = b = 7.32$ Å and $c = 6.42$ Å which are in good agreement with standard values of $a = b = 7.33$ Å and $c = 6.43$ Å which is shown in Fig. 3.

$$K = \frac{0.9\lambda}{\beta \cos\theta}. \tag{2}$$

Crystallite size was calculated by using Debye–Scherer's Formula by using Eq. (2). It was found to be 27 nm.

3.3. FT-IR analysis

The functional groups of synthesized $NdVO_4$ nanoparticles analyzed by FT-IR spectra recorded in the region of 400 – 4000 cm^{-1} are shown in Fig. 4. A sharp peak at 446 cm^{-1} is due to stretching vibrations of VO_4 [26]. A broad peak at 798 cm^{-1} is attributed to V–O vibrations of VO_4 [27]. A broad peak at 3433 cm^{-1} is easily assigned to O–H stretching vibrations from adsorbed water on the surface of $NdVO_4$ [28].

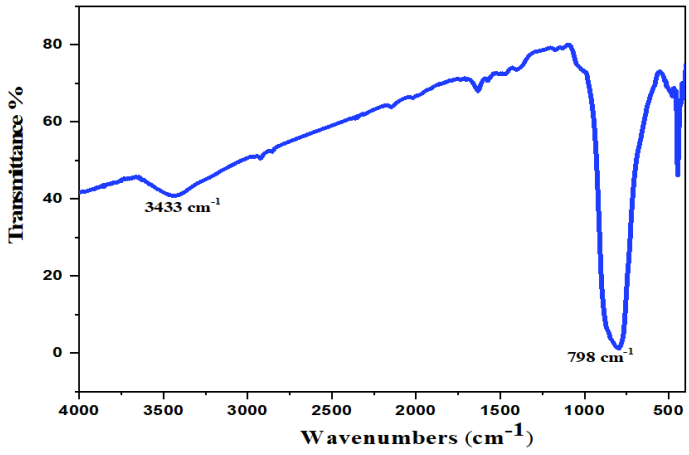

FIG. 4. FTIR spectra of synthesized $NdVO_4$ nanoparticles

3.4. SEM analysis

Morphologies and sizes of synthesized $NdVO_4$ nanoparticles were examined by SEM techniques. These micrographs reveal micro structural aspects related to size and morphology of particles or grains and pores at the sintering temperature 800 °C. The sample showed micro structural aspects of initial stage of the solid state sintering (SSS) process. Most of the $NdVO_4$ nanoparticles were linked to adjacent particles forming a neck between particles and interconnected network of tortuous porous channels (open porosity) in Fig. 5(a, b, c, d). It was seen that the $NdVO_4$ powder has smooth morphologies and developed grain size. A random distribution and agglomeration of particles was observed. The average particle size is 40 to 80 nm.

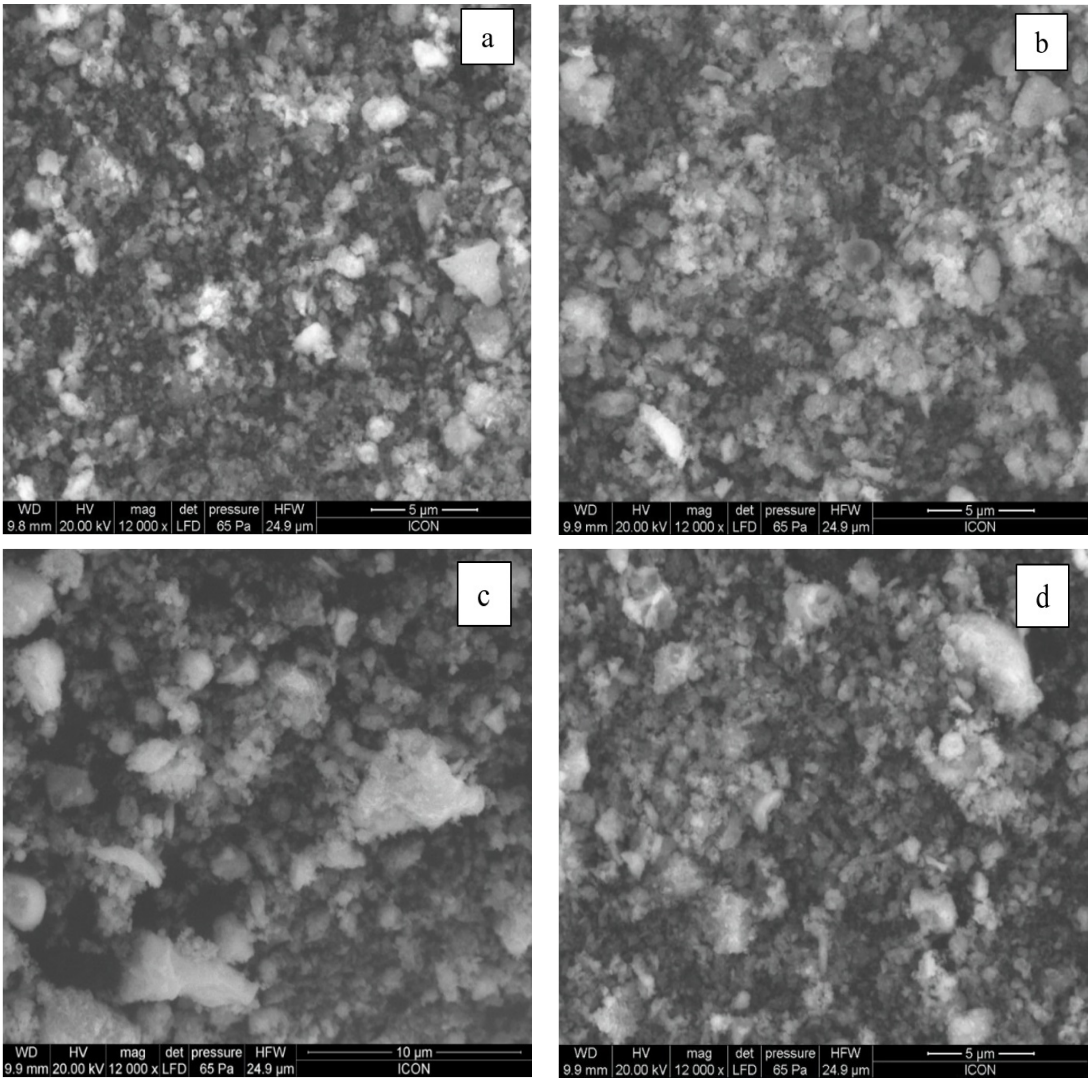

FIG. 5. SEM images of synthesized $NdVO_4$ nanoparticles sintered at 800 °C for 4 hrs

3.5. EDX analysis

The composition of the synthesized nanoparticles was analyzed by investigating the Energy Dispersive X-ray Spectroscopy (EDX) as shown in Fig. 6. The sharp peaks corresponds to Nd, V, O elements without impurity and the composition approaches the right stoichiometry of $NdVO_4$.

3.6. TEM analysis

To get a better understanding of the morphology of $NdVO_4$ TEM images were taken (Fig. 7(a, b, c, d)). It indicates the presence of $NdVO_4$ with size 45 – 90 nm which form bead type of aggregation throughout the region, on the contrary the image shows distinct nanoparticles of nearly spherical structure which are correlated well with the XRD results. SAED pattern also shows the spot type pattern which is indicative of the presence of single crystallite particles. No evidence was found for more than one pattern, suggesting the single phase crystalline nature of the material.

3.7. UV-Visible spectrum analysis

UV-Visible spectrum shows (Fig. 8) strong absorption peaks at 280, 593, and 753 nm as shown in Fig. 8 the peak at 280 nm originates from ultraviolet (UV) absorption of VO_4^{3-} ions of $NdVO_4$ nanoparticles while a peak at 593 nm can be attributed to the Nd^{3+} transition of $NdVO_4$ nanoparticles. Extrapolating absorption edge would give band gap energy for $NdVO_4$ nanoparticles which is 3.50 eV. Due to wide band gap $NdVO_4$ is a UV active material.

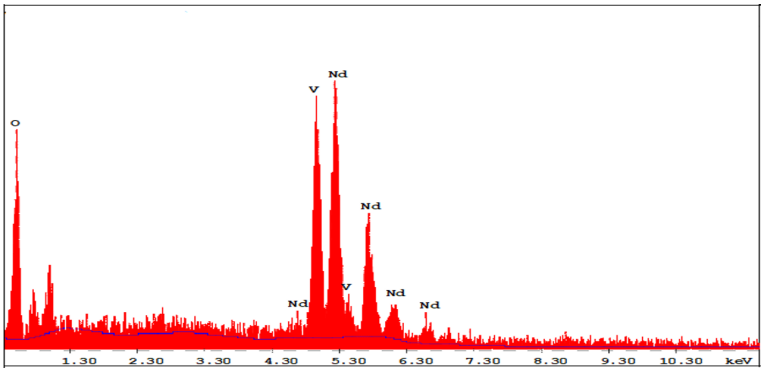

FIG. 6. EDX pattern synthesized $NdVO_4$ nanoparticles sintered 800 °C for 4 hrs

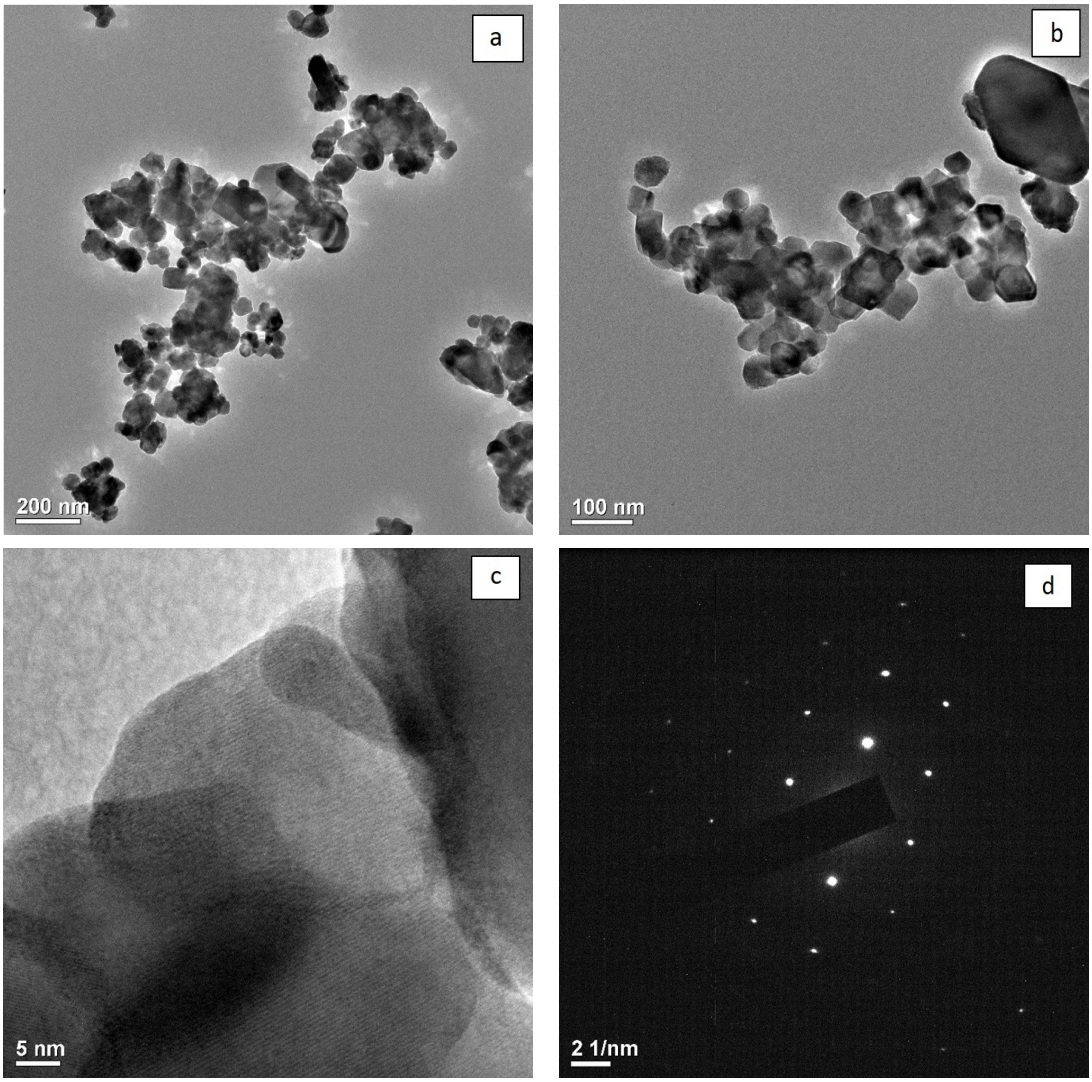

FIG. 7. TEM image with SAED pattern of synthesized $NdVO_4$ nanoparticles

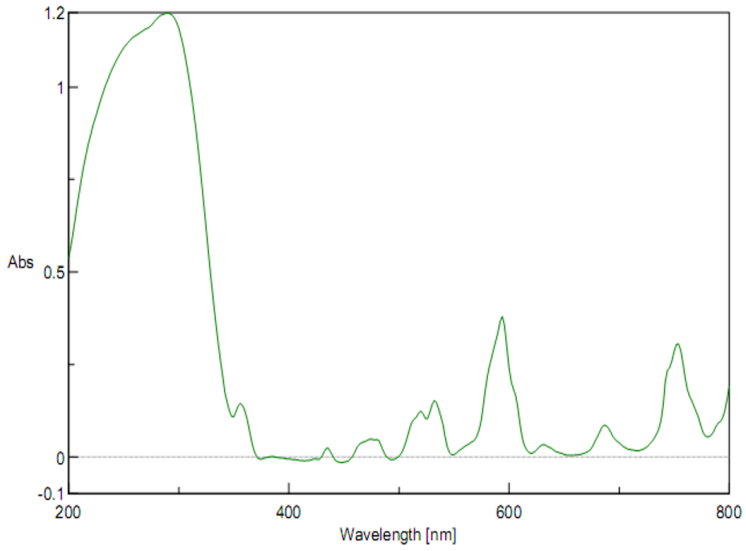

FIG. 8. UV-Visible spectrum (DRS) of $NdVO_4$ nanoparticles

4. Electrical properties of sensor

4.1. I–V characteristics

Figure 9 depicts I–V characteristics of $NdVO_4$ films. It is clear from the symmetrical I–V characteristics that the silver contacts on the films were ohmic in nature. The voltage applied was in the range 1 – 30 V.

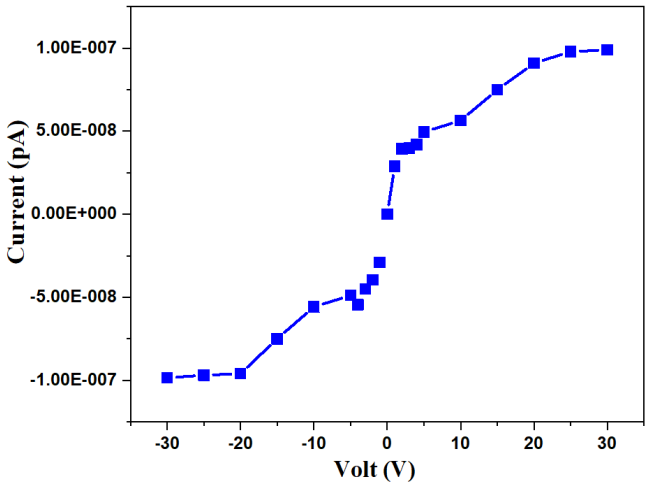

FIG. 9. I–V characteristics of the $NdVO_4$ film

4.2. Electrical conductivity

Figure 10 shows variation of conductivity with temperature. Conductivity values of the sample increases with operating temperature. The increase in conductivity with an increase in temperature is attributed to the semiconducting nature of $NdVO_4$ nanoparticles. It is observed from the Fig. 10 that electrical conductivities of the $NdVO_4$ thick film samples increases with an increase in the temperature range from 25 to 350 °C in air ambient.

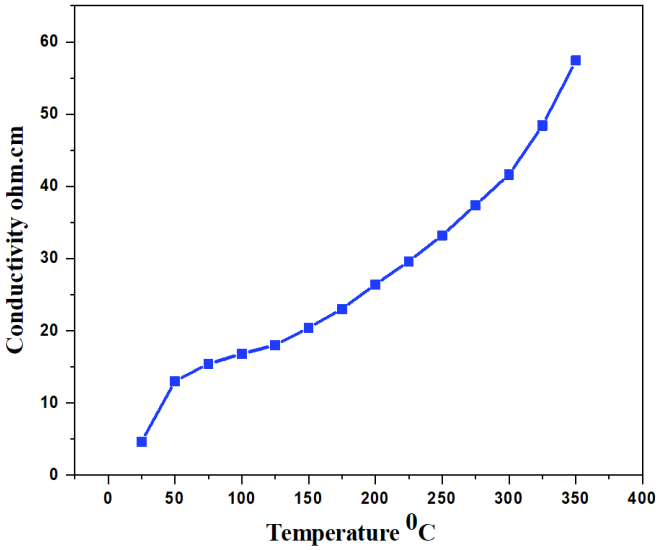

FIG. 10. Conductivity-temperature profiles of $NdVO_4$

5. Sensing performance of sensor

5.1. Gas response, selectivity, response and recovery time

The relative response (S) to a target gas is defined as the ratio of the change in conductance of a sample upon exposure of the gas to the original conductance in air, which can be calculated by fallowing equation:

$$S = \frac{G_g - G_a}{G_a},$$

where G_a – conductance in air and G_g – conductance in a sample gas.

Specificity or selectivity is defined as the ability of a sensor to respond to a certain gas in the presence of different gases. Response time (RST) is defined as the time requires for a sensor to attain 90 % of the maximum increases in conductance on exposure to the target gas.

Recovery time (RCT) is the time taken to get back 90 % of the original conductance in air.

5.2. Sensing performance of $NdVO_4$ thick films. Response of sensors to various gases

The response of $NdVO_4$ sample variation for different gases with operating temperature is represented in Fig. 11. It is clear from the figure that the gas responses goes on increasing and attain to their respective maxima and decreased further with increase in operating temperatures. It is clear from the figure that the $NdVO_4$ shows the largest response to LPG at 275 °C.

5.3. LPG gas response and gas concentration

Figure 12 represents the variation of LPG response with $NdVO_4$ thick film sensor. For $NdVO_4$ thick films the response values were observed to increase continuously with increasing gas concentration up to 1000 ppm at 275 °C. The rate of increase in response was up to 1000 ppm continuously. But there is larger increase in response from 300 to 600 ppm.

5.4. Selectivity factor of $NdVO_4$ for various gases

Figure 13 depicts the selectivity of $NdVO_4$ thick film to 1000 ppm of LPG gas against various gases at 275 °C. It is clear from the Fig. 13. That $NdVO_4$ sensor shows not only enhanced response towards LPG but also high selectivity.

5.5. Response and recovery time

The response and recovery of $NdVO_4$ sensor are the response was quick ($\sim$ 13 s) to 1000 ppm of LPG, while the recovery was fast ($\sim$ 15 s, Fig. 14). The quick response may be due to faster oxidation of gas. The negligible quantity of the surface reaction product and its high volatility explains its quick response and fast recovery to its initial chemical status.

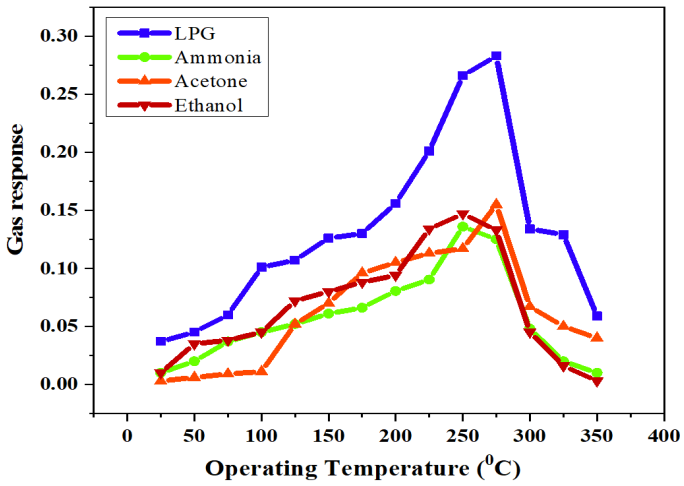

FIG. 11. Variation for different gas responses with operating temperatures

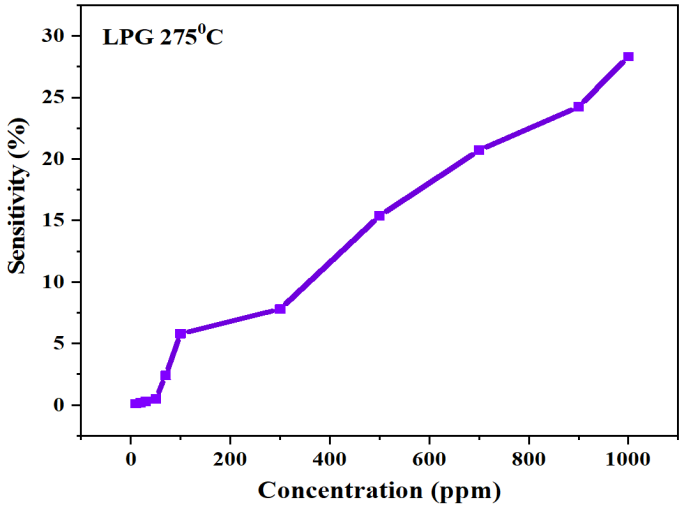

FIG. 12. Variation of gas response with gas concentration

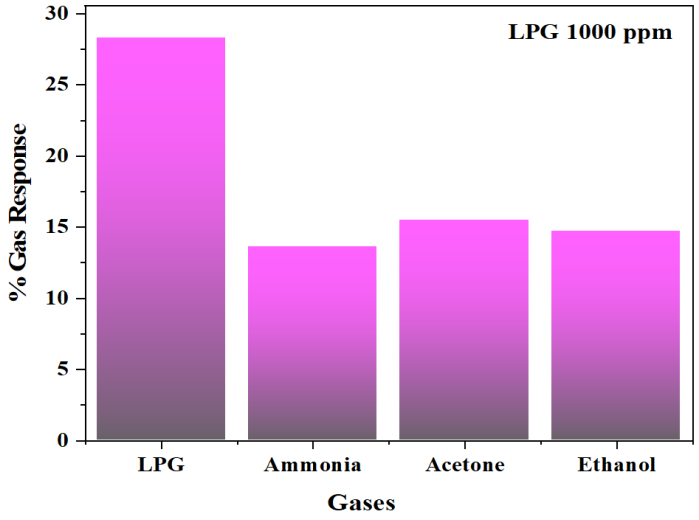

FIG. 13. Selectivity factor of sensor for various gases

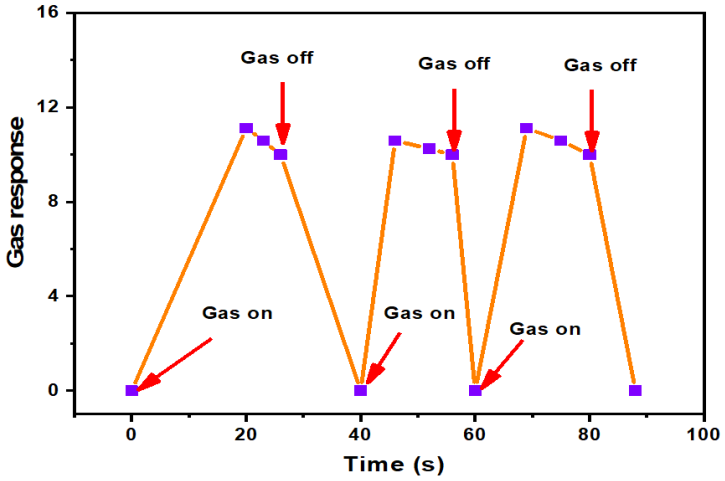

FIG. 14. Variation of gas response with gas concentration

6. Discussion

Gas sensing mechanism is generally explained in terms of conductance either by adsorption of atmospheric oxygen on the surface and/or by direct reaction of lattice oxygen or interstitial oxygen with the test gases. In case of former, the atmospheric oxygen adsorbs on the surface by extracting an electron from conduction band, in the form of super-oxide or peroxides, which are mainly responsible for the detection of the test gases. At higher temperature, the adsorbed oxygen captures the electrons from conduction band as:

$$O_{2(\text{air})} + 4e^- \rightarrow 2O^{2-}_{(\text{film surface})}.$$

It would result in decreasing conductivity of the film. When LPG reacts with the adsorbed oxygen on the surface of the film, it gets oxidized to CO_2 and H_2O by following series of intermediate stage. This liberates free electrons in the conduction band. The final reaction takes place as:

$$C_4H_{10(\text{gas})} + 13O^-_{(\text{film surface})} \rightarrow 4CO_{2(\text{gas})} + 5H_2O_{(\text{gas})} + 13e^-_{(\text{cond. band})}.$$

This shows n-type conduction mechanism. Thus generated electrons contribute to a sudden increase in conductance of the thick film. The $NdVO_4$ misfit regions dispersed on the surface would enhance the ability of base materials to absorb more oxygen species giving high resistance in air ambient. Therefore response was obtained to 1000 ppm LPG.

7. Conclusions

Nanocrystalline $NdVO_4$ has been synthesized by the self-combustion route. This synthetic route may be used for the synthesis of other metal oxide. Among all other additives tested, $NdVO_4$ is outstanding in promoting the LPG gas sensing mechanism. $NdVO_4$ was found to be optimum and showed the highest response to LPG gas at 275 °C. The sensor showed very rapid response and recovery to LPG gas. Sensing mechanism of $NdVO_4$ was the substitution of lattice oxygen by LPG gas. The material gains electrons in this substitution. The sensor has good selectivity to LPG against, Acetone, Ethanol and NH_3.

Acknowledgements

The authors are thankful to Honorable Principal Dr. V. M. Sarode and N. G. Vedak for providing necessary facilities during the research work. We are thankful to CIF Savitribai Phule Pune University, Shivaji University Kolhapur, BIT Bengaluru, SAIF IIT Powai and SAIF IIT Madras for providing the technical, instrumental and supports for this research work. We are also thankful to Nagesh Bhandri for his help during experimental work.

Conflict of interest

The authors declare no conflicts of interest.

References

[1] Kohl D. Surface processes in the detection of reducing gases with SnO_2-based devices. *Sensors Actuators*, 1989, **18**, P. 71–113.

[2] Bangale S.V., Prakshale R.D., Bamane S.R. Nanostructured $CdFe_2O_4$ Thick Film Resistors as Ethanol Gas Sensors. *Sensors & Transducers Journal*, 2012, **146** (11), P. 133–144.

[3] Akiyama M., Yamazoe N. High-temperature potentiometric/amperometric NO_x sensors combining stabilized zirconia with mixed-metal oxide electrode. *Sensors Actuators B*, 1998, **13/14**, 619.

[4] Bangale S.V., Patil D.R., Bamane S.R. Nanostructured spinel $ZnFe_2O_4$ for the detection of chlorine. *Sensors & Transducers Journal*, 2011, **134** (11), P. 107–119.

[5] Bangale S.V., Patil D.R., Bamane S.R. Simple Synthesis of $ZnCo_2O_4$ Nanoparticles as Gas-sensing Materials. *Sensors & Transducers Journal*, 2011, **134** (11), P. 95–106.

[6] Bangale S.V., Bamane S.R. Nanostructured $MgFe_2O_4$ Thick Film Resistors as Ethanol Gas Sensors Operable at Room Temperature. *Sensors & Transducers Journal*, 2012, **137** (2), P. 176–188.

[7] Anand M. Study of tin oxide for hydrogen gas sensor applications. Thesis, University of South Florida, Graduate School, 2005, 98 p.

[8] Aono H., Sato M., Traversa E., et al. Design of Ceramic Materials for Chemical Sensors: Effect of $SmFeO_3$ Processing on Surface and Electrical Properties. *J. Am. Ceram. Soc.*, 2001, **84**, P. 341–347.

[9] Aono H., Traversa E., Sakamoto M., Sadaoka Y. Crystallographic characterization and NO_2 gas sensing property of $LnFeO_3$ prepared by thermal decomposition of Ln–Fe hexacyanocomplexes, $Ln[Fe(CN)_6]\cdot nH_2O$, Ln = La, Nd, Sm, Gd, and Dy. *Sens. Actuators B*, 2003, **94**, P. 132–139.

[10] Das S., Chakraborty S., et al. Vanadium doped tin dioxide as a novel sulfur dioxide sensor. *Talanta*, 2008, **75**, P. 385–389.

[11] Yu J.H., Choi G.M. Selective CO gas detection of CuO- and ZnO-doped SnO_2 gas sensor. *Sens. Actuators B*, 2001, **75**, P. 56–61.

[12] Ansari Z.A., Ansari S.G., Ko T., Oh J.-H. Effect of MoO_3 doping and grain size on SnO_2-enhancement of sensitivity and selectivity for CO and H_2 gas sensing. *Sens. Actuators B*, 2002, **87**, P. 105–114.

[13] Ivanovskaya M., Bogdanov P., et al. On the role of catalytic additives in gas-sensitivity of SnO_2-Mo based thin film sensors *Sens. Actuators B*, 2001, **77**, P. 268–274.

[14] Bose S., Chakraborty S., et al. Methane sensitivity of Fe-doped SnO_2 thick films. *Sens. Actuators B*, 2005, **105**, P. 346–350.

[15] Barsan N., Koziej D., Weimar U. Metal oxide-based gas sensor research: How to? *Sens. Actuators B*, 2007, **121**, P. 8–35.

[16] Kamble D.R., Bangale S.V., Ghotekar S.K., Bamane S.R. Efficient Synthesis of $CeVO_4$ Nanoparticles Using Combustion Route and Their Antibacterial Activity. *J. Nanostruct.*, 2018, **8** (2), P. 144–151.

[17] Yi Zhao, Mingwang Shao, et al. Hydrothermal synthesis of lanthanide orthovanadate: $EuVO_4$ particles and their fluorescence application. *Cryst.Eng.Comm.*, 2012, **14**, P. 8033–8036.

[18] Tian Li, Chen Shan-min, et al. Effect of Eu^{3+}-doping on morphology and fluorescent properties of neodymium vanadate nanorod-arrays. *Transactions of Nonferrous Metals Society of China*, 2020, **30**, P. 1031–1037.

[19] Amarilla J.M., Casal B., Ruiz-Hitzky. Synthesis and characterization of the new mixed oxide $NbVO_5$. *Mater. Let.*, 1989, **8**, 132.

[20] Parag A., Deshpande P.A., Giridhar M. Photocatalytic degradation of dyes over combustion-synthesized $Ce_{1-x}Fe_xVO_4$. *Chemical Engineering Journal*, 2010, **185**, P. 571–577.

[21] Suzuki H., Masuda Y., Miyamoto M. Magnetic and Specific Heat Studies of $NdVO_4$. *J. Phys. Soc. Jpn.*, 1983, **52**, 250.

[22] Saji H., Yamadaya Y., Asanuma M. Magnetic Properties of RXO_4 System. *J. Phys. Soc. Jpn.*, 1970, **28**, 913.

[23] Peng X.N., Zhang X., Yu I., Zhou I. Phase relations and optoelectronic characteristics in the $NdVO_4$–$BiVO_4$ system. *Mod. Phys. Lett. B*, 2013, **22**, 2647.

[24] Bangale S.V., Prakshale R.D., et al. A New Hydrogen Sensor with Nanostructured Zinc Magnesium Oxide. *Sensors & Transducers Journal*, 2012, **137** (2), P. 176–188.

[25] Khamkar K.A., Bangale S.V., et al. A Novel Combustion Route for the Preparation of Nanocrystalline $LaAlO_3$ Oxide Based Electronic Nose Sensitive to NH_3 at Room Temperature. *Sensors & Transducers Journal*, 2012, **146** (11), P. 145–155.

[26] Mahapatra S., Madras T., Guru T.N. Row Kinetics of photoconversion of cyclohexane and benzene by $LnVO_4$ and $LnMo_{0.15}V_{0.85}O_4$ (Ln = Ce, Pr and Nd). *Ind. Eng. Chem. Res.*, 2007, **46**, 1013.

[27] Amarilla J.M., Casal B., Ruiz-Hitzky E. Synthesis and characterization of the new mixed oxide $NbVO_5$. *Mater. Lett.*, 1989, **8**, P. 132–136.

[28] Ekthammathat N., Thongtem T., Phuruangrat A., Thongtem S. Synthesis and Characterization of $CeVO_4$ by Microwave Radiation Method and Its Photocatalytic Activity. *J. Nanomater.*, 2013, **1**, 434197.

NANOSYSTEMS: PHYSICS, CHEMISTRY, MATHEMATICS, 2021, 12 (2), P. 210–217

Synthesis of Ce:YIG nanopowder by gel combustion

M. N. Smirnova[1], I. S. Glazkova[2], G. E. Nikiforova[1], M. A. Kop'eva[1], A. A. Eliseev[2], E. A. Gorbachev[2], V. A. Ketsko[1]

[1]Kurnakov Institute of General and Inorganic Chemistry of the Russian Academy of Sciences, 119991, 31 Leninsky Prospect, Moscow, Russia

[2]Department of Chemistry, Lomonosov Moscow State University 119234, 1 Leninskie Gory, Moscow, Russia

smirnovamn@igic.ras.ru, janglaz@bk.ru, gen@igic.ras.ru, mkopieva@mail.ru, artem.a.eliseev@gmail.com, gorbach.ev.genij@gmail.com, ketsko@igic.ras.ru

PACS 61.46.+w **DOI 10.17586/2220-8054-2021-12-2-210-217**

Nanocrystalline Ce-substituted yttrium iron-gallium garnet $Y_{2.5}Ce_{0.5}(Fe_{0.5}Ga_{0.5})_5O_{12}$ was obtained by a metal-organic gel combustion method using PVA as a fuel with subsequent calcining in vacuum at 700 °C. According to SEM and XRD data, an additional heat treatment in air led only to an increase in the crystallinity of the sample. The element composition and the phase purity were confirmed by X-ray fluorescence spectroscopy and X-ray powder diffraction, respectively. Mössbauer spectroscopy on ^{57}Fe nuclei revealed the presence of only Fe^{3+} ions in the sample, which can be considered as indirect evidence of the absence of tetravalent cerium impurity.

Keywords: gel combustion, ferrites, cerium yttrium iron garnet, nanoparticles.

Received: 21 January 2021

Revised: 22 March 2021

1. Introduction

For a number of years, ferrite-garnets have been the subject of numerous studies [1–7]. Interest in this class of compounds is due to their unique magnetic and magneto-optical properties [1–3]. The presence in the crystal lattice of three different crystallographic positions (dodecahedral, tetrahedral, octahedral) and the tendency of garnets to undergo isomorphic substitution allows changing their physicochemical and functional characteristics within wide limits [3].

One of the most well known ferrite garnets is yttrium iron garnet (YIG) – $Y_3Fe_5O_{12}$, which is used in microwave technology because of the extremely narrow ferromagnetic resonance absorption line [2]. According to theoretical estimates, replacing Y^{3+} in YIG with Ce^{3+} enhances magneto-optical activity in the visible and near infrared ranges [4–8], reduces optical power losses (attenuation of the light signal) [8], and helps to lower the crystallization temperature of garnet. These factors expand the possible areas of application of materials based on YIG for the creation of new generation magneto-optical devices [3–5].

However, the possibility of replacing Y^{3+} with Ce^{3+} in garnet has structural limitations. Since the effective ionic radius of Ce^{3+} (1.14 Å) is larger than the radius of yttrium Y^{3+} (1.02 Å) [9], with an increase in the cerium concentration, internal stresses and structural distortions of the crystal are induced [10]. This problem can be solved by the introduction of smaller ions (for example, Al^{3+} or Ga^{3+} cations) into YIG together with Ce^{3+}, which makes it possible to compensate for structural limitations and promotes the formation of garnet of a given composition [11–14]. The literature contains data on the preparation of Ce:YIG ceramics without replacing Fe^{3+} with other cations, but in these studies, the cerium content in garnet did not exceed 8 %, for example, $Ce_{0.122}Y_{2.878}Fe_5O_{12}$ [5], $Ce_{0.15}Y_{2.85}Fe_5O_{12}$ [14], $Ce_{0.25}Y_{2.75}Fe_5O_{12}$ [4].

Another factor limiting the solubility of cerium in YIG is the tendency of Ce^{3+} to oxidize and transform into a diamagnetic tetravalent state. Huang et al. [5] considered the possibility of increasing the concentration of Ce^{3+} ions in the YIG structure and "suppressing" the formation of nonmagnetic Ce^{4+} ions by means of charge compensation due to the introduction of Eu^{3+} ions into the dodecahedral yttrium positions. Nevertheless, the maximum possible content of Ce^{3+} in this case did not exceed 12 %, $Ce_{0.349}Eu_{0.195}Y_{2.456}Fe_5O_{12}$.

Another significant problem is the necessity of using high processing temperatures in the synthesis of polycrystalline Ce-substituted garnets by the solid-state reactions [4–6]. High-temperature annealing in an oxidizing atmosphere inevitably leads to partial oxidation of Ce^{3+} and the formation of a stable CeO_2 impurity that does not possess magnetic ordering, which impairs the magnetic and magneto-optical properties of YIG.

Previously, Opuchovic et al. [15] tried to solve the problem of CeO_2 formation by annealing the precursor obtained during the synthesis of $Y_{3-x}Ce_xFe_5O_{12}$ by the sol-gel method in a reducing atmosphere of CO. However, this treatment prevented not only the formation of CeO_2, but also the formation of the garnet itself. The main phase for all

compositions was perovskite. In the Y–Fe–O system, the perovskite structure is energetically more favorable and is formed at lower temperatures [16]. On the contrary, in the yttrium-gallium oxide system, the preparation of perovskite is extremely difficult [17]. Thus, the partial substitution of gallium for iron ions, which allows stabilizing the garnet structure, together with the use of an oxygen-deficient calcination atmosphere, may be promising for the production of Ce:YIG with a higher degree of substitution.

In this regard, our studies were aimed at studying $Y_{3-x}Ce_x(Fe_{1-y}Ga_6)_5O_{12}$ solid solutions in order to obtain a composition with the highest possible substitution of Ce^{3+} for Y^{3+} in the absence of tetravalent cerium impurities in the resulting garnet.

For the synthesis of the samples, the method of the gel combustion was chosen [12, 13], the advantages of which are largely associated with the short duration of the high-temperature stage of decomposition of the gel-like precursor, which contributes to the relatively rapid formation of the crystalline phase, hinders the formation of undesirable impurities and makes it possible to obtain nanosized polycrystalline powder materials [17–21]. Nitrates of the yttrium, cerium, iron, gallium and polyvinyl alcohol (PVA) were used as starting reagents for the preparation of $Y_{3-x}Ce_x(Fe_{1-y}Ga_y)_5O_{12}$ garnets. The efficiency of PVA application for the synthesis of cation-substituted garnets by gel combustion was shown earlier [12, 20, 22]. Due to the hydrophilic OH groups, polyvinyl alcohol ensures the complexation process, which contributes to the uniform distribution of hydrated metal cations in the gel structure, prevents segregation and the formation of undesirable individual oxide compounds during solution evaporation.

Particular attention was paid to the creation of oxygen-deficient conditions during heat treatment of the samples to reduce the probability of the oxidation of Ce^{3+} ions to Ce^{4+}. In this regard, the calcination of the samples immediately after synthesis was carried out in vacuum.

2. Experimental

2.1. Synthesis procedure

Aqueous solutions of yttrium, cerium, iron and gallium nitrates were prepared separately for each sample by dissolving stoichiometric amounts of yttrium carbonate trihydrate ($Y_2(CO_3)_3 \cdot 3H_2O$, > 99.9 %), cerium nitrate hexahydrate ($Ce(NO_3)_3 \cdot 6H_2O$, > 99.8 %), carbonyl iron powder (Fe, > 99.99 %) and metallic gallium (Ga, > 99.99 %) in dilute nitric acid. Polyvinyl alcohol (PVA) was added to the resulting solution at the ratio of 0.12 mol of $(CH_2CHOH)_n$ per 0.01 mol of garnet.

The reaction mixtures were evaporated in porcelain bowls on a hotplate with constant stirring until gels were formed. With a further increase in temperature to 100 °C, the gels burned and turned into fine powders, the color of which varied from yellow-beige to brown. After cooling, the powders were dispersed with a ball mill and annealed at 700 °C in an oven for 2 hours at a pressure of about 10^{-2} Pa.

2.2. Characterization of the samples

X-ray powder diffraction (XRD) was performed using a Bruker D8 Advance diffractometer equipped with Ni-filtered ($CuK_{\alpha 1}$-radiation) and a LYNXEYE detector in the angle range $2\theta = 10^\circ - 70^\circ$ with a scanning step of 0.0133° and a counting time of 0.3 s per step. The results of XRD experiments were interpreted using the Bruker DIFFRAC.EVA software package and the ICDD PDF-2 database.

The chemical composition of the samples was determined using a Bruker M4 TORNADO μ-X-ray fluorescence spectrometer equipped with a Rh-anode X-ray tube with a polycapillary lens. The accuracy of μ-XRF analysis was ± 5 %.

The surface morphology and microstructure of $Y_{3-x}Ce_x(Fe_{1-y}Ga_y)_5O_{12}$ were investigated using a Carl Zeiss NVision 40 scanning electron microscope (SEM). SEM micrographs were obtained with an Everhart–Thornley secondary electron (SE2) detector.

The specific surface area of sample obtained was measured by the low-temperature nitrogen adsorption method using a Katakon ATKh-06 analyzer. Before measurements, the sample was degassed in a nitrogen flow at 200 °C for 60 min. The specific surface area of the sample S_{BET} was calculated using the Brunauer–Emmett–Teller (BET) model at 5 points in the range of partial pressures of 0.05 – 0.25 P/P_0.

^{57}Fe Mössbauer spectra were measured using a conventional constant-acceleration MS-110Em spectrometer. To analyze the Mössbauer data, we used the methods of model interpretation and reconstruction of the distribution of hyperfine parameters, implemented in the SpectrRelax software [23]. Isomer shifts of the ^{57}Fe Mössbauer spectra are given relative to α-Fe at 298 K.

3. Results and discussion

The effect of oxygen-deficient heat treatment conditions on the formation of the garnet structure was studied on the samples of the $Y_{2.8}Ce_{0.2}Fe_{5-y}Ga_yO_{12}$ solid solution with different contents of iron and gallium, synthesized by the gel combustion method followed by annealing in vacuo at 700 °C. The X-ray diffraction patterns (Fig. 1) show that in the absence of gallium dopant ($y = 0$), both garnet and perovskite crystalline phases are formed in almost equal amounts. In this case, cerium atoms were not incorporated into any of the structures, but formed a cubic solid solution based on yttrium oxide $(Y,Ce)_2O_{3+\delta}$. When a small amount of gallium ($y = 1$) was added to the composition, the crystalline phase of garnet became the main one. However, the X-ray diffraction patterns retained a small number of additional reflections, which completely disappeared only for the composition with $y = 2.5$.

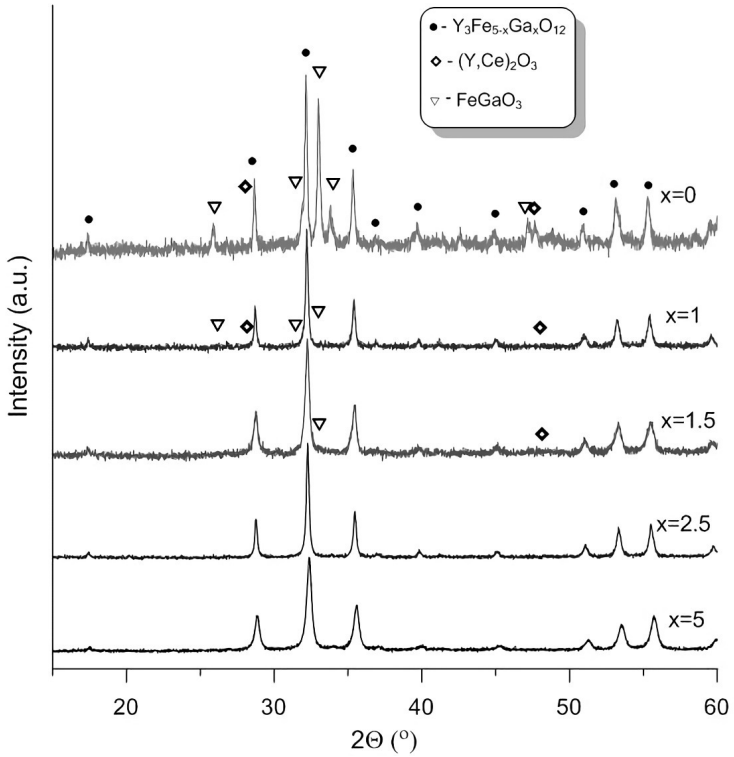

FIG. 1. XRD patterns of $Y_{2.8}Ce_{0.2}Fe_{5-y}Ga_yO_{12}$ powders prepared by vacuum heat treatment at 700 °C for 2 h

Thus, the results of this experiment allow us to conclude that, when Fe^{3+} ions are replaced by Ga^{3+}, the garnet structure is more stable than perovskite not only in air, but also in an oxygen-deficient atmosphere. In addition, the presence of Ga^{3+} ions compensates for the crystal stresses in the garnet structure arising from the substitution of Ce^{3+} for Y^{3+}. To further study the incorporation of cerium ions into the garnet structure, a composition with 50 % substitution of gallium for iron was chosen.

The X-ray powder diffraction of Ce-substituted garnets $Y_{3-x}Ce_x(Fe_{0.5}Ga_{0.5})_5O_{12}$ annealed in vacuum at 700 °C (Fig. 2) showed that, with the partial substitution of cerium for yttrium, the homogeneity of the garnet phase was retained only up to the cerium content $x = 0.5$. A further increase in the amount of cerium in the nominal composition of the samples led to the appearance of diffuse reflections in the XRD patterns, which could be attributed to the formation of a cerium dioxide impurity. The incorporation of cerium ions into the garnet structure and the formation of a solid solution could be confirmed by a monotonic change in the crystal lattice parameter a from 12.346(2) to 12.397(1) Å as the cerium content increased to $x = 0.5$.

The ratio of cations in the $Y_{2.5}Ce_{0.5}(Fe_{0.5}Ga_{0.5})_5O_{12}$ sample was confirmed by X-ray fluorescence analysis and energy-dispersive X-ray spectroscopy. Both methods showed that the composition of the studied sample was close to the theoretical one within the experimental error (Fig. 3, Table 1).

Figure 4 shows SEM images of $Y_{2.5}Ce_{0.5}(Fe_{0.5}Ga_{0.5})_5O_{12}$ garnet obtained in an oxygen-deficient atmosphere. After vacuum heat treatment, the sample consists of tightly "pressed" large agglomerates, forming almost monolithic plates. At the fracture site, these agglomerates of indefinite shape have a porous spongy structure. With such sample

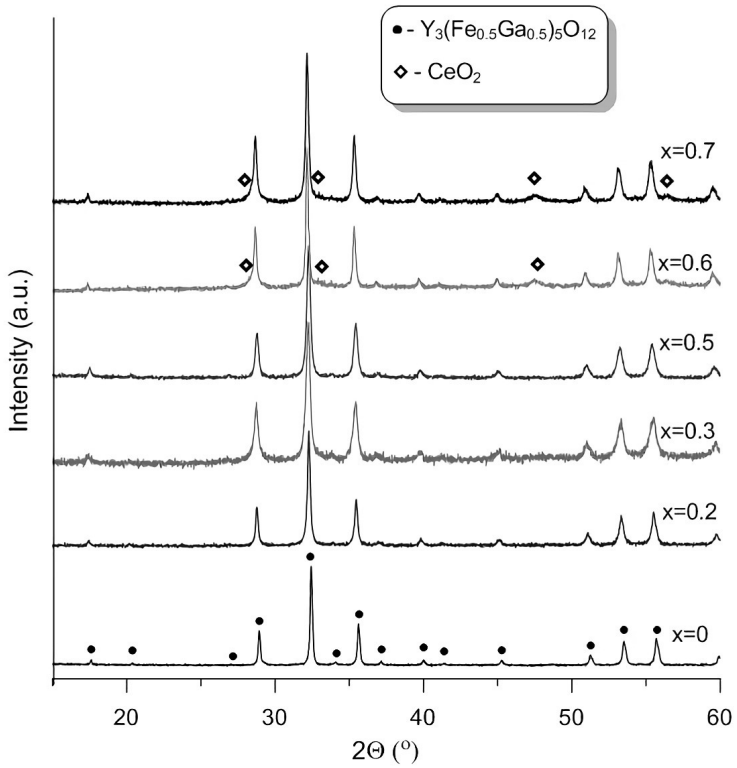

FIG. 2. XRD patterns of $Y_{3-x}Ce_x(Fe_{0.5}Ga_{0.5})_5O_{12}$ powders prepared by vacuum heat treatment at 700 °C for 2 h

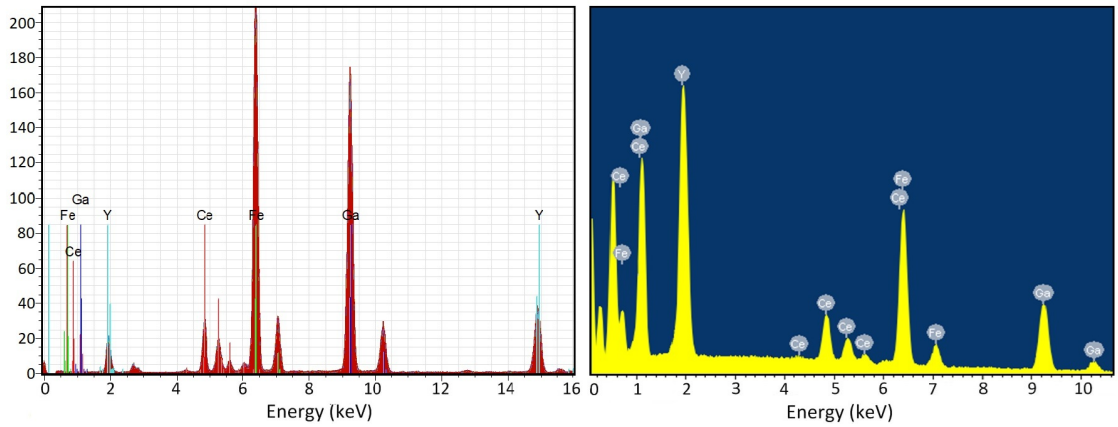

FIG. 3. μ-XRF and EDS spectra of $Y_{2.5}Ce_{0.5}(Fe_{0.5}Ga_{0.5})_5O_{12}$ nanopowder

morphology, there is a possibility that some of the Ce^{3+} ions are not incorporated into the garnet structure and are present in the sample as an amorphous impurity. Additional annealing in air at a higher temperature should promote the oxidation of unbound cerium and its transition to the tetravalent state.

After heat treatment in vacuum, the $Y_{2.5}Ce_{0.5}(Fe_{0.5}Ga_{0.5})_5O_{12}$ sample was additionally calcined in air at 800 °C for 5 hours. SEM images (Fig. 5) show that the surface of the plates did not change, however, the morphology of the sample underwent significant changes on the spalls. Each plate consists of small monodisperse randomly located particles, 70 – 80 nm in size, forming a porous structure resembling an openwork fabric. This morphology of the sample is associated with the use of the gel combustion method for its preparation. The main stage of this process is the combustion of the organometallic gel, accompanied by the removal of gaseous pyrolysis products, which contributes to the dispersion of the precursor and the formation of a highly dispersed final powder.

TABLE 1. Results of μ-XRF and EDS studies of $Y_{2.5}Ce_{0.5}(Fe_{0.5}Ga_{0.5})_5O_{12}$ nanopowder

Element	wt. %		
	Theoretical value	Observed value	
		μ-XRF	EDS
Y	36.66	36.41	36.46
Ce	11.56	11.43	11.78
Fe	23.03	23.23	22.94
Ga	28.75	28.93	28.82

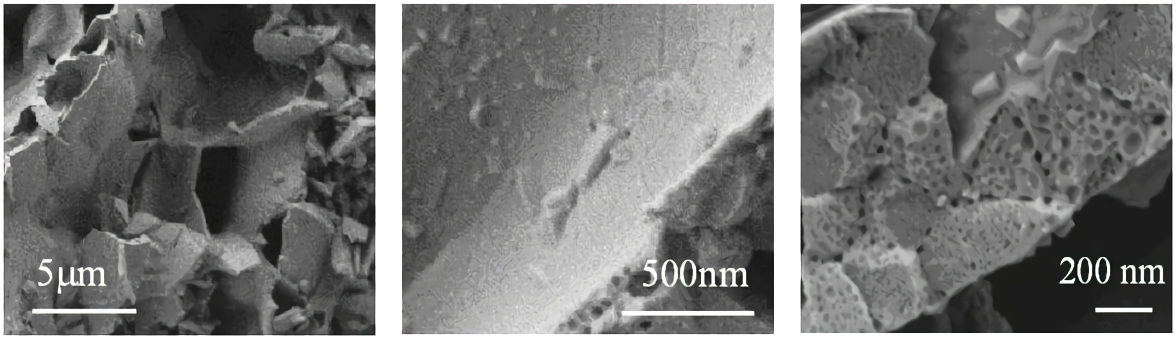

FIG. 4. SEM images of $Y_{2.5}Ce_{0.5}(Fe_{0.5}Ga_{0.5})_5O_{12}$ nanopowder after vacuum heat treatment at 700 °C, obtained at different magnifications

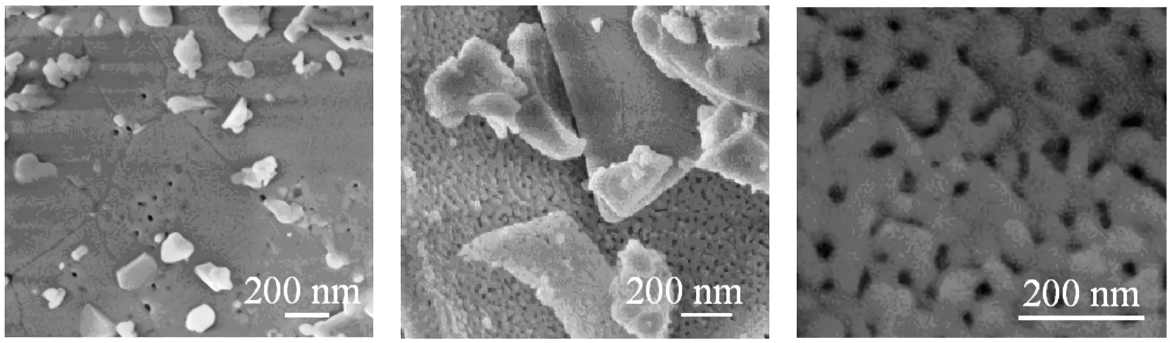

FIG. 5. SEM images of $Y_{2.5}Ce_{0.5}(Fe_{0.5}Ga_{0.5})_5O_{12}$ nanopowder after annealing in air at 800 °C, obtained at different magnifications

According to X-ray diffraction data, the sample after annealing in air remained single-phase; no reflections of impurity phases were recorded. The results of a full-profile analysis of the XRD data of the $Y_{2.5}Ce_{0.5}(Fe_{0.5}Ga_{0.5})_5O_{12}$ powder additionally annealed in air at 800 °C are shown in Fig. 6. The sample has a cubic garnet structure ($Ia-3d$) with the parameters: $a = 12.397$ Å, $V = 1905.2$ Å^3.

The size of the coherent scattering domains, taken as the average particle size, was calculated using the Scherrer equation and amounted to 67 nm. This value, calculated from the broadening of the X-ray lines, agrees very well with the particle size observed by SEM.

The specific surface area (S_{BET}) of the $Y_{2.5}Ce_{0.5}(Fe_{0.5}Ga_{0.5})_5O_{12}$ nanopowder calculated using the multipoint BET-equation was 9.3 m^2/g. Since the sample consists of monodisperse isotropic particles, the average particle size D_{BET} (nm) can be calculated using the equation:

$$D_{BET} = 6000/(\rho_{cr} \cdot S_{BET}),$$

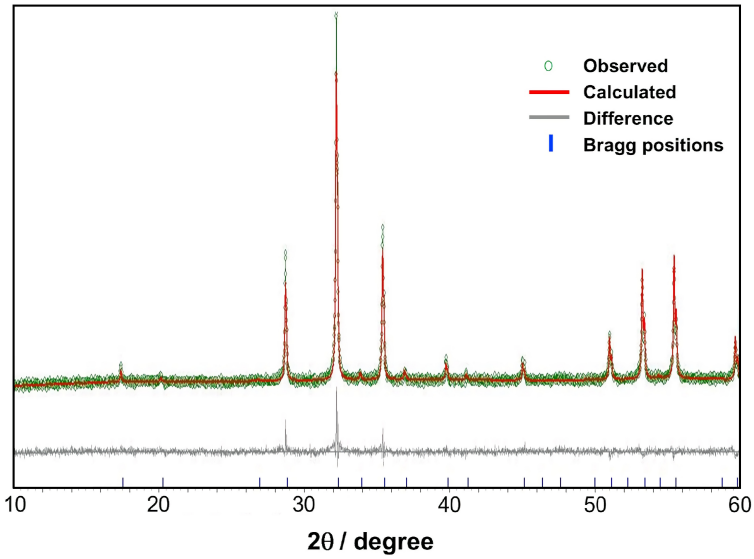

FIG. 6. The Pawley refinement plot of the XRD data for the $Y_{2.5}Ce_{0.5}(Fe_{0.5}Ga_{0.5})_5O_{12}$ nanopowder

where ρ_{cr} is a crystallographic density (5.57 g/cm^3).

The average particle size calculated from BET analysis was 115 nm. This value is greater than the above-mentioned particle sizes determined from the results of SEM and X-ray diffraction. The reason for this may be that some nanoparticles are agglomerated into plates (Fig. 5), which led to an overestimation of the D_{BET} value.

When cerium is incorporated into the garnet structure, cation-cation interactions between octahedral crystallographic positions, in which iron and gallium atoms are located, and dodecahedral crystallographic positions, in which yttrium and cerium atoms are located, are enhanced [24, 25]. This can lead to a redistribution of charges within the crystal structure and a change in the valence state of iron and cerium.

The ^{57}Fe Mössbauer spectra of the $Y_3(Fe_{0.5}Ga_{0.5})_5O_{12}$ and $Y_{2.5}Ce_{0.5}(Fe_{0.5}Ga_{0.5})_5O_{12}$ garnets measured at room temperature represent a complex superposition of two asymmetrically broadened quadrupole doublets (Fig. 7a).

Both spectra resemble those of unsubstituted garnets [26–28] and do not contain magnetically-split components, which confirms the absence of impurity phases like perovskite- or spinel-type ferrites. At the same time, the replacement of some of the iron cations with gallium cations and the replacement of Y^{3+} with Ce^{3+} leads to a significant broadening of the resonance lines. Therefore, the fitting procedure of the spectra was performed by the reconstruction of the distribution of quadrupole doublets taking into account the linear correlation of shifts δ and quadrupole splitting Δ (Fig. 7b). The obtained values of the hyperfine parameters of the spectra (Table 2) show that the iron cations in both garnets are stabilized only in 3+ oxidation state in two nonequivalent sites. This experimental fact indirectly indicates that in the structure of $Y_{2.5}Ce_{0.5}(Fe_{0.5}Ga_{0.5})_5O_{12}$, as a result of the replacement of some of the yttrium atoms with cerium atoms, the latter are not oxidized. It should be noted that the obtained ratio of iron cations in tetrahedral and octahedral positions calculated from the relative partial spectra (I) deviates somewhat from 3:2 ratio given by the structure (Table 2), which indicates a greater preference for gallium atoms in the structures of these garnets for tetrahedral oxygen positions.

4. Conclusions

Here, we present the results of the synthesis and study of a solid solution of cerium-substituted yttrium iron garnet aimed at achieving the maximum possible substitution of Y^{3+} with Ce^{3+}. The replacement of Fe^{3+} ions by Ga^{3+} in a 1:1 ratio and the use of vacuum annealing of the precursor obtained by gel combustion method made it possible to increase cerium content in the garnet structure to 16.7 % relative to yttrium and avoid the formation of CeO_2 impurities.

The study of the $Y_{2.5}Ce_{0.5}Fe_{2.5}Ga_{2.5}O_{12}$ nanopowder by ^{57}Fe Mössbauer spectroscopy showed the presence of iron cations in the structure only in 3+ formal oxidation state, which is an additional confirmation of the phase homogeneity of this composition, as well as indirect evidence of the absence of both CeO_2 impurities and Ce^{4+} ions in the $Y_{2.5}Ce_{0.5}(Fe_{0.5}Ga_{0.5})_5O_{12}$ structure.

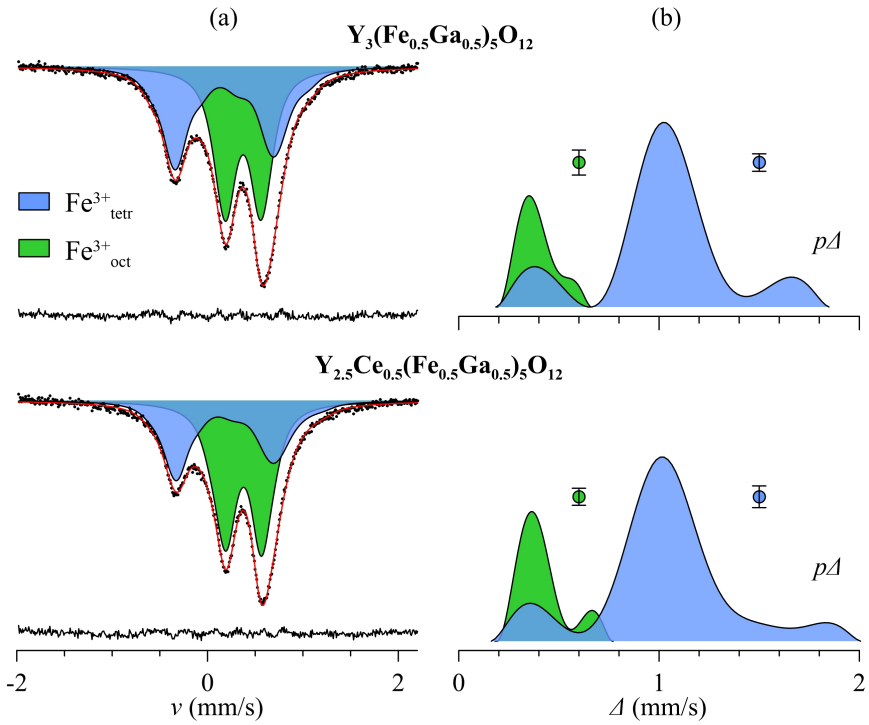

FIG. 7. (a) The ^{57}Fe Mössbauer spectra of $Y_{3-x}Ce_x(Fe_{0.5}Ga_{0.5})_5O_{12}$ ($x = 0, 0.5$) nanopowders measured at $T = 298$ K; (b) the corresponding distributions of the quadrupole splittings $p\Delta$

TABLE 2. The hyperfine parameters of the ^{57}Fe Mössbauer spectra of $Y_{3-x}Ce_x(Fe_{0.5}Ga_{0.5})_5O_{12}$ ($x = 0, 0.5$) nanopowders at $T = 298$ K

Cerium content x	Partial spectrum	δ^* (mm/s)	Δ^* (mm/s)	I (%)
0	Fe^{3+}_{tetr}	0.18(1)	1.02(1)	47.6(5)
	Fe^{3+}_{oct}	0.37(1)	0.39(1)	52.4(5)
0.5	Fe^{3+}_{tetr}	0.18(1)	1.02(1)	40.0(5)
	Fe^{3+}_{oct}	0.38(1)	0.41(1)	60.0(5)

δ – isomer shift; Δ – quadrupole splitting;

I – relative intensity of the corresponding partial spectrum;

* – the mean values of the mean values of δ and Δ was estimated from the distributions $p\delta$ and $p\Delta$.

Thus, low-temperature heat treatment of the samples under vacuum conditions prevents the oxidation of Ce^{3+} to Ce^{4+} and minimizes the probability of CeO_2 formation.

The synthesized nanocrystalline Ce:YIG powder has a developed surface and a monodisperse porous structure, which makes it promising for industrial and technical applications. Optimal conditions for the formation of this morphology of $Y_{2.5}Ce_{0.5}Fe_{2.5}Ga_{2.5}O_{12}$ nanopowder, such as short-term high-temperature combustion of a gel-like precursor with the release of a large amount of gaseous products, were provided by the PVA assisted gel combustion method. The results obtained in this work could be used in the future to develop efficient approaches to the synthesis of functional Ce-containing materials and to improve their properties.

Acknowledgements

This synthesis and study of the samples was supported by the Russian Foundation for Basic Research (project No. 19-08-00643). The measurements were performed using the equipment of the Joint Research Centre (JRC PMR) IGIC RAS supported by IGIC RAS state assignment (Ministry of Education and Science of the country-regionplaceRussian Federation). Mössbauer studies were supported by the Russian Science Foundation (project No. 19-73-10034).

References

[1] Garskaite E., Gibson K., et al. On the synthesis and characterization of iron-containing garnets ($Y_3Fe_5O_{12}$, YIG and $Fe_3Al_5O_{12}$, IAG). *Chemical Physics*, 2006, **323**, P. 204–210.

[2] McCloy J.S., Walsh B. Sublattice Magnetic Relaxation in Rare Earth Iron Garnets. *IEEE Transactions on Magnetics*, 2013, **49** (7), P. 4253–4256.

[3] Park M.B., Cho N.H. Structural and magnetic characteristics of yttrium iron garnet (YIG, Ce:YIG) films prepared by RF magnetron sputter techniques. *Journal of Magnetism and Magnetic Materials*, 2001, **231**, P. 253–264.

[4] Shen T., Dai H., Song M. Structure and Magnetic Properties of Ce-Substituted Yttrium Iron Garnet Prepared by Conventional Sintering Techniques. *Journal of Superconductivity and Novel Magnetism*, 2017, **30**, P. 937–941.

[5] Huang M., Zhang S. Growth and characterization of cerium-substituted yttrium iron garnet single crystals for magneto-optical applications. *Applied Physics A*, 2002, **74**, P. 177–180.

[6] Dastjerdi O.D., Shokrollahi H., Yang H. The enhancement of the Ce-solubility limit and saturation magnetization in the $Ce_{0.25}Bi_xPr_yY_{2.75-x-y}Fe_5O_{12}$ garnet synthesized by the conventional ceramic method. *Ceramics International*, 2020, **46** (315), P. 2709–2723.

[7] Ibrahim N.B., Edwards C., Palmer S.B. Pulsed laser ablation deposition of yttrium iron garnet and cerium-substituted YIG films. *Journal of Magnetism and Magnetic Materials*, 2000, **220**, P. 183–194.

[8] Xu H., Yang H. Magnetic properties of YIG doped with cerium and gadolinium ions. *Journal of Materials Science: Mater Electron*, 2008, **19**, P. 589–593.

[9] Shannon R.D. Revised effective ionic radii and systematic studies of interatomic distances in halides and chalcogenides. *Acta Crystallographica Section A*, 1976, **32**, P. 751–767.

[10] Gilleo M.A., Geller S. Magnetic and crystallographic properties of substituted yttrium-iron garnet, $3Y_2O_3{\cdot}xM_2O_3 \cdot (5-x)Fe_2O_3$. *Physical Review*, 1958, **110** (1), P. 73–78.

[11] Bokshyts Y.V., Shevchenko G.P., et al. Structure and luminescence properties of $(Y_{1-x}La_x)_3(La_{1-y}Ga_y)O_{12}$:$Ce^{+3}$. *Inorganic Materials*, 2019, **55** (8), P. 820–826.

[12] Smirnova M.N., Nikiforova G.E., Goeva L.V. One-stage synthesis of $(Y_{0,5}Bi_{0.5})_3(Fe_{0.5}Ga_{0.5})_5O_{12}$ garnet using the organometallic gel auto-combustion approach. *Ceramics international*, 2018, **45** (4), P. 4509–4513.

[13] Smirnova M.N., Nipan G.D., Nikiforova G.E. $(Y_{1-x}Bi_x)_3(Fe_{1-y}Ga_y)_5O_{12}$ Solid Solution Region in the Ieneke Diagram. *Inorganic materials*, 2018, **54** (7), P. 683–688.

[14] Sharm V., Kuanr B.K. Magnetic and crystallographic properties of rare-earth substituted yttrium-iron garnet. *Journal of Alloys and Compounds*, 2018, **748**, P. 591–600.

[15] Opuchovic O., Andrulevicius M., et al. Cerium doping and cerium aluminium co-doping effects on the sol-gel processing of $Y_3Fe_5O_{12}$ (YIG): Bulk and thin films. *Solid State Sciences*, 2020, **99**, 106065.

[16] Kum J.S., Kim S.J., Shim I.B., Kim C.S. Magnetic properties of Ce-substituted yttrium iron garnet ferrite powders fabricated using a sol-gel method. *Journal of Magnetism and Magnetic Materials*, 2004, **272**, P. 2227–2229.

[17] Popova V.F., Petrosyan A.G., et al. Y_2O_3-Ga_2O_3 phase diagram. *Russian Journal of Inorganic Chemistry*, 2009, **54**, P. 624–629.

[18] Lomanova N.A., Tomkovich M.V., et al. Formation of $Bi_{1-x}Ca_xFeO_{3-\delta}$ Nanocrystals via Glycine-Nitrate Combustion. *Russian Journal of General Chemistry*, 2019, **89** (9), P. 1843–1850.

[19] Almjasheva O.V., Lomanova N.A., et al. The minimum size of oxide nanocrystals: phenomenological thermodynamic vs crystal-chemical approaches. *Nanosystems: Physics Chemistry Mathematics*, 2019, **10** (4), P. 428–437.

[20] Lisnevskaya I.V., Bobrova I.A., Lupeiko T.G. Synthesis of magnetic and multiferroic materials from polyvinyl alcohol-based gels. *Journal of Magnetism and Magnetic Materials*, 2016, **397**, P. 86–95.

[21] Zhuravlev V.D., Khaliullin S.M., Ermakova L.V., Bamburov V.G. Synthesis and Properties of Manganese Oxides Obtained via Combustion Reactions with Glycine and Citric Acid. *Russian Journal of Inorganic Chemistry*, 2020, **65**, P. 1522–1528.

[22] Nguyen A.T., Tran H.L.T., et al. Sol-gel synthesis and the investigation of the properties of nanocrystalline holmium orthoferrite. *Nanosystems: Physics Chemistry Mathematics*, 2020, **11** (6), P. 698–704.

[23] Matsnev M.E., Rusakov V.S. SpectrRelax: An Application for Mössbauer Spectra Modeling and Fitting. *AIP Conference Proceedings*, 2012, **1489**, P. 178–185.

[24] Nakatsuka A., Yoshiasa A., Takeno S. Site preference of cations and structural variation in $Y_3Fe_{5-x}Ga_xO_{12}$ ($0 \leq x \leq 5$) solid solutions with garnet structure. *Acta Crystallographica Section B*, 1995, **51**, P. 737–745.

[25] Sifat R., Beam J.C., Grosvenor A.P. Investigation of Factors That Affect the Oxidation State of Ce in the Garnet-Type Structure. *Inorganic Chemistry*, 2019, **58** (4), P. 2299–2306.

[26] Nicholson W.J., Bums G. Quadrupole Coupling Constant, eq/Qh, of Fe^{3+} in Several Rare-Earth Iron Garnets. *Physical Review A*, 1964, **133**, 1568.

[27] Sawatzky G.A., van der Woude F., Morrish A.H. Recoilless-Fraction ratios for Fe57 in octahe dral and tetrahedral sites of a spinel and a garnet. *Physical Review*, 1969, **183**, P. 383–386.

[28] Belogurov V.N., Bilinkin V.A. Dependence of the dynamic and hyperfine characteristics of Fe^{3+} ions on the rare-earth ion parameters in garnets above the Néel temperature. *Physica Status Solidi*, 1981, **63**, P. 45–53.

NANOSYSTEMS: PHYSICS, CHEMISTRY, MATHEMATICS, 2021, 12 (2), P. 218–223

Study of stability of luminescence intensity of β-$NaGdF_4$:Yb:Er nanoparticle colloids in aqueous solution

I. D. Kormshchikov[1,2], V. V. Voronov[1], S. A. Burikov[3], T. A. Dolenko[3], S. V. Kuznetsov[1,*]

[1]Prokhorov General Physics Institute of the Russian Academy of Sciences, Vavilov str, 38, Moscow, 119991 Russia

[2]Faculty of Chemistry, Moscow State University, Moscow, 119991 Russia

[3]Faculty of Physics, Moscow State University, Moscow, 119991 Russia

[*]kouznetzovsv@gmail.com

DOI 10.17586/2220-8054-2021-12-2-218-223

Hexagonal modification β-$NaGdF_4$:Yb:Er with a particle size of 24 nm was synthesized by the solvothermal technique. Concentrated aqueous colloids of nanoparticles were prepared using polyvinylpyrrolidone as the surfactant. The study of the luminescence characteristics for 25 days revealed that the luminescence intensity did not significantly change and hydrolysis of nanoparticles was not observed.

Keywords: nanofluoride, up-conversion luminescence, luminescence stability of the aqueous colloid.

Received: 15 February 2021

Revised: 10 April 2021

1. Introduction

The development of bioimaging allows *in vivo* determination of the impact of pharmaceuticals on cells. Dyes [1–3], quantum dots [1, 2], carbon nanoparticles [3–7] and up-conversion luminescence fluoride nanoparticles [1, 8, 9] are used as biosensors. Fluorides possess chemical stability and high values for up-conversion luminescence quantum yields [10–12]. Up-conversion luminescence is convenient for bioimaging, since it allows the excitation of the phosphor in the near-infrared region of the spectrum and the registration of the luminescence response in the visible range of the spectrum [13, 14]. Various techniques have been developed which allow *in vivo* determination of temperature [15–18], pH, and a viscosity [19] inside cells based on up-conversion nanoparticles. The highest quantum yields of up-conversion luminescence (PLQY) were recorded for β-$NaYF_4$:21.4%Yb^{3+}, 2.2%Er^{3+} (PLQY=10.5% at 35 W/cm^2) [20], BaY_2ZnO_5:7%Yb^{3+}, 3%Er^{3+} (PLQY=5% at 2.2 W/cm^2) [21], La_2O_2S:9%Yb^{3+}, 1%Er^{3+}(PLQY=5,8% at 13 W/cm^2) [22], SrF_2:3%Yb, 2%Er (PLQY=6.5% at 230 W/cm^2) [11]. Instead of the $NaYF_4$ matrix, $NaGdF_4$ is being actively investigated, since gadolinium, in comparison to yttrium, is an NMR, X-ray, and photosensitive ion [23]. Cell-based research requires aqueous colloids of nanoparticles demonstrating stable luminescent characteristics. One of the effective luminescence quenchers is hydroxyl ion, which lead to the hydrolysis of nanoparticles. Hydrolysis study of the nanoparticles through the stages of formation of hydroxides and oxides was carried out in [24] based on HAADF-TEM for CaF_2:Yb nanoparticles to explain the source of optical losses in optical ceramics. From a chemical point of view, the scenario of obtaining oxofluorides rather than hydroxides is more probable due to the significant difference between the rates of hydrolysis of rare earth, alkaline, and alkaline earth fluorides [25, 26]. An illustrative example is the BaF_2-BiF_3 system, for which it is impossible to obtain bismuth fluoride by precipitation from aqueous solutions [27]. Stability of the luminescence characteristics, possibility of hydrolysis under the action of laser pumping, hydration of the nanoparticle surface in aqueous solutions are important questions at investigation of luminescence characteristics of aqueous colloids of nanoparticles. Decrease in the luminescence intensity during exposure of nanoparticles in aqueous solutions due to hydrolysis processes, which can be prevented by using a NaF as a buffer or organic or inorganic shell [28, 29]. Colloid measurements are often limited to a few days, which make it impossible to estimate the reproducibility of the measured data. Finally, the task of comparing the nanoparticles' luminescent characteristics becomes much more complicated. In our research, aqueous colloids of β-$NaGdF_4$:Yb:Er nanoparticles were synthesized and the stability of their luminescent characteristics was studied with an unchanged optical scheme for 25 days. It was reliably shown that the luminescence intensity of colloids does not change and the absence of the influence of the hydrolysis impact on the luminescence characteristics.

2. Experimental part

Gadolinium, ytterbium, and erbium acetates with a purity of 99.99 (LANHIT, Russia), ammonium fluoride, and sodium hydroxide (chemically pure, Chimmed), octadecene-1 (90%, VEKTON), oleic acid (pure, Chimmed) were used as initial chemicals.

The synthesis of β-$NaGdF_4$:Yb:Er nanoparticles were carried out in several stages as described in [30]. In the first step, 1.2199 g $Gd(CH_3COO)_3{\cdot}4H_2O$, 0.3249 g of $Yb(CH_3COO)_3{\cdot}4H_2O$, and 0.0321 g of $Er(CH_3COO)_3{\cdot}4H_2O$ were placed in a 250 ml three-necked flask with a reflux condenser, and oleic acid (10.9 ml) and octadecene-1 (58 ml) were added. The system was filled with argon after preliminary evacuation. The reaction mixture was heated to 130 °C with stirring until the solid acetates were completely dissolved. Then, water and acetic acid were removed by vacuum pumping with control until foaming ceased. At this stage, RE oleates were synthesized by reactions (1-3).

$$Gd(CH_3COO)_3 \cdot 4H_2O + 3C_{17}H_{33}COOH = Gd(C_{17}H_{33}COO)_3 + 3CH_3COOH + 4H_2O \quad (1)$$

$$Yb(CH_3COO)_3 \cdot 4H_2O + 3C_{17}H_{33}COOH = Yb(C_{17}H_{33}COO)_3 + 3CH_3COOH + 4H_2O \quad (2)$$

$$Er(CH_3COO)_3 \cdot 4H_2O + 3C_{17}H_{33}COOH = Er(C_{17}H_{33}COO)_3 + 3CH_3COOH + 4H_2O \quad (3)$$

In the second step, the formed oleates were fluorinated with α-$NaGdF_4$:Yb:Er nanoparticles formation with a cubic crystal structure by reaction (4-5).

$$NH_4F + NaOH = NaF + NH_3 + H_2O \quad (4)$$

$$\begin{gathered} 4NaF + (1-x-y)Gd(C_{17}H_{33}COO)_3 + xYb(C_{17}H_{33}COO)_3 + yEr(C_{17}H_{33}COO)_3 = \\ = NaGd_{1-x-y}Yb_xEr_yF_4 + 3C_{17}H_{33}COONa \quad (x = 0,20; y = 0,02) \end{gathered} \quad (5)$$

Appropriate weights of NaOH (0.1540 g) and NH_4F (0.5698 g) were dissolved in methanol and was added to the reaction mixture with oleates at room temperature. The reaction mixture was heated to 50–60 °C for methanol removal during vacuum pumping. The removal of all methanol was monitored by the end of the foaming of the solution. The resulting reaction mixture was held for 1 hour at 60 °C to nucleate nanoparticles of a cubic metastable modification. In the third step, the polymorphic transformation from the cubic into the hexagonal phase was carried out at 290–300 °C for 1.5 hours. The choice of temperature 290–300 °C is due to the phase transition from the cubic to the hexagonal phase.

Nanoparticles were isolated by centrifugation (7000 rpm, 6 min). The precipitate was washed three-times in chloroform with intermediate centrifugation. Aqueous solutions of nanoparticle colloids were prepared in two stages using polyvinylpyrrolidone (PVP) as a surfactant. Sodium-gadolinium nanofluorides are insoluble in water and poorly dispersed indirect interaction with water. Appropriate weighed quantities of β-$NaGdF_4$:Yb:Er nanoparticles were dispersed in chloroform and sonicated for 20 minutes at room temperature. An aqueous solution of PVP (1 wt.% or 2 wt.%) was slowly added dropwise to a suspension of β-$NaGdF_4$:Yb:Er nanoparticles in chloroform under vigorous stirring. The resulting mixture was kept in an ultrasonic bath at 63 °C to remove chloroform (boiling point 61.2 °C) for colloid formation. Control of the completeness of chloroform removal was carried out by changing the volume of the solution. X-ray powder diffraction analysis was performed on a Bruker D8 Advance diffractometer (from 12 to 55 2θ with 0.02 2θ step) with CuKα radiation. The unit cell parameters were calculated using the Powder 2.0 software (calculation error ΔQ <10), where $\Delta Q = 10^4/d^2_{theor} - 10^4/d^2_{calc}$, d is the interplanar distance. The coherent scattering region was calculated using the Scherrer formula. Transmission electron microscopy was performed on a JEOL JEM-2100 microscope. The particle size was estimated using the ImageJ software. Energy dispersive analysis (EDX) was performed on a Carl Zeiss NVision 40 microscope.

The photoluminescence spectra of β-$NaGdF_4$:Yb:Er nanoparticles were obtained in the 90-degree geometry on a setup consisting of a pulsed laser (Solar LS, 980 nm excitation, pulse duration 12 ns, pulse repetition rate 100 Hz, average power density 3.4 MW/cm^2 or 40.7 mJ/cm^2 in impulse), monochromator (MVR-80, focal length 500 mm, diffraction grating 600 lines/mm) and a CCD camera (1024 * 128 Synapse BIUV, Horiba Jobin Yvon).

3. Results and discussion

A typical X-ray diffraction pattern of synthesized β-$NaGdF_4$: Yb:Er solid solution is shown in Fig. 1. Comparison with JCPDS 27-0699 for hexagonal modification β-$NaGdF_4$ revealed complete agreement of the X-ray diffraction reflections with a slight shift in the peak positions. The deviation of the calculated unit cell parameters $a = 5.981(6)$, $c = 3.63(2)$ Å from the JCPDS 27-0699 data ($a = 6.020$ Å, $c = 3.601$ Å) arise from a difference in the sizes of the gadolinium, ytterbium, and erbium ions [31]. The coherent scattering region was 12 nm.

The transmission electron microscopy (TEM) image is presented in Fig. 2. The particles have average size of about 24 nm. TEM image and coherent scattering region allows us to conclude that nanoparticles grow by cooperative growth mechanism [32].

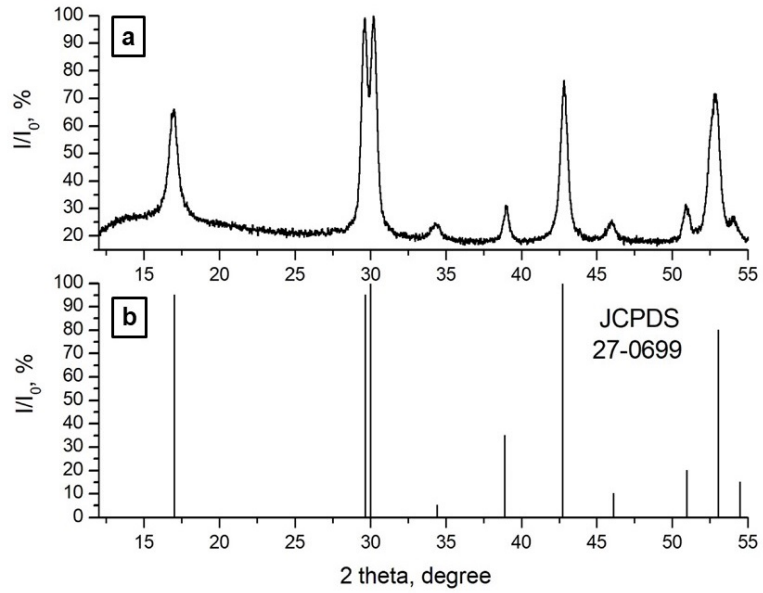

FIG. 1. X-ray diffraction patterns of (a) β-$NaGdF_4$:Yb:Er and (b) JCPDS 27-0699

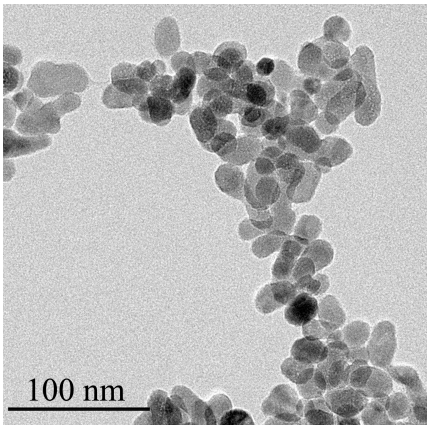

FIG. 2. Transmission electron microscopy of β-$NaGdF_4$:Yb:Er nanoparticles

The actual composition was determined by EDX as $Na_{1,186}Gd_{0,606}Yb_{0,192}Er_{0,016}F_{3,628}$, while the nominal composition was $NaGd_{0,78}Yb_{0,20}Er_{0,02}F_{4,00}$. The distribution coefficients (k) were: k(Na)= 1.19, k(Gd)= 0.78, k(Yb)= 0.96, k(Er)= 0.80, which means there is an incongruent crystallization of the powders.

The aqueous colloids with different concentrations of nanoparticles and PVP were prepared (Table 1).

TABLE 1. Concentration of β-$NaGdF_4$:Yb:Er colloids

Sample	Colloid concentration, mg/ml	PVP, wt.%
1	1.0	1.0
2	1.0	2.0
3	2.0	1.0
4	2.0	2.0

The luminescence spectra with excitation at 980 nm on the first day of the experiment are presented in Fig. 3. The luminescence spectra of colloids contain luminescence bands with maxima at 522 nm, 544 nm and 655 nm, which correspond to the transitions $^2H_{11/2} \rightarrow ^4I_{15/2}$, $^4S_{3/2} \rightarrow ^4I_{15/2}$, $^4F_{9/2} \rightarrow ^4I_{15/2}$ of the erbium ion. Analysis of the

luminescence spectra revealed that an increase of nanoparticles concentration from 1.0 to 2.0 mg/ml led to an increase in the luminescence intensity in ten times at the same PVP content (1.0 wt.%). An increase in the PVP content up to 2.0 wt.% at a particle concentration of 2.0 mg/ml resulted in a decrease in the luminescence intensity by two-fold, which is associated with an increase in scattering due to the appearance of turbidity of the colloid. An increase in the luminescence intensity of samples with increase in the PVP content from 1.0 to 2.0 wt.% at the same nanoparticle content of 1 mg/ml was associated with the prevention of luminescence quenching processes due to the interaction of hydroxyl ions with surface of nanoparticles. The effect of an aqueous medium on the luminescence intensity was analyzed based on sample 3, which demonstrated the most intense luminescence and low solution turbidity. This sample has a low PVP concentration, which does not prevent the interaction of water with the nanoparticle surface.

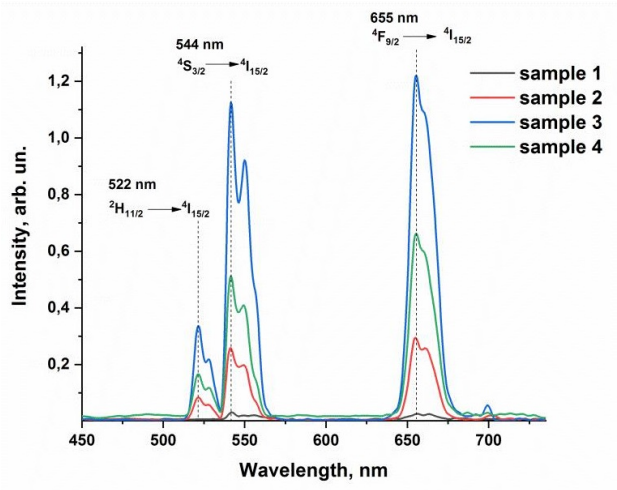

FIG. 3. Luminescence spectra of β-NaGdF$_4$:Yb:Er aqueous colloids on the first day of the experiment

Studying the luminescent properties of nanoparticle suspensions complicated by elastic scattering. This contribution is expressed in a decrease in the luminescence intensity and distortion of the shape of its spectra. Strong scattering at the exciting radiation wavelength effectively reduces the power density of the probe radiation in the signal collection region, which leads to a decrease in the luminescence intensity. The signal intensity also decreases directly due to the scattering of luminescence photons. Since the scattering efficiency depends on the wavelength, the shape of the spectra is also distorted. In the case of small particles (less than the radiation wavelength), the dependence of the scattering intensity on the wavelength obeys the $1/\lambda^4$ law. If the scattering intensity increases due to an increase in the particle size due to aggregation, the spectra are distorted i.e. the ratios between the intensities of the luminescence bands change. Control of the possible contribution of scattering to the change in the luminescence spectra was revealed by calculation of band intensities ratios in the region of 540 nm and 520 nm. Decrease in this ratio would indicate an increase in scattering. A clear tendency to change this ratio with time was not found (Fig. 4), which indicates that the intensity of radiation scattering remains unchanged within the framework of this experiment.

The luminescence spectra were recorded regularly for 25 days. The results are presented in the form of histograms characterizing the change in the integral intensity of the luminescence bands in the 496–583 nm and 636–689 nm ranges (Fig. 5). The reproducibility of luminescence spectra during a measuring day was ensured by repeating the measurement 5 times. Reproducibility of luminescence spectra was about 10%. Finally, the mean value and standard deviation were calculated. Analysis of the histograms did not demonstrate the change in luminescent characteristics within 25 days. This indicates the absence of hydrolysis processes on the surface of nanoparticles and the possible compatibility of using aqueous colloids of β-NaGdF$_4$:Yb:Er nanoparticles for long-term biomedical research.

4. Conclusion

Nanoparticles of β-NaGdF$_4$:Yb:Er were synthesized by the solvothermal technique. Based on the data on the coherent scattering region (12 nm) and transmission electron microscopy (24 nm), it is shown that the growth of nanoparticles occurs by the cooperative growth mechanism. Stable colloidal solutions of nanoparticles with a concentration of 1–2 mg/ml were prepared by using polyvinylpyrrolidone as a surfactant. Measurement of the luminescence

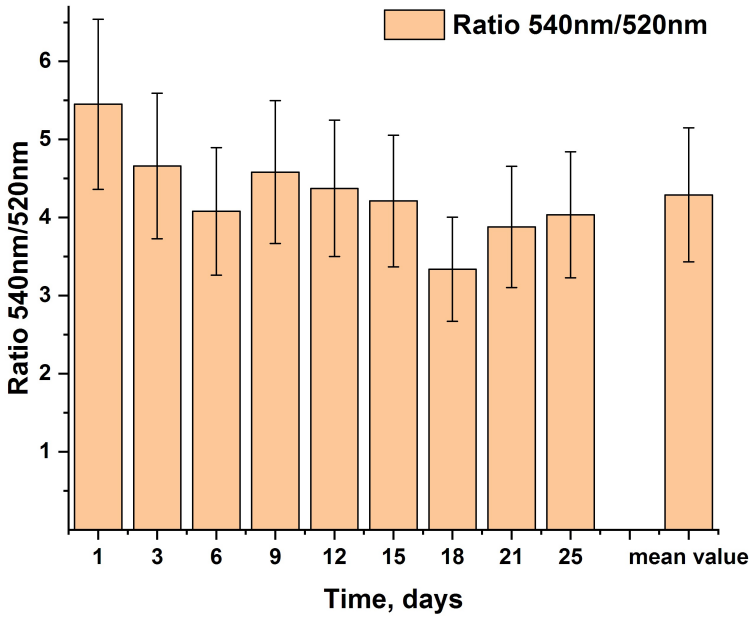

FIG. 4. The ratio of band intensities in the region of 540 nm and 520 nm on different days

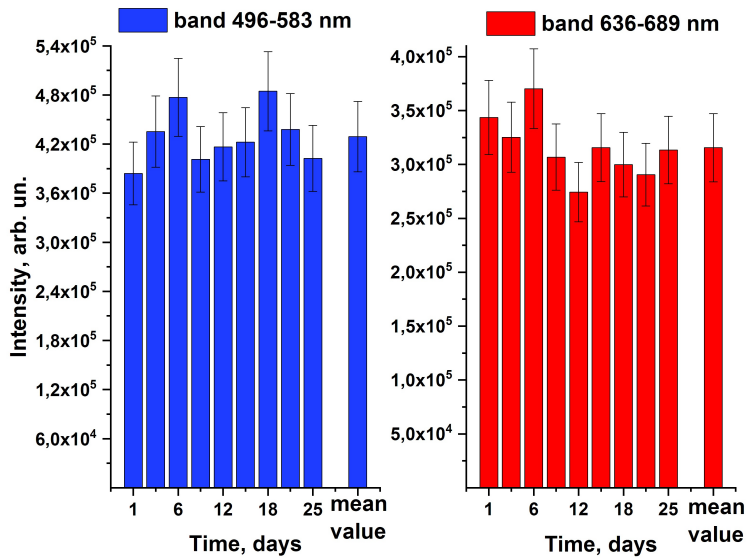

FIG. 5. Intensities of the luminescence bands of the aqueous colloid of β-$NaGdF_4$:Yb:Er in 496–583 nm and 636–689 nm ranges over a 25 day period

spectra for 25 days revealed the retention of the luminescence intensity at the level of measurement error. This indicates the possibility of using such colloids for biomedical applications and the absence of intense hydrolysis of nanoparticles.

Acknowledgements

Authors thanks to Tabachkova N. Yu. for transmission electron microscopy.

References

[1] Wolfbeis O.S. An overwiew of nanoparticles commonly used in fluorescent bioimaging. *Chem. Soc. Rev.*, 2015, **44**, P. 4743–4768.
[2] Fei X., Gu Y. Progress in modifications and applications of fluorescent dye probe. *Progress in Natural Science*, 2009, **19**, P. 1–7.
[3] Fan J.Y., Chu P.K. Group IV Nanoparticles: Synthesis, properties, and biological applications. *Small*, 2010, **6**, P. 2080–2098.

[4] Khan W.U., Wang D., Wang Y. Highly Green Emissive Nitrogen-Doped Carbon Dots with Excellent Thermal Stability for Bioimaging and Solid-State LED. *Inorganic Chemistry*, 2018, **57**, P. 15229–15239.
[5] Molaei M.J. Carbon quantum dots and their biomedical and therapeutic applications: a review. *RSC Advances*, 2019, **9**, P. 6460–6481.
[6] Rosenholm J.M., Vlasov I.I., Burikov S.A., Dolenko T.A., Shenderova O.A. Nanodiamond-Based Composite Structures for Biomedical Imaging and Drug Delivery (Review). *J. of Nanoscience and Nanotechnology*, 2015, **15**, P. 959–971.
[7] Sarmanova O.E., Burikov S.A., Dolenko S.A., Isaev I.V., Laptinskiy K.A., Prabhakar N., Karaman D.S., Rosenholm J.M., Shenderova O.A., Dolenko T.A. A method for optical imaging and monitoring of the excretion of fluorescent nanocomposites from the body using artificial. *Nanomedicine: Nanotechnology, Biology, and Medicine*, 2018, **14**, P. 1371–1380.
[8] Rodríguez-Sevilla P., Sanz-Rodríguez F., Peláez R.P., Delgado-Buscalioni R., Liang Liangliang, Liu Xiaogang, Jaque Daniel. Single-cell diagnosis by upconverting nanorockers. *Advanced Biosystems*, 2019, **3**, P. e1900082.
[9] Wua Wei, Wanga Xian, Tiana Yuexing, Wanga Shasha, Deab Gejihu. Controlled synthesis and luminescent properties of $Ca_{0.80}Yb_{0.20}F_{2.2}$: 0.2% Tm^{3+} nanocrystals. *J. Fluor.Chem.*, 2021, **242**, P. 109696.
[10] Fedorov P.P., Kuznetsov S.V., Osiko V.V. Elaboration of nanofluorides and ceramics for optical and laser applications. Chapter in the book *Photonic and Electronic Properties of Fluoride Materials*. Ed. A.Tressaud, K. Poeppelmeier, Print Book, 2016, P. 7-31.
[11] Reig David Saleta, Grauel Bettina, Konyushkin V.A., Nakladov A.N., Fedorov Pavel P., Busko Dmitry, Howard Ian Arthur, Richards Bryce S., Resch-Genger Ute, Kuznetsov Sergey, Turshatov Andrey, Würth Christian. Upconversion properties of SrF_2:Yb^{3+},Er^{3+} single crystals. *J. Mater. Chem. C.*, 2020, **8**, P. 4093–4101.
[12] Ermakova Yu.A., Pominova D.V., Voronov V.V., Kuznetsov S.V. Algorithm for calculation of up-conversion luminophores mixtures chromaticity coordinates. *J. Fluor. Chem.*, 2020, **237**, P. 109607.
[13] Pominova D.V., Romanishkin I.D., Proydakova V.Yu., Grachev P.V., Moskalev A.S., Ryabova A.V., Makarov V.I., Linkov K.G., Kuznetsov S.V., Uvarov O.V., Loschenov V.B. Comparison of 920, 940 and 970 nm wavelengths in terms of penetration depth and thermal effects on biological tissues as well as up-conversion luminescence excitation efficiency. *Methods Appl. Fluoresc.*, 2020, **8**, P. 025006.
[14] Liu W., Chen R., He S. Ultra-stable near-infrared Tm^{3+}-doped upconversion nanoparticles for in vivo wide-field two-photon angiography with a low excitation intensity. *Journal of Innovative Optical Health Sciences*, 2019, **12**, P. 1950013.
[15] Brites C.D.S., Balabhadra S., Carlos L.D. Lanthanide-based thermometers: at the cutting-edge of luminescence thermometry. *Adv. Opt. Mater.*, 2019, P. 71801239.
[16] Jaque D., Vetrone F. Luminescence nanothermometry. *Nanoscale*, 2012, **4**, P. 4301–4326.
[17] Brites C.D.S., Kuznetsov S.V., Konyushkin V.A., Nakladov A.N., Fedorov P.P., Carlos L.D. Simultaneous measurement of the emission quantum yield and local temperature: the illustrative example of SrF_2:Yb^{3+}/Er^{3+} single crystals. *Eur. J. Inorg. Chem.*, 2020, **2020**, P. 1555–1561.
[18] Sarmanova O.E., Burikov S.A., Laptinskiy K.A., Kotova O.D., Filippova E.A., Dolenko T.A. In vitro temperature sensing with up-conversion $NaYF_4$:Yb^{3+}/Tm^{3+}-based nanocomposites: peculiarities and pitfalls. *Spectrochimica Acta Part A: Molecular and Biomolecular Spectroscopy*, 2020, **241**, P. 118627(8 p).
[19] Sevilla Paloma Rodríguez, Rodriguez Francisco Sanz, Pelez Raúl P., Buscalioni Rafael Delgado, Liang Liangliang, Liu Xiaogang, Jaque Daniel. Upconverting Nanorockers for Intracellular Viscosity Measurements During Chemotherapy. *Advanced in Biosystems*, 2019, **3**, P. 1900082.
[20] Kaiser M., Wurth C., Kraft M., Hyppanen I., Soukka T., Resch-Genger U., *Nanoscale*, 2017, **9**, P. 10051–10058.
[21] Etchart I., Huignard A., Berard M., Nordin M.N., Hernandez I., Curry R.J., Gillin W.P., Cheetham A.K. *J. Mater. Chem.*, 2010, **20**, P. 3989-3994.
[22] Pokhrel M., Kumar G.A., Sardar D.K. *J. Mater. Chem. A*, 2013, **1**, P. 11595–11606.
[23] Yu Songxia, Wang Zhiqiang, Cao Ruijun, Meng Lingjie. Microwave–assisted synthesis of water–disperse and biocompatible $NaGdF_4$:Yb,Ln@$NaGdF_4$ nanocrystals for UCL/CT/MR multimodal imaging. *J. Fluor. Chem.*, 2017, **200**, P. 77–83.
[24] Lyberis A., Patriarche G., Gredin P., Vivien D., Mortier M. Origin of light scattering in ytterbium doped calcium fluoride transparent ceramic for high power lasers. *J. Eur. Ceram. Soc.*, 2011, **31**, P. 1619–1630.
[25] Warf J.C., Cline W.C., Tevebaugh R.D. Pyrohydrolysis in Determination of Fluoride and Other Halides. *Analytical Chemistry*, 1954, **26**, P. 342–346.
[26] Banks C.V., Burke K.E., O'Laughlin J.W. The determination of fluorine in rare-earth fluorides by high temperature hydrolysis. *Analytica Chimica Acta*, 1958, **19**, P. 230–243.
[27] Fedorov P.P., Mayakova M.N., Kuznetsov S.V., Voronov V.V., Osiko V.V., Ermakov R.P., Gontar' I.V., Timofeev A.A., Iskhakova L.D. Coprecipitation of barium-bismuth fluorides from aqueous solutions: Nanochemical effects. *Nanotechnologies in Russia*, 2011, **6**, P. 203–210.
[28] Dukhno O., Przybilla F., Muhr V., Buchner M., Hirsch T., Mely Y. Time-dependent luminescence loss of individual upconversion nanoparticles upon dilution in aqueous solutions. *Nanoscale*, 2018, **10**, P. 15904–15910.
[29] Andresen E., Würth C., Prinz C., Michaelis M., Resch-Genger U. Time-resolved luminescence spectroscopy for monitoring the stability and dissolution behaviour of upconverting nanocrystals with different surface coatings. *Nanoscale*, 2020, **12**, P. 12589–12601.
[30] Li Zhengquan, Zhang Yong. An efficient and user-friendly method for the synthesis of hexagonal-phase $NaYF_4$:Yb, Er/Tm nanocrystals with controllable shape and upconversion fluorescence. *Nanotechnology*, 2008, **19**, P. 345606.
[31] Shannon R.D. Revised effective ionic radii and systematic studies of interaction distance in halides and chalcogenides. *Acta Crystallogr. A*, 1976, **32**, P. 751–767.
[32] Ivanov V.K., Fedorov P.P., Baranchikov A.Y., Osiko V.V. Oriented aggregation of particles: 100 years of investigations of non-classical crystal growth. *Russ. Chem. Rev.*, 2014, **83**, P. 1204–1222.

NANOSYSTEMS: PHYSICS, CHEMISTRY, MATHEMATICS, 2021, 12 (2), P. 224–231

The effect of co-precipitation temperature on the crystallite size and aggregation/agglomeration of $GdFeO_3$ nanoparticles

V. I. Popkov[1,*], Y. Albadi[2,3]

[1]Ioffe Institute, Saint Petersburg, 194021, Russia

[2]Saint Petersburg State Institute of Technology, Saint Petersburg, 190013, Russia

[3]Al-Baath University, Homs, 77, Syrian Arab Republic

*vadim.i.popkov@mail.ioffe.ru

PACS 81.20.Fw, 61.46.+w, 75.20.-g **DOI 10.17586/2220-8054-2021-12-2-224-231**

In this work, a series of $GdFeO_3$ nanopowders was successfully synthesized via a reverse co-precipitation technique at different solution temperatures (0, 25 and 50 °C) followed by thermal treatment. Co-precipitated hydroxides and heat treatment products were analyzed using EDXS, DTA-TGA, PXRD, ASA and LD methods. It was shown that the formation temperature of $GdFeO_3$ nanoparticles varies in the range of 737.5–758.8 °C and total weight loss varies in the range of 23.6–26.4% depending on the temperature of initial solutions. The specific surface areas of nanopowders were found to be strongly dependent on the factor mentioned above and belong to 2.5–16.3 m^2/g values interval. The hierarchical structure of the obtained nanopowders was established and the effect of co-precipitation temperature on the average crystallite (21.4–34.3 nm), aggregate (46.2–301.2 nm) and agglomerate (33.5–40.9 μm) sizes was discussed in detail.

Keywords: co-precipitation, gadolinium orthoferrite, nanoparticles, aggregation, agglomeration.

Received: 2 February 2021

Revised: 10 April 2021

1. Introduction

Currently, (co)precipitation followed by thermal treatment is one of the most common and powerful techniques to synthesize a wide range of nanostructured oxides, fluorides, sulfides, etc [1–4]. This approach successfully allows one to obtain both nanocrystalline simple and complex oxides with desired chemical/phase composition and structure [5]. Depending on the type of thermal treatment employed (sonochemical [6], hydro/solvothermal [7, 8], quenching in the air [9, 10]), (hydro)oxide nanocrystals of different morphology and surface characteristics can easily be obtained [11]. An additional feature of the (co)precipitation technique is the high chemical purity of the resulting products, since hydroxide precipitate often is obtained and fully decomposed to pure oxide(s) [12].

For the further functional application of oxide materials obtained using the co-precipitation method, such materials are often subject to high requirements regarding small crystallite sizes and a high specific surface area [13, 14]. However, even when low crystallite sizes are achieved by (co)precipitation followed by thermal treatment, the specific surface area of the resulting nanopowders can be low due to the aggregation and agglomeration of oxide nanoparticles [15]. Varying the temperature of reaction solutions during (co)precipitation seems to be an effective way to control these processes and parameters [16, 17]; however, such studies to date are quite selective and few [18, 19].

Gadolinium orthoferrite ($GdFeO_3$) is one of the representatives of orthorhombic (Pbnm space group) complex oxides - orthoferrites of rare-earth elements (REE) with the general formula of $RFeO_3$ (R = Sc, Y, Ln) [20, 21]. Due to the perovskite-like structure of this compound, as well as the unique combination of semiconducting, magnetic, thermal and chemical properties, materials based on $GdFeO_3$ are now widely used as (photo)catalysts [22–24], electromagnetic materials [25], biomedical agents [26, 27], etc. In our previous work [15], it was shown that aggregation/agglomeration processes play a key role in the magnetic behavior of $GdFeO_3$-based nanopowders, and it was assumed that varying the co-precipitation temperature of gadolinium and iron(III) hydroxides could be an effective way to control the processes of the spatial organization of $GdFeO_3$ nanocrystals, and, consequently, their promising functional properties.

In this work, the effect of co-precipitation temperature (0, 25 and 50 °C) on the structural and morphological features of $GdFeO_3$ nanopowders is analyzed and discussed. Complex physicochemical characterization of thermal treatment products allows one to obtain detailed information on the "synthesis – composition – structure – morphology" relations and proposing a possible explanation of co-precipitation temperature impact.

2. Experimental

In this work, three samples of $GdFeO_3$ nanoparticles were synthesized by reverse co-precipitation of gadolinium and iron(III) hydroxides at three different temperatures, followed by thermal treatment of the obtained co-precipitated hydroxides in the air.

2.1. Synthesis technique

An aqueous solution of stoichiometric amounts of gadolinium nitrate hexahydrate "$Gd(NO_3)_3{\cdot}6H_2O$" (puriss., 99.9%) and iron(III) nitrate nonahydrate "$Fe(NO_3)_3{\cdot}9H_2O$" (pur., 98.0%), with a concentration of 0.01 mol/L for each salt, was used as a source of gadolinium ions "Gd^{3+}" and iron(III) ions "Fe^{3+}". An aqueous solution of ammonia with a concentration of 1 mol/L prepared from aqueous ammonia "NH_4OH" (puriss. spec., 23.5%) was used as the precipitating medium. The co-precipitation was carried out at three different temperatures (0, 25 and 50 °C) by adding the solution of nitrates in a drop-wise manner to the solution of ammonia which was on a magnetic stirrer. The obtained samples of co-precipitated hydroxides (CPH-0, CPH-25 and CPH-50, respectively) were washed several times with distilled water and dried at 45 °C for 24 hours. After that, the dried precipitates were heated at a temperature of 750 °C for 4 hours in air to obtain $GdFeO_3$ nanoparticles (GFO-0, GFO-25 and GFO-50, respectively).

2.2. Physicochemical characterization

The content of gadolinium and iron in the samples of co-precipitated hydroxides was determined by energy-dispersive X-ray spectroscopy (EDXS) using a "TESCAN VEGA3" scanning electron microscope coupled with an "x-act" EDX microprobe analyzer from "Oxford Instruments". The samples of co-precipitated hydroxides were investigated by differential thermal and thermogravimetric analysis (DTA-TG) using a "Shimadzu DTG-60" simultaneous thermal analyzer. The powder X-ray diffraction (PXRD) patterns of the co-precipitated hydroxides and the thermally treated products were obtained using a "Rigaku SmartLab 3" diffractometer. The processing of PXRD data was carried out using "SmartLab Studio II" software. The Brunauer-Emmett-Teller (BET) specific surface area was determined by low-temperature nitrogen adsorption-desorption isotherm measurements at 77 K on a "Micromeritics ASAP 2020" nitrogen adsorption apparatus. The characteristic particle size of $GdFeO_3$ was estimated by spherical morphology approximation using the formula $D = 6/(S \cdot \rho_{XRD})$, where D – characteristic particle size, S – specific surface area, and ρ_{XRD} – X-ray density of $GdFeO_3$.

2.3. Preparation and characterization of colloidal suspensions of $GdFeO_3$ nanoparticles

Colloidal suspensions of the as-synthesized $GdFeO_3$ nanoparticles were prepared by mixing 10 mg of the heat-treated product with 50 mL of distilled water and sonicating the mixture for 4 hours. Thereafter, the obtained colloidal suspensions were centrifuged for 30 minutes at a speed of 1000 rpm, followed by 15 minutes at a speed of 3500 rpm. After that, the supernatants were collected. The size distribution of particles in each prepared colloidal suspension was investigated by laser diffraction (LD) on a "Shimadzu SALD-7500nano" nanoparticle size analyzer.

3. Results and discussion

The gadolinium and iron(III) hydroxides co-precipitated at 0, 25 and 50 °C were analyzed using a complex of physicochemical analysis methods and results are presented below.

3.1. Energy-dispersive X-ray spectroscopy (EDXS)

The elemental analysis of co-precipitated gadolinium and iron(III) hydroxides was carried out using energy-dispersive X-ray spectroscopy and the typical spectrum is presented in Fig. 1. As one can see, no chemical impurities were detected, excluding carbon, which is a consequence of the sample preparation procedure for EDXS analysis.

Then obtained results were recalculated concerning key elements (gadolinium and iron) to compare their composition with the stoichiometry of gadolinium orthoferrite (Table 1). In accordance with the data presented, the elemental composition of all the samples is in good agreement with that planned in the synthesis. The deviation of the composition, according to these data, does not exceed 1% at. Thus high chemical purity and elemental stoichiometry were achieved via co-precipitation processes, carried out at different temperatures.

3.2. Differential thermal analysis (DTA) / Thermogravimetric analysis (TGA)

To define the optimal temperature for the sintereing of co-precipitated hydroxides, simultaneous thermal analysis (DTA/TGA) was performed over a wide temperature range (Fig. 2). TGA results show that hydroxides lost from 23.6 to 26.4%wt. during the thermal treatment and weight loss rises in the row GFO-0 → GFO-50 → GFO-25. In all cases, the weight loss stopped at the temperature of about 750 °C, which agreed with our earlier work [21]. It should be noted

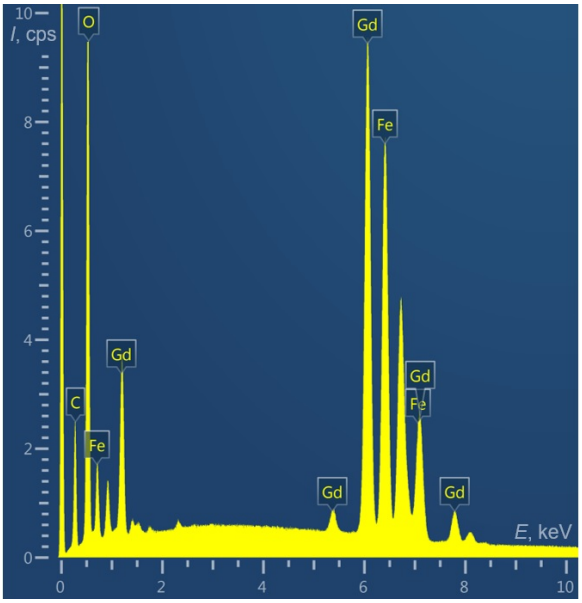

FIG. 1. Energy-dispersive X-ray spectrum of CPH-0 sample

TABLE 1. Results of EDXS analysis of $GdFeO_3$ samples

At. %	GFO-0		GFO-25		GFO-50	
	Gd	Fe	Gd	Fe	Gd	Fe
Minimum	50.25	49.65	50.26	49.50	49.10	50.78
Maximum	50.35	49.75	50.50	49.74	49.22	50.90
Average	**50.31**	**49.69**	**50.35**	**49.65**	**49.16**	**50.84**
St. deviation	0.05	0.05	0.13	0.13	0.06	0.06

that before this temperature, several physicochemical processes occurred, including water elimination, hydroxides decomposition, etc, but this issue is not an aim of this work and a detailed description could be found in [15].

Despite similar TGA thermograms, a more detailed examination of DTA thermograms in a narrow temperature range (700–800 °C) revealed a noticeable difference in the formation temperature of gadolinium orthoferrite. The minimal formation temperature is observed for the GFO-0 sample (737.5 °C) and then rises for GFO-50 (741.7 °C) and GFO-25 (758.8 °C). Even taking into account that the maximums of thermal effects (T_{max}) are indicated, the corresponding onset points (T_{onset}) follow a similar relationship. It should be noted that the narrow width of the thermal effect indicates a higher rate of gadolinium orthoferrite formation in the case of the GFO-25 sample than for GFO-0 and GFO-50. This may be due to the higher morphological and chemical homogeneity of the corresponding co-precipitated hydroxides, which facilitates diffusion processes of dehydration and crystallization.

3.3. Powder X-ray diffractometry (PXRD)

The thermal treatment products of co-precipitated hydroxides were analyzed using PXRD and corresponding results are shown in Fig. 3. PXRD patterns of all synthesized GFO samples indicate the presence of the main phase of orthorhombic gadolinium orthoferrite (Pbnm, ICSD #189729). The weak reflexes of minor phases can also be seen, but they are at the level of statistical noise. So the phase composition of GFO samples is on a high level, consistent with the results of other works [21, 28].

To estimate crystallite sizes of synthesized $GdFeO_3$ samples, a fundamental parameter approach was used and crystallite size distributions were calculated from PXRD patterns (Fig. 4). The presented results indicate that both GFO-0 and GFO-50 samples are characterized by the narrow lognormal distribution curves with average crystallite size (distribution center) of 21.4 and 26.7 nm, correspondently. Conversely, sample GFO-25 has a much broader size distribution and an average crystallite size of 34.3 nm. This fact is explained by the results of the thermal analysis

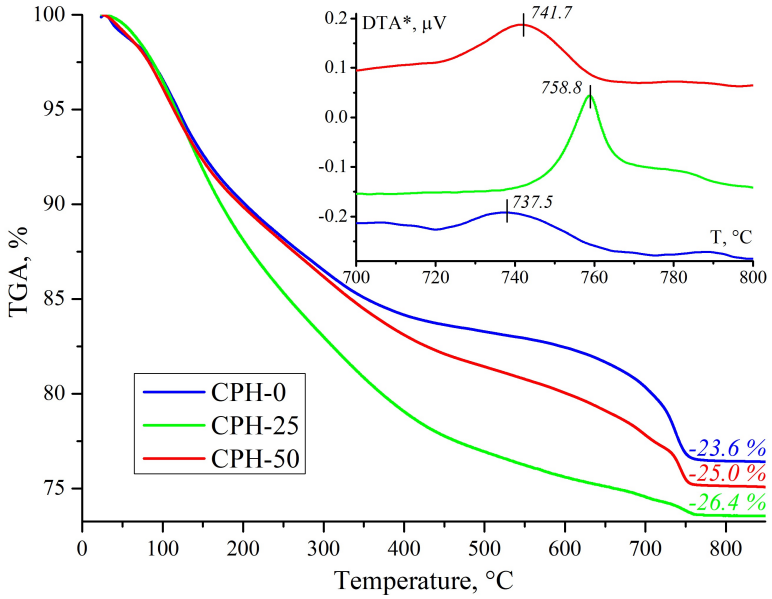

FIG. 2. TGA and DTA (inset) curves of the samples of co-precipitated hydroxides. For the DTA* dependences, the signal values are given in relative μV for illustrative comparison of results

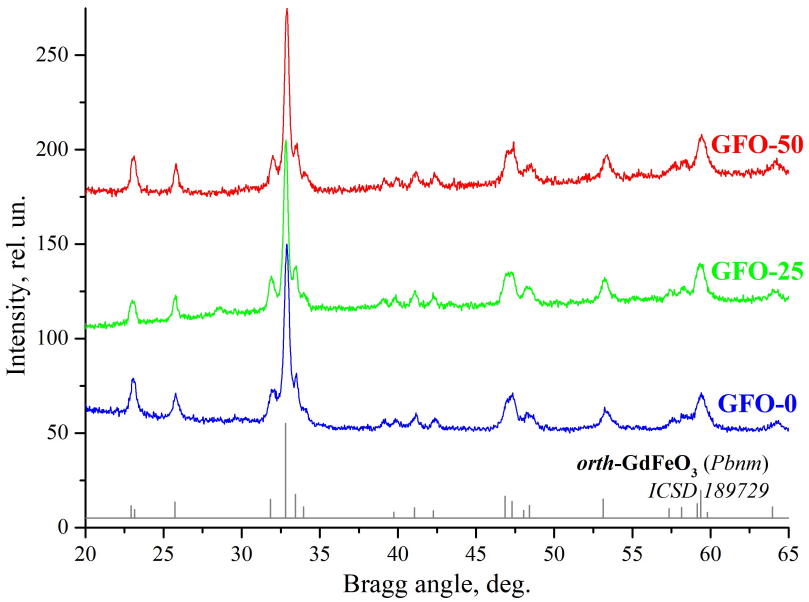

FIG. 3. PXRD patterns of the heat-treated products

– lower diffusion restrictions for the formation of ferrite lead to more intense mass transfer during thermal treatment and, as a consequence, to a larger crystallite size. In this case, the presence of more water in the initial co-precipitated hydroxides comparing to other samples can lead in the case of GFO-25 to a less uniform nucleation process, which, as a result, leads to a wide range of $GdFeO_3$ nanocrystals with different sizes.

3.4. Adsorption-structural analysis (ASA)

The nanopowders based on the GFO samples were subjected to adsorption-structural analysis to better understand their available surface performance. Since gadolinium orthoferrite synthesized via the thermal treatment of co-precipitated hydroxides commonly has IV-type isotherm and the H3-type hysteresis loop, only 5-point BET analysis was performed to estimate the specific surface areas of the samples (Fig. 5).

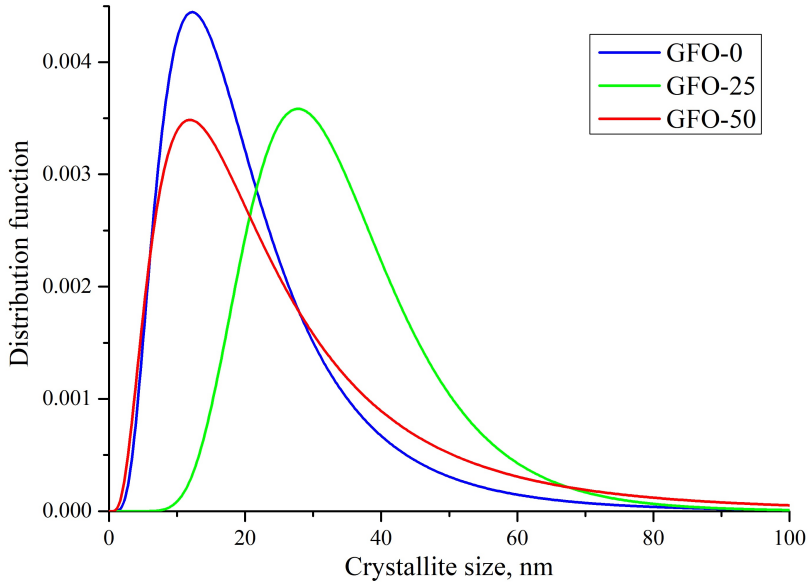

FIG. 4. Crystallite size distributions of $GdFeO_3$ nanocrystals synthesized at different co-precipitation temperatures

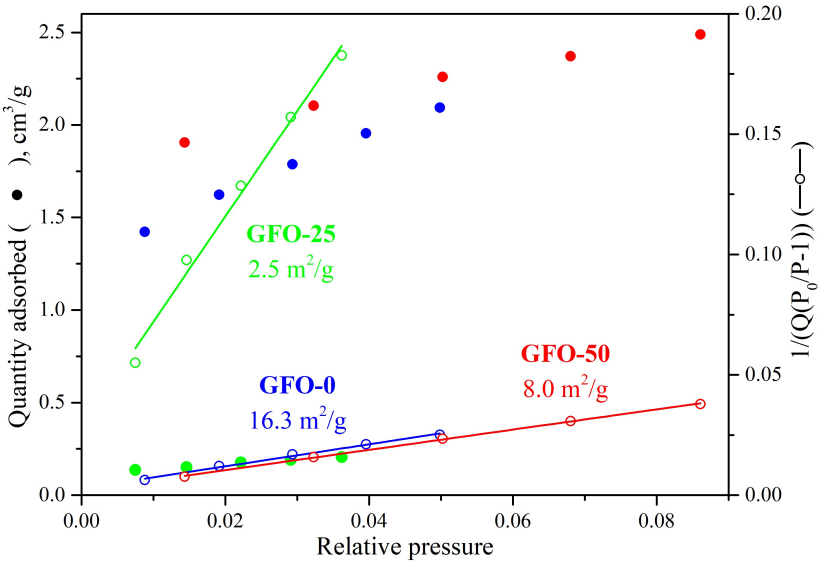

FIG. 5. Sorption-desorption (N_2, 77 K) isotherms and BET plots for $GdFeO_3$ samples

Accordingly to sorption-desorption isotherms and BET plots, the specific surface area of the samples decreases linearly GFO-0 → GFO-50 → GFO-25 as 16.3 m^2/g → 8.0 m^2/g → 2.5 m^2/g. This tendency repeats the changes in average crystallite sizes (see 3.3 subsections). Thus, the observed difference in the available surface of GFO samples seems to be related to the corresponding difference in $GdFeO_3$ crystallite sizes. But it is not the sole reason, since the samples GFO-0 and GFO-50 have closer sizes of 21.4 nm and 26.7 nm, respectively, and at the same time have twice the difference in the specific surface area (16.3 m^2/g and 8.0 m^2/g, respectively). Thus, strong aggregation of nanocrystals was supposed that decreasing the available surface area of $GdFeO_3$ nanopowders.

To estimate the characteristic size of aggregates a simple spherical approximation was used. The calculated values for the GFO-0, GFO-25 and GFO-50 were 46.2, 301.2 and 94.1 nm, respectively. These results indicate the presence of from nano to submicron aggregates of $GdFeO_3$ nanoparticles in GFO series. The observed effect arises due to the high surface energy of individual nanoparticles, which tends to reduce it due to aggregation, sometimes resulting in their oriented attachment [29]. But there is also an effect of the next order associated with the formation of much weaker bound agglomerates based on these aggregates, and this effect is considered in the next subsection.

3.5. Laser diffraction (LD)

Colloidal suspensions prepared via ultrasonic dispergation of the GFO-series nanopowders were analyzed using a laser diffraction technique, and the obtained particle size distributions are presented in Fig. 6.

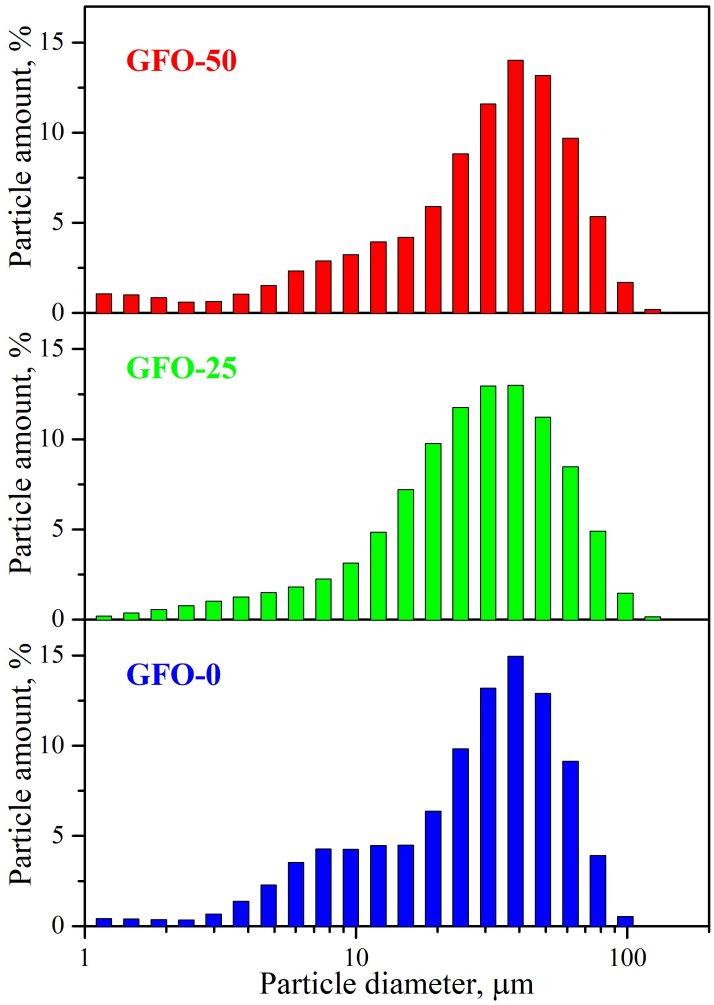

FIG. 6. LD particle size distributions for $GdFeO_3$ samples

Accordingly to the data a bimodal distribution of the particles is observed for the GFO-0 and GFO-50 samples, while that of the GFO-25 sample is unimodal. The shape of the distribution curves in all cases corresponds to the lognormal distribution. The presence of the bimodal distribution feature may be caused by the partial spatial separation of gadolinium and iron-containing hydroxide components during co-precipitation, which leads to an additional type of particle agglomeration as a result of thermal treatment. In the case of co-precipitation of hydroxides at 25 °C, this process seems to be suppressed. The main distribution center grows in the row GFO-25 → GFO-0 → GFO-50 and equal to 33.5, 37.7 and 40.9 μm correspondently. So considering the agglomeration of particles, the maximal co-precipitation temperature possesses the highest agglomerate size on average. However, it should be noted that all these values are in the narrow range within a deviation at the level of the analysis method accuracy.

3.6. The impact of co-precipitation temperature on the aggregation/agglomeration of $GdFeO_3$ nanocrystals

To define the impact of co-precipitation temperature on the aggregation/agglomeration of $GdFeO_3$ nanocrystals, the comparison of crystallite (PXRD) vs aggregate (ASA) vs agglomerate (LD) sizes was performed and summarized in Fig. 7.

Presented results indicate that different levels of the spatial organization of a substance (nanocrystals, aggregates of nanocrystals, agglomerates of aggregates) depend on the co-precipitation temperature to varying degrees:

The first organization level (nanocrystals) seems to have a moderate correlation with this parameter, since the chemical composition and structure of co-precipitated hydroxides are different (see 3.1 and 3.2 subsection for details).

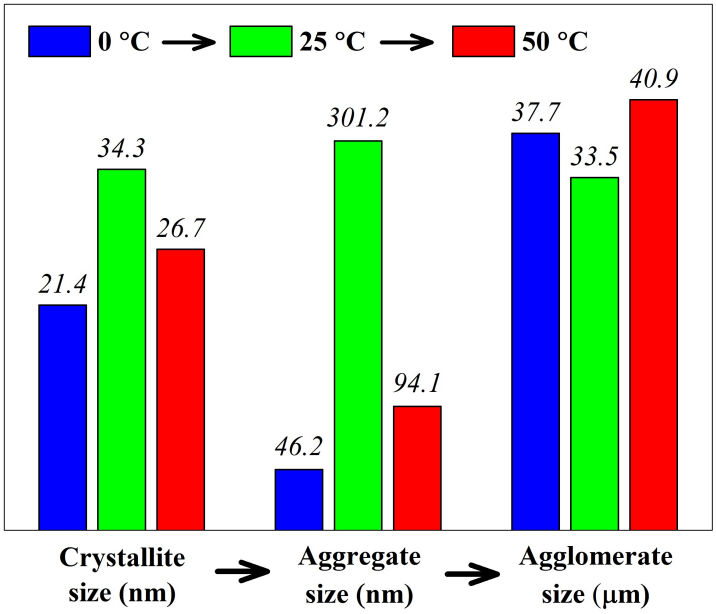

FIG. 7. Comparison of average crystallite (PXRD), aggregate (ASA) and agglomerate (LD) sizes for $GdFeO_3$ samples synthesized via co-precipitation at different temperatures followed by the thermal treatment in air. Dependencies of the corresponding sizes are given in independent scales for clarity and comparison

It is explained by the fact that the size of the critical nucleus, solubility, the degree of saturation, and the diffusion rate in the system grow with an increasing temperature that leads to a difference in the size of the amorphous hydroxide particles. During the subsequent thermal treatment at constant temperature and sintering time, the chemical, structural, and morphological differences lead to the noticeable difference in average crystallite size for the resulting $GdFeO_3$ nanocrystals. However, the solid-phase reaction of the components mentioned above smooths the difference in the synthetic prehistory between initial hydroxides, and as a result, weakly affects the $GdFeO_3$ formation rate.

The second organization level (aggregates of nanocrystals) has the highest dependence on the co-precipitation temperature, since the aggregate formation is mainly a result of aggregation of the initial hydroxide particles immediately after co-precipitation. The process of aggregation of hydroxide particles is higher, the lower the absolute value of the charge of their surface, which, as it is well-known, has a non-monotonic temperature dependence [30]. That is why for the 25 °C co-precipitation temperature, with apparently minimal surface charge, the average aggregate size is the highest in the GFO-series.

The third organization level (agglomerates of aggregates) shows the weakest dependence on the co-precipitation temperature, which is explained by the weak nature of the interparticle interaction forces that hold the aggregates of nanocrystals in the form of larger agglomerates. As it is well-known, these forces are not different enough due to the same nature of the $GdFeO_3$ surface. So, observed dependences indicate that crystallite and aggregate sizes can be effectively controlled by the temperature conditions of co-precipitation while the agglomerate size cannot.

4. Conclusions

As a result of the work, hierarchically organized $GdFeO_3$ nanopowders were synthesized via simple co-precipitation followed by thermal treatment. Their structural organization includes $GdFeO_3$ nanocrystals (first level), aggregates of nanocrystals (second level) and agglomerates of aggregates (third level). It was shown that co-precipitation temperature has a moderate impact on crystallite size, a strong impact on aggregate size and a weak impact on agglomerate size. The possible reasons for these effects were suggested and discussed in the work that makes it possible to synthesize nanocrystalline $GdFeO_3$ powders with the desired structural organization and potentially controllable functional properties.

Acknowledgements

The research was supported by the Russian Science Foundation (project No. 19-73-00286). The study was partially performed on equipment of the Engineering Center of Saint Petersburg State Institute of Technology. The

authors acknowledge D.P. Danilovich (EDXS, DTA-TGA, LD) and M.I. Chebanenko (ASA) for their help with the physicochemical characterization of the samples.

References

[1] Tretyakov Y.D. Development of inorganic chemistry as a fundamental for the design of new generations of functional materials. *Russian Chemical Reviews*, 2004, **73**(9), P. 831–846.

[2] Storozhenko P.A., Guseinov S.L., Malashin S.I. Nanodispersed powders: Synthesis methods and practical applications. *Nanotechnologies in Russia*, 2009, **4**(5-6), P. 262–274.

[3] Kuznetsov S.V., Osiko V.V., Tkatchenko E.A., Fedorov P.P. Inorganic nanofluorides and related nanocomposites. *Russian Chemical Reviews*, 2006, **75**(12), P. 1065–1082.

[4] Sadovnikov S.I., Gusev A.I., Rempel A.A. Nanostructured lead sulfide: synthesis, structure and properties. *Russian Chemical Reviews*, 2016, **85**(7), P. 731–758.

[5] Bukhtiyarova M.V. A review on effect of synthesis conditions on the formation of layered double hydroxides. *Journal of Solid State Chemistry*, 2019, **269**(June 2018), P. 494–506.

[6] Pinkas J., Reichlova V., Serafimidisova A., Moravec Z., Zboril R., Jancik D., Bezdicka P. Sonochemical Synthesis of Amorphous Yttrium Iron Oxides Embedded in Acetate Matrix and their Controlled Thermal Crystallization toward Garnet ($Y_3Fe_5O_{12}$) and Perovskite ($YFeO_3$) Nanostructures. *The Journal of Physical Chemistry C*, 2010, **114**(32), P. 13557–13564.

[7] Meskin P.E., Gavrilov A.I., Maksimov V.D., Ivanov V.K., Churagulov B.P. Hydrothermal/microwave and hydrothermal/ultrasonic synthesis of nanocrystalline titania, zirconia, and hafnia. *Russian Journal of Inorganic Chemistry*, 2007, **52**(11), P. 1648–1656.

[8] Popkov V.I., Almjasheva O.V. Formation Mechanism of $YFeO_3$ Nanoparticles under the Hydrothermal Conditions. *Nanosystems: Physics, Chemistry, Mathematics*, 2014, **5**(5), P. 703–708.

[9] Tugova E.A., Karpov O.N. Nanocrystalline perovskite-like oxides formation in Ln_2O_3-Fe_2O_3-H_2O (Ln = La, Gd) systems. *Nanosystems: Physics, Chemistry, Mathematics*, 2014, **5**(6), P. 854–860.

[10] Popkov V.I., Almjasheva O.V., Schmidt M.P., Gusarov V. V. Formation mechanism of nanocrystalline yttrium orthoferrite under heat treatment of the coprecipitated hydroxides. *Russian Journal of General Chemistry*, 2015, **85**(6), P. 1370–1375.

[11] Yapryntsev A.D., Baranchikov A.E., Ivanov V.K. Layered rare-earth hydroxides: a new family of anion-exchangeable layered inorganic materials. *Russian Chemical Reviews*, 2020, **89** (6), P. 629–666.

[12] Albadi Y., Sirotkin A.A., Semenov V.G., Abiev R.S., Popkov V.I. Synthesis of superparamagnetic $GdFeO_3$ nanoparticles using a free impinging-jets microreactor. *Russian Chemical Bulletin*, 2020, **69**(7), P. 1290–1295.

[13] Rempel A.A. Nanotechnologies . Properties and applications of nanostructured materials. *Russian Chemical Reviews*, 2007, **76**(5), P. 435–461.

[14] Nikam A.V., Prasad B.L.V., Kulkarni A.A. Wet chemical synthesis of metal oxide nanoparticles: a review. *CrystEngComm*, 2018, **20**(35), P. 5091–5107.

[15] Albadi Y., Martinson K.D., Shvidchenko A.V., Buryanenko I.V., Semenov V.G., Popkov V.I. Synthesis of $GdFeO_3$ nanoparticles via low-temperature reverse co-precipitation: the effect of strong agglomeration on the magnetic behavior. *Nanosystems: Physics, Chemistry, Mathematics*, 2020, **11**(2), P. 252–259.

[16] Ivanova O.S., Teplonogova M.A., Yapryntsev A.D., Baranchikov A.E., Ivanov V.K. Hydrothermal Microwave Synthesis of MnO_2 in the Presence of Melamine: The Role of Temperature and pH. *Russian Journal of Inorganic Chemistry*, 2018, **63**(6), P. 708–713.

[17] Nguyen A., Nguyen N., Mittova I., Perov N., Mittova V., Hoang T., Nguyen V., Nguyen V., Pham V., Bui X. Crystal structure, optical and magnetic properties of $PrFeO_3$ nanoparticles prepared by modified co-precipitation method. *Processing and Application of Ceramics*, 2020, **14**(4), P. 355–361.

[18] Tien N.A., Mittova I.Y., Almjasheva O.V., Kirillova S.A., Gusarov V.V. Influence of the preparation conditions on the size and morphology of nanocrystalline lanthanum orthoferrite. *Glass Physics and Chemistry*, 2008, **34**(6), P. 756–761.

[19] Tien N.A., Mittova I.Y., Almjasheva O.V. Influence of the synthesis conditions on the particle size and morphology of yttrium orthoferrite obtained from aqueous solutions. *Russian Journal of Applied Chemistry*, 2009, **82**(11), P. 1915–1918.

[20] Xu H., Hu X., Zhang L. Generalized Low-Temperature Synthesis of Nanocrystalline Rare-Earth Orthoferrites $LnFeO_3$ (Ln = La, Pr, Nd, Sm, Eu, Gd). *Crystal Growth and Design*, 2008, **8**(7), P. 2061–2065.

[21] Popkov V.I., Tugova E.A., Bachina A.K., Almjasheva O.V. The formation of nanocrystalline orthoferrites of rare-earth elements $XFeO_3$ (X = Y, La, Gd) via heat treatment of coprecipitated hydroxides. *Russian Journal of General Chemistry*, 2017, **87**(11), P. 2516–2524.

[22] Li L., Wang X., Lan Y., Gu W., Zhang S. Synthesis, Photocatalytic and Electrocatalytic Activities of Wormlike $GdFeO_3$ Nanoparticles by a Glycol-Assisted Sol–Gel Process. *Industrial and Engineering Chemistry Research*, 2013, **52**(26), P. 9130–9136.

[23] Li L., Wang X. Self-propagating combustion synthesis and synergistic photocatalytic activity of $GdFeO_3$ nanoparticles. *Journal of Sol-Gel Science and Technology*, 2016, **79**(1), P. 107–113.

[24] Kryuchkova T.A., Sheshko T.F., Kost' V.V., Chislova I.V., Yafarova L.V., Zvereva I.A., Lyadov A.S. Dry Reforming of Methane over $GdFeO_3$-Based Catalysts. *Petroleum Chemistry*, 2020, **60**(9), P. 1052–1058.

[25] Li X., Duan Z.-Q. Synthesis of $GdFeO_3$ microspheres assembled by nanoparticles as magnetically recoverable and visible-light-driven photocatalysts. *Materials Letters*, 2012, **89**, P. 262–265.

[26] Deka S., Saxena V., Hasan A., Chandra P., Pandey L.M. Synthesis, characterization and in vitro analysis of α-Fe_2O_3-$GdFeO_3$ biphasic materials as therapeutic agent for magnetic hyperthermia applications. *Materials Science and Engineering: C*, 2018, **92**, P. 932–941.

[27] Pinho S.L.C., Amaral J.S., Wattiaux A., Duttine M., Delville M.-H., Geraldes C.F.G.C. Synthesis and Characterization of Rare-Earth Orthoferrite $LnFeO_3$ Nanoparticles for Bioimaging. *European Journal of Inorganic Chemistry*, 2018, **2018**(31), P. 3570–3578.

[28] Tugova E.A., Zvereva I.A. Formation Mechanism of $GdFeO_3$ Nanoparticles under the Hydrothermal Conditions. *Nanosystems: Physics, Chemistry, Mathematics*, 2013, **4**(6), P. 851–856.

[29] Ivanov V.K., Fedorov P.P., Baranchikov A.Y., Osiko V.V. Oriented attachment of particles: 100 years of investigations of non-classical crystal growth. *Russian Chemical Reviews*, 2014, **83**(12), P. 1204–1222.

[30] Yam C.H., Lee C.H., Siu Y.S., Ho K.M., Li P. Synthesis of dual stimuli-responsive amphiphilic particles through controlled semi-batch emulsion polymerization. *Polymer (Guildf)*, 2016, **106**, P. 294–302.

NANOSYSTEMS: PHYSICS, CHEMISTRY, MATHEMATICS, 2021, 12 (2), P. 232–245

Synthesis of nanostructured composite materials of MoO_3/TiO_2–SiO_2 with spherical shape prepared with resins

S. A. Kuznetsova[1], O. S. Khalipova[1], K. V. Lisitsa[1], A. A. Ditts[2], A. G. Malchik[2], V. V. Kozik[1]

[1]National Research Tomsk State University, Lenin, 36, Tomsk, 634050 Russia

[2]National Research Tomsk Polytechnic University, Lenin, 30, Tomsk, 634050 Russia

onm@mail.tsu.ru

DOI 10.17586/2220-8054-2021-12-2-232-245

The aim of this work was to synthesize of nanostructured MoO_3/TiO_2–SiO_2 composites with hollow spherical shape by thermal decomposition of anion exchangers saturated with $Mo_7O_{24}^{6-}$ ions and treated with the TBT–TEOS sol. The effect of the kinetics (Kissinger and the Metzger-Horowitz methods) of thermal decomposition of resins of porous and gel structures on the size of MoO_3 nanoparticles and the strength of MoO_3/TiO_2–SiO_2 spheres was shown. The formation of dense spherical nanostructured agglomerates of the composite is facilitated by reactions occurring at the interface between the phases of cylindrical and spherical symmetry when using an anion exchange resin with a porous structure. The decomposition reactions of the anion-exchange resin of the gel structure, accompanied by random nucleation, lead to the formation of hollow spherical agglomerates of the composite with cracks on the surface. The materials were characterized by DSC–TGA, XRD and SEM.

Keywords: MoO_3/TiO_2–SiO_2; metal oxide; anion-exchange resin; decomposition; hollow sphere.

Received: 18 February 2021

Revised: 19 March 2021

1. Introduction

Hollow spheres of metal oxides are intensively investigated for applications, such as controlled release capsules for drugs, fillers, filters [1], gas sensitive materials [1, 2], absorbents and separation materials, especially for fixed-bed reactors or chromatography columns [3]. In recent years, hollow spheres of metal oxides have also been intensively investigated for applications as catalysts [3–7]. This is because metal oxide with hollow micro and nanospheres only has low density and good porous structure (usually contain both mesopores and macropores [3]), but also provides a high surface area with more active acid-base oxide centers on the pore surface [4].

Many approaches to the preparation of oxide materials with spherical form of agglomerates have been proposed to date, such as emulsion approaches [8], spray pyrolysis techniques [2], and templating synthesis [1]. Among these numerous techniques of hollow spheres production, thermal decomposition of ion-exchange resins loaded with the metal ions is the most attractive one due to its simplicity, ease for scale–up (in industry), and high quality resulting materials [1, 4, 5]. In addition, templates and precursors are all commercially available and inexpensive. Moreover, it has been reported [4] that using ion-exchange resin as a template can promote the formation of crystalline framework with high structural stability in spherical agglomerates that can endure high temperature and other rigorous conditions. This method was used for the first time for preparing plutonium oxide microspheres as early as 1989 [9]. Later it was successfully applied to obtain spherical particles of Fe_2O_3 [3, 10], porous Al_2O_3, TiO_2 [3] and ZrO_2/Al_2O_3 macrobeads [4], MoO_3 microspheres [1] and TiO_2–SiO_2/M_xO_y (M = Co, Cr) [6] and MoO_3–TiO_2–SiO_2 composites [5]. Resins with various compositions and structures were used in these studies. Wang et al. [3] have reported a method of preparing Fe_2O_3, Al_2O_3, TiO_2 macrobeads using a cation-exchange resin with sulfonic acid groups as templates and aqueous solutions of metal salts as precursors. In a follow-up work, Wang et al. [4] have reported a method to prepare porous ZrO_2 and ZrO_2/Al_2O_3 macrobeads using cation exchange resins with sulfonate groups as templates (D72 in H^+ – type, poly (styrene-co-divinylbenzene) – matrix). Wang et al. [3] have shown that the loading content of metal ions plays a key role in the preparation of metal oxide macrobeads with uniformity and integrity. Li et al. [1] have successfully prepared hollow MoO_3 microspheres by using anion exchange resin spheres Dowex 2 (Sigma Company) in carbonated form and 12-molybdodiphosphoric acid solution (1 M, $H_3PMo_{12}O_{40}$) as precursors. In their work [1], it was shown that the choosing of appropriate calcination temperature is important to obtain hollow spheres. If the temperature was increased to above 650 °C, no hollow spheres but white needle crystals form. In addition, they reported that the heating temperature should not be raised too rapidly, otherwise the gas resulting from the organic resin decomposition and oxidation created pressure which breaked the sphere shells.

Despite numerous studies, there is no explanation which allows us to obtain strong spheres of oxide composites by the thermal decomposition of ion-exchange resins. It is still an urgent problem to select an ion-exchange resin, which allows one to obtain agglomerates with strong spherical form. We believe that the formation of strong spherical

agglomerates is primarily influenced by the mechanism of thermal destruction of the ion-exchange resin. In a previous study [5], we demonstrated a route to prepare spherical particles of MoO_3–TiO_2–SiO_2 composites using TOKEM-400 and TOKEM-840 anion-exchange resins of the gel structure. It was established that the resin type influenced the surface morphology of the composites. Materials based on molybdenum(VI) and titanium(IV) oxides are very important because of their wide applications in gas sensors, solar cells, supercapacitors; electrochromic and photochromic materials, and catalysts [11–18]. Silicon (IV) oxide was chosen as a binder for the formation of mechanically strong spheres. Although several efforts have been reported to study the kinetics of the thermal decomposition of ion-exchange resins [19, 20], the study on spheres formation as a result of thermal decomposition of ion-exchange resins preliminarily loaded with the metal ions is still limited. The scientific literature contains information on molybdenum-containing polymer-salt precursors, which shows the effect of the polymer composition on their thermal stability and properties of the obtained oxide compositions based on molybdenum oxides [21–23].

The aim of this study was to determine how the decomposition kinetics of anion-exchange resins TOKEM-320Y and TOKEM-400 influences the formation of the MoO_3/TiO_2–SiO_2 nanocomposites with spherical shape of agglomerates. The detailed analysis of thermal decomposition of anion-exchange resins preliminarily loaded with the $Mo_7O_{24}^{6-}$ ions with the applied $Ti(C_4H_9O)_4$ – $Si(C_2H_5O)_4$ – C_4H_9OH sol and structural and morphological characteristics of prepared nanocomposites was carried out. The kinetics of the thermal decomposition of resins in hydroxyl form were also studied in the same conditions.

2. Experimental

2.1. Preparation of composites

The preparation of composites based on MoO_3/TiO_2–SiO_2 with spherical shape of agglomerates was done according to the procedure, which was proposed in our previous works [5, 7]. In the first step, TOKEM-320Y and TOKEM-400 anion-exchange resins preliminarily loaded with $Mo_7O_{24}^{6-}$ ions were prepared. Weakly basic anion exchangers consisting of the styrene–divinylbenzene matrix (TOKEM-320Y) and polyacrylate matrix (TOKEM-400) with tertiary amine in the hydroxyl form manufactured by PO Tokem (Kemerovo, Russia) were used as organic matrices. These resins consist of spherical granules of 0.40–1.25 mm size. The anion exchangers were placed in a saturated aqueous solution of $(NH_4)_6Mo_7O_{24}{\cdot}4H_2O$ (0.24 M) (Yugraktiv, Russia) at room temperature for 24 h with continuous stirring on a magnetic stirrer. The resins were then filtered off, washed with a small amount of water, and dried at 60°C to constant weight in air. The synthesized samples were designated as $Mo_7O_{24}^{6-}$ (320Y) and $Mo_7O_{24}^{6-}$ (400).

In the second stap, the dried resins loaded with $Mo_7O_{24}^{6-}$ ions were placed in the sol based on tetrabutoxytitanium (TBT, Acros, USA) and tetraethoxysilane (TEOS, Ecos-1, Russia). The aggregatively stable sol was prepared in accordance with a procedure proposed earlier by Shamsutdinova et al. [24, 25]. The mixture of TBT and TEOS was dissolved in a solution consisting of C_4H_9OH (Ecos-1, Russia), H_2O and HNO_3. The solute concentrations of TBT, TEOS and HNO_3 were 0.1; $2.2{\cdot}10^{-2}$ and $2.5{\cdot}10^{-3}$ mol L^{-1} respectively (initial HNO_3 concentration was 70 wt. %). The composition was selected based on the earlier study [5]. The sol was kept at room temperature for 3 days. After applying the sol onto the prepared $Mo_7O_{24}^{6-}$ (320Y) and $Mo_7O_{24}^{6-}$ (400) samples, they were dried at 60°C to constant weight. The samples were denoted as TBT–TEOS/$Mo_7O_{24}^{6-}$ (320Y) and TBT–TEOS/$Mo_7O_{24}^{6-}$ (400).

At the last stage, the dried samples were annealed at 350°C for 6 h and at 500°C for 5 h. The heating rate of the muffle furnace was 14 deg min^{-1}. The MoO_3/TiO_2–SiO_2 composites with spherical shape of agglomerates were formed and denoted as MoO_3/TiO_2–SiO_2 (320Y) and MoO_3/TiO_2–SiO_2 (400).

2.2. Characterization

The working range of pH of the TOKEM-320Y and TOKEM-400 resins in which they exhibit the maximal exchange capacity was determined by potentiometric titration [26]. Potentiometric titration was performed by the method of individual batches. The series of 0.1 g portions of the resins in the OH form were placed in glass flasks (volume 50 mL) with glass stopper and poured of the HCl with various concentrations. The ionic strength of solution was kept at 0.1 by adding NaCl. The total solution volume was 20 mL. The range of acid concentrations was from 0 to 12 mmol g^{-1} (C_{init} = 0.1 mol L^{-1})). After the equilibrium was attained (24 h), the pH value of the equilibrium solutions was measured with an I-160 MI pH meter (ESK-1062 combined glass electrode). The titration curve in the pH–titrant amount (HCl, mmol g^{-1} resin) coordinates was obtained.

The total static ion exchange capacity was determined as described in our previously work [5]. Portions (0.1 g) of the air-dry resin (TOKEM-320Y or TOKEM-400) in the OH form were placed in Erlenmeyer flasks, poured over with 25 mL of 0.1 mol L^{-1} HCl, and left for a week to attain the equilibrium. The solution was then separated from the resin, and the decrease in the HCl concentration was determined by titration with 0.1 mol L^{-1} NaOH in the presence

of the mixed indicator until the green color of the solution changed to pink. The total ion exchange capacity (TEC, mmol g^{-1} resin) was calculated by the equation:

$$TEC = \frac{(c_0 - c_1)\, V \cdot 100}{m\,(100 - W)}, \tag{1}$$

where c_0 is the initial HCl concentration (mol L^{-1}); c_1 is the HCl concentration after attaining the equilibrium (mmol L^{-1}); V is the HCl solution volume (L); m is the weight of the air-dry resin portion (g); and W is the weight fraction of moisture in the resin.

The determination of moisture content was carried out experimentally. A portion of the air-dry ion-exchange resin in the OH form was weighed and placed in a weighing bottle preliminarily dried to constant weight. The weighing bottle with sample was weighed, placed in an oven and dried at 100°C to constant weight. Then, the weighing bottle was allowed to cool to room temperature and weighed again. Before and after drying the weighing bottle with a resin was weighed on an analytical balance with an accuracy of 0.0001 g. The weight fraction of moisture in the resin ($W\%$) was defined as follows:

$$W = \frac{(m_1 - m_2)}{m_1} \cdot 100, \tag{2}$$

where m_1 and m_2 are the weights of the swollen and dry resin (g), respectively.

The $Mo_7O_{24}^{6-}$ concentration in the initial and equilibrium solutions after the sorption was determined gravimetrically [5, 27] by precipitation of $Mo_7O_{24}^{6-}$ ions in the form of $PbMoO_4$.

The main stages of composites formation and the temperature conditions of the samples annealing were chosen on the basis of thermal analysis of TOKEM-320Y, TOKEM-400 and anion-exchange resins preliminarily loaded with $Mo_7O_{24}^{6-}$ ions and treated with the $Ti(C_4H_9O)_4$ – $Si(C_2H_5O)_4$ – C_4H_9OH sol. Synchronous thermal analysis was conducted using an STA 449 F1 Jupiter thermoanalyzer interfaced with a QMS 403 Aolos gas mass spectrometer (Netzsch-Gertebau GmbH, Germany). The samples were heated in air in the temperature interval from 25 to 1000°C and a heating rate of 7, 10, and 12 deg min^{-1}, respectively. The measurements for each sample were conducted twice. The kinetic parameters of the decomposition of anion exchangers were established by using Kissinger and Metzger-Horowitz methods. According to the Kissinger method [28–31], at a constant rate of heating of a solid substance, the maximum decomposition rate (β) of a substance is achieved at temperature ($T_{\max}$), which is related by the equation:

$$\frac{d\left(\ln \frac{\beta}{T_{\max}^2}\right)}{d\left(\frac{1}{T_{\max}}\right)} = -\frac{E}{R} \tag{3}$$

Therefore, the activation energy can be calculated from the slope of the line between $\ln\left(\frac{\beta}{T_{\max}^2}\right)$ and $\frac{1}{T_{\max}}$. In equation (3), the activation energy is independent of the order of the reaction. The reaction order (n) can be calculated from shape index (S) of endothermic or exothermic peaks (Fig. 1) as follows:

$$n = 1.26 \cdot S^{0.5}, \tag{4}$$

$$S = \frac{a}{b}. \tag{5}$$

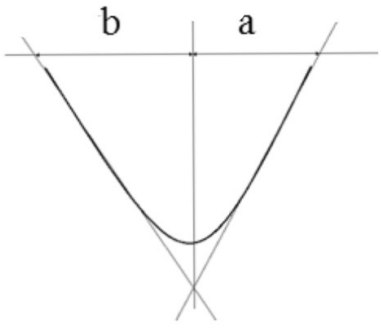

FIG. 1. Shape index for typical endothermic DSC peak

TABLE 1. The properties of TOKEM-400 and TOKEM-320Y anion-exchange resins

Resin	SC ± 0.06, mmol-equiv g^{-1}	TEC ± 0.2, mmol-equiv g^{-1}	W ± 0.3, %
TOKEM-400	6.64	9.2	29.1
TOKEM-320Y	1.97	7.2	51.0

The activation energy can be calculated by the Metzger-Horowitz method [32]. The Metzger-Horowitz equation is as follows:

$$\frac{(1-\alpha)^{1-n}-1}{1-n} = -\frac{RT_{\max}^2}{Ea}\exp\left[-\frac{Ea}{RT}\left(1-\frac{\Theta}{T_{\max}}\right)\right], \tag{6}$$

where Θ – the difference between the maximum temperature and the current temperature, α – degree of conversion.

If the reaction order is known, one can determine the activation energy from the angle of the straight line, obtained in a graphical dependence $\dfrac{(1-\alpha)^{1-n}-1}{1-n}$ on Θ. When $\Theta = 0$, that is, if the decomposition reaction rate reaches a maximum, then $(1-\alpha_{\max}) = n^{1/(1-n)}$. The reaction order determined by the Kissenger method was used to calculate the activation energy by the Metzger-Horowitz method. The kinetic equation for each stage of decomposition of the sample was selected by the Shatava method [33]. The linearity of the function $\log(\alpha)$ versus $\dfrac{1}{T}$ for the selected kinetic equation on the linearity segment of the dependence of $-\log(\alpha)$ on $\dfrac{1}{T}$ was checked by trial and error. Of the several kinetic equations tested, one was selected for which the correlation coefficient was maximum.

The phase composition of the samples was determined by X-ray diffraction (XRD) using a Rigaku Miniflex 600 diffractometer (Rigaku, Japan) with CuKα radiation in the 2θ range 10° to 80°. The diffraction pattern was scanned by steps of 0.02° and recording rate of 2 deg min^{-1}. Resulting diffractograms were interpreted with JCPDS-ICDD diffraction database. The MoO_3 structure was refined by the Rietveld method by using the ReX powder diffraction program [34, 35]; the crystal structure model was constructed using the VESTA program [36].

The morphology of the samples was studied by scanning electron microscopy (SEM). The distribution of the elements on the surface was determined on the basis of energy-dispersive X-ray spectroscopic (EDS) analysis. It was performed on a Hitachi TM-3000 scanning electron microscope with a ShiftED 3000 electron microprobe (Hitachi High-Technologies Corporation, Japan).

3. Results and discussion

3.1. Properties of anion-exchangers

TOKEM-320Y and TOKEM-400 anion-exchangers have different structures and compositions. TOKEM-320Y is a weakly basic anion-exchange resin of porous structure with the styrene–divinylbenzene matrix and tertiary amine functional groups. TOKEM-400 is a weakly basic non-porous anion-exchange resin of gel structure with a polyacrylate matrix and tertiary amino functional groups. These resins are free bases that undergo dissociation in an aqueous solution as follows:

(TOKEM-320Y)

$[[–CH_2–CHC_6H_5–]_n–C_6H_4N(CH_3)_2OH–]_m \leftrightarrows [[–CH_2–CHC_6H_5–]_n–C_6H_4N(CH_3)_2–]_m + mOH^-$,

(TOKEM-400)

$[[–CH_2–CH(COOR)–]_n–C_6H_4N(CH_3)_2OH–]_m \leftrightarrows [[–CH_2–CH(COOR)–]_n–C_6H_4N(CH_3)_2–]_m + mOH^-$.

These resins are capable of ion exchange with $Mo_7O_{24}^{6-}$. The ion exchange reaction can be expressed as follow:

$[[–R–]_n–C_6H_4N(CH_3)_2OH–]_m + kMo_7O_{24}^{6-} = [–R–]_n–C_6H_4N(CH_3)_2(Mo_7O_{24})_k–]_m + aOH^-$.

The titration curves of anion-exchange resins are shown in Fig. 2.

One single pH drop on the titration curves indicates that the resins are monofunctional. The titration curves exhibit no ascents throughout the examined pH interval. This infers that there are no intramolecular interactions of the functional groups. The equivalence points coincide and correspond to a pH value of 4.6 for TOKEM-400 and TOKEM-320Y. Hence, the maximum exchange capacity of anion-exchange resins is realized at pH < 4.6. The pH of a saturated aqueous solution of ammonium paramolybdate corresponds to a value of 6.79 ± 0.03, which is within the working interval of the maximal capacity of the above anion-exchangers resins. The properties of the resins (sorption capacity of SC, total exchange capacity of TEC and moisture absorption W) are presented in Table 1.

The sorption capacity of the TOKEM-400 and TOKEM-320Y resins with respect to $Mo_7O_{24}^{6-}$ is less than the exchange capacity. This indicates that not all the OH^- groups of the resins participate in the exchange reaction. This

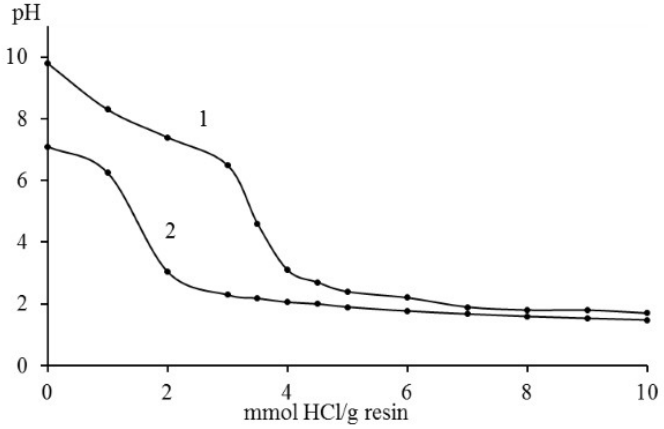

FIG. 2. Titration curves of OH forms of anion-exchange resins with HCl solution: (1) TOKEM-400 and (2) TOKEM-320Y

fact can be explained by an increase in the rigidity of the polymer framework from the surface to the center of the resin grain in swelling in the saturated solution and a decrease in the size of the voids between polymer chains, which leads to a decrease in the cell size between the chains of the polymer preventing penetration of bulky $Mo_7O_{24}^{6-}$ ions into the exchange sites.

The differential thermogravimetric (DTG) and thermogravimetric (TG) curves of TOKEM-320Y and TOKEM-400 resins are shown in Fig. 3.

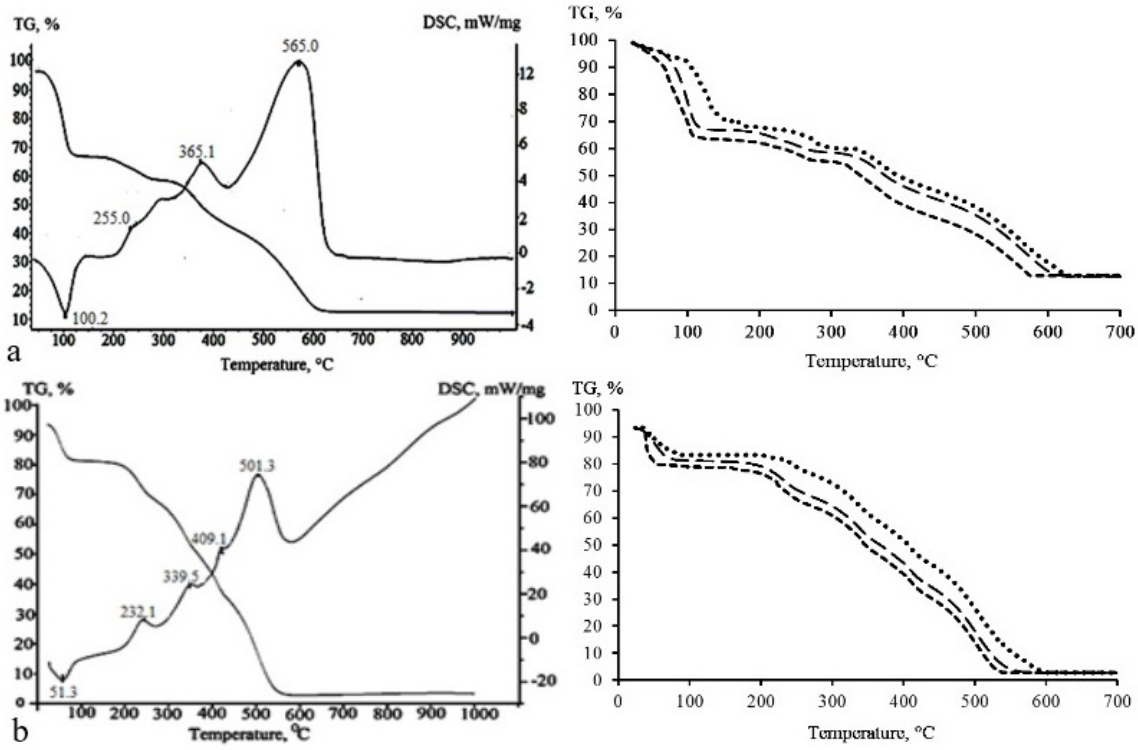

FIG. 3. Thermograms and TG-curves of degradation of resins (a) TOKEM-320Y, (b) TOKEM-400; at heating rates 7(- - -), 10(— — —), 12(····) deg min^{-1}

The shape of the thermograms suggests that TOKEM-320Y underwent four-step thermal decomposition and TOKEM-400 underwent five-step thermal decomposition. The peak temperatures T_{max} of each step with different heating rates are shown in Table 2. Kinetic parameters of thermal decomposition of resins by modified Kissinger

and Metzger-Horowitz methods have been determined. Kissinger plots were done using the data for $T_{\max}$ at various heating rates (Table 2). They are shown in Fig. 4.

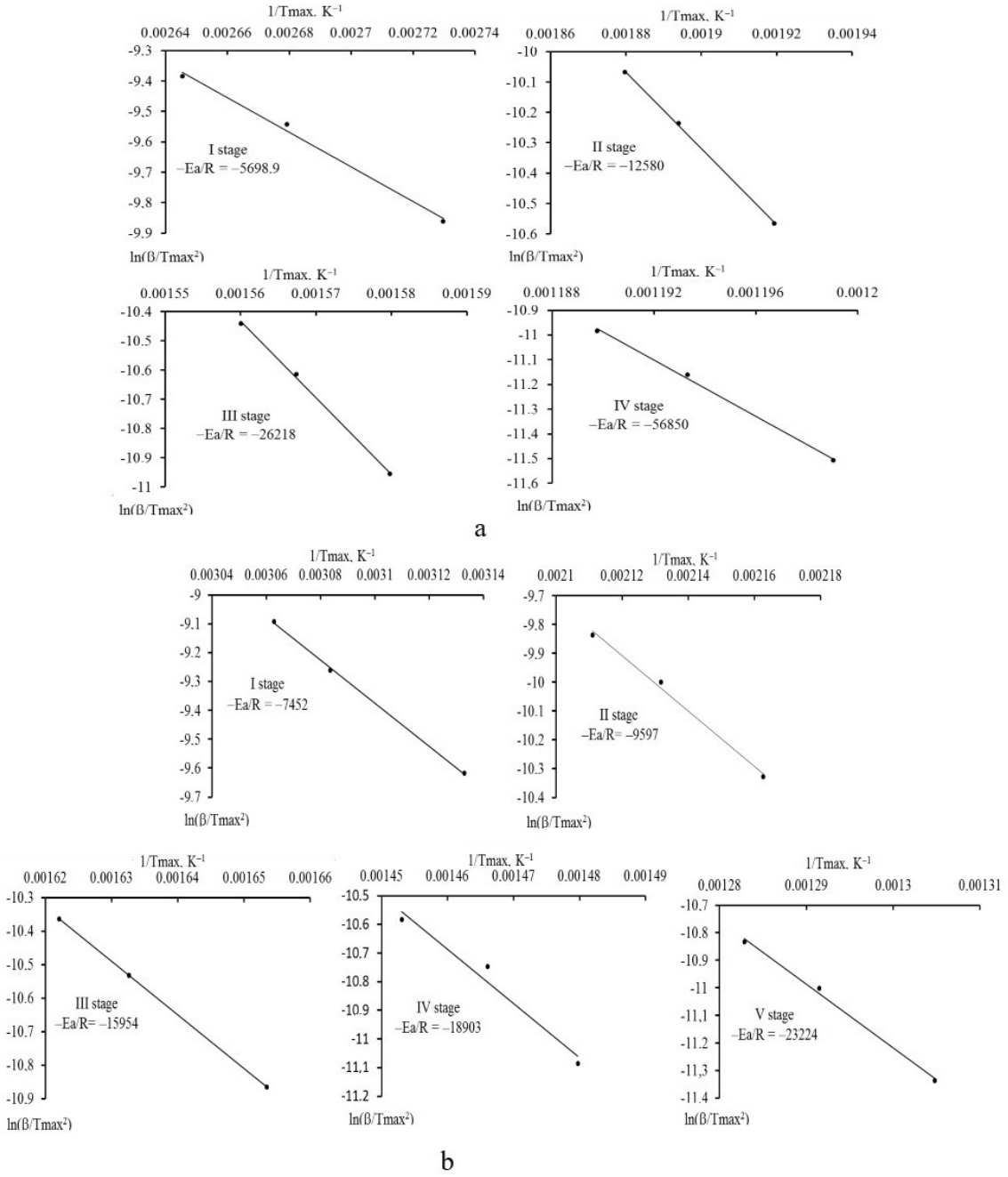

FIG. 4. Kissinger plots for the thermal decomposition of (a) TOKEM-320Y and (b) TOKEM-400 resins

The Metzger-Horowitz plots (Fig. 5) were performed for the thermograms of the TOKEM-320Y and TOKEM-400 decomposition at a rate of 10 deg min^{-1} using the values of the reaction order (n) which were determined by the Kissinger and calculated by the Metzger-Horowitz methods. The reaction order obtained by the Kissinger method was used to determine the activation energy by the Metzger-Horowitz method, since in this method there is an error in the determination of $(1-\alpha)_{T_{\max}}$, which may lead to an incorrect value of n. However, the value of n for all stages of thermal decomposition of the resins could not be determined by the Kissinger method since some lines on the DSC (differential scanning calorimetry) curve have no clearly defined basis: II stage for the TOKEM-320Y; III and IV

TABLE 2. The peak temperatures T_{max} of each step with different heating rates

Heating rate (β),°/min	Stage 1	Stage 2	Stage 3	Stage 4	Stage 5
	T_{max}, °C				
	TOKEM-320Y/TOKEM-400				
7	95.3 / 46.2	248.1 / 225.4	360.4 / 331.8	561.1 / 402.8	- / 493.4
10	100.2 / 51.3	255.0 / 232.1	365.1 / 339.5	565.0 / 409.1	- / 501.3
12	112.0 / 53.5	259.3 / 236.7	368.2 / 343.5	567.5 / 415.2	- / 506.5

TABLE 3. Kinetic parameters of the decomposition of TOKEM-320Y and TOKEM-400 resins

TOKEM-320Y					
Method / Stage	I 25–160 °C	II 160–325 °C	III 325–445 °C	IV 445–660 °C	V
Ea, kJ mol^{-1}					
Kissinger	47	105	218	473	no stage
Metzger-Horowitz	73/0.9	81/0.9	-	138/0.9	no stage
Metzger-Horowitz (n Kissinger)	69/0.9	-	168/1.4	115/0.6	no stage
TOKEM-400					
Method / Stage	I 25–100 °C	II 100–275 °C	III 275–365 °C	IV 365–450 °C	V 450–600 °C
Ea, kJ mol^{-1}					
Kissinger	62	80	133	157	193
Metzger-Horowitz	22/2.8	78/2.1	128/0.8	103/2.5	131/2.8
Metzger-Horowitz (n Kissinger)	63/1.0	76/2.0	-	-	80/1.2

stages for the TOKEM-400. The limitation of the applicability of the Metzger-Horowitz method does not allow us to determine the reaction order of the third stage of the TOKEM-320Y decomposition.

The kinetic parameters of each stage of thermal decomposition of the resins are presented in Table 3.

The activation energies for the first stage of the decomposition of the TOKEM-320Y and TOKEM-400 resins with endothermic effects as well as the mass spectra (Fig. 6) of their decomposition products suggest that at this stage the most mobile water molecules adsorbed on the resins were removed. Also, water molecules formed as a result of the destruction of weakly basic anion exchangers in the functional group were removed.

The Shatava method (Fig. 7) shows that the dehydration rate of resins is described by the Avrami kinetic equation $-\ln(1-\alpha) = k\tau$ and corresponds to the process of diffusion of water molecules through a layer of a solid phase with random nucleation and their growth. The activation energies of the second stage decomposition of the resins indicate chemical destruction of the anion-exchange resins matrix, which is accompanied with exothermic effects. As can be seen from the Fig. 6, at this stage, $C_3H_7^+$, $C_3H_4^+$ CH_3N^+ hydrocarbon fragments with mass numbers m/z=43, m/z=40, m/z=29 respectively were found in the gas phase from both resins.

In addition, the presence of CO (m/z=28) in the mass spectra of resins in the temperature range of the second stage was also observed, which indicates the oxidation of hydrocarbon structures. The decomposition rate of the TOKEM-320Y resin polymer matrix can be described by the equation with the maximum coefficient in the correlation

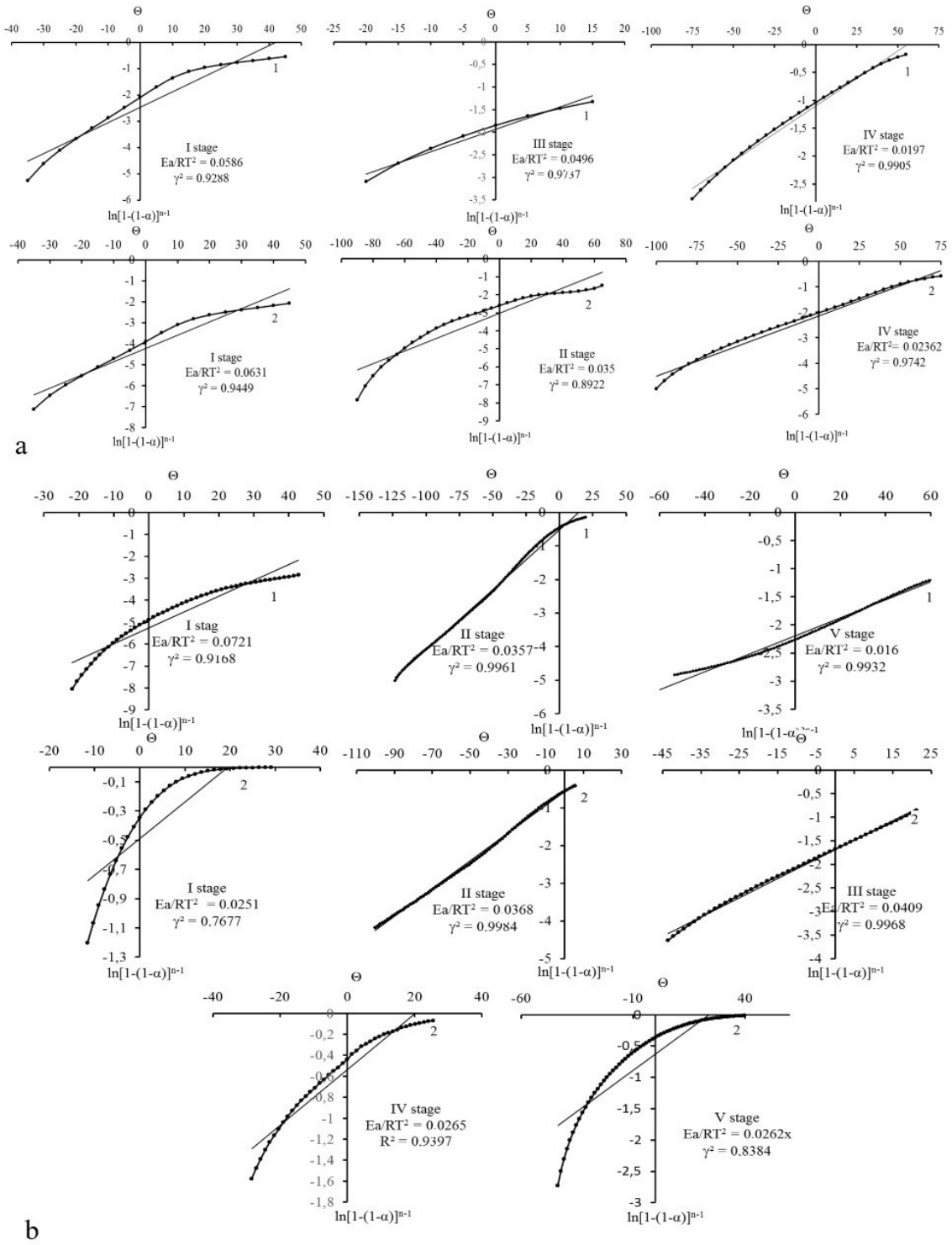

FIG. 5. Metzger-Horowitz plots for the decomposition of (a) TOKEM-320Y and (b) TOKEM-400 (reaction order (n) determined by the Kissinger (curves 1) and the Metzger-Horowitz (curves 2) methods)

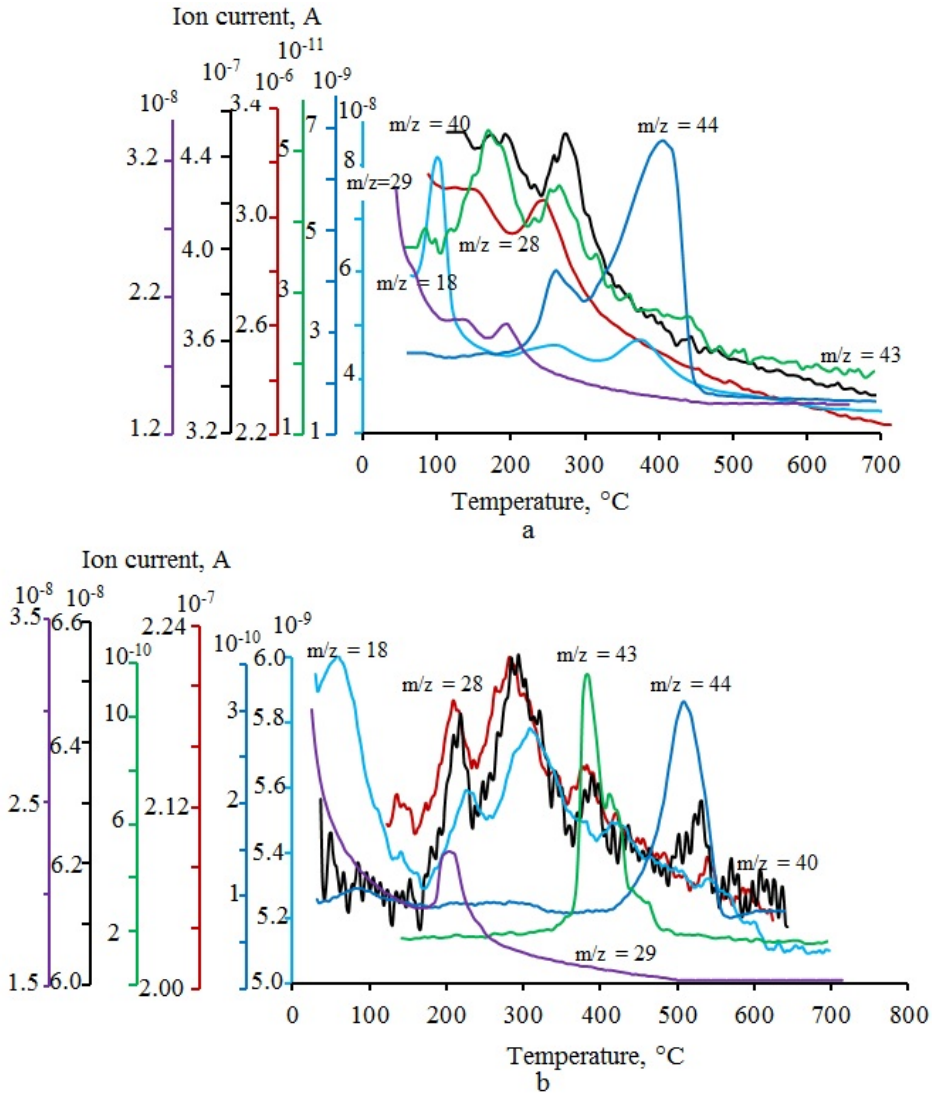

FIG. 6. Mass-spectrometric data for degradation products of the (a) TOKEM-320Y and (b) TOKEM-400 resins

coordinates of the linearity of the function $\log(g(\alpha))$ from $\frac{1}{T}\ 1-(1-\alpha)^{\frac{1}{2}} = k\tau$ which corresponds to the description of the reaction at the phase boundary of cylindrical symmetry. The decomposition of the TOKEM-400 resin polymer matrix is limited by a process that can be described using the Avrami equation (as well as in the first stap. See Fig. 5). Random nucleation is a limiting stage. The polymer matrix of the TOKEM-400 resin continues to decompose in the third stage as well. The rate of its decomposition cannot be described by the Shatava method because the kinetic equations of different mechanisms of heterogeneous processes in coordinates $[\log(g(\alpha))] - \left[\frac{1}{T}\right]$ have linear character with correlation coefficients R = 0.995–0.999. The rate of decomposition of the TOKEM-320Y resin polymer matrix is described by two equations for the third stap: the Yander equation $(1-(1-\alpha))^{\frac{1}{3}})^2 = k\tau$ and the reaction equation at the phase boundary of spherical symmetry $1-(1-\alpha)^{\frac{1}{3}} = k\tau$. At the fourth stage, the TOKEM-320Y anion exchange resin burns out with the formation of CO_2 and H_2O (Fig. 6) in the temperature range from 450 to 660°C. The limiting stage is described by the Avrami equation $-\ln(1-\alpha) = k\tau$ (Fig. 7).

3.2. Thermal analysis of TOKEM-320Y and TOKEM-400 resins with $Mo_7O_{24}^{6-}$ ions and treated with the TBT–TEOS sol

Thermograms of the decomposition of TOKEM-320Y and TOKEM-400 resins loaded with $Mo_7O_{24}^{6-}$ ions and treated with the TBT–TEOS sol are presented in Fig. 8. The one endothermic and four exothermic peaks (Fig. 8b)

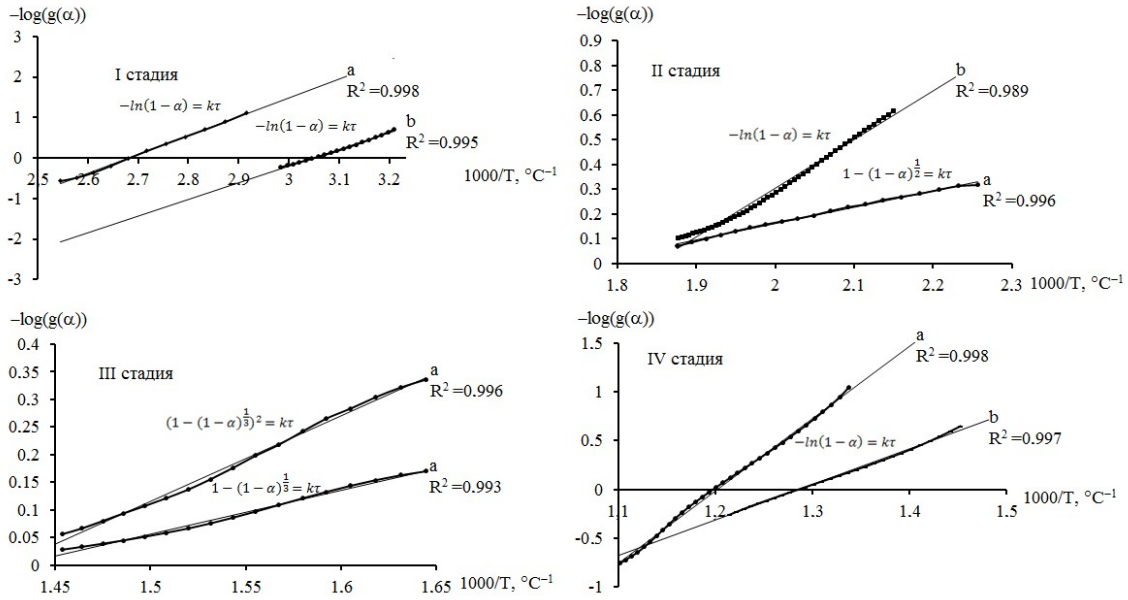

FIG. 7. The linearity of the function $\log(g(\alpha))$ of 1000/T for decomposition of (a) TOKEM-320Y and (b) TOKEM-400 resins

corresponding to the four stages of decomposition are observed on the thermogram of the decomposition of TOKEM-400 resin with $Mo_7O_{24}^{6-}$ ions and TBT–TEOS sol as well as on the thermogram of the decomposition of TOKEM-400 resin. Two high-temperature exothermic peaks with maxima at 485.1°C and 564.6°C, respectively, are observed in the fourth stage (450–600°C). Therefore in this temperature range, parallel decomposition reactions are observed, the total activation energy of which is 193 kJ/mol and the reaction order was 1.1 (Horowitz-Metzger method); 156 kJ/mol and 0.8 (Kissinger method). Mass spectra indicate that these reactions were reactions of the burning of hydrocarbon residues with the formation of CO (m/z = 28), CO_2 (m/z = 44) and H_2O (m/z = 18) (Fig. 6b). It is known, that ammonium paramolybdate decomposes in three stages, which are accompanied by endothermic effects [31]. The formation of MoO_3 began in the third stap above 290°C. The activation energy of this stage is 150 kJ/mol and the reaction order is ∼1. The decomposition of paramolybdate ion on the anion exchange resin cannot be established from the thermogram. The total process in the temperature range (162–360 °C, stap two), where, according to the literature the formation of molybdenum oxide begins, is accompanied by an exothermic peak and is characterized by an activation energy of 65 kJ/mol with the reaction order 1.1 (Horowitz-Metzger method); 74 kJ/mol and 0.8 (Kissinger method). In this temperature range, the formation of H_2O (m/z = 18), CO (m/z = 28) and hydrocarbon residues with (m/z = 40) were observed in the gas phase. The thermogram of the TBT–TEOS/$Mo_7O_{24}^{6-}$ (320Y) decomposition (Fig. 8a) indicates three stages, which were accompanied by one endothermic effect with a maximum of 93.8°C and exothermic effects that cannot be separated.

The Shatava method is not applicable to determine a suitable kinetic equation that would describe each stap of the thermolysis of TOKEM-400 and TOKEM-320Y resins loaded with $Mo_7O_{24}^{6-}$ ions and treated with the TBT–TEOS sol because the kinetic equations of different mechanisms of heterogeneous processes in coordinates $[\lg(g\alpha)] - \left[\frac{1}{T}\right]$ have linear character with correlation coefficients R = 0.995–0.999. The decomposition temperature, at which the thermolysis of the TBT–TEOS/$Mo_7O_{24}^{6-}$ (320Y) sample ends, is ≈500°C and for the TBT–TEOS/$Mo_7O_{24}^{6-}$ (400) sample is ≈600°C.

3.3. Phase composition, structure and surface morphology of oxide composites MoO_3/TiO_2–SiO_2

Phase compositions of the MoO_3/TiO_2–SiO_2 (320Y) and MoO_3/TiO_2–SiO_2 (400) composites obtained at 600°C were installed based on the results of XRD analysis. XRD patterns of the samples were identical. The XRD (Fig. 9) and refinement of the crystal structure by the Rietveld method indicate that the oxide composites are a mixture consisting of the main component of orthorhombic α-MoO_3 and an admixture of TiO_2 with an anatase structure. The diffraction lines of the samples belong to orthorhombic α-MoO_3 with the unit cell parameters $a = 1.387$, $b = 0.370$ and $c = 0.396$ nm. Based on the atomic coordinates, the structure of α-MoO_3 was visualized using the VESTA

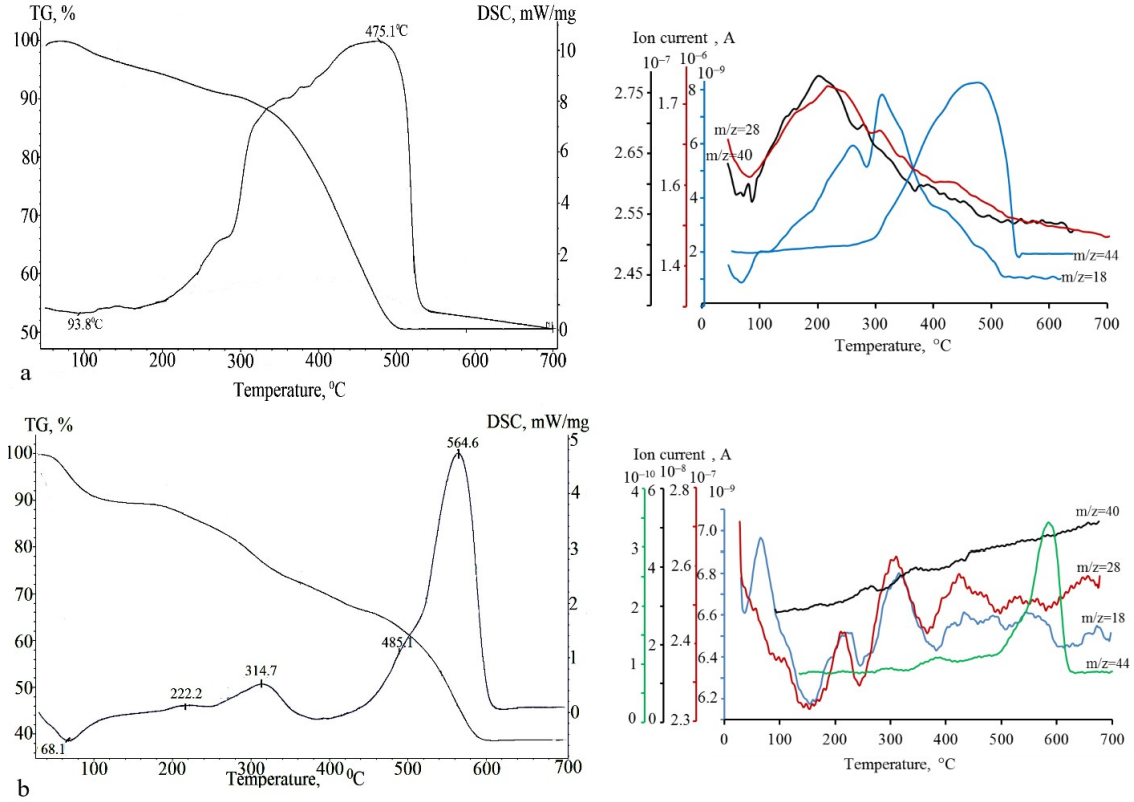

FIG. 8. Thermograms ($\beta = 10$ °C/min) and mass-spectrometric data for degradation products of (a) TBT–TEOS/$Mo_7O_{24}^{6-}$ (320Y) and (b) TBT–TEOS/$Mo_7O_{24}^{6-}$ (400) samples

program (Fig. 10). The samples obtained from different anion-exchange resins differ only in the grain size, which was estimated from the value of the coherent scattering region. The use of TOKEM-320Y resin makes it possible to obtain nanostructured composites with an average grain size of 25.6 nm, which form an agglomerate up to 7 μm. The use of TOKEM-400 resin leads to the formation of composite grains with an average size of 55.5 nm, the grains of which form sintered agglomerates up to 150 μm.

The structural characteristics are in good agreement with the literature data [37]. The presence of silicon oxide in the composites is confirmed by the results of MRSA (Fig. 11). X-ray emission spectra of MoO_3/TiO_2–SiO_2 (320Y) and MoO_3/TiO_2–SiO_2 (400) samples were identical. The spectrum contains characteristic lines corresponding to Mo, Ti, Si and O (Fig. 11). Consequently, the composites were a mixture of molybdenum and titanium crystalline oxides, as well as X-ray- amorphous silicon oxide.

SEM images show that the dense and non-destroyed spheres of the MoO_3/TiO_2–SiO_2 composites with diameters ranging from 0.3 to 0.5 mm were formed from the precursors with TOKEM-320Y resin (Fig. 12a). As can be seen from the micrograph (the sphere we have broken), spheres are hollow inside.

The surfaces of the MoO_3/TiO_2–SiO_2 (320Y) spheres consists of many lamellar particles of various sizes and shapes. The particle size is from 0.5 to 3 microns. These particles are arranged irregularly and their appearance indicates the presence of several phases. The presence of several phases on the surface is also observed for MoO_3/TiO_2–SiO_2 (400) sample (Fig. 12b). As can be seen from the micrograph, dense spheres are not formed. Fig. 12b (the broken spheres) clearly shows that these spheres are hollow inside. The surface of the destroyed and non-destroyed spheres consists of sintered particles and has a large number of cracks. In addition, unlike the spheres obtained from precursors with TOKEM-320Y, these spheres are easily destroyed by mechanical action.

4. Conclusion

The nanostructured MoO_3/TiO_2–SiO_2 composites with hollow spherical form were obtained by the method of thermal decomposition of anion exchangers (TOKEM-320Y – porous structure, TOKEM-400 – gel structure) saturated with $Mo_7O_{24}^{6-}$ ions and treated with the TBT–TEOS sol. The MoO_3/TiO_2–SiO_2 composite was a mixture of orthorhombic MoO_3, TiO_2 (anatase structure) and amorphous SiO_2. The presence of TiO_2 and SiO_2 in the composite

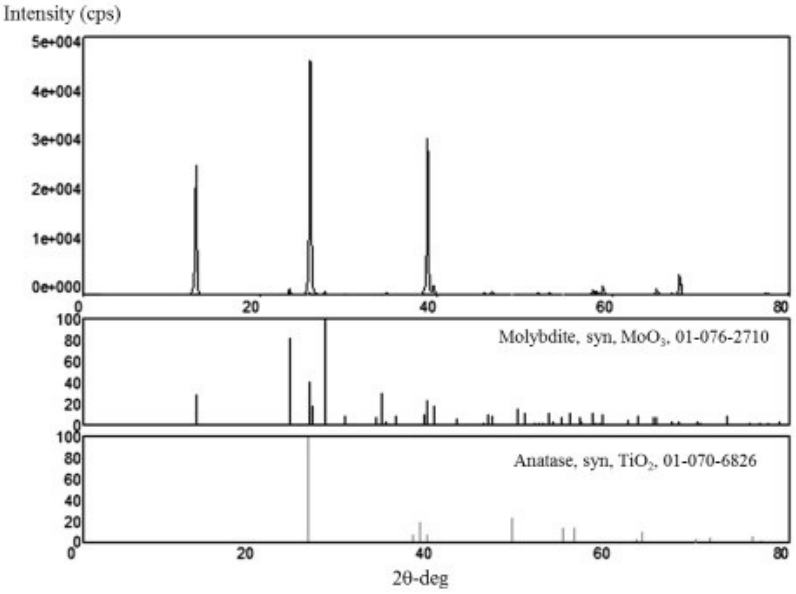

FIG. 9. X-ray diffraction patterns of prepared MoO_3/TiO_2–SiO_2 composites

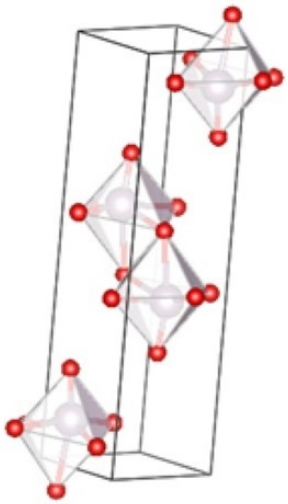

FIG. 10. Structure of α-MoO_3 (Pnma)

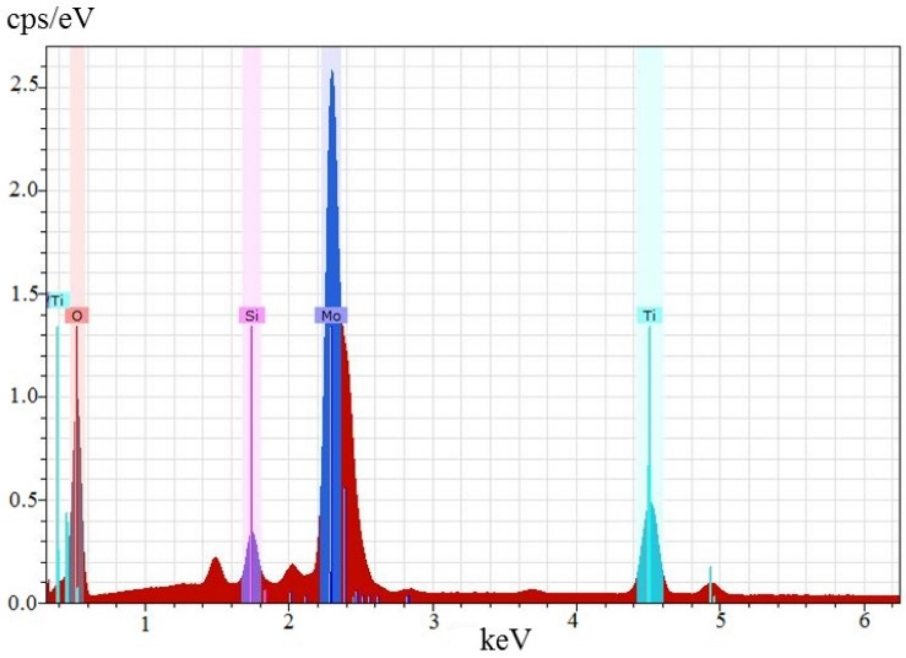

FIG. 11. X-ray emission spectrum of MoO_3/TiO_2–SiO_2 composites

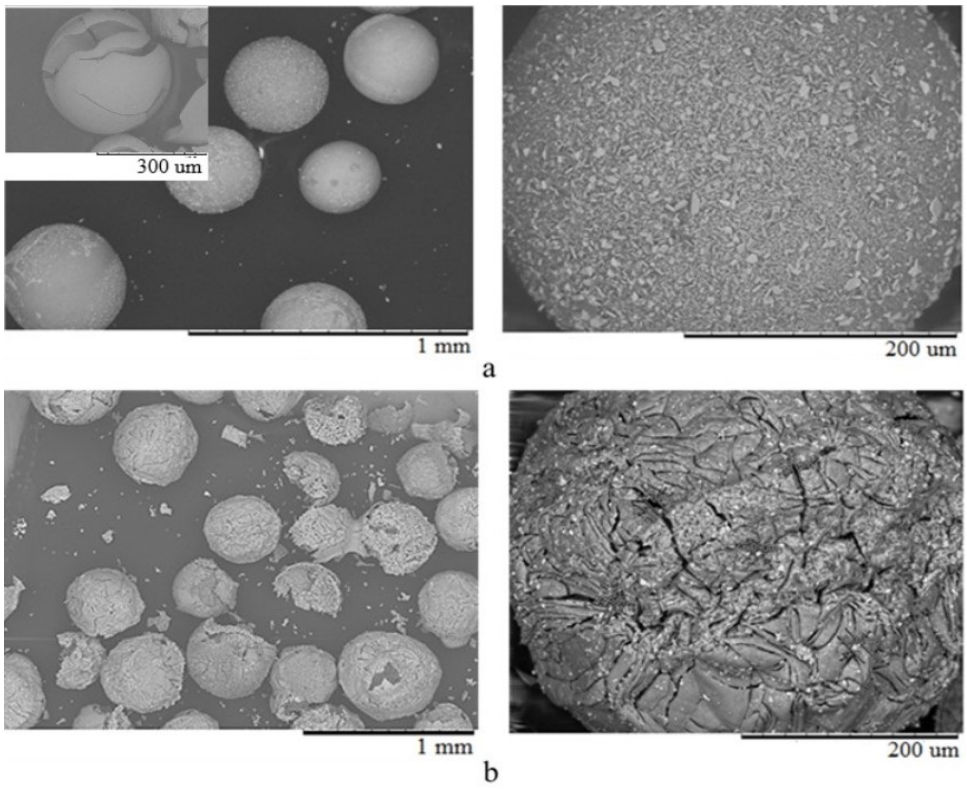

FIG. 12. Scanning electron micrographs of (a) $MoO_3/TiO_2–SiO_2$ (320Y) and (b) $MoO_3/TiO_2–SiO_2$ (400) composites

did not affect the MoO_3 structure. The decomposition kinetics of TOKEM-320Y and TOKEM-400 anion exchangers affected the surface morphology and strength of the spherical $MoO_3/TiO_2–SiO_2$ composites. Reactions and diffusive processed at the interface of cylindrical and spherical symmetries, where the velocity of the reaction boundary is the same in all directions contribute to the formation of dense spherical agglomerates. The decomposition reactions of the anion-exchange resin, accompanied with random nucleation, resulted in spherical agglomerates that had cracks on the surface. The activation energy of each stage of thermal destruction of anion exchange resins obtained by the Kissinger method slightly differed from the values of activation energies obtained by the Metzger-Horowitz method. However, there is a pattern, i.e., an increase in the decomposition temperature of resins leads to an increase in activation energy. The discrepancy between the reaction order by Shatava method and that by the Kissinger and Metzger-Horowitz methods proved the low sensitivity of the latter method in multistage processes. The reactions and diffusion proceeded at the interface of cylindrical and spherical symmetries, where the velocity of the reaction boundary was the same in all directions contributed to the formation of dense spherical agglomerates.

Acknowledgements

This work was performed within the framework of the government assignment of the Ministry of Science and Higher Education of the Russian Federation, project no. 0721-2020-0037.

References

[1] Li W.Z., Qin C.G., Xiao W.M., Sheng J. Preparation of hollow layered MoO_3 microspheres through a resin template approach. *J. Solid State Chem*, 2005, **178**, P. 390–394.

[2] Vladimirova E.V., Gyrdasova O.I., Dmitriev A.V. Synthesis of nanostructured hollow microspheres of vanadium (III, V) oxides. *Nanosystems: physics, chemistry, mathematics*, 2020, **11**(5), P. 572–577.

[3] Wang M.L., Wang C.H., Wang W. Porous macrobeads composed of metal oxide nanocrystallites and with percolated porosity. *J. Mater. Chem.*, 2007, **17**, P. 2133–2138.

[4] Wang M.L., Wang, C.H. Wang W. Preparation of porous ZrO_2/Al_2O_3 macrobeads from ion-exchange resin templates. *J. Mater. Sci.*, 2011, **46**, P. 1220–1227.

[5] Kuznetsova S.A., Brichkov A.S., Lisitsa K.V., Shamsutdinova A.N., Kozik V.V. Preparation and Properties of $MoO_3–TiO_2–SiO_2$ Composites with Spherical Shape of Agglomerates. *Russ. J. Appl. Chem.*, 2019, **92**, P. 171–180.

[6] Rogacheva A., Shamsutdinova A., Brichkov A., Larina T., Paukshtis E., Kozik V. Synthesis and Properties of Spherical Catalysts TiO_2-SiO_2/M_xO_y (M=Co and Cr). *AIP Conf. Proc.*, 2017, **1899**, P. 020007.
[7] Rogacheva A.O., Buzaev A.A., Brichkov A.S., Khalipova O.S., Klestov S.A., Paukshtis E.A., Kozik V.V. Catalytically active composite material based on TiO_2/Cr_2O_3 hollow spherical particles. *Kinet. Catal.*, 2019, **60**(4), P. 484–489.
[8] Chandra P., Doke D.S., Umbarkara S.B., Birada A.V. One-pot synthesis of ultrasmall MoO_3 nanoparticles supported on SiO_2, TiO_2, and ZrO_2 nanospheres: an efficient epoxidation catalyst. *J. Mater. Chem. A.*, **2**(44), 2014, P. 219060–19066.
[9] Ion exchange method for preparing metal oxide microspheres. Patent. 3438749 USA, Lonadier F.D., Brown W.B., Fushimi F.C., Silver G.L., p. 3.
[10] Apblett A.W., Kuriyavar S.I., Kiran B.P. Preparation of micron-sized spherical porous iron oxide particles. *J. Mater. Chem.*, 2003, **13**, P. 983–985.
[11] Castro I.A.D., Datta R.S., Ou J.Z., Gomez A.C., Sriram S., Daeneke T., Zadeh K.K. Molybdenum oxides from fundamentals to functionality. *Adv. Mater.*, 2017, **29**, P. 1701619.
[12] Santos-Beltrán M., Paraguay-Delgado F., Garc´ıa R., Antúnez-Flores W., Ornelas-Gutiérrez C., Beltrán A.S. Fast methylene blue removal by MoO_3 nanoparticles. *J. Mater. Sci: Mater. Electron.*, 2017, **28**, P. 2935–2948.
[13] Liu K., Huang X., Pidko E.A., Emiel J.M. MoO_3–TiO_2 synergy in oxidative dehydrogenation of lactic acid to pyruvic acid, *Green Chem.*, 2017, **19**, P. 3014–3022.
[14] Li C.J., Tseng C.M., Lai S.N., Yang C.R., Hung W.H. Photocatalytic activities enhanced by Au-plasmonic nanoparticles on TiO_2 nanotube photoelectrode coated with MoO_3. *Nanoscale Res. Lett.*, 2017, **12**, P. 560–566.
[15] Wang X., Cui W., Chen M., Xu Q. Supercritical CO_2-assisted phase transformation from orthorhombic to hexagonal MoO_3. *Mater. Lett.*, 2017, **201**, P. 129–132.
[16] Bian L., Wang S.P., Ma X.B. The effect of catalyst preparation on the activity of MoO_3-SiO_2 catalyst in transesterification of diethyl oxalate. *Kinet. Catal.*, 2014, **55**, P. 763–769.
[17] Kozik V.V., Brichkov A.S., Shamsutdinova A.N., Paukshtis E.A., Brichkova V.Y., Parmon V.N., Ivanov V.K. Stabilization of TiO_2–Co_3O_4 thin films on a glass fiber material by introduction of silica into the matrix. *Dokl. Phys. Chem.*, 2016, **470**, P. 154–157.
[18] Li Y., Yu H., Huang X., Wu Z., Xu H. Improved performance for polymer solar cells using CTAB-modified MoO_3 as an anode buffer layer. *Sol. Energy Mater. Sol. Cells*, 2017, **171**, P. 72–84.
[19] Kociołek-Balawejder E., Stanisławska E., Mucha I. Freeze dried and thermally dried anion exchanger doped with iron(III)(hydr)oxide – Thermogravimetric studies. *Thermochim. Acta*, 2019, **680**, P. 178359–178370.
[20] Kalistratova V.V., Rodin A.V., Emel'yanov A.S., Vidanov V.L., Milyutin V.V., Belova E.V., Shmidt O.V., Myasoedov B.F. Kinetics of thermal degradation of VP-1AP anion-exchange resin in the nitrate form. *Radiochem.*, 2018, **60**, P. 287–293.
[21] Ostroushko A.A., Mogil'nikov Yu.V., Ostroushko I.P. Synthesis of molybdenum- and vanadium-containing mixed oxides in polymer-salt systems. *Inorganic Materials*, 2000, **36**(12), P. 1256-1263.
[22] Ostroushko A.A., Mogil'Nikov Yu.V., Popov K.A. Thermal destruction of polymer-salt compositions containing d-metals in the form of oxygen-bearing anions. *Inorganic Materials*, 2000, **36**(6), P. 603–611.
[23] Bogdanov S.G., Ostroushko A.A., Valiev E.Z., Pirogov A.N., Teplykh A.E. Effect of acidity of polymer-salt composition on the formation mechanism of the tungsten and molybdenum oxide partiles. *J. of Surf. Investig.: X-Ray, Synchrotron and Neutron Techniques*, 2011, **5**(4), P. 21–32.
[24] Shamsutdinova A.N., Brichkov A.S., Paukshtis E.A., Larina T.V., Cherepanova S.V., Glazneva T.S., Kozik V.V. Composite TiO_2/fiberglass catalyst: Synthesis and characterization. *Catal. Commun.*, 2017, **89**, P. 64–68.
[25] Brichkov A.S., Shamsutdinova A.N., Khalipova O.S., Rogacheva A.O., Larina T.V., Cherepanova S.V., Glazneva T.S., Paukshtis E.A., Buzaev A.A., Kozik V.V., Chen Y.-W. Preparation of a fiberglass-supported Ni-Si-Ti oxide catalyst for oxidation of hydrocarbons: effect of SiO_2. *J. Chem. Technol. Biotechnol.*, 2019, **94**, P. 3618–3624.
[26] Leykin Y.A., Meychik N.R., Solovyov V.K. Acid-base equilibrium of polyamfolitov with pyridine and phosphate groups. *Russian J. Phys. Chem.*, 1978, **52**, P. 1420–1424.
[27] Busev A.I. *Analytical Chemistry of Molybdenum*. Ann Arbor-Humphrey Science Publishers, Moscow, 1969, 253 p.
[28] Kissinger H.E. Variation of peak temperature with heating rate in differential thermal analysis. *J. Res. Nat. Bur. Standards*, 1956, **57**, P. 217–221.
[29] Kissinger H.E. Reaction kinetics in differential thermal analysis. *Anal. Chem.*, 1958, **29**, P. 1702–1706.
[30] Zeng W., Zhou H., Chen Q., Chen X. Kinetics of thermal decomposition of synthetic gibbsite. *Transactions of Nonferrous Metals Society of China*, 1993, **3**(2), P. 41–44.
[31] Yin Z., Li X., Chen Q. Study on the kinetics of the thermal decomposition of ammonium molybdates. *Thermochim. Acta.*, 2000, **352–353**, P. 107–110.
[32] Gul S., Shah A.A., Bilal S. Calculation of activation energy of degradation of polyaniline-dodecylbenzene sulfonic acid salts via TGA. *J. Sci. Innovative Research*, 2013, **2**, P. 673–684.
[33] Šatava V., Škvara Fr. Mechanism and kinetics of the decomposition of solids by a thermogravimetric method. *J. Am. Ceram. Soc.*, 1969, **52**, P. 591–595.
[34] Bortolotti M., Lonardelli I. ReX. Cell: a user-friendly program for powder diffraction indexing. *J. Appl. Cryst.*, 2013, **46**, P. 259–261.
[35] Boultif A., Louër D. Powder pattern indexing with the dichotomy method. *J. Appl. Cryst.*, 2004, **37**, P. 724–731.
[36] Momma K., Izumi F. VESTA 3 for three-dimensional visualization of crystal, volumetric and morphology data. *J. Appl. Crystallogr.*, 2011, **44**, P. 1272–1276.
[37] Crystallography Open Database: www.crystallography.net.

NANOSYSTEMS: PHYSICS, CHEMISTRY, MATHEMATICS, 2021, 12 (2), P. 246–251

High performance tandem perovskite-silicon solar cells with very large bandgap photoelectrodes

A. B. Nikolskaia[1], M. F. Vildanova[1], S. S. Kozlov[1], O. V. Almjasheva[2], V. V. Gusarov[2,3], O. I. Shevaleevskiy[1]

[1]Department of Solar Photovoltaics, Institute of Biochemical Physics RAS, Kosygin St. 4, Moscow, 119334, Russia

[2]Saint Petersburg Electrotechnical University "LETI", Saint-Petersburg, Professora Popova St., 5, Saint Petersburg, 197376, Russia

[3]Ioffe Physical-Technical Institute RAS, Politekhnicheskaya St., 26, Saint Petersburg, 194021, Russia

shevale2006@yahoo.com, victor.v.gusarov@gmail.com

PACS 84.60.Jt **DOI 10.17586/2220-8054-2021-12-2-246-251**

Nanostructured layers of metal oxides with very large bandgaps ($E_g > 5$ eV), such as ZrO_2 and HfO_2, were used as photoelectrodes in semitransparent perovskite solar cells (PSCs) with the device architecture of glass/FTO/c-TiO_2/ZrO_2 (or HfO_2)/$CH_3NH_3PbI_3$/PTAA/PEDOT:PSS/FTO/glass. The obtained PSCs were used as top elements for manufacturing high-performance four-terminal tandem perovskite-silicon solar cells. The comparative analysis of photovoltaic parameters measured for PSCs, crystalline silicon (c-Si) solar cells and tandem PSC/c-Si solar cells demonstrated that the application of very large-bandgap materials allows to improve the PSC performance and to increase the efficiency of tandem PSC/c-Si solar cell up to $\sim$24% in comparison with a standalone c-Si solar cell.

Keywords: photoelectrode, perovskite, solar cells, tandem solar cells, solar photovoltaics.

Received: 3 January 2021

Revised: 1 April 2020

1. Introduction

To date, well-developed crystalline silicon (c-Si) solar cells under AM1.5G (1000 W/m^2) lighting conditions demonstrate nearly 25% power conversion efficiency (PCE), that is already approaching their practical limit [1, 2]. The further increase of c-Si cell performance can be attained by integration into the tandem configuration. Extensive possibilities for the design of tandem cells are associated with the recent appearance of effective perovskite solar cells (PSCs) [3,4]. This type of solar cell, in which a perovskite layer based on organic-inorganic hybrid compounds with a common ABX_3 (A – $CH_3NH_3^+$, $HC(NH_2)_2^+$, B – Pb^{2+}, Sn^{2+}, X – I^-, Br^-, Cl^-) formula is deposited on the surface of a nanostructured photoelectrode (usually TiO_2), has attracted a considerable interest as the most demanded and cost-effective photovoltaic (PV) devices for the future mass production [5–7].

In tandem, perovskite-silicon (PSC/c-Si) solar cells PSCs are usually used as top elements in combination with bottom c-Si cells [8,9]. Tandem PSC/c-Si solar cells are commonly fabricated in two configurations: two-terminal and four-terminal [10,11]. The overall current output of the two-terminal tandem cell is limited by the lower of the currents generated by the connected in series individual sub cells That is why a four-terminal tandem configuration, in which the top and bottom cells are mechanically stacked and electrically isolated from each other, is preferable [12, 13].

The efficiency and the degree of transparency of top cell strongly affects the tandem PSC/c-Si solar cell performance and depend on the structure and transport characteristics of the photoelectrodes used in PSCs [14–16]. In our previous works [17, 18], we demonstrated that very wide-bandgap nanostructured materials, like ZrO_2 with E_g values of 5.26 and 5.53 eV for two direct band transitions and HfO_2 with the E_g value of 5.56 eV for indirect band transition, can be successfully used as photoelectrodes for PSCs. The incorporation of mesoscopic ZrO_2 (or HfO_2) layer into the PSCs with the standard architecture of glass/FTO/c-TiO_2/ZrO_2 (or HfO_2)/$CH_3NH_3PbI_3$/Spiro-MeO-TAD/Au led to the improvement of PV performance of PSCs [17]. However, these PV devices cannot be used as top elements in tandem systems because of the low optical transparency of Spiro-MeO-TAD layer and Au contacts in the visible range of the visible light spectrum. PTAA or P3HT as a hole transporting material and PEDOT:PSS-based counter electrode can be used for fabrication semi-transparent PSCs [19, 20].

In this work, photoelecrodes based on very wide-bandgap materials such as ZrO_2 and HfO_2 ($E_g > 5$ eV) were successfully used for fabrication of semi-transparent PSCs with the cell architecture of glass/FTO/c-TiO_2/ZrO_2 (or HfO_2)/$CH_3NH_3PbI_3$/PTAA/PEDOT:PSS/FTO/glass under ambient conditions. The obtained PSCs were used as top

elements for manufacturing highly efficient four-terminal tandem PSC/c-Si solar cells. The PV performance of PSCs, standalone c-Si and tandem PSC/Si solar cells was studied. The obtained results provide a novel effective approach to increase the overall efficiency of light conversion to electricity.

2. Experimental

2.1. Materials and samples preparation

ZrO_2 and HfO_2 nanoparticles were obtained by hydrothermal treatment of co-precipitated zirconium and hafnium hydroxides from solutions of the corresponding metal salts [21]. TiO_2 nanoparticles (P25 Aeroxide Degussa) were purchased from Sigma-Aldrich (USA) and were used for fabrication of state-of-the-art TiO_2 photoelectrode [22]. Thick pastes from MO_2 (where M=Ti, Zr or Hf) nanopowders were prepared in organic solvent following the method described in [23]. The pastes were dissolved in ethanol in mass ratio 1:5 and spin-coated onto FTO conductive glass (Solaronix, 2×2 cm) covered by compact layer (c-TiO_2) with subsequent annealing at 500°C for 30 min. Mesoscopic MO_2 photoelectrodes with thickness 180–220 nm were obtained.

Perovskite ($CH_3NH_3PbI_3$) layers were formed on MO_2 using a conventional one-step deposition method [24,25]. PTAA with Li-TFSI and 4-tert-Butylpyridine additives in toluene was used as a hole transporting material. It was drop-casted onto the perovskite surface and then covered by counter electrode of PEDOT:PSS/FTO according to the procedure described elsewhere [19]. PTAA, PEDOT:PSS, Li-TFSI and 4-tert-Butylpyridine were purchased from Sigma Aldrich. All the steps of PSC fabrication process were provided under ambient conditions with a relative humidity about 40%.

Samples of c-Si solar cells were kindly provided by the research group of G. Untila from Skobeltsyn Institute of Nuclear Physics, Moscow State University.

2.2. Characterization studies

The optoelectronic properties of MO_2 photoelectrodes were characterized using UV-vis spectroscopy (Shimadzu UV-3600 spectrophotometer (Shimadzu, Japan) with an ISR-3100 integrating sphere at wavelengths ranging from 300–1200 nm). The measurements of the PV parameters for PSCs fabricated, for c-Si solar cells and for tandem PSC/c-Si solar cells were provided under standard illumination conditions of 1000 W/m^2 (AM1.5G) using Semiconductor Characterization System (Keithley, USA). The incident photon-to-current conversion efficiency (IPCE) spectra were recorded using QEX10 Solar Cell Quantum Efficiency Measurement System (PV Measurements, USA) in the range of 300–1100 nm.

3. Results and discussion

Optical transmittance spectra of mesoscopic MO_2 photoelectrodes are plotted in Fig. 1. All samples are characterized by a high degree of transparency in the visible light range and can be used for constructing top elements in tandem systems. It is seen that transmittance region is wider for very wide-bandgap materials (ZrO_2 and HfO_2) than for TiO_2 due to the area of 250–350 nm in UV radiation range. This correlates with energy bandgap data obtained in earlier studies [18].

Semi-transparent PSCs with the architecture glass/FTO/c-TiO_2/MO_2/$CH_3NH_3PbI_3$/PTAA/PEDOT: PSS/FTO/glass were fabricated under ambient conditions. Comparative $J-V$ curves for all samples recorded under standard illumination (1000 W/m^2, AM1.5G) are shown in Fig. 2. The PV parameters of PSCs including short circuit current density (J_{SC}), open circuit voltage (V_{OC}), fill factor (*FF*) and power conversion efficiency (PCE) are listed in Table 1.

TABLE 1. The PV characteristics of PSC devices based on mesoscopic MO_2 photoelectrodes

Photoelectrode type	J_{SC}, mA/cm^2	V_{OC}, V	FF, a.u.	PCE, %
TiO_2	17.58 ± 0.17	0.99 ± 0.01	0.69 ± 0.01	11.94 ± 0.15
ZrO_2	16.30 ± 0.24	1.06 ± 0.02	0.74 ± 0.02	12.72 ± 0.29
HfO_2	13.40 ± 0.32	1.06 ± 0.01	0.70 ± 0.02	9.96 ± 0.36

PSC devices with mesoscopic TiO_2 photoelectrodes show the average PCE of 11.94%. The substitution of TiO_2 layer by a very wide-bandgap materials leads to the improvement of the V_{OC} values, which is attributed to the difference in the conduction band positions of TiO_2 and ZrO_2 (HfO_2) [17, 18]. However, a drop in J_{SC} values is found with incorporation of ZrO_2 and HfO_2 materials, which can be explained by their insulating nature [18].

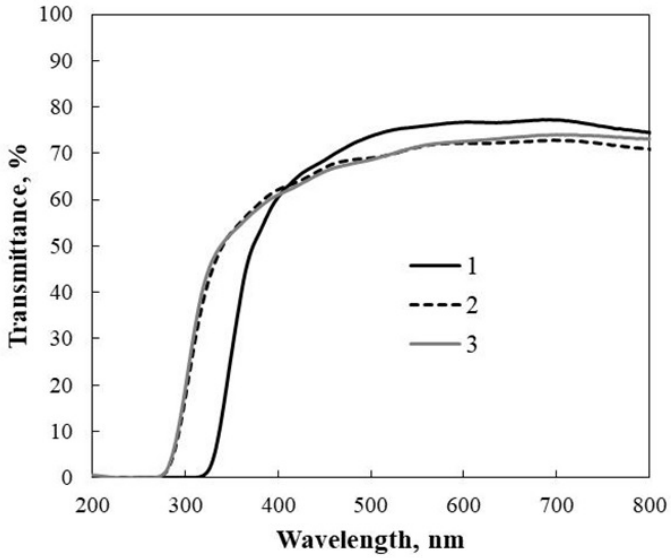

FIG. 1. Optical transmittance spectra of mesoscopic MO_2 photoelectrodes (1 – TiO_2, 2 – ZrO_2, 3 – HfO_2)

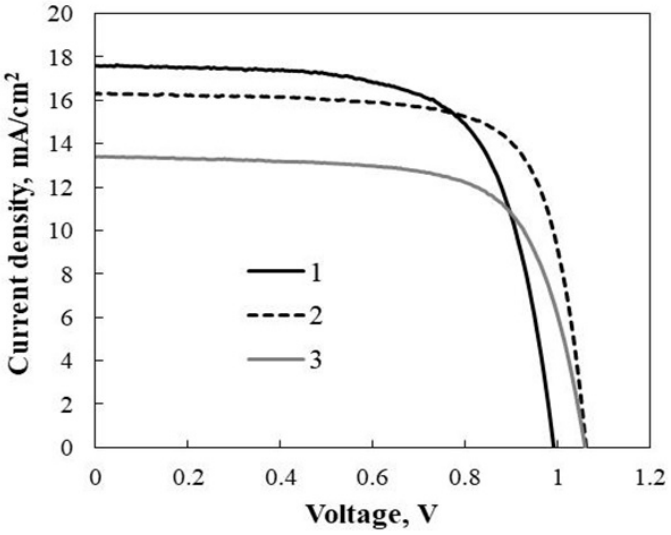

FIG. 2. $J - V$ curves for the PSC devices based on mesoscopic MO_2 photoelectrodes (1 – TiO_2, 2 – ZrO_2, 3 – HfO_2)

The highest average performance of 12.72% is demonstrated by PSC samples with ZrO_2 photoelectrode and it is 6.5% higher than for TiO_2-based device. The observed difference is due to various charge transfer mechanisms. The charge transfer in TiO_2 layer is carried out through the conduction band, whereas the charge transfer in ZrO_2 photoelectrode occurs via the hopping conduction mechanism through localized states within forbidden zone [17]. As a result, the recombination losses at the ZrO_2/perovskite interface are lower than for TiO_2/perovskite. The PCE of HfO_2-based PSCs is lower than for others due to lower J_{SC} values. This is more likely attributed to the insufficient layer morphology and less favorable positions of the electronic states in HfO_2 forbidden zone [18].

All fabricated PSC devices based on mesoscopic MO_2 photoelectrodes were used as top elements in four-terminal tandem PSC/c-Si solar cells. The c-Si solar cells were used as bottom elements and were mechanically stacked with PSCs according scheme on Fig. 3a. The $J - V$ curves measured under standard illumination (1000 W/m^2, AM1.5G) as well as the IPCE data for standalone c-Si sample and for c-Si elements in combination with PSCs are shown on Fig. 3b and Fig. 3c. According to the IPCE spectra, tandem PSCs/c-Si systems provide efficient output in a wide range

(from 300 to 1000 nm) of solar spectrum. The performance of the bottom c-Si cells is shown to be nearly independent on the type of material used as photoelectrode in the top PSC (Fig. 3c).

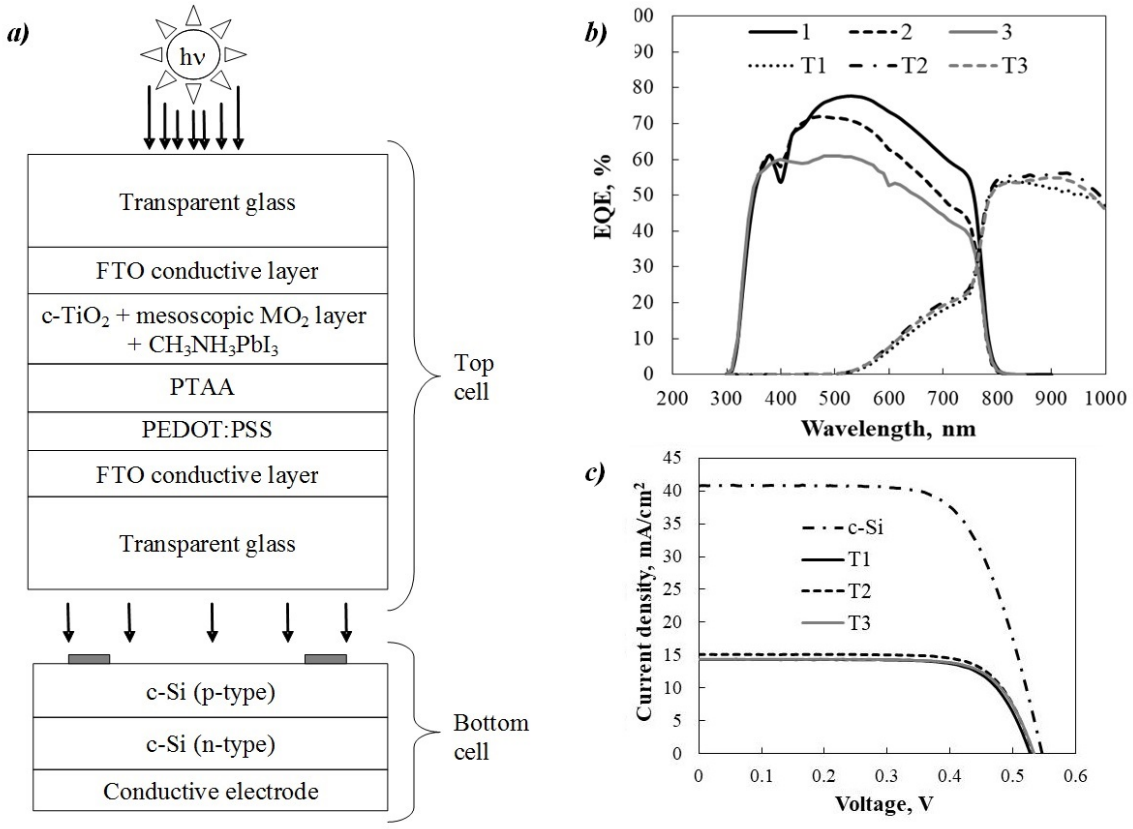

FIG. 3. Scheme of four-terminal tandem PSC/c-Si solar cell (a), the IPCE spectra (b) and the $J-V$ curves (c) for c-Si solar cell, PSCs with mesoscopic MO_2 photoelectrodes (1 – TiO_2, 2 – ZrO_2, 3 – HfO_2) and for c-Si in combination with PSC (T1 – PSC with TiO_2, T2 – PSC with ZrO_2, T3 – PSC with HfO_2)

The PV parameters of the bottom c-Si cells and comparative charts, illustrating the relative contributions of both top and bottom sub-cells into the resulting PCE of tandem PSC/c-Si solar cells, are presented in Table 2 and Fig. 4. The overall conversion efficiency for all tandem systems is higher than for standalone c-Si and strongly depends on the top cell PCE. The best performance under standard illumination conditions (1000 W/m^2, AM1.5G) was achieved for PSC based on mesoscopic ZrO_2 photoelecrode in combination with c-Si. It was found to be 18.69%, which exceeded the PCE of a standalone c-Si solar cell by $\sim 24\%$. The obtained data reveals that PSCs based on very wide-bandgap materials can be successfully used as top elements in tandem systems with the bottom c-Si cells and its allows to significantly increase the overall conversion efficiency. Also, mesoscopic ZrO_2-based material can be an efficient alternative to standard TiO_2 layer as photoelectrode for PSCs.

4. Conclusions

Photoelecrodes based on very wide-bandgap materials such as ZrO_2 and HfO_2 ($E_g > 5$ eV) were successfully used for fabrication of high efficient semi-transparent PSCs with the cell architecture of glass/FTO/c-TiO_2/ZrO_2 (or HfO_2)/$CH_3NH_3PbI_3$/PTAA/PEDOT:PSS/FTO/glass under ambient conditions at high humidity levels ($\sim 40\%$). The best PCE of 12.72% (1000 W/m^2, AM1.5G) was demonstrated by PSC samples with ZrO_2 photoelectrode and it was 6.5% higher than for state-of-the-art TiO_2-based device.

Fabricated PSCs were used as top elements in four-terminal tandem PSC/c-Si solar cells. Comparative analysis of PV parameters for bottom c-Si elements in combination with PSC based on TiO_2, ZrO_2 or HfO_2 photoelectrodes revealed that the PCE value of a top cell was a major factor affecting the overall tandem cell performance. The best PCE was achieved for the tandem PSC/c-Si solar cell with PSC based on ZrO_2 photoelectrode. It was found to be 18.69% (1000 W/m^2, AM1.5G) and it exceeded the PCE value for a standalone c-Si solar cell by 24%.

TABLE 2. The PV characteristics of c-Si solar cells in combination with PSC devices (T1 – PSC with TiO_2, T2 – PSC with ZrO_2, T3 – PSC with HfO_2)

Tandem type	J_{SC}, mA/cm^2	V_{OC}, V	FF, a.u.	PCE, %
Standalone c-Si	40.79 ± 0.23	0.55 ± 0.02	0.68 ± 0.02	15.07 ± 0.11
T1	14.32 ± 0.14	0.53 ± 0.01	0.74 ± 0.01	5.61 ± 0.15
T2	15.10 ± 0.18	0.54 ± 0.02	0.74 ± 0.01	5.97 ± 0.22
T3	14.36 ± 0.19	0.54 ± 0.01	0.74 ± 0.02	5.71 ± 0.22

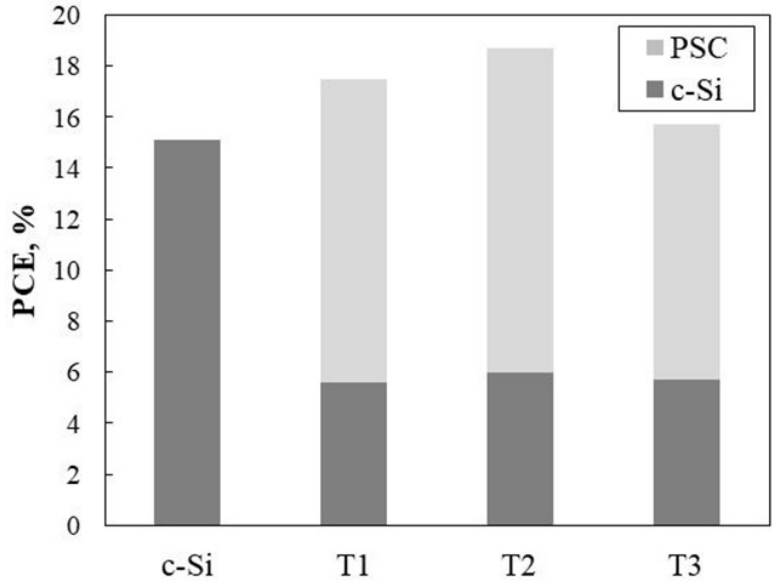

FIG. 4. Comparative diagrams for standalone c-Si solar cell and for four-terminal tandem PSC/c-Si solar cells (T1 – PSC with TiO_2, T2 – PSC with ZrO_2, T3 – PSC with HfO_2)

The obtained results demonstrated that application of very wide-bandgap materials as photoelectrodes in PSCs allows not only to improve their performance under ambient conditions but also to increase significantly the overall conversion efficiency of four-terminal tandem PSC/c-Si solar cells.

Acknowledgements

This work is supported by the Russian Foundation for Basic Research according to the research project No19-08-01042.

References

[1] Green M.A., Dunlop E.D., Hohl-Ebinger J., Yoshita M., Kopidakis N., Hao X. Solar cell efficiency tables (version 56). *Prog. Photovolt.: Res. Appl.*, 2020, **28**, NREL/JA-5900-77544.

[2] Battaglia C., Cuevas A., De Wolf S. High-efficiency crystalline silicon solar cells: status and perspectives. *Energy Environ. Sci.*, 2016, **9**, P. 1552–1576.

[3] Yu Z., Leilaeioun M., Holman Z. Selecting tandem partners for silicon solar cells. *Nat. Energy*, 2016, **1**, P. 16137.

[4] Leijtens T., Bush K.A., Prasanna R., McGehee M.D. Opportunities and challenges for tandem solar cells using metal halide perovskite semiconductors. *Nat. Energy*, 2018, **3**, P. 828–838.

[5] Park N.G. Research direction toward scalable, stable, and high efficiency perovskite solar cells. *Adv. Energy Mater.*, 2020, **10**(13), P. 1903106.

[6] Tejeda A., Choy W.C.H., Deleporte E., Graetzel M. Hybrid perovskites for photovoltaics and optoelectronics. *J. Phys. D: Appl. Phys.*, 2020, **53**(7), P. 070201.

[7] Ansari M.I.H., Qurashi A., Nazeeruddin M.K. Frontiers, opportunities, and challenges in perovskite solar cells: a critical review. *J. Photochem. Photobiol. C: Photochem. Rev.*, 2018, **35**, P. 1–24.

[8] Jiang Y., Almansouri I., Huang S., Young T., Li Y., Peng Y., Hou Q., Spiccia L., Bach U., Cheng Y., Greena M.A., Ho-Baillie A. Optical analysis of perovskite/silicon tandem solar cells. *J. Mater. Chem. C*, 2016, **4**, P. 5679–5689.

[9] Messmer C., Goraya B.S., Nold S., Schulze P.S., Sittinger V., Schön J., Goldschmidt J.C., Bivour M., Glunz S.W., Hermle M. The race for the best silicon bottom cell: efficiency and cost evaluation of perovskite–silicon tandem solar cells. *Prog. Photovolt.: Res. Appl.*, 2020, https://doi.org/10.1002/pip.3372.

[10] Dewi H.A., Wang H., Li J., Thway M., Sridharan R., Stangl R., Lin F., Aberle A.G., Mathews N., Bruno A., Mhaisalkar S. Highly efficient semitransparent perovskite solar cells for four terminal perovskite-silicon tandems. *ACS Appl. Mater. Interfaces*, 2019, **11**(37), P. 34178–34187.

[11] Chen B., Zheng X., Bai Y., Padture N.P., Huang J. Progress in tandem solar cells based on hybrid organic–inorganic perovskite. *Adv. Energy Mater.*, 2017, **7**, P. 1602400.

[12] Jaysankar M., Filipic M., Zielinski B., Schmager R., Song W., Qiu W., Paetzold U.W., Aernouts T., Debucquoy M., Gehlhaar R., Poortmans J. Perovskite–silicon tandem solar modules with optimized light harvesting. *Energ. Environ. Sci.*, 2018, **11**, P. 1489–1498.

[13] Löper P., Moon S.-J., de Nicolas S.M., Niesen B., Ledinsky M., Nicolay S., Bailat J., Yum J.-H., De Wolf S., Ballif C. Organic–inorganic halide perovskite/crystalline silicon four-terminal tandem solar cells. *Phys. Chem. Chem. Phys.*, 2015, **17**, P. 1619–1629.

[14] Noh M.F.M., Teh C.H., Daik R., Lim E.L., Yap C.C., Ibrahim M.A., Ludin N.A., Yusoff A.R., Jange J., Teridi M.A.M. The architecture of the electron transport layer for a perovskite solar cell. *J. Mater. Chem. C*, 2018, **6**, P. 682–712.

[15] Wang K., Olthof S., Subhani W.S., Jiang X., Cao Y., Duan L., Wang H., Du M., Liu S. Novel inorganic electron transport layers for planar perovskite solar cells: progress and prospective. *Nano Energy*, 2020, **68**, P. 104289.

[16] Mahmood K., Sarwar S., Mehran M.T. Current status of electron transport layers in perovskite solar cells: materials and properties. *RSC Adv.*, 2017, **7**, P. 17044–17062.

[17] Larina L.L., Alexeeva O.V., Almjasheva O.V., Gusarov V.V., Kozlov S.S., Nikolskaia A.B., Vildanova M.F., Shevaleevskiy O.I. Very wide-bandgap nanostructured metal oxide materials for perovskite solar cells. *Nanosystems: Physics, Chemistry, Mathematics*, 2019, **10**(1), P. 70–75.

[18] Vildanova M.F., Nikolskaia A.B., Kozlov S.S., Shevaleevskiy O.I. Charge transfer mechanisms in multistructured photoelectrodes for perovskite solar cells. *J. Phys.: Conf. Ser.*, 2020, **1697**, P. 012187.

[19] Heo H., Han H.J., Lee M., Song M., Kim D.H., Im S.H. Stable semi-transparent $CH_3NH_3PbI_3$ planar sandwich solar cells. *Energ. Environ. Sci.*, 2015, **8**(10), P. 2922.

[20] Chen B., Bai Y., Yu Z., Li T., Zheng X., Dong Q., Shen L., Boccard M., Gruverman A., Holman Z., Huang J. Efficient semitransparent perovskite solar cells for 23.0% efficiency perovskite/silicon four terminal tandem cells. *Adv. Energy Mat.*, 2016, **6**(19), P. 1601128.

[21] Vildanova M.F., Nikolskaia A.B., Kozlov S.S., Karyagina O.K., Larina L.L., Shevaleevskiy O.I., Almjasheva O.V., Gusarov V.V. Nanostructured ZrO_2–Y_2O_3-based system for perovskite solar cells. *Doklady Physical Chemistry*, 2019, **484**(2), P. 36–38.

[22] Nikolskaia A., Vildanova M., Kozlov S., Tsvetkov N., Larina L., Shevaleevskiy O. Charge transfer in mixed phase TiO_2 photoelectrodes for perovskite solar cells. *Sustainability*, 2020, **12**, P. 788.

[23] Ito S., Chen P., Comte P., Nazeeruddin M.K., Liska P., Péchy P., Grätzel M. Fabrication of screen-printing pastes from TiO_2 powders for dye?sensitized solar cells. *Prog. Photovolt.: Res. Appl.*, 2007, **15**, P. 603–612.

[24] Nikolskaia A.B., Kozlov S.S., Vildanova M.F., Shevaleevskiy O.I. Power conversion efficiencies of perovskite and dye-sensitized solar cells under various solar radiation intensities. *Semiconductors*, 2019, **53**(4), P. 540–544.

[25] Ahn N., Son D.-Y., Jang I.-H., Kang S.M., Choi M., Park N.-G. Highly reproducible perovskite solar cells with average efficiency of 18.3% and best efficiency of 19.7% fabricated via lewis base adduct of lead (II) iodide. *J. Am. Chem. Soc.*, 2015, **137**(27), P. 8696–8699.

NANO ФИХМ

NANOSYSTEMS:

PHYSICS, CHEMISTRY, MATHEMATICS

INFORMATION FOR AUTHORS

The journal publishes research articles and reviews, and also short scientific papers (letters) which are unpublished and have not been accepted for publication in other magazines. Articles should be submitted in English. All articles are reviewed, then if necessary come back to the author to completion.

The journal is indexed in Web of Science Core Collection (Emerging Sources Citation Index), Chemical Abstract Service of the American Chemical Society, Zentralblatt MATH and in Russian Scientific Citation Index.

Author should submit the following materials:

1. Article file in English, containing article title, the initials and the surname of the authors, Institute (University), postal address, the electronic address, the summary, keywords, MSC or PACS index, article text, the list of references.
2. Files with illustrations, files with tables.
3. The covering letter in English containing the article information (article name, MSC or PACS index, keywords, the summary, the literature) and about all authors (the surname, names, the full name of places of work, the mailing address with the postal code, contact phone number with a city code, the electronic address).
4. The expert judgement on possibility of publication of the article in open press (for authors from Russia).

Authors can submit a paper and the corresponding files to the following addresses: nanojournal.ifmo@gmail.com, popov1955@gmail.com.

Text requirements

Articles should be prepared with using of text editors MS Word or LaTex (preferable). It is necessary to submit source file (LaTex) and a pdf copy. In the name of files the English alphabet is used. The recommended size of short communications (letters) is 4-6 pages, research articles– 6-15 pages, reviews – 30 pages.

Recommendations for text in MS Word:

Formulas should be written using Math Type. Figures and tables with captions should be inserted in the text. Additionally, authors present separate files for all figures and Word files of tables.

Recommendations for text in LaTex:

Please, use standard LaTex without macros and additional style files. The list of references should be included in the main LaTex file. Source LaTex file of the paper with the corresponding pdf file and files of figures should be submitted.

References in the article text are given in square brackets. The list of references should be prepared in accordance with the following samples:

[1] Surname N. *Book Title*. Nauka Publishing House, Saint Petersburg, 2000, 281 pp.
[2] Surname N., Surname N. Paper title. *Journal Name*, 2010, **1** (5), P. 17-23.
[3] Surname N., Surname N. Lecture title. In: Abstracts/Proceedings of the Conference, Place and Date, 2000, P. 17-23.
[4] Surname N., Surname N. Paper title, 2000, URL: http://books.ifmo.ru/ntv.
[5] Surname N., Surname N. Patent Name. Patent No. 11111, 2010, Bul. No. 33, 5 pp.
[6] Surname N., Surname N. Thesis Title. Thesis for full doctor degree in math. and physics, Saint Petersburg, 2000, 105 pp.

Requirements to illustrations

Illustrations should be submitted as separate black-and-white files. Formats of files – jpeg, eps, tiff.

NANOSYSTEMS:

PHYSICS, CHEMISTRY, MATHEMATICS

Журнал зарегистрирован
Федеральной службой по надзору в сфере связи, информационных технологий и массовых коммуникаций
(свидетельство ПИ № ФС 77 - 49048 от 22.03.2012 г.)
ISSN 2220-8054

Учредитель: федеральное государственное автономное образовательное учреждение высшего образования
«Санкт-Петербургский национальный исследовательский университет информационных технологий, механики и оптики»

Издатель: федеральное государственное автономное образовательное учреждение высшего образования
«Санкт-Петербургский национальный исследовательский университет информационных технологий, механики и оптики»

Отпечатано в Учреждении «Университетские телекоммуникации»
Адрес: 197101, Санкт-Петербург, Кронверкский пр., 49

Подписка на журнал НФХМ
На второе полугодие 2021 года подписка осуществляется через
ОАО «АРЗИ», подписной индекс Э57385